Université de Lille

Thèse de Doctorat

Université Lille 1, Sciences et Technologies

and

Xiamen University

Novel Fischer-Tropsch Catalysts Based on Mesoporous Zeolites and Carbon Materials for the Production of Gasoline-range Hydrocarbons and Lower Olefins

PhD candidate: Mr Kang Cheng

N°: 41675
NIP: 11309643

Université Lille 1 – Sciences et Technologies

Ecole Doctorale des Sciences de la Matière et du Rayonnement

and

Xiamen University

PhD thesis

For obtaining a title of

Doctor of Université Lille 1 - Sciences et Technologies

Spécialité: Molécules et Matière Condensée

and a title of

Doctor of Science of Xiamen University

by

Kang CHENG

Novel Fischer-Tropsch Catalysts Based on Mesoporous Zeolites and Carbon Materials for the Production of Gasoline-range Hydrocarbons and Lower Olefins

Publicly defended in University Lille 1 on January 22nd, 2015

Jury members:

Reviewers :	Prof. Minghua Qiao, Université Fudan (Chine)
	Dr Cuong Pham-Huu, Directeur de recherche CNRS, Université de Strasbourg
Invited Members:	Dr Valentin Valtchev, Directeur de recherche CNRS, ENSICAEN
	Dr. Mirella Virginie, Maitre de conférences, ENSCL
PhD supervisors:	Dr Andrei Khodakov, Directeur de recherche CNRS, Université Lille 1
	Prof. Ye Wang, Xiamen University

Contents

Preface **7**

Chapter 1. Literature Review **9**

1.1 General Introduction **9**

1.2 Liquid Fuel and Lower Olefins Produced via Fischer-Tropsch synthesis **10**

1.2.1 Brief introduction of Fischer-Tropsch synthesis 10

1.2.2 World-wide development of FT synthesis 11

1.3 Mechanism of FT reaction and remaining challenges **13**

1.3.1 Mechanism and characteristics of FT reaction 13

1.3.2 Catalysts for FT synthesis 15

1.3.3 Challenge for catalysts for Fischer-Tropsch synthesis 17

1.4 Selectivity Control **17**

1.4.1 Some key factors affecting selectivity in FT reaction 17

1.4.2 Non-ASF product distributions by secondary reactions 23

1.4.3 Introduction of hydrocracking catalysts 25

1.4.4 Application of novel mesoporous zeolites in catalysis 27

1.4.5 Preparation method of mesoporous zeolite 29

1.4.6 Application of mesoporous zeolite in FT synthesis 30

1.4.7 Strategies for increasing lower olefins selectivity in FT synthesis 32

1.5 The Objectives and Research Methods of this Thesis **33**

1.5.1 From bifunctional Ru-based catalyst to Co-based catalyst 33

1.5.2 Design of Co/meso-zeolite catalyst with high performance 34

1.5.3 The effect of catalysts pore size and sodium promotion 34

1.6 Outline of the Thesis **35**

1.7 Reference **37**

Chapter 2. Experimental **43**

2.1 Catalyst preparation **43**

2.1.1 Preparation of mesoporous beta zeolite 43

2.1.2 Preparation of mesoporous ZSM-5 zeolite 43

2.1.3 Preparation of silica supports with different pore diameters 44

2.1.4 Preparation of carbon supports 45

2.1.5 Preparation of supported Ru catalysts 46
2.1.6 Preparation of supported Co catalysts 46
2.1.7 Preparation of supported Fe catalysts 46
2.2 Evaluation of Catalytic Performance 47
2.2.1 Equipment for evaluation of Ru and Co catalysts 47
2.2.2 Equipment for evaluation of *n*-hexadecane hydrocracking 48
2.2.3 Equipment for catalytic evaluation of Fe catalysts 48
2.3 Analysis of Reaction Products 50
2.4 Catalyst Characterization 51
2.4.1 X-ray diffraction 51
2.4.2 Transmission electron microscopy images 51
2.4.3 Hydrogen temperature-programmed reduction 51
2.4.4 Temperature-programmed desorption of CO_2 52
2.4.5 Temperature-programmed desorption of NH_3 52
2.4.6 Temperature-programmed oxidation 52
2.4.7 Pulse oxidation 53
2.4.8 Surface area and pore size distribution 53
2.4.9 In situ magnetic characterization 53
2.4.10 Mössbauer spectrometry 55
2.4.11 H_2 chemisorption measurements 55
2.4.12 Infrared spectroscopy analysis 56
2.4.13 Elemental analysis 56
2.4.14 ^{27}Al MAS NMR 57
2.5 Reference 58
Chapter 3. Mesoporous Beta Zeolite-Supported Ruthenium Nanoparticles for Selective Conversion of Synthesis Gas to C_5-C_{11} Isoparaffins 59
3.1 Introduction 60
3.2 Result and Discussion 62
3.2.1 Structure of Mesoporous Beta Zeolites 62
3.2.2 Acidity of Mesoporous Beta Zeolites 65
3.2.3 Characterizations of Mesoporous Beta Zeolite-Supported Ru Catalysts 67
3.2.4 Catalytic Behaviors of H-meso-beta Supported Ru Catalysts for FT Synthesis 69
3.2.5 Performance of *n*-hexadecane hydrocarcking over Ru/H-meso-beta catalysts 72

3.3 Conclusion ····· 73

3.4 Reference ····· 75

Chapter 4. Selective Transformation of Syngas into Gasoline-Range Hydrocarbons over Mesoporous H-ZSM-5-Supported Cobalt Nanoparticles ····· 77

4.1 Introduction ····· 78

4.2 Results and Discussion ····· 80

4.2.1 Support effect of Co-based catalysts for FT synthesis ····· 80

4.2.2 Structural properties of mesoporous ZSM-5 ····· 82

4.2.3 Acidities of mesoporous ZSM-5 ····· 85

4.2.4 Preparation of zeolites with different Brønsted acid densities ····· 88

4.2.5 Preparation of Co nanoparticles loaded on ZSM-5 and mesoporous ZSM-5 ····· 89

4.2.6 Catalytic behaviors of Co/ZSM-5 and Co/meso-ZSM-5 for FT synthesis ····· 94

4.2.7 Catalyst deactivation ····· 97

4.2.8 The effect of Brønsted acid densities on hydrocarbon selectivity ····· 99

4.2.9 Catalytic behaviors of *n*-hexadecane hydrocracking ····· 102

4.3 Discussion on the roles of acidity and mesoporosity ····· 104

4.4 Conclusions ····· 106

4.5 Reference ····· 107

Chapter 5. Pore Size Effects in High Temperature Fischer-Tropsch Synthesis over Supported Iron Catalysts ····· 111

5.1 Introduction ····· 112

5.2 Results and discussion ····· 114

5.2.1 Support Porosity ····· 114

5.2.2 Iron species in mesoporous silicas ····· 116

5.2.3 Magnetic characterization of iron carbides ····· 121

5.2.4 FT performance of iron catalysts supported by mesoporous silicas ····· 126

5.2.5 Discussion of pore size effects on silica supported iron catalysts ····· 129

5.3 Conclusion ····· 133

5.4 Reference ····· 134

Chapter 6. Support Effects in High Temperature Fischer-Tropsch Synthesis on Iron Catalysts ····· 137

6.1 Introduction ····· 138
6.2 Result and Discussion ····· 138
6.2.1 Characterization of supports ····· 138
6.2.2 Calcined catalysts ····· 140
6.2.3 Catalyst activation in CO ····· 144
6.3 FT performance over carbon and silica supported Fe catalysts ····· 152
6.4 Conclusions ····· 155
6.5 Reference ····· 156
Chapter 7. The effect of Na addition over different supports in high temperature Fischer-Tropsch synthesis on iron catalysts ····· 159
7.1 Introduction ····· 160
7.2 Results and discussion ····· 161
7.2.1 Structure and surface groups of catalysts ····· 161
7.2.2 Activation with CO ····· 163
7.2.3 Effect of Na introduction on the basicity of catalysts ····· 166
7.2.4 Effect of Na introduction on the activity of iron carbides ····· 166
7.2.5 Fischer-Tropsch synthesis ····· 168
7.3 Conclusion ····· 177
7.4 Reference ····· 178
Chapter 8. General Conclusions and Perspectives ····· 181
8.1 General Conclusion ····· 181
8.1.1 Bifunctional FT catalysts for C_{5-11} isoparaffins ····· 181
8.1.2 Pore size effects for supported iron catalysts ····· 182
8.1.3 Support Effect on Performace of Iron FT Catalysts ····· 183
8.1.4 Na Effect on Performace of Iron FT Catalysts ····· 184
8.2 Perspectives ····· 185
8.2.1 Bifunctional FT catalysts ····· 185
8.2.2 Effect of support and promotion for iron catalysts in FT synthesis ····· 186

Abstract

Novel bifunctional Fischer-Tropsch (FT) catalysts were developed for the selective production of gasoline-range (C_5−C_{11}) hydrocarbons from syngas. These catalysts are constituted by ruthenium or cobalt nanoparticles and mesoporous zeolites. Our results reveal that heavier hydrocarbons form on metal nanoparticles, while hydrocarbon hydrocracking/isomerization occurs on the Brønsted acid sites of the catalysts. The zeolite mesoporosity contributes to suppressing formation of lighter (C_1−C_4) hydrocarbons. The selectivity of C_5−C_{11} hydrocarbons could reach 65-70% with a high ratio of isoparaffins to n-paraffins, markedly higher than the maximum value (~45%) expected from the theory.

The pore size effects, the effect of support chemical composition and sodium addition effect on the performance of iron catalysts in high temperature FT synthesis were also investigated in this thesis. It was found that larger iron oxide crystallites in large pore silicas were much easier to transform to iron carbides than smaller Fe_2O_3 crystallites in smaller pore supports. Higher FT reaction rates, better olefin selectivities were observed over iron catalysts supported by large pore silicas with higher concentration of iron carbide active phase. Iron catalysts supported on carbon nanotubes (CNT) and activated carbon showed very high activity in FT synthesis. This phenomenon was attributed to the formation of stable nanocomposites of iron carbide and magnetite. The interaction of Na with the catalysts strongly depends on the amount of added Na and type of the support. The strong interaction of Fe and Na promoter leads to higher olefin selectivity.

Keywords: Fischer-Tropsch synthesis; bifunctional; mesoporous zeolite; pore size effect; Na promoter; support effect; gasoline-range hydrocarbons; lower olefin

Résumé

Des catalyseurs Fischer-Tropsch bifonctionnels ont été mis en œuvre pour la production sélective d'hydrocarbures C_5-C_{11} à partir du gaz de synthèse. Ces catalyseurs ont été constitués de nanoparticules métalliques de ruthénium ou de cobalt, ainsi que de zéolithes mésoporeuses. Nos résultats démontrent que la synthèse d'hydrocarbures lourds implique des nanoparticules métalliques, tandis que les réactions d'hydrocraquage/isomérisation se produisent sur les sites acides Bronsted de ces catalyseurs. La mésoporosité des zéolithes contribue de facon très importante à la suppression de la formation d'hydrocarbures légers. La sélectivité en hydrocarbures C_5-C_{11} atteint 65-70% avec un rapport iso-paraffines/n-paraffines très élevé, beaucoup plus important que celui prédit par la théorie (~45%).

Les effets de la taille des pores, de la composition chimique du support et de l'ajout de sodium sur les performances des catalyseurs à base de fer pour la synthèse Fischer-Tropsch à haute température ont été aussi étudiés dans cette thèse. Nous avons découvert que les grosses cristallites d'oxyde de fer situées dans les pores larges de silice sont beaucoup plus faciles à transformer en nanoparticules de carbure de fer que les petits cristallites Fe_2O_3 dans les pores étroits du support. Des vitesses de réaction Fischer-Tropsch plus importantes, de meilleures sélectivités en oléfines ont été observées sur les catalyseurs à base de fer, à pores plus larges, supportés par les silices. Des catalyseurs à base de fer supportés par des nanotubes de carbone et du charbon actif ont présenté des activités très élevées dans la réaction Fischer-Tropsch. Ce phénomène a été attribué à la formation de nanocomposites stables de carbure de fer et de magnétite. L'interaction entre le sodium et le catalyseur dépend fortement du taux du promoteur et du type de support catalytique. Une interaction forte entre le fer et le sodium dans les catalyseurs promus nous a permis d'obtenir des sélectivités plus importantes en oléfines.

Mots-Clefs: synthèse Fischer-Tropsch; catalyseurs bifonctionnels; zéolithe mesoporeux; effet de la taille de pores; promoteur sodium; effet du support; hydrocarbures de coupe essence; oléfines légers

Preface

Fischer-Tropsch (FT) synthesis is a key reaction in the utilization of non-petroleum carbon resources, such as coal, nature gas, shale gas and biomass, for the sustainable production of clean liquid fuels and other valuable chemicals from synthesis gas (syngas, a mixture of H_2 and CO). The primary product of FT reaction follows the Anderson–Schulz–Flory (ASF) distribution because of the polymerization mechanism, which restricts the selectivity of desired products. Selectivity control is always one of the hot topics in this area. In this thesis, the story unfolds according to two plotlines: (1) design of bifunctional catalysts which integrated CO hydrogenation metals and acidic zeolites, with the target to transform syngas into gasoline fraction with high selectivity; (2) the effects of support, support pore size and Na promoter in high temperature Fischer-Tropsch synthesis over iron catalysts.

To transform syngas into gasoline-range hydrocarbons with high selectivity, catalytic behaviors of mesoporous beta zeolite supported Ru catalysts were investigated in Chapter 3. Compared with conventional oxide-supported catalysts, Ru/H-meso-beta exhibited a 67.2% selectivity of C_{5-11} hydrocarbons with mainly isoparaffins, which was much higher than that of maximum 45% predicted from ASF distribution. Brønsted acid sites provided by beta zeolite were supposed to be the active sites for cracking and isomerization of long-chain hydrocarbons. Bifunctional catalysts consisting of Ru nanoparticles and Brønsted acids showed high activity in both CO hydrogenation and *n*-hexadecane hydrocracking. The introduction of mesopores could significantly suppress the CH_4 and C_{2-4} selectivity.

Furthermore, in Chapter 4 we focus on Co/meso-zeolite catalyst which has potential industrial applications. Over oxide-supported Co catalysts, the product distribution of Fischer-Tropsch reaction was wide and unselective. The employment of H-form zeolites as the support decreased the selectivity to $C_{\geq 12}$ hydrocarbons and increased those to C_{5-11} isoparaffins. A 50.7% selectivity of C_{5-11} fraction was obtained over Co/H-ZSM-5(18) catalyst. By desilication method through NaOH treatment, a series of mesoporous ZSM-5 with different mesoporous structure were prepared. Co nanoparticles with an average particle size of 8 - 10 nm are integrated into the mesoporous ZSM-5. Similar to the Ru/H-meso-Beta catalyst, with the introduction of the mesoporous structure, Co/H-meso-ZSM-5 catalyst significantly reduced the selectivity of light hydrocarbons and increased the C_{5-11} selectivity

in Fischer-Tropsch reaction. Over Co/H-meso-ZSM-5-0.5M catalyst which was pretreated with NaOH solution of 0.5 M concentration, C_{5-11} selectivity could reach as high as 70.1% with C_{iso}/C_n ratio of 2.3. By careful characterizations, we concluded that a sufficient amount of Brønsted acid sites was necessary for hydrocracking and isomerization. The introduction of mesopores could effectively inhibit excessive cracking, so as to decrease the C_{1-4} selectivity and increase C_{5-11} selectivity in the final product of FT reaction.

Chapter 5 addresses the effect of support pore sizes on the structure and performance of iron catalysts supported by mesoporous silicas in high temperature Fischer-Tropsch synthesis. A combination of characterization techniques showed that the size of supported iron particles was controlled by silica pore sizes. The larger iron particles were localized in large pore supports. Iron carbidization with carbon monoxide resulted in preferential formation of Hägg iron carbide (χ-Fe_5C_2). The extent of iron carbidization was strongly affected by silica pore diameters. Larger iron oxide crystallites in large pore supports were much easier to carbidize than smaller iron oxide counterparts in small pore supports. Higher Fischer-Tropsch reaction rates, higher olefin and C_5^+ selectivity were observed over iron catalysts supported by large pore catalysts with higher concentration of iron carbide active phase.

Chapter 6 and chapter 7 studied the effect of support and sodium addition in the supported iron catalysts for FT synthesis in high temperature. Iron phase composition and dispersion in both calcined and activated catalysts were strongly affected by the support. Hematite was the major iron phase in calcined silica supported catalysts, while carbon supported counterparts contain magnetite. Iron catalysts supported on carbon nanotubes and activated carbon showed highest activity in Fischer-Tropsch, which could be attributed to the formation of composites of iron carbide and residual magnetite.The interaction of Na with the catalysts strongly depends on the amount of added Na and type of the support. In the case of alumina, the effect of Na over catalytic properties is weak due to the strong interaction with support. Over silica and CMK-3 iron oxide interacts with Na with formation of inactive mixed oxides but with partial suppression of hydrogenation activity and high olefin/paraffin ratio over rest carbide. The strong interaction of CNT with Fe results in formation of stable carbide but with strong effect of Na which results in the high contribution of olefins for short and long chain hydrocarbons. Excessive Na addition would result in a decline in CO conversion.

Chapter 1. Literature Review

1.1 General Introduction

Energy is the most important fundamental elements for human development and even survival [1]. The category of energy is broad, such as fossil energy, nuclear, wind, hydroenergy and solar. In a variety of fossil energy, oil is the most important industrial raw materials and primary energy, especially as the source of liquid fuels [2]. Although new energy is developing fast, the world-wide demand for liquid fuels is stilling increasing [3]. The need for liquid fuels will never completely go away and liquid fuels are very difficult to substitute [4]. BP Global predicts that liquid fuels demand will increase by 19 Mb/d, and total consumption will increase to 109 Mb/d (Figure 1-1) in 2035 [5]. The increment mainly comes from China, India and the Middle East. However, in recent years, high oil prices, the depletion of oil reserves, concerns about energy security, severe environmental situation have prompted scientists to develop other resources such as coal, biomass, natural gas to replace petroleum resources [6-8].

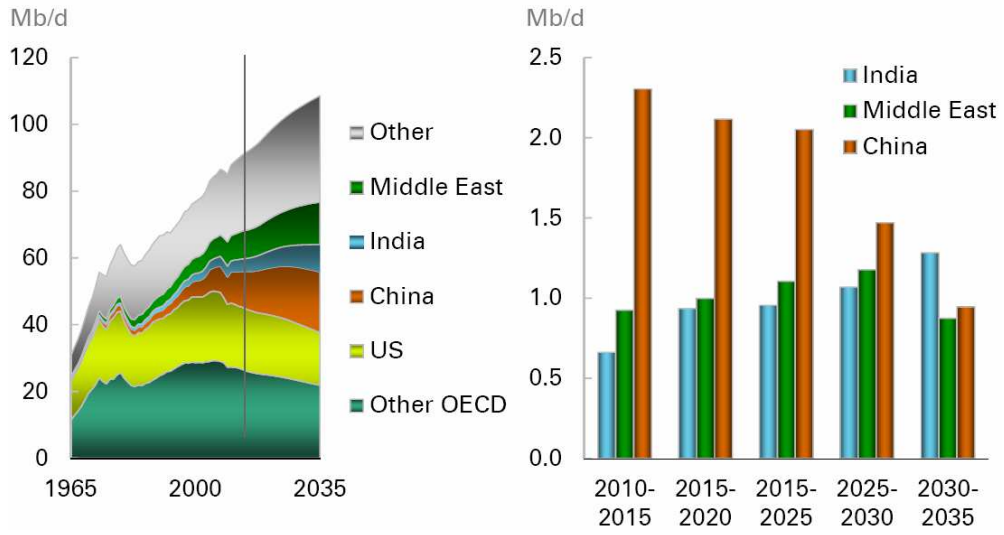

Figure 1-1. Worldwide liquid fuel demand by region and five year increments.[5]

Similar to liquid fuels, lower olefins are also very fundamental chemicals, which are primarily used for production of plastics, fibers, drugs [9, 10]. In the past decade, the production of light olefins has been growing rapidly with an increase of 4–5% every year and in 2010 the global yield reached 210 million tons [11]. Up to now, the traditional way to produce them is thermal or catalytic cracking of petroleum fractions [12, 13]. For the coming

petroleum depletion, new alternative routes are imperative to produce light olefins from other carbon resources such as coal, biomass or natural gas [14, 15].

1.2 Liquid Fuel and Lower Olefins Produced via Fischer-Tropsch synthesis

Most liquid fuels in widespread use are derived from fossil fuels. Some common properties of liquid fuels are that they are easy to transport and store, excellent combustion performance, easy to use for all engineering applications and home use [16]. There are numerous ways to produce liquid fuel from non-petroleum carbon resources, such as direct/indirect coal to liquid (CTL), gas to liquid, methanol and dimethyl ether (GTL) [17-20]. Most of these ways need to transform carbon-containing materials into syngas (a mixture of H_2 and CO) as platform molecules. Many of above-mentioned processes have proven technology, demonstration projects or small-scale production, and can be commercialized on a large scale. Recently, developing biomass-based method of preparing liquid fuels was also supposed to be highly importance [21-24].

The famous methanol-to-olefins process (MTO) has been developed and commercialized in China recently [25]. The methanol resource in this process comes from coal by CTL technology. Actually the lower olefins could be synthesized directly from syngas (FTO process), and this route has been considered for more than 50 years [15]. However, the olefin selectivity cannot meet the requirements of industrialization. Many efforts have been devoted to improve this process to replace the conventional petroleum route [15, 26-28].

1.2.1 Brief introduction of Fischer-Tropsch synthesis

In 1922, German scientists Franz Fischer and Hans Tropsch firstly discovered that at high temperature and pressure (673 K, >100 bar) aliphatic oxygenated hydrocarbons can be synthesized over alkaline iron catalyst. This process was then called synthol process. In 1923, they found that when using Fe/ZnO and Co/Cr_2O_3 catalysts, long-chain hydrocarbons are the main products of CO hydrogenation. In 1926, Franz Fischer and Hans Tropsch firstly published articles about the preparation of hydrocarbons from synthesis gas (syngas, a mixture of H_2 and CO), then, this reaction became known as the Fischer-Tropsch (FT) synthesis reaction [29, 30].

FT synthesis is an important process which can transform natural gas, coal, biomass and other carbon resources into liquid fuels, lower olefins and other chemicals [31]. Compared with petroleum resources, there are more reserves of coal and methane. Base on consumption

of the fossil energy in 2012, BP Global predicted that the reserve of petroleum could last for 52.9 years, while for natural gas and coal are 55.9 and 109 years respectively [32]. Biomass is a source of renewable energy that can be converted into liquid fuels [23]. As the reactant of FT reaction, syngas can be abundantly produced by steam reforming of methane and gasification of coal, biomass. Besides gasoline and diesel which can be directly used, the long-chain waxes in FT products are available through highly selective hydrocracking into gasoline, kerosene, diesel, and lubricant [33]. In addition, the FT products are free of sulphur, nitrogen, aromatic compounds and other toxic substances typically found in petroleum products, which is especially true for FT diesel with a very high cetane number [34, 35]. According to the different sources of raw materials, the above processes are known as CTL (Coal-To-Liquids), GTL (Gas-To-Liquids) and BTL (Biomass-To-Liquids) [24], and CTL and GTL process has been already industrialized [36].

1.2.2 World-wide development of FT synthesis

With a history of 90 years, commercial interests and research effort about FT synthesis fluctuates with oil prices and political conflicts [37]. During World War II, due to cutting of oil supply, Germany synthesized a large amount of transportation fuel from country's vast coal resources. A few decades later, South Africa invested significant research and construction projects in the FT process during its 1970s-1980s oil embargo. Besides, the world-wide oil crisis has prompted scientists to develop new technologies to synthesize transportation fuels, lower olefins and chemicals, including FT synthesis [29]. Figure 1-2 shows the variation tendency of academic papers about FT synthesis and the international crude oil prices from 2002 to 2013. It is clear that oil price is rising year by year, except a slump in 2008 because of international financial crisis, and now maintains at around 100 $/barrel. During this period of time, the passion of academic research about FT synthesis also increases persistently, and academic papers increased from 140 in 2002 to 522 in 2013.

In the past decade, some countries such as China and the U.S. with large reserves of natural and shale gas or coal are taking the lead on the research and development of direct processes for the production of C_{2-4} lower olefins to ensure a reliable supply of these bulk chemicals and to achieve independence from oil imports [15].

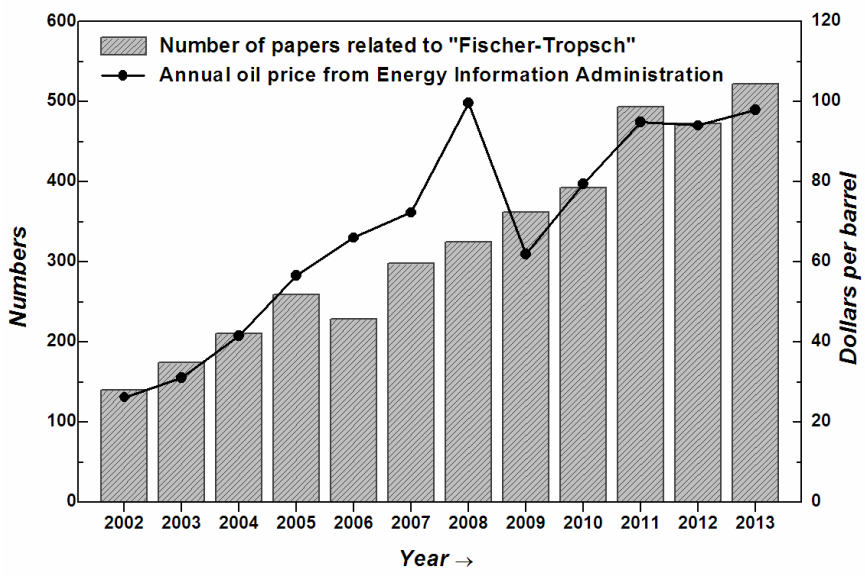

Figure 1-2. Number of papers related to "Fischer-Tropsch" from Web of Science VS annual oil price from US Energy Information Administration.

Figure 1-3 shows world-wide FT plants in operation or under construction in 2012. Distribution of FT plants show a strong regional character, often located on coal-rich or natural gas-rich country or region such as the Middle East, China, South Africa, and Malaysia. In addition, some developed countries such as the United States, Japan, and Italy are also developing FT technology and built up projects on a certain scale [38]. South Africa has the mature and applicable FT technology. In 1955, coal-based synthetic oil plant (Sasol-I) using precipitated iron catalyst reached a capacity of 8000 bpd. 1980 and 1982, Sasol has successively built Sasol-II and Sasol-III coal-based synthetic oil plants using high temperature fluidized bed technology. After nearly 60 years of development, now Sasol can produce 170 000 bpd of liquid fuels and other chemicals through Fischer Tropsch technology, occupying more than 40% domestic market share of liquid fuels [39]. With the development of coal and natural gas, more FT factories are built or planned. In 1993, Shell started running its FT plant to produce hydrocarbons fuels from natural gas in Malaysia. The technology is based on cobalt-based catalyst and fixed bed reactor with a capacity of 12 500 bpd. The 34 000 bpd Oryx GTL plant based on the Sasol Slurry Phase Distillate (SPD) process started to produce mainly diesel fuel and naphtha as a byproduct at Qatar in 2006. In addition, BP Global and Exxon Mobil also kept concerns about FT process built pilot plants. It can be said that FT technology has finally come to the stage of full-scale industry and worldwide commercialization [29]. The Fischer-Tropsch manufacturing capacity has now reached 400 000 bpd [24].

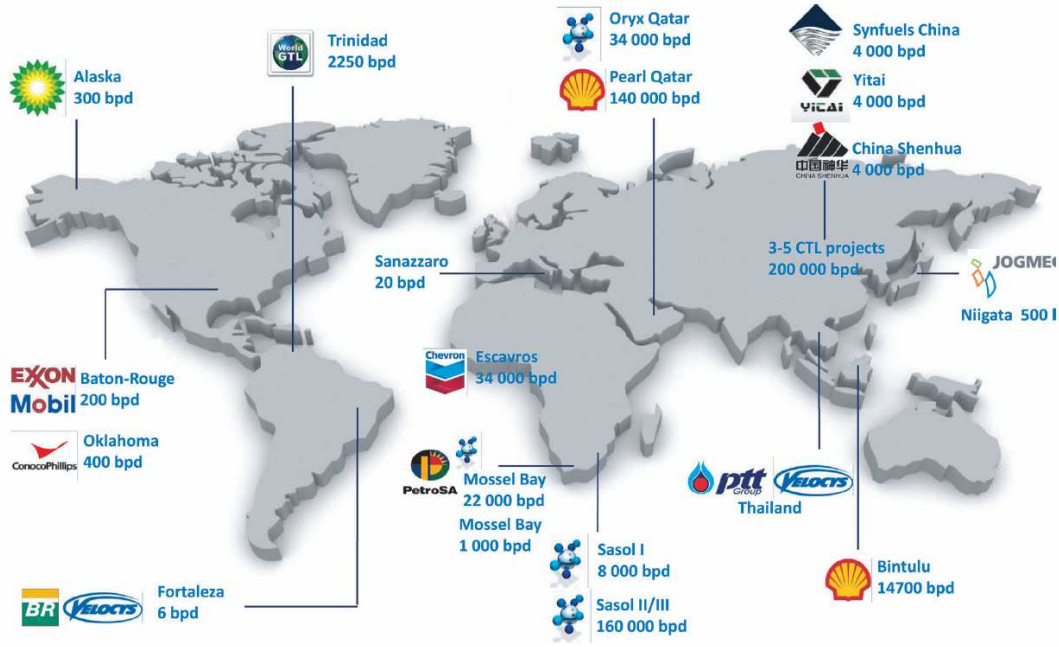

Figure 1-3. Worldwide FT plants in operation or under construction. (From Total, 2012)

1.3 Mechanism of FT reaction and remaining challenges

1.3.1 Mechanism and characteristics of FT reaction

The first stage of FT synthesis is CO adsorption with formation of a surface bound "C1 monomer". This monomer then undergoes polymerisation at the surface to form long chain hydrocarbons [40-42]. The kinetics of the polymerisation are controlled by a balance of C1 addition (propagation) versus chain termination [43]. Figure 1-4 shows a transient visualization of CO hydrogenation and chain growth process, including H_2 dissociation, CO dissociation, methane generation, H_2O generation and so on.

FT synthesis is a heterogeneous process which consists of many elementary reactions. Table 1-1 shows the main reactions. Depending on difference of the catalyst and operating conditions, the probability of each reaction is different [44, 45]. The product of FT synthesis is also complicated, including light hydrocarbon gases, paraffinic waxes, olefins, and oxygenates. [3]. Some FT catalyst has high reactivity of the water-gas-shift reaction (WGS) which can adjust H_2/CO ratio, but lead to CO_2 formation [46]. Boudouard reaction will form carbon deposits on the surface of the catalyst which may deactivate the catalysts. During activation and reaction process, active metals may go through oxidation, reduction, carbidization process [29]. The olefins could be hydrogenated into paraffins. Olefins and paraffins are widely supposed to be primary products of FT synthesis.

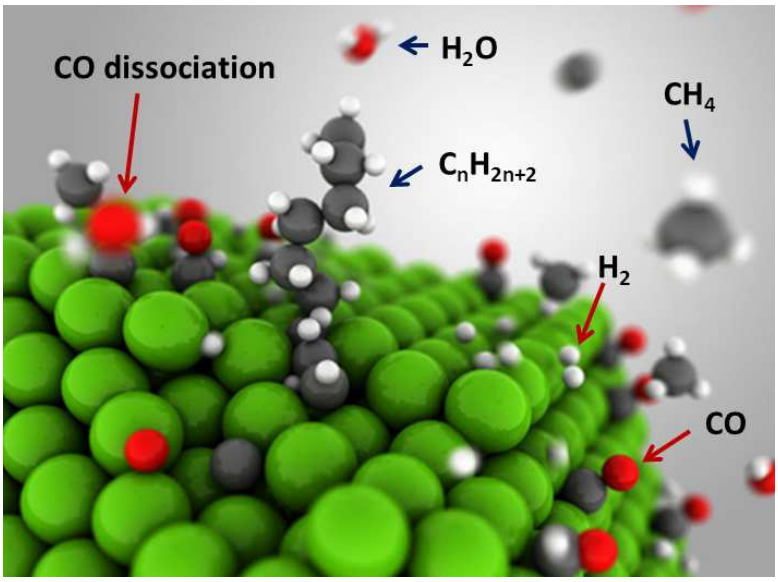

Figure 1-4. Scheme for hydrogenation of CO on transition metal catalyst, download from website of Institute for Complex Molecular Systems, Eindhoven University of Technology (green: transition metal atoms, black: carbon atom, red: oxygen atom, white: hydrogen atom).

Table 1-1. Major Overall Reactions in the Fischer–Tropsch Synthesis [44].

Main reactions	
1. Paraffin	$(2n + 1)H_2 + nCO \rightarrow C_nH_{2n+2} + nH_2O$
2. Olefin	$2nH_2 + nCO \rightarrow C_nH_{2n} + nH_2O$
3. WGS reaction	$CO + H_2O \rightleftharpoons CO_2 + H_2$
Side reactions	
4. Alcohols	$2nH_2 + nCO \rightarrow C_nH_{2n+2}O + (n - 1)H_2O$
5. Catalyst oxidation/reduction	(a) $M_xO_y + yH_2 \rightleftharpoons yH_2O + xM$
	(b) $M_xO_y + yCO \rightleftharpoons yCO_2 + xM$
	(c) $M_x + yH_2O \rightleftharpoons yH_2 + M_xO_y$
6. Bulk carbide formation	$yC + xM \rightleftharpoons M_xC_y$
7. Boudouard reaction	$2CO \rightarrow C + CO_2$

Specific mechanism of FT synthesis is very complex. In early stage, a dozen mechanisms and models of FT reaction based on different catalyst systems have beed proposed [47, 48], four of them are widely accepted: carbide mechanism, hydroxycarbene intermediate mechanism, CO insertion mechanism and multiple paths mechanism. All of these mechanisms have evidence to support them, but contradictory data also exist for all of them [47]. Four classical mechanisms are briefly summarized in Table 1-1. No matter what kind of mechanism

assumed, there are always six elementary reaction steps [37]:

(1) Adsorption of reactant

(2) Chain initiation

(3) Chain growth

(4) Chain termination

(5) Product desorption

(6) Readsorption and further reaction

In most cases, steps 2 through 4 are accurately described by the Anderson-Schulz-Flory (ASF) kinetics model [49]. This model assumes that FTS is an ideal aggregation reaction in which there is one single growth probability factor α. Using equation can be represented as $Mn = (1 - \alpha)\ \alpha^{n-1}$. *Mn* is the mole fractions of hydrocarbons with *n* carbon numbers. In conventional FT process, C-C chain growth is affected by ASF distribution with wide distribution of hydrocarbon products (C_1-C_{80}). The selectivity of desired products is restricted by ASF distribution, such as maximum selectivity of C_{5-11} gasoline-range is 45%, for C_{12-20} diesel-range is 26% and for C_{2-4} range is 55%. How to break the ASF product distribution, and selectively synthesize hydrocarbon products within a specific range of carbon carbons, is one of the hot topics and frontier researches in FT synthesis [31, 50-52].

1.3.2 Catalysts for FT synthesis

The most common FT catalysts are group VIII metals, such as Co, Ru, Ni and Fe (or their carbides and nitrides) [44, 53]. And their positions in the periodic table of the elements are showed in Figure 1-5. Vannice compared the intrinsic activity and selectivity of transition metals supported on γ-Al_2O_3 at temperatures between 240-280 °C and at 1 bar [54]. It was found that that the activity for methanation follows the order of Ru>Fe>Ni>Co>Rh>Pd>Pt>Ir, whereas the average molecular weight of the product follows the order of Ru>Fe>Co>Rh>Ni>Ir>Pt>Pd. Figure 1-5 also lists the relative prices and FT activity of various transition metals. Nickel catalyst is often chosen for methanation reaction due to its stronger hydrogenation ability. Rh catalysts is suitable for preparation of oxygenates. Cu, Ag and Au could be used as promoters for FT catalysts. Fe, Co, and Ru are the most common catalysts for FT synthesis [44], in which Ru is often used as a promoter or for fundamental research due to its high price. Fe is economically attractive and highly abundant, favouring the production of olefins and oxygenates. Although Co is more expensive than Fe, Co has a good selectivity to paraffins, and low selectivity to olefins and oxygen. Co is also more resistant to deactivation [17, 45, 55].

Fe M[1]: 55.847 Rp[2]: 1 A[3]: 1	**Co** M[1]: 58.9332 Rp[2]: 235 A[3]: 250	**Ni** M[1]: 58.69 Rp[2]: 140 A[3]: 150	**Cu** M[1]: 63.546 Rp[2]: 32 A[3]: -
Ru M[1]: 101.07 Rp[2]: 76 000 A[3]: 138 000	**Rh** M[1]: 102.906 Rp[2]: 824 000 A[3]: 1517 000	**Pd** M[1]: 106.42 Rp[2]: 49 000 A[3]: 94 000	**Ag** M[1]: 107.868 Rp[2]: 2 100 A[3]: -
Os M[1]: 190.2 Rp[2]: 408 000 A[3]: 1390 000	**Ir** M[1]: 192.22 Rp[2]: 59 000 A[3]: 203 000	**Pt** M[1]: 195.08 Rp[2]: 203 000 A[3]: 711 000	**Au** M[1]: 196.967 Rp[2]: 114 000 A[3]: -

[1] *Molar weight in g/mol*

[2] *Price per kg in 2007 relative to the price of 1 kg of scrap iron*

[3] *Required activity per surface atom over the life time of the catalyst relative to the activity of iron per surface atom over the life time of an iron-based catalyst (required activity of group IB metals not given, since they don't display Fischer-Tropsch activity, but can be used as promoters).*

Figure 1-5. Relevant metals as catalysts for the Fischer-Tropsch synthesis and their reduction promoters.[53]

Currently there are two FT operating modes [46, 56]. High temperature (300-350 ^{o}C) conditions using Fe catalyst is used for the production of synthetic gasoline and lower olefins (HTFT process). The low temperature (200-240 ^{o}C) process using Fe catalysts or Co catalysts is used for synthesis of heavier hydrocarbons, known as LTFT process. Fe catalyst is available for large-scale use for its low prices. Most of iron catalysts are prepared by precipitation method. The Fe catalysts modified by alkali metal have been used in industry for many years [37]. Fe catalyst can not only produce paraffinic wax in LTFT process, but also produce gasoline, naphtha and light olefins in HTFT process. Iron catalyst is very active toward WGS reaction in contrast to most cobalt-based and Ru-based FT catalysts. Co catalysts produce much methane at high temperatures, so it is just used for low temperature LTFT process with better one-way conversion. It is generally accepted that metallic cobalt is the active phase for FT reaction [57, 58]. Hence, smaller metallic crystallites should display a higher activity per unit mass of catalytically active material [53]. However, it was recently observed that the intrinsic catalytic activity decreases with decreasing average crystallite size (<6 nm) of the cobalt crystallites [59, 60]. SiO_2 Al_2O_3, TiO_2 and carbon materials are often used as supports for Co catalyst, and cobalt nitrate and cobalt acetate are the most common precursors for preparation of FT catalysts [29]. A variety of promoters such as Pt, Ru, Re and Zr, are usually introduced to improve reduction degree and Co dispersion [61, 62].

1.3.3 Challenge for catalysts for Fischer-Tropsch synthesis

Liquid fuel is the main desired product of FT synthesis [63]. Ideal catalysts for FT synthesis should have good stability and high selectivity towards liquid fuels [64]. As mentioned in section 1.3.1, the chain growth of FT products follows the ASF distribution with a wide carbon number distribution (C_{1-80}), selectivity to gasoline-range or diesel-range hydrocarbons is restricted. Improving the selectivity of hydrocarbons to desired fraction is one of challenges in this field [31, 41]. The conventional FT process firstly converts syngas into long-chain hydrocarbons, and then through hydrocracking and isomerization process, paraffinic hydrocarbons are transformed into liquid fraction [35, 65, 66]. So one-step transformation of syngas into liquid distillates is of great industrial interest and promising research topics, which can reduce the complexity of FT technology [67, 68].

In order to secure their supply of C_{2-4} olefins, many countries are motivated to develop catalysts and processes for the production of these important commodity chemicals from non-petroleum resource [15, 69, 70]. FT synthesis provides a flexibile route to utilize the no-petroleum resource, in spite of the FT synthesis still displays lower ethylene and propylene yield up to now. The design of effective iron-based catalysts for the selective production of light olefins involves several factors [15]:

- The selection of a support that enables the formation of the active phase and its intimate contact with the chemical promoters.
- The adequate choice of promoters to increase the selectivity to light olefins and minimize methaneproduction.
- The use of preparation methods that allow obtaining a homogeneous spatial distribution of iron-containing particles with narrow size distribution in the optimum size range.
- The selection of optimum process conditions to maximize the catalyst life without compromising product selectivity.

1.4 Selectivity Control

1.4.1 Some key factors affecting selectivity in FT reaction

FT synthesis is very complex catalytic process. Besides the model of reactors and operating conditions, many factors affect the selectivity and catalytic activity of FT reaction [51, 71-73]. These factors include the type of active metals, chemical status of metals,

supports effect, use of promoters, size effect, micro-environment of active sites, and so on.

First, the distribution of products depends on the active metal. Co and Ru catalysts are suitable for producing long-chain hydrocarbons with almost no oxygenates byproduct. Fe catalyst with appropriate additives (mainly K, Cu and Mn) can be used to synthesize gasoline and naphtha at high temperatures, or long-chain hydrocarbons at lower temperatures. In addition, the reaction products also contain considerable amounts of lower olefins and oxygenates [37, 45, 50, 53].

Second, the chemical state of active metals has an impact on the catalytic activity and product selectivity [47, 74-76]. With variance in types of catalysts, preparation method and reaction conditions, active metals for FT reaction may be in its oxidic state, metallic or carbided state. For example, metallic cobalt are supposed to be active phase for FT reaction [29]. Optimum Co catalysts should have high cobalt concentration and site density for producing C_5^+ hydrocarbons [57]. Co catalyst with low reduction degree showed low CO conversion and high CH_4 selectivity [29]. On the contrary, it is recently reported that cobalt oxide supported on TiO_2 could contain active sites for FT synthesis [77]. Ding et al. [78, 79] found that the generation of Co_2C in Co/AC catalyst decreased the activity in FT reaction. While Co/AC showed low selectivity towards hydrocarbons and high C_{1-18} alcohols selectivity (39%) with La_2O_3 promotion. The authors concluded that the synergistic effects between metallic Co and Co_2C could promote the transformation of syngas into alcohols.

For iron catalysts, iron carbides are believed to be active phase for CO hydrogenation [80-82]. However, even after many recent detailed characterization studies, the exact identity of the active phase remains controversial [37]. Bengoa et al. [83] studied the influence of the intermediate iron species on the activity and selectivity in the FT synthesis (Figure 1-6). They prepared two glassy carbon with low (22 m^2g^{-1}) and high (292 m^2g^{-1}) surface areas, denoted as C(l.s) and C(h.s), respectively, to support Fe through incipient wetness impregnation. Before reduction with H_2, only Fe_3O_4 was found in these catalysts, but with different particle size distributions. Only large Fe_3O_4 particles was found in Fe/C(l.s), while two types of Fe_3O_4 particles was found over Fe/C(h.s). All the Fe_3O_4 particles over Fe/C(l.s) were reduced to α-Fe whereas Fe/C(h.s) catalyst showed lower reduction degree. After the FT reaction, all α-Fe phases were carburized into χ-Fe_5C_2 on Fe/C(l.s) whereas the presence of the intermediate reduction species of iron on Fe/C(h.s) led to the formation of a non-stoichiometric carbide (“O”carbide), less stable, more active and more selective towards olefins than χ-Fe_5C_2 carbide. The authors concluded that it is not convenient to reduce completely the iron to metallic state, since this species leads only to non-optimal χ-Fe_5C_2

carbide during the FTS.

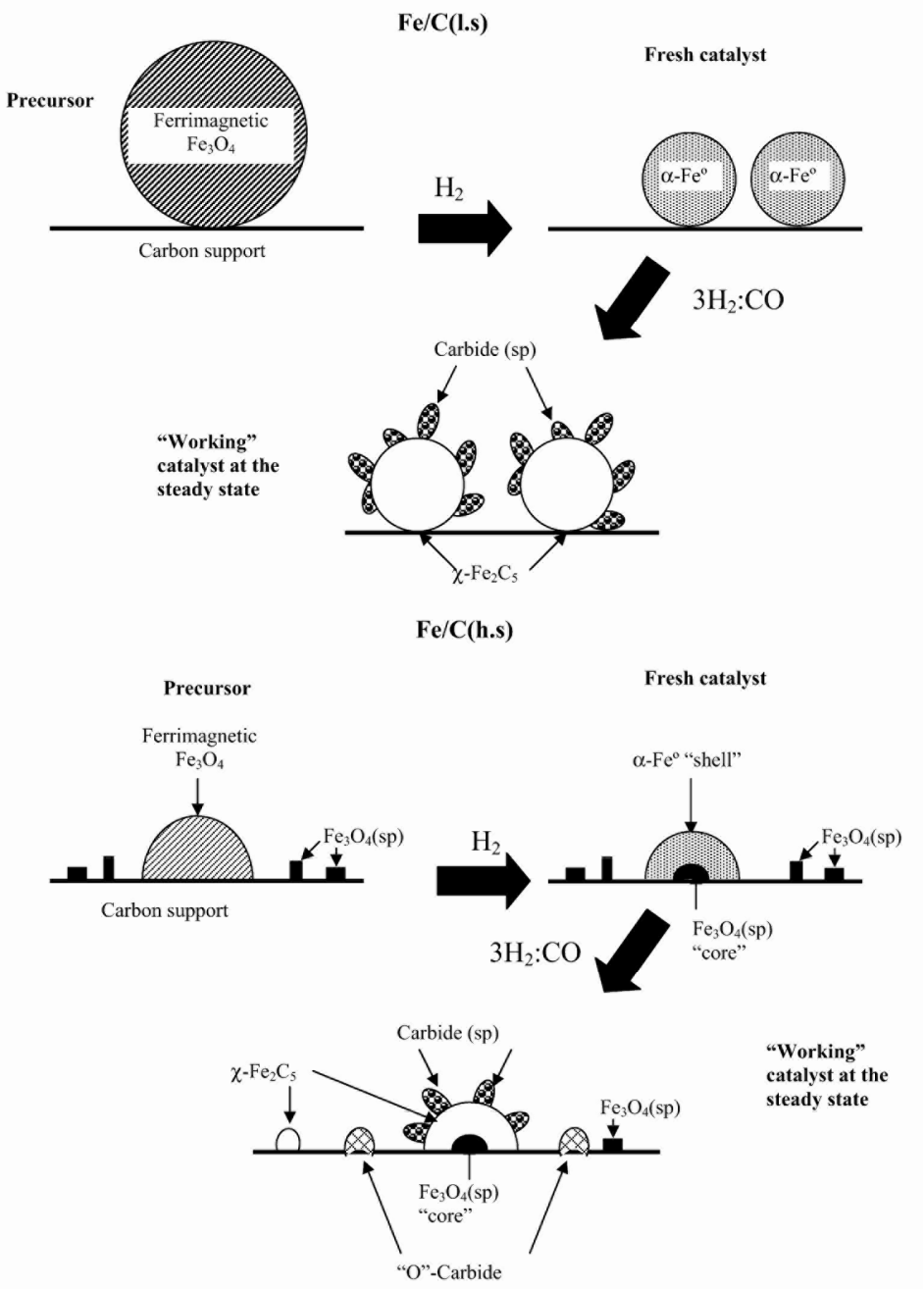

Figure 1-6. Schematic representation of the different steps followed by each solid to reach the structure of the ‘‘working’’ catalyst at the steady state.[83]

Promoters play important roles in tuning the FT product selectivity [84-86]. For example, alkaline promoters are necessary for Fe catalyst to suppress CH_4 selectivity and increase C_5^+ selectivity [87, 88]. Fe catalysts with suitable content of alkali metals can increase CO conversion and olefins content in C_{2-4} hydrocarbons [15]. It is stated that alkali metal increases electron density of iron catalysts by charge donation into the conduction band of

iron, thereby favours dissociation of the C-O bond to form iron carbides and undesired carbon deposits [86]. Iglesia et al. [87-89] found that the activity of Fe and Fe-Zn catalysts increased significantly by addition of K and Cu promoters, which facilitated the reduction and carbidization of Fe catalysts. Torres Galvis et al. [9] report that with promotion of sulfur plus sodium, iron catalysts supported on α-Al_2O_3 and carbon nanofibers showed 60% selectivity towards C_{2-4} lower olefins (Figure 1-7). The addition of sodium and sulfur promoters limits the extent of the hydrogenation reaction, thus suppressing the thermodynamically favored methane formation [69]. In addition, high reaction temperature (340-350 ^{o}C) is not favorable for the chain growth, leading to a higher C_{2-4} selectivity [15, 90]. Jiao et al. [91] using density functional theory (DFT) method and experimental study revealed that potassium promoter (K_2O) could stabilize the high-index and much more active facets such as Fe(211) and Fe(310) to be the energetically favored facets. As the catalyst under high pressure atmosphere may undergo complex reconstruction [81], more studies are necessary in that field.

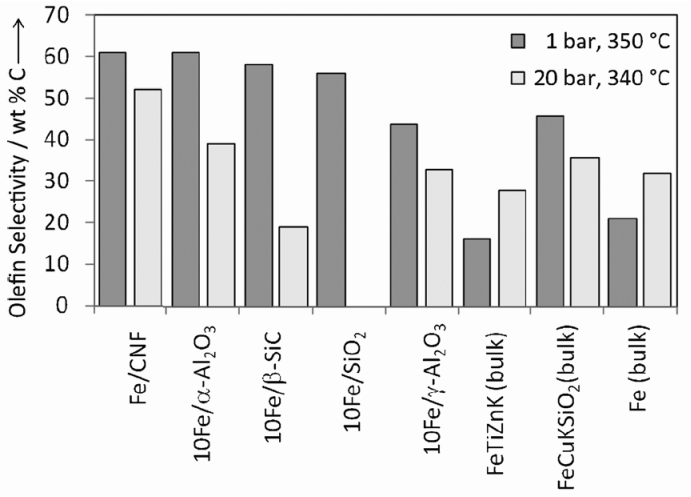

Figure 1-7. C_{2-4} olefin selectivity of different catalysts promoted with Na and S.[69]

Supports are typically used to disperse reactive metals, which also influence the selectivity of FT product [9, 67, 92]. SiO_2, Al_2O_3, and TiO_2 and other oxide materials with high surface area are usually chosen as supports of the FT catalyst [29, 58]. Ohtsuka et al. [93] found that the mesoporous structure of Co/MCM-41 and Co/SBA-15 is beneficial for the generation of C_{10-20} hydrocarbons in FT synthesis. Osa et al. [94-96] used SiC as support for Co catalysts, and found that the catalysts displayed excellent catalytic stability, high C_5^+ selectivity and high diesel-fraction selelctivity. Besides oxide supports, carbon materials such as activated carbon (AC), carbon nanotube (CNT), carbon spheres (CS), carbon nanofibers

(CNF) and ordered mesoporous carbon have been used as supports for FT syntheisis [97, 98]. Qiao et al. [99] synthesized highly dispersed iron oxide nanoparticles embedded in carbon spheres (Fe@C spheres, Figure 1-8) by a hydrothermal cohydrolysis–carbonization process afforded a catalyst with a high fraction of iron carbides after reduction and a high C_5-C_{12} selectivity. Recently carbon materials have attracted attention as novel supports for FT synthesis. Sun et al. [100, 101] reported that Co catalysts supported on nitrogen-doped mesoporous carbon material (NMC) displayed higher specific activity than its analogue without nitrogen-doping. The nitrogen-doping facilitated the reduction of Co species. Hu et al. [27] prepared nitrogen-doped carbon nanotubes (NCNT) as support for iron catalyst. The nitrogen-doping is beneficial for anchoring Fe species and increasing support basicity, thus enhancing the CO adsorption and inhibiting the secondary hydrogenation in FT reactions. The selectivity of C_{2-4} olefins can reach as high as 46.7%.

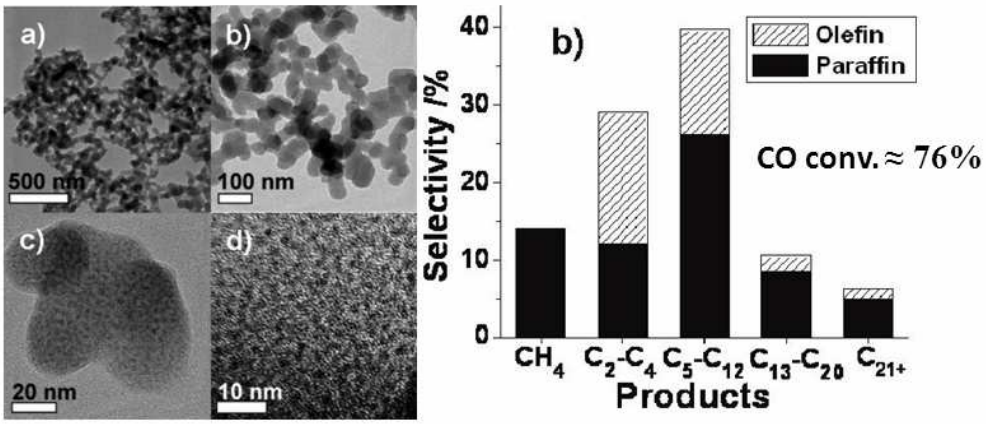

Figure 1-8. TEM images of ground Fe_xO_y@C spheres at different magnifications and FTS performance after reaction for 70 h.

The size of active phase is also a key factor on the performance of FT catalyst. Iglesia et al. [57, 75, 102] summarized the studies about Co size effect using SiO_2, Al_2O_3 and TiO_2 as supports. It was found that in the range of 9-200nm of Co size, the CO turnover frequency (TOF) was independent with Co size. Due to strong interaction between the support and small Co nanoparticles which is hard to reduce, the Co size effect in the smaller range is difficult to acquire. Bezemer et al. [59, 60] chose carbon nanofibers (CNF) as support which was weakly interacted with Co nanoparticles, and studied the Co size effect in the range of 2.6-27 nm (Figure 1-9a). It was found that the TOF first increased with increasing Co size from 2.6 nm up to about 8 nm, and then remained almost unchanged with further increases in Co size. The C_5^+ selectivity first increased with the Co particle size from 2.6 to around 8 nm, and then

remained unchanged or increased slightly. Torres Galvis et al. [82] also studied the effect of iron carbide size in the range of 2-7 nm in FT synthesis (Figure 1-9b). It was found that at 20 bar the TOF_{HC} and TOF_{CH4} (corresponding to the CO converted into hydrocarbons and CH_4) decreased with the iron carbide size increasing from 2 nm to 7 nm, while the TOF_{C2+} did not change in this range. Kang et al. [103] reported the effect of Ru size on FT catalytic behavior of the Ru/CNT catalysts, which exhibited high $C_{10–20}$ selectivity. Under reaction conditions of T=533 K, P=20 bar and H_2/CO=1, CO conversions over the Ru/CNT catalysts with mean Ru sizes of 2.3–10 nm changed only slightly in the range of 25–35%, whereas the product selectivity varied significantly. On changing the mean size of Ru particles from 2.3 to 10.2 nm, both the C_5^+ and the C_{10-20} selectivities passed through maxima, and the optimum Ru size was 7-8 nm. Carballo et al. [104] also found that FTS with Ru-based catalysts is a highly structure-sensitive reaction when Ru<10 nm. In this range, the CO TOF increases as the particle size increases, reaching a constant value for Ru particles larger than 10 nm.

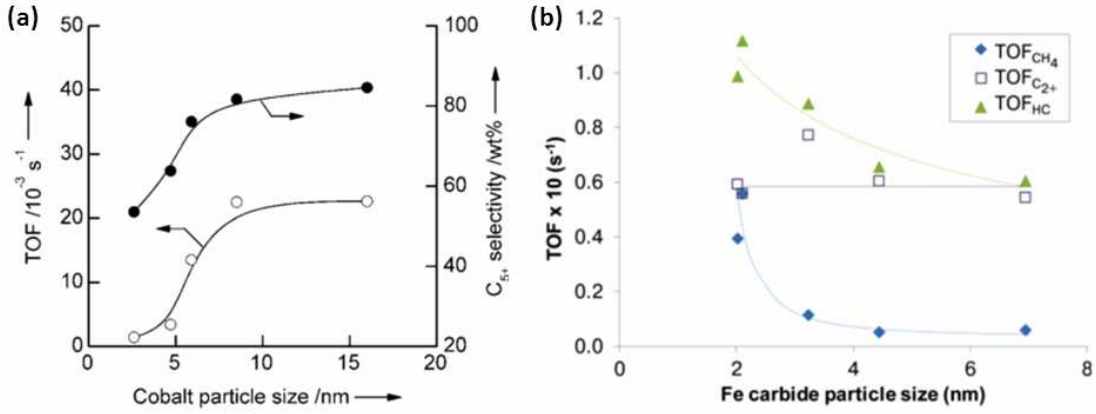

Figure 1-9. (a) The influence of cobalt particle size on the TOF and C_5^+ selectivity [59, 105]. Reaction conditions: T=483 K, P=35 bar, H_2/CO=2. (b) Apparent turnover frequencies (TOF) as a function of iron carbide size (TOS = 1 h). TOF_{HC} and TOF_{C2+} correspond to the CO conversion to hydrocarbons and conversion to C_2^+ hydrocarbons, respectively [82]. Reaction conditions: T= 613 K, P=20 bar, H_2/CO=1.

Besides, the microenvironments of active phase have a great impact on activity and selectivity of FT catalysts [31, 70, 80, 106]. Tang et al. [107] reported that compared with Co nanoparticles located outside the molecular sieve, the Co nanoparticles confined in faujasite super cage show the high C_5^+ selectivity. Bao et al. [80] compared the performance of iron catalysts inside the CNT and outside the CNT with similar Fe_2O_3 size (Fe-out-CNT and

Fe-in-CNT). It was found that the Fe_2O_3 particles inside the CNT are easier to reduce. Thus Fe-in-CNT showed higher CO conversion and C_5^+ selectivity. In situ XRD study shows that during the reaction Fe-in-CNT catalyst contained higher percentage of iron carbide. Generally, iron carbide is supposed to active sites for FT synthesis [37].

1.4.2 Non-ASF product distributions by secondary reactions

Most of the studies about FT synthesis focus on increasing the C_5^+ selectivity. To improve the selectivity of middle distillate in FT syntheisis requires new strategies [108]. Product distribution of FT synthesis is restricted by the mechanism of polymerization, hydrocarbon products is unselective. However, it is reported that the distribution of FTS product often deviates from ASF distribution [109]. Novak et al. [73] and Kuipers et al. [109] considered that the secondary reactions were the reason of product distribution deviations, such as α-olefin reinsertion, hydrogenation, hydrogenolysis and cracking reaction. The selectivity of FT products could be tuned therefore by these secondary reactions. The α-olefin reinsertion reaction can increase the selectivity of long-chain hydrocarbons [110, 111]. Hydrogenolysis reaction led to rising the selectivity of middle distillate product[112]. The hydrogenation reaction can terminate the chain growth reaction of *n*-alkanes [113]. Cracking reaction (from acid sites) will convert the long-chain hydrocarbons into short-chain hydrocarbons [41].

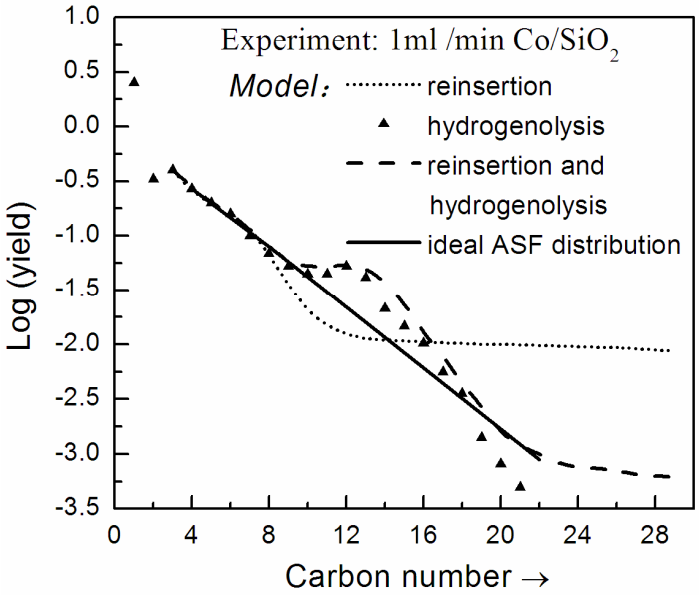

Figure 1-10. Fits to the total product yield of 50 nm Co particles on a flat SiO_2 wafer, the black full line was added from ref[113].

Based on Co/SiO_2 catalyst, Kuipers [109] confirmed that the conventional CO hydrogenation catalysts could couple the function of reinsertion, hydrogenolysis, reinsertion & hydrogenolysis for tuning the selectivity of FT synthesis (Figure 1-10). Experimental results showed that the reinsertion reaction decreased the selectivity of hydrocarbons with around 15 carbon numbers and increased the C_{18}^+ selectivity. C_{16}^+ hydrocarbons can be transformed into $C_{11\text{-}16}$ fraction and CH_4 by hydrogenolysis reaction, and the selectivity of other C_{11}^- hydrocarbons did not change. Lafyatis and Foley [114] used theoretical calculations based on diffusivity matrice and hydrogenolysis to confirm that the $C_{5\text{-}12}$ selectivity of FT product can reach as high as 80%, however, it was not experimentally confirmed.

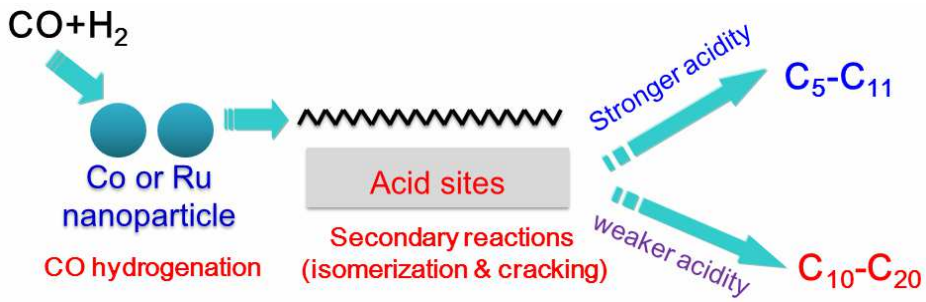

Figure 1-11. Schematic illustration of the strategy for using a bifunctional catalytic system with CO hydrogenation and hydrocarbon hydrocracking/isomerization functions.

The current commerial FT technology uses two-stage method: CO hydrogenation for long-chain hydrocarbons and hydrocracking by acid catalysts [66, 112]. Bifunctional catalyst which integrates CO hydrogenation metal and solid acid could be used for FT reactions to realize the direct conversion of syngas into $C_{5\text{-}11}$ gasoline paroducts (Figure 1-11) [67, 115]. It was comfirmed that such catalysts had high $C_{5\text{-}11}$ selectivity about 50% in FT synthesis [50, 67, 108, 116], which is slightly higher than the maximum 45% predicited by ASF distribution. Kang et al. [103] prepared Ru catalysts supported on CNTs with mild acidity, it was found that the pretreatment of CNTs with concentrated HNO_3 is crucial for obtaining higher $C_{10\text{-}20}$ selectivity. The NH_3-TPD studies suggested that pretreatment with concentrated HNO_3 led to the generation of acid sites on the CNT surfaces. The acidities may correspond to the oxygen-containing functional groups generated on the surfaces of CNTs after pretreatment with HNO_3. The C_{21}^+ selectivity of Ru/CNTs was lower, thus the authors speculated that the mild acidity may enhance the hydrocracking of C_{21}^+ hydrocarbons.

Fujimoto and Tsubaki's group [52, 68, 115, 117-125] conducted a systematic research of bifunctional FT catalysts which combined acid molecular sieves with CO hydrogenation

metal for producing gasoline-range hydrocarbons. The combination modes are divided into 3 categories (Figure 1-12): using a dual-bed reactor configuration with an acidic zeolite downstream from a conventional FT catalyst (Figure 1-12a); using a hybrid catalyst containing both components (Figure 1-12b), so syngas can be directly transformed into C_{5-11} hydrocarbons with good selectivity owing to the catalytic function of acidic zeolite in the hydrocracking/isomerization reactions. To further increase the efficiency of the tandem reactions, Tsubaki and coworker successfully designed a kind of core-shell-structured bifunctional catalyst (Figure 1-12c). Conventional FT catalysts such as Co/Al_2O_3 and Co/SiO_2 were used as core. Acidic molecular sieves such as H-beta and H-ZSM-5 were coated on the outer layer of conventional FT catalysts. This kind of hybrid catalysts showed promising performances for the conversion of syngas into isoparaffins. The selelctivity towards C_{5-11} selective can reach as high as 60%-65% with mainly isoparaffins. However, the catalyst showed high CH_4 selectivity. Methane is an undesired product of FT synthesis. For example, the Co/Al_2O_3@H-beta catalyst displayed a 15% selectivity to CH_4 [122]. This may be due to strong acidity of molecular sieve and mass transformation limitation of long micropores in zeolite.

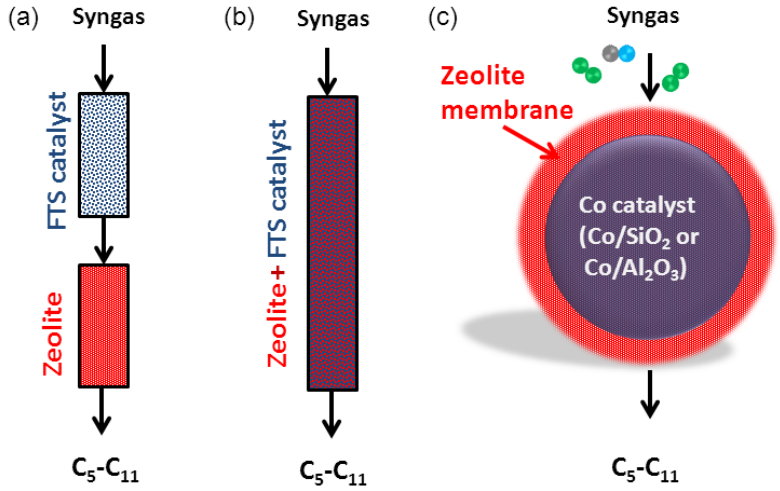

Figure 1-12. Representative bifunctional FT catalytic systems: (a) Dual-bed reactor configuration, (b) hybrid catalyst, (c) core–shell structured catalyst.[31]

1.4.3 Introduction of hydrocracking catalysts

Solid acid catalysis involves the largest amounts of catalysts used and the largest economical effort in the oil refining and chemical industry [126]. Solid acid catalyst is very

effective for cracking and isomerization reactions. Acidic molecular sieves are known as typical solid acid catalysts [127]. Hydrocracking reactions are normally operated in the temperature range of 623-713 K using solid acid catalysts. At such temperatures, incorporation of a (de)hydrogenation function into the acidic catalyst is the key to enhance catalyst activity and stability. Conventionally, the (de)hydrogenation function is introduced by a metal, supported on the solid acid catalyst (Table 1-2) [127]. Integration of different metals and acidic supports could regulate the hydrocracking activity. Amorphous Al_2O_3-SiO_2 composite was the most extensive used cracking catalyst in early stage, then replaced by zeolite [128]. Besides the metals in Table 1-2, Fe, Co and Ru of active FT metals also possess the ability of hydrogenation [129].

Table 1-2. Various (de)hydrogenation and acid functions of hydrocracking catalysts.[127]

	Hydrogenation function	Acidic function (support)	
Increasing Hydrogenation Power ↓	Ni/Mo Ni/W Pt/Pd	Al_2O_3 Al_2O_3/halogen SiO_2/Al_2O_3 Zeolites	↓ Increasing Acidity
	Low-S conditions		

Hydrocracking and hydroisomerization reactions have similar reaction intermediates. The catalysts all consist of acidic component and (de)hydrogenation component. Hydrocracking process is often accompanied with isomerization reaction [130]. Hydrocracking reaction follows the carbocation mechanism. The reaction steps of hydrocracking of *n*-alkane are shown in Figure 1-13:

(a) Dehydrogenation of absorpt *n*-alkane on active metals;

(b) Desorption of *n*-alkene, then, diffuse to the acidic sites;

(c) The *n*-alkene converts into carbocation on a protonic acid;

(d) Isomerization of carbocation into stable branched structure;

(e) β-scission of branched carbocation into *iso*-olefin and new smaller carbocation;

(f) New carbocation losts one proton and becomes olefin.

(g) Hydrogenation of olefins or olefin diffusion to protonic acid sites for successive hydrocracking.

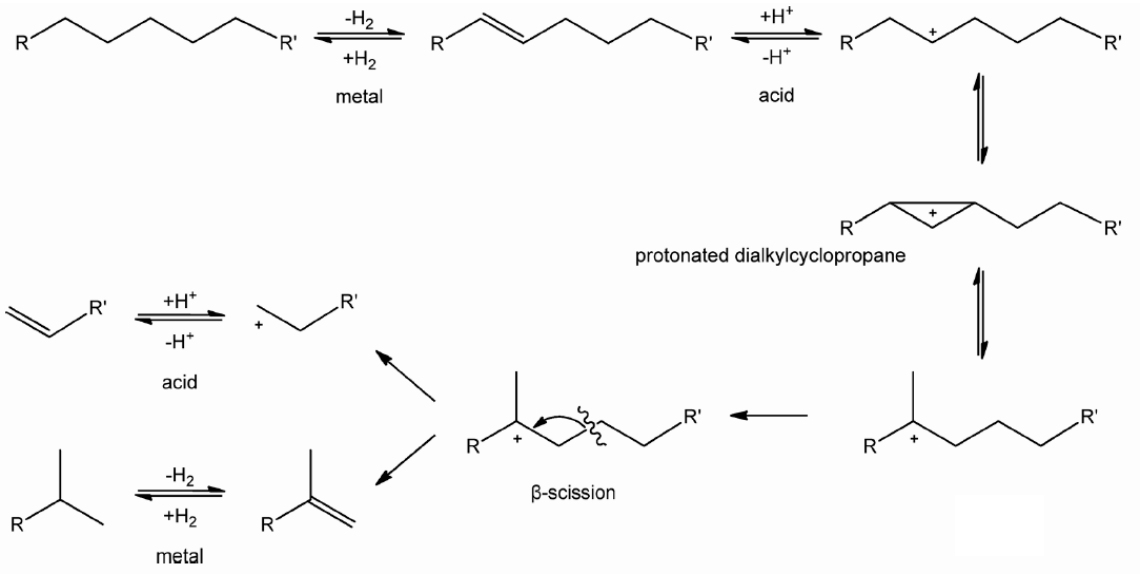

Figure 1-13. Hydrocracking reaction mechanism for a representative hydrocarbon.[131]

1.4.4 Application of novel mesoporous zeolites in catalysis

The elementary building units of zeolites are SiO_4 and AlO_4 tetrahedra. Adjacent tetrahedra are linked at their corners via a common oxygen atom, and this results in an inorganic macromolecule with a structurally distinct three-dimensional framework [132]. Zeolite crystals with intricate micropores, strong acidity, and redox sites have been widely used as heterogeneous catalysts in the petrochemical and fine chemical industries [133]. Besides the number and strength of active sites in zeolite, the mass transfer efficiency of zeolite also strongly affects the catalytic performance [126, 134-136]. In the case of catalytic conversion of hydrocarbons by zeolites, when the size of hydrocarbon molecular is close to pore size of zeolite, the diffusion efficiency would affect the catalytic reaction. The diffusion of tightly fitting molecules into the micropores of zeolites, referred as “configurational diffusion”, is often the rate-limiting step of a catalyzed reaction. While the pore size of catalyst is larger than that of molecule, the diffusivity drops sharply to orders of the Knudsen-diffusion and molecular-diffusion regimes.

The microporous structure of zeolites not only excludes certain large molecules, such as paraffinic hydrocarbons, from accessing the active sites that are located within the micropores of a zeolite, but they also impose significant diffusional limitations to molecules that can only tightly fit within the pores [137]. To address this complication, the class of mesoporous zeolites (sometimes called hierarchical zeolites) was developed, in which a secondary network of mesopores is coupled to the intrinsic micropores, aimed to reduce access and diffusion limitations [138-143]. In addition, more acid sites are exposed to large molecules

[144, 145]. Compared with mesoporous materials such as MCM-41 and SBA-15, the mesoporous zeolites have better hydrothermal stability and more strong acid sites [138]. Most of the papers about mesoporous zeolites focus on the preparation methods, and few studies have addressed application of mesoporous zeolites in catalysis. Recently, more and more research groups and companies are conducting studies on mesoporous zeolites [139, 146].

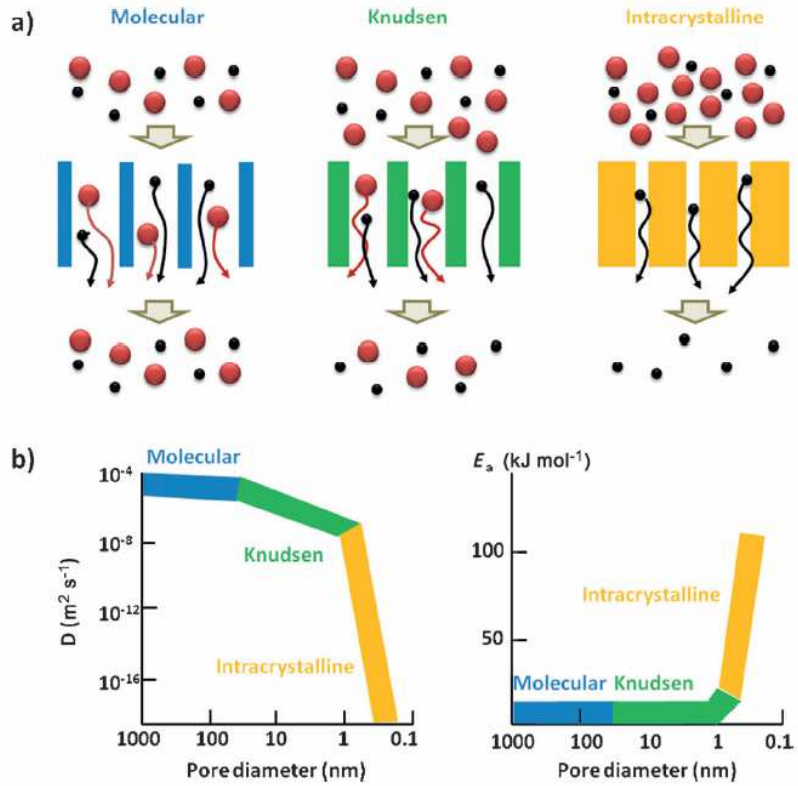

Figure 1-14. a) Schematic representation of the effect of pore size on the diffusion of large (red) and small (black) molecules, b) Effects of pore diameter on molecular diffusivity (*D*) and of the energy of activation (*Ea*) on diffusion.[126, 134]

Christensen et al. [147] summaries and categorizes the catalytic studies utilizing hierarchical zeolites that have been reported hitherto (Figure 1-15). Alkylation, isomerization and cracking reactions follow the mechanism of carbocation, and Brønsted acid sites are supposed to be the active sites. The introduction of mesopores is benificial for exposing more acid sites which faciliates the diffusing of reagents. Thus, mesoporous zeolites showed better activity for these three reactions. Meanwhile, benefit from improved mass transfer performance, the content of carbon deposition decreased, and the stability of catalyst was prolonged. Introduction of the mesoporous structure not only promotes the activity of catalysts, but also increases the selectivity to larger molecular products.

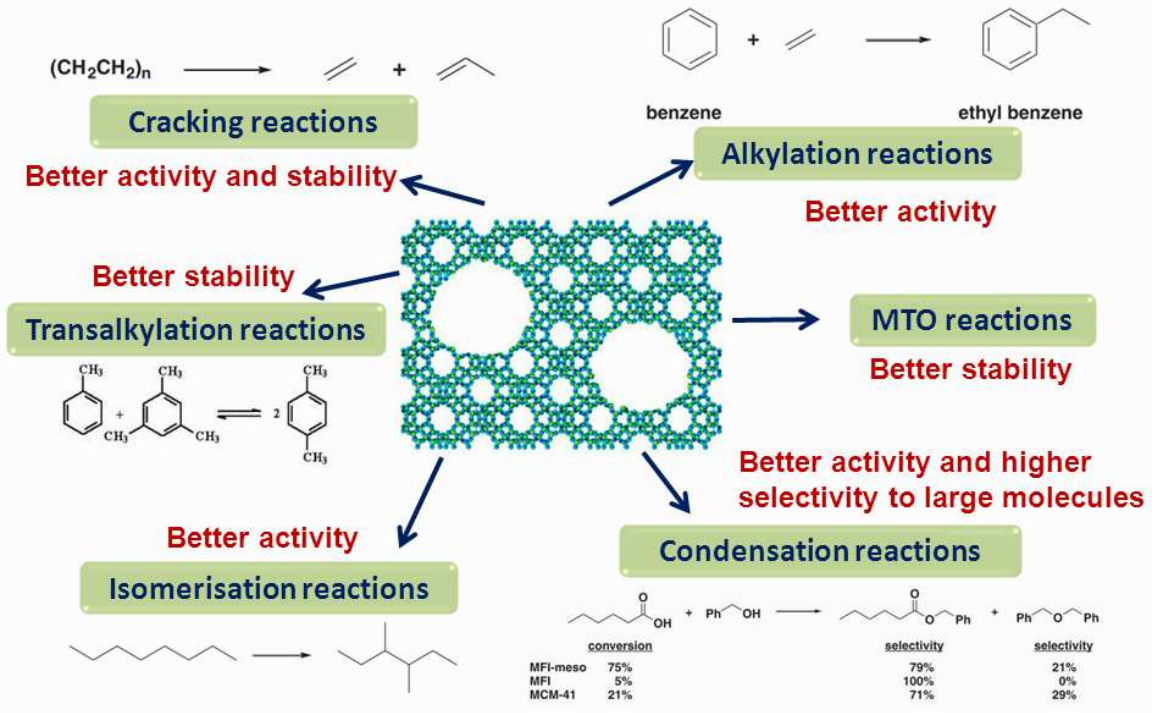

Figure 1-15. Overview of the different reaction classes and the main effect of mesoporous zeolites, based on ref [147].

1.4.5 Preparation method of mesoporous zeolite

In the past decade, much progress has been made in the synthesis, characterization, and application of mesoporous zeolites [137, 140, 148-152]. Generally, these methods can be classified into two categories: “Top-Down” or post-synthetic modification method (destructive method) and “Bottom-Up” or primary syntheses method (constructive method), which mostly involve the use of templates [137]. Top-Down method is based chemical modification of zeolite, which is easy to operate and reproduce. However, the crystallinity of zeolite decreases to some extent due to structure colapse. The feature of Bottom-Up method is the use of templates, from the raw materials to construct mesoporous structure in zeolite. But the template is expensive and difficult to synthesize.

Desilication with alkaline solution is one of the typical Top-Down methods to generate mesopores in zeolite. Ramírez et al. [138, 153, 154] conduct systematic studies about the desilication process and mechanism. Aluminium in framework positions directs the preferential extraction of framework Si upon alkaline treatment of MFI zeolites, leading to controlled mesopores formation [153]. The presence of framework Al plays a key role in the mechanism of mesopores formation in MFI zeolites treated with alkaline solution. The high concentration of Al in the MFI zeolite framework (Si/Al≤15) prevents Si from being extracted, and thus limited mesopores formation is obtained. While highly siliceous zeolites (Si/Al≥50)

show excessive and unselective Si dissolution, leading to creation of relatively large pores. A framework Si/Al ratio of 25-50 (Figure 1-16) was optimal for obtaining substantial mesopores and generally preserved Al centers [155].

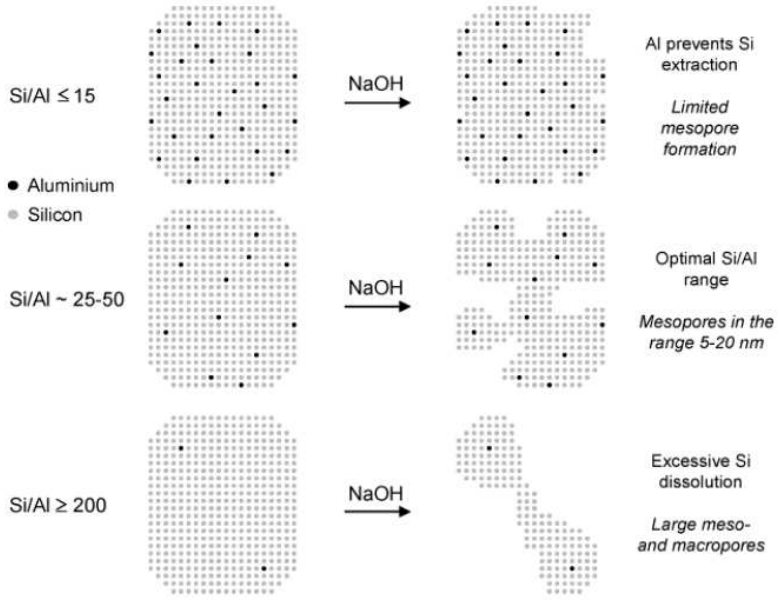

Figure 1-16. The influence of the Si/Al ratio on the desilication treatment of MFI zeolites in NaOH solution and the associated mechanism of pore formation.[155]

1.4.6 Application of mesoporous zeolite in FT synthesis

Although many progresses have been made in preparing mesoporous zeolites, few papers concerned the application of mesoporous zeolites in FT synthesis. Pereira et al [156] reported that the mesostructured beta zeolite-supported cobalt (10%) catalyst increased the FT activity, and also showed a low selectivity to methane and the lowest olefin/paraffin ratio. At the same time, Wang et al. [157] has used mesoporous ZSM-5 (denoted as meso-ZSM-5) prepared by a simple alkaline treatment method, that is, treating H-ZSM-5 in aqueous solutions of NaOH with appropriate concentrations, to fabricate bifunctional FT catalysts. Characterization by Ar adsorption and TEM clarified that the mesoporous ZSM-5 prepared by this technique contained both micropores with a size of about 0.55 nm, which is typical for ZSM-5, and mesopores with sizes ranging from about 3 to 12 nm (Figure 1-17). The meso-ZSM-5 samples with different sizes of mesopores have been utilized for FT synthesis. Ruthenium nanoparticles were loaded onto meso-ZSM-5 with high reduction degree. TEM studies showed that the mean sizes of Ru nanoparticles in these samples were almost the same, ranging from 6.5 to 7.2 nm.

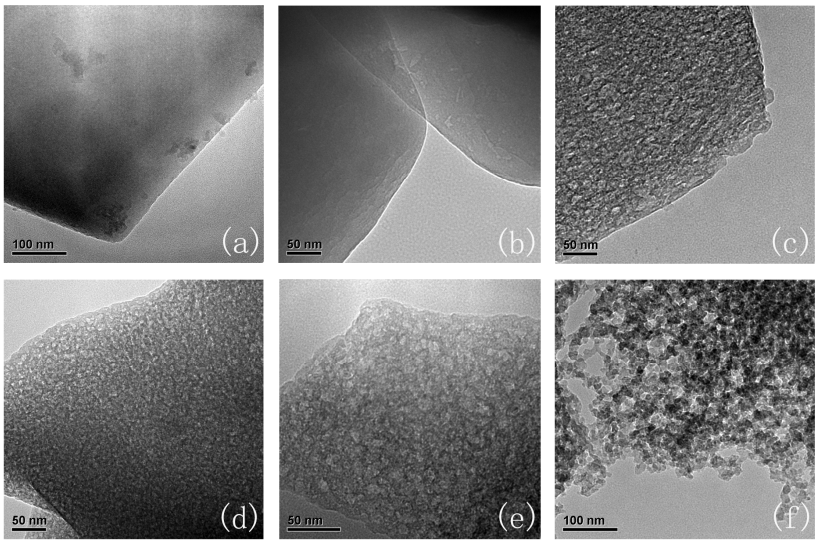

Figure 1-17. TEM micrographs of H-ZSM-5 pretreated by NaOH with different concentrations: (a) 0, (b) 0.1 M, (c) 0.3 M, (d) 0.5 M, (e) 1.0 M, (f) 1.5 M.

Catalytic studies showed that the use of meso-ZSM-5 instead of conventional H-ZSM-5 for the loading of Ru nanoparticles significantly decreased the selectivities to CH_4 and C_2–C_4 and increased that to C_5–C_{11} hydrocarbons (Figure 1-18). The selectivity also depended on the concentration of NaOH used for the preparation of meso-ZSM-5. At an appropriate concentration of NaOH (1.0 M), the selectivity of C_5-C_{11} selectivity increased to about 80%, which was markedly higher than that expected from the ASF distribution (maximum ~45%). CO conversion also increased when meso-ZSM-5 was used instead of HZSM-5, probably owing to enhanced mass transport. The C_{iso}/C_n ratio was maintained at approximately 2.5-2.7 in C_5-C_{11} which means that the main products in the C_5-C_{11} range are iso-paraffins.

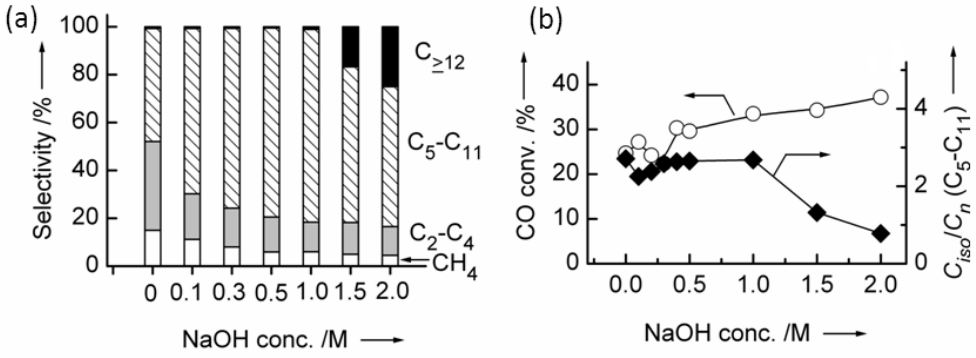

Figure 1-18. (a) Selectivity of Ru catalysts loaded on meso-ZSM-5 prepared by treating H-ZSM-5 with different concentrations of NaOH, (b) CO conversion and C_{iso}/C_n. Reaction conditions: catalyst 0.5 g, H_2/CO=1.0, temperature 533 K, pressure 20 bars, total flow rate 20 $mLmin^{-1}$, time on stream 12 h.

Recently, Sartipi et al. [158-161] prepared series of cobalt catalysts supported on mesoporous zeolites to tune the C_5-C_{11} hydrocarbons selectivity. It was found that the use of meso-H-ZSM-5 to replace H-ZSM-5 as the support for Co particles decreased the selectivity to CH_4 and increased that to C_5–C_{11} hydrocarbons, although the degrees of changes were not so significant relative to those of Ru-based catalysts. The selectivity to CH_4 decreased from 21% for Co/H-ZSM-5 to 18% for Co/meso-H-ZSM-5 and that to C_5–C_{11} hydrocarbons increased from 50 to 58% at the same time under the following reaction conditions: T=513 K, P=1.5 MPa, H_2/CO=2. The selectivity improvement over the Co/meso-H-ZSM-5 catalyst could be attributed to enhanced diffusion of both reactants and products. However, these catalysts displayed higher methane selectivity which may be caused by direct hydrogenation of CO by lower coordinated cobalt sites or hydrogenolysis.

1.4.7 Strategies for increasing lower olefins selectivity in FT synthesis

It is sometimes assumed that the olefins are the primary products of the synthesis, and that the paraffins could be formed therefrom by subsequent hydrogenation [113]. Bulk iron catalysts are typically used for the olefin production via FT synthesis [9]. It is well known that addition of alkali to iron causes an increase in both the α-alkene selectivity and the average carbon number of produced hydrocarbons [86, 162]. In order to shift the the product selectivity to lower hydrocarbons, higher temperature and low pressure is efficient [15]. Promotional effects of alkali metals have been explained in terms of modification of the local electron density of the active transition metal [163, 164], and through blockage of sites [165]. However, the alkali promoters may enhance the WGS reaction and the basicity of the promoter appears to be the determining factor for the rate of catalyst deactivation and on the secondary hydrogenation of ethane [88, 166]. The bulk iron catalysts are also mechanically unstable when the reaction is performed at high temperature. So supported iron catalyst are believed to be more suitable for FTO process [9, 90]. Torres Galvis et al. [9] used series of supported iron catalysts for the production of lower olefins by FT synthesis. It was found that the properties of supports and a trace of impurities play a key role on the lower olefins selectivity. The best catalyst has been achieved by combining the use of a weakly interactive support (CNF and α-Al_2O_3) with the homogenous distribution of iron carbide nanoparticles modified with Na and S (Figure 1-19). The C_{2-4} selectivity could reach as high as 61%, which is significantly higher than in other reports. The remarkable differences in the catalytic performances of both Fe/CNF and Fe/α-Al_2O_3 compared to the other catalysts present an excellent opportunity to investigate and compare the active phases of these catalysts to

understand the contribution of the different iron carbide species to CO conversion and product selectivity [69].

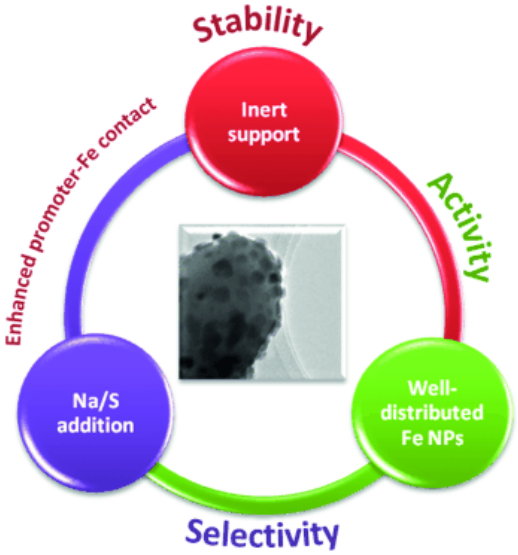

Figure 1-19. Design strategy for the development of FTO catalysts.[69]

1.5 The Objectives and Research Methods of this Thesis

1.5.1 From bifunctional Ru-based catalyst to Co-based catalyst

Although ruthenium is expensive, it has the best activity and chain-growth ability in FT reaction [45]. So ruthenium is suitable for fundamental research [45, 125]. Cobalt catalysts have similar chain-growth ability and activity in FT reaction, but much lower price than ruthenium (Figure 1-5). World-demanded transportation fuel is the main product of FT synthsis [63]. To develop bifunctional Co-based catalysts with high selectivity to gasoline-range hydrocarbons is therefore promising for FT plants. Compared with Fe-based catalysts, the price of cobalt is relatively higher. Therefore utilization of active cobalt is the primary issue considered in the design of the catalyst. De jong et al. [59, 167] indicated that the maximum activity of cobalt catalysts can be reached, when the metal particle size is regulated in the range of 6-8 nm with narrow distribution. Cobalt nitrate is usually used as precursor of Co catalysts. However, supported cobalt oxides prepared from nitrates generally display relatively large particle sizes [168], and decomposition cobalt precursors will result in a strong metal-support interaction favoring the formation of the less reducible cobalt silicate or cobalt aluminate [67, 74]. Designed of Co/meso-zeolite catalyst with high activity and high $C_{5\text{-}11}$ selectivity is challenging.

1.5.2 Design of Co/meso-zeolite catalyst with high performance

In the early reports, cobalt species were simply impregnated onto the surface of zeolites with poor dispersion (Figure 1-20a). These catalysts produced much CH_4 in FT product, and C_{5-11} selectivity could reach about 50-60% [50, 169, 170]. Co/zeolite catalysts with core-shell structure (Figure 1-20b) improved the cracking efficiency. The C_{5-11} selectivity could be further increased to 60-65%, but still with high selelctivity to lower hydrocarbons [68, 122, 123]. The membrane (thickness in μm scale) effect of the coating, however, results in mass transport resistances, lowering the productivity. Acid sites on zeolites and CO hydrogenation metals are not in intimate contact with each other [171]. In this thesis, we plan to use acidic mesoporous zeolites as catalyst support to disperse cobalt nanoparticles (Figure 1-20c). By overcoming the transportation limitations, we would like to further increase the C_{5-11} selelctivity.

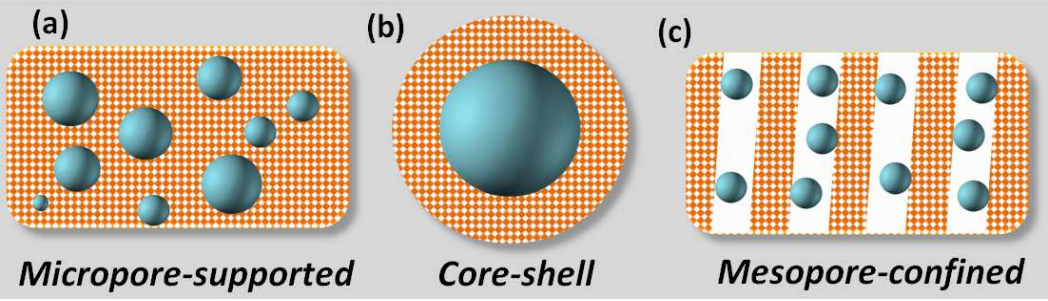

Figure 1-20. Schematic representation of three bifuntional catalysts coupled with metal nanoparticles and acid zeolites.

1.5.3 The effect of catalysts pore size and sodium promotion

The pore size effect for supported cobalt catalysts were well investigated by several groups [172-175]. It was found that the dispersion and reduction degree of supported cobalt species strongly depended on the pore size of supports, thus affecting the catalytic performance of FT synthesis. However, most of the studies about iron catalysts address bulk systems, because of low iron cost. Even so, supported iron catalysts showed better mechanical stability than bulk iron catalysts, especially in high temperature [9]. Many porous materials such as CNT, SBA-15, γ-Al_2O_3, MCM-41 and zeolites, were used as supports for iron catalysts [176-179]. To our knowledge, the effect of support and its porosity on FT performance of iron catalyst remains unclear in the literature. In this thesis, we address the effects of pore size on the structure of iron species and catalytic behavior in FT synthesis of iron catalysts supported by mesoporous silicas. Both periodic and commercial mesoporous

silicas are used as catalytic supports.

Then, the effect of sodium addition over different types of supports with iron has been studied. Different types of promoters have been proposed in the literature to increase the selectivity to olefins like sodium [180, 181], potassium [87], zinc [88], copper [88], vanadium [182], and sulfur [90, 183]. Sodium has been found to be one of the most effective promoters. Addition of it leads to significant increase of the olefin to paraffin ratio, WGS activity and decrease methane selectivity [180, 181, 184]. The effect of sodium is usually explained by decrease of the strength of C-O bonds in the presence of Na increasing the coverage of dissociated CO on the surface [86, 90, 181, 185]. However, these studies are mostly based on bulk iron catalyst, and it is still not clear the role of support in the effect of promoter over iron catalyst. In this thesis, we chose three typical supports CNT, SiO_2 and γ-Al_2O_3 to load iron catalysts with different amount of sodium. A kind of ordered mesoporous carbon (CMK-3) with large surface area was also synthesized as support. We aim to have a deeper understanding about effect of sodium addition over different supported iron catalysts, especially how the sodium affect the activation behavior, metal-support interaction and product selectivity in FT synthesis.

1.6 Outline of the Thesis

This thesis consists of eight chapters as follows:

Chapter 1 summarizes the development of FT technology and FT catalysts. Analysis of literature suggests that selectivity control of FT product is a promising and challenging research field. Most of publications focus on developing catalysts for improving C_5^+ selectivity in FT synthesis. Construction of bifunctional FT catalysts may break ASF distribution by secondary reactions. Very few studies address the pore size effect on the supported iron catalysts, and also the generation process of active iron phase.

Chapter 2 introduces the methods of catalyst preparation, catalytic evaluation and characterization.

Chapter 3 focuses on design of mesoporous beta zeolite supported Ru catalysts for $C_{5\text{-}11}$ isoparaffin. Compared to ZSM-5, beta zeolite possesses better isomerization activity. This study aims to enhance the secondary hydrocracking reaction to further increase the *iso*-paraffins content in the FT products.

Chapter 4 is based the results of Chapter 3. The support effect for Co catalysts is firstly investigated. Then, much effort has been made to prepare uniform Co nanoparticles and

mesoporous ZSM-5 with high density of Bronsted acid. The contribution of mesopores and acid sites are discussed in details.

In chapter 5, we study the pore size effect of supported iron catalysts. Series of ordered mesoporous silica supports were synthesized, and two commercial silicas were also used. The supported iron catalysts with pore diameters from 2 to 50 nm were characterized in this chapter at different stages of their preparation, activation and reaction using a wide range of techniques: BET, XRD, H_2-TPR, in-situ magnetic measurements, Mössbauer spectroscopy.

In chapter 6, we discuss the effect of support. Most of the previous papers have reported characterization and catalytic data obtained with iron catalysts prepared using only one support. This makes difficult a direct comparision between iron catalysts supported on different materials. This chapter is aimed at clarifying this point. In this chapter, iron catalysts for FT synthesis on carbon supports (active carbon, CMK-3 and carbon nanotubes) at different stages of preparation and activation are compared with silica supported counterparts (amorphous silica and SBA-15).

In chapter 7, the sodium effect for iron catalysts supported on different supports is investigated. Sodium is regarded as an effective promoter for iron catalysts used in FT synthesis. However, most of papers studied the bulk iron catalysts, and the information about sodium effect on different supported iron catalysts is very limited. The sodium effect on activation behavior and olefin selectivity is discussed in this chapter.

Chapter 8 gives general conclusion and draws perspectives of this work.

1.7 Reference

[1] N. Zhang, N. Lior, H. Jin, Energy, 36 (2011) 3639-3649.

[2] X. Wang, C. Zhang, Energy Policy, 68 (2014) 394-402.

[3] Z. Liu, S. Shi, Y. Li, Chem. Eng. Sci., 65 (2010) 12-17.

[4] K. Kim, Nature, 508 (2014) 448–449.

[5] Energy Outlook 2035 - BP, in, BP Global, bp.com/energyoutlook, 2014.

[6] O.P.R. van Vliet, A.P.C. Faaij, W.C. Turkenburg, Energ. Convers. Manag., 50 (2009) 855-876.

[7] S.Y. Yang, L. Xiao, S.Y. Yang, A. Kraslawski, Y. Man, Y. Qian, Acs Sustainable Chem. Eng., 2 (2014) 80-87.

[8] D.A. Ruddy, J.A. Schaidle, J.R. Ferrell Iii, J. Wang, L. Moens, J.E. Hensley, Green Chem., 16 (2014) 454-490.

[9] H.M. Torres Galvis, J.H. Bitter, C.B. Khare, M. Ruitenbeek, A.I. Dugulan, K.P. de Jong, Science, 335 (2012) 835-838.

[10] D. Xiang, S. Yang, X. Liu, Z. Mai, Y. Qian, Chem. Eng. J., 240 (2014) 45-54.

[11] Y.-K. Park, C. Lee, N. Kang, W. Choi, S. Choi, S. Oh, D. Park, Catalysis Surveys from Asia, 14 (2010) 75-84.

[12] N. Rahimi, R. Karimzadeh, Appl. Catal. A, 398 (2011) 1-17.

[13] T. Ren, M. Patel, K. Blok, Energy, 31 (2006) 425-451.

[14] M. Salmasi, S. Fatemi, A. Taheri Najafabadi, J. Ind. Eng. Chem., 17 (2011) 755-761.

[15] H.M. Torres Galvis, K.P. de Jong, ACS Catal., 3 (2013) 2130-2149.

[16] http://www.wikipedia.org/

[17] I. Mochida, O. Okuma, S.-H. Yoon, Chem. Rev., 114 (2013) 1637-1672.

[18] C. Higman, S. Tam, Chem. Rev., 114 (2014) 1673-1708.

[19] E. Jin, Y. Zhang, L. He, H.G. Harris, B. Teng, M. Fan, Appl. Catal. A, 476 (2014) 158-174.

[20] T.G. Kreutz, E.D. Larson, G. Liu, R.H. Williams, Fischer-Tropsch fuels from coal and biomass, in: 25th Annual International Pittsburgh Coal Conference, 2008.

[21] H.L. Chum, R.P. Overend, Fuel Process. Technol., 71 (2001) 187-195.

[22] A.M. Niziolek, O. Onel, J.A. Elia, R.C. Baliban, X. Xiao, C.A. Floudas, Ind. Eng. Chem. Res., (2014).

[23] R.C. Baliban, J.A. Elia, C.A. Floudas, Energy Environ. Sci., 6 (2013) 267-287.

[24] R. Luque, A.R. de la Osa, J.M. Campelo, A.A. Romero, J.L. Valverde, P. Sanchez, Energy Environ. Sci., 5 (2012) 5186-5202.

[25] Y. Zhao, H. Li, M. Ye, Z. Liu, Ind. Eng. Chem. Res., 52 (2013) 11354-11364.

[26] A.C. Koeken, H.M. Torres Galvis, T. Davidian, M. Ruitenbeek, K.P. de Jong, Angew Chem Int Ed Engl, 51 (2012) 7190-7193.

[27] J. Lu, L. Yang, B. Xu, Q. Wu, D. Zhang, S. Yuan, Y. Zhai, X. Wang, Y. Fan, Z. Hu, ACS catal., 4 (2014) 613-621.

[28] J.-D. Xu, K.-T. Zhu, X.-F. Weng, W.-Z. Weng, C.-J. Huang, H.-L. Wan, Catal. Today, 215 (2013) 86-94.

[29] A.Y. Khodakov, W. Chu, P. Fongarland, Chem. Rev., 107 (2007) 1692-1744.

[30] F. Fischer, H. Tropsch, Berichte der deutschen chemischen Gesellschaft (A and B Series), 59 (1926) 830-831.

[31] Q. Zhang, K. Cheng, J. Kang, W. Deng, Y. Wang, ChemSusChem, 7 (2014) 1251-1264.

[32] BP statistical review of world energy, in, 2013.

[33] Y. Liu, O. Ersen, C. Meny, F. Luck, C. Pham-Huu, ChemSusChem, 7 (2014) 1218-1239.

[34] T. Takeshita, K. Yamaji, Energy Policy, 36 (2008) 2773-2784.

[35] M.E. Dry, J. Chem. Technol. Biotechnol., 77 (2002) 43-50.

[36] R.H. Williams, E.D. Larson, G.J. Liu, T.G. Kreutz, Energy Procedia, 1 (2009) 4379-4386.

[37] E. de Smit, B.M. Weckhuysen, Chem. Soc. Rev., 37 (2008) 2758-2781.

[38] C. Perego, R. Bortolo, R. Zennaro, Catal. Today, 142 (2009) 9-16.

[39] J.C. van Dyk, M.J. Keyser, M. Coertzen, Int. J. Coal. Geol., 65 (2006) 243-253.

[40] A. Nakhaei Pour, H. Khodabandeh, M. Izadyar, M. Housaindokht, Reaction Kinetics, Mechanisms and Catalysis, (2013) 1-16.

[41] E. Iglesia, S.C. Reyes, R.J. Madon, S.L. Soled, Adv. Catal., 39 (1993) 221-302.

[42] H. Schulz, M. Claeys, Appl. Catal. A, 186 (1999) 91-107.

[43] S.K. Beaumont, Phys. Chem. Chem. Phys., 16 (2014) 5034-5043.

[44] G.P. Van Der Laan, A.A.C.M. Beenackers, Catal. Rev., 41 (1999) 255-318.

[45] H. Schulz, Appl. Catal. A, 186 (1999) 3-12.

[46] M.E. Dry, Catal. Today, 71 (2002) 227-241.

[47] C.K. Rofer-DePoorter, Chem. Rev., 81 (1981) 447-474.

[48] R.A. van Santen, A.J. Markvoort, I.A.W. Filot, M.M. Ghouri, E.J.M. Hensen, Phys. Chem. Chem. Phys., 15 (2013) 17038-17063.

[49] R.B. Anderson, Catalysts for the Fischer-Tropsch synthesis, Van Nostrand-Reinhold: New York, 1956.

[50] Q. Zhang, J. Kang, Y. Wang, ChemCatChem, 2 (2010) 1030-1058.

[51] Q. Zhang, W. Deng, Y. Wang, J. Energy. Chem., 22 (2013) 27-38.

[52] Q.H. Lin, G.H. Yang, X.N. Li, Y. Yoneyama, H.L. Wan, N. Tsubaki, Chemcatchem, 5 (2013) 3101-3106.

[53] E. van Steen, M. Claeys, Chem. Eng. Technol., 31 (2008) 655-666.

[54] M.A. Vannice, J. Catal., 37 (1975) 449-461.

[55] H. Jahangiri, J. Bennett, P. Mahjoubi, K. Wilson, S. Gu, Catal. Sci. Technol., 5 (2014) 2210-2229.

[56] B. Jager, R. Espinoza, Catal. Today, 23 (1995) 17-28.

[57] E. Iglesia, Appl. Catal. A, 161 (1997) 59-78.

[58] G. Jacobs, T.K. Das, Y. Zhang, J. Li, G. Racoillet, B.H. Davis, Appl. Catal. A, 233 (2002) 263-281.

[59] G.L. Bezemer, J.H. Bitter, H.P.C.E. Kuipers, H. Oosterbeek, J.E. Holewijn, X. Xu, F. Kapteijn, A.J. van Dillen, K.P. de Jong, J. Am. Chem. Soc., 128 (2006) 3956-3964.

[60] J.P. den Breejen, P.B. Radstake, G.L. Bezemer, J.H. Bitter, V. Frøseth, A. Holmen, K.P.d. Jong, J. Am. Chem. Soc., 131 (2009) 7197-7203.

[61] C.J. Weststrate, A.M. Saib, J.W. Niemantsverdriet, Catal. Today, 215 (2013) 2-7.

[62] J. Hong, W. Chu, P.A. Chernavskii, A.Y. Khodakov, Appl. Catal. A, 382 (2010) 28-35.

[63] A. de Klerk, Energy Environ. Sci., 4 (2011) 1177-1205.

[64] E.F. Sousa-Aguiar, F.B. Noronha, A. Faro Jr, Catal. Sci. Technol., 1 (2011) 698-713.

[65] D. Leckel, M. Liwanga-Ehumbu, Energ. Fuel, 20 (2006) 2330-2336.

[66] J.P. Collins, J.J.H.M. Font Freide, B. Nay, Journal of Natural Gas Chemistry, 15 (2006) 1-10.

[67] B. Sun, M. Qiao, K. Fan, J. Ulrich, F.F. Tao, ChemCatChem, 3 (2011) 542-550.

[68] J. He, Z. Liu, Y. Yoneyama, N. Nishiyama, N. Tsubaki, Chem. Eur. J., 12 (2006) 8296-8304.

[69] C. López, A. Corma, ChemCatChem, 4 (2012) 751-752.

[70] C. Wang, X. Pan, X. Bao, Chin. Sci. Bull., 55 (2010) 1117-1119.

[71] E. Iglesia, S.C. Reyes, R.J. Madon, S.L. Soled, Selectivity Control and Catalyst Design in the Fischer-Tropsch Synthesis: Sites, Pellets, and Reactors, in: H.P. D.D. Eley, B.W. Paul (Eds.) Adv. Catal., Academic Press, 1993, pp. 221-302.

[72] M.E. Dry, Appl. Catal. A, 138 (1996) 319-344.

[73] S. Novak, R.J. Madon, H. Suhl, J. Catal., 77 (1982) 141-151.

[74] N.E. Tsakoumis, M. Rønning, Ø. Borg, E. Rytter, A. Holmen, Catal. Today, 154 (2010) 162-182.

[75] E. Iglesia, S.L. Soled, R.A. Fiato, J. Catal., 137 (1992) 212-224.

[76] M. Ehrensperger, J. Wintterlin, J. Catal., 319 (2014) 274-282.

[77] G. Melaet, W.T. Ralston, C.-S. Li, S. Alayoglu, K. An, N. Musselwhite, B. Kalkan, G.A. Somorjai, J. Am. Chem. Soc., 136 (2014) 2260-2263.

[78] G. Jiao, Y. Ding, H. Zhu, X. Li, J. Li, R. Lin, W. Dong, L. Gong, Y. Pei, Y. Lu, Appl. Catal. A, 364 (2009) 137-142.

[79] J. Xiong, Y. Ding, T. Wang, L. Yan, W. Chen, H. Zhu, Y. Lu, Catal. Lett., 102 (2005) 265-269.

[80] W. Chen, Z. Fan, X. Pan, X. Bao, J. Am. Chem. Soc., 130 (2008) 9414-9419.

[81] E. de Smit, F. Cinquini, A.M. Beale, O.V. Safonova, W. van Beek, P. Sautet, B.M. Weckhuysen, J. Am. Chem. Soc., 132 (2010) 14928-14941.

[82] H.M. Torres Galvis, J.H. Bitter, T. Davidian, M. Ruitenbeek, A.I. Dugulan, K.P. de Jong, J. Am. Chem. Soc., 134 (2012) 16207-16215.

[83] J.F. Bengoa, A.M. Alvarez, M.V. Cagnoli, N.G. Gallegos, S.G. Marchetti, Appl. Catal. A, 325 (2007) 68-75.

[84] F. Diehl, A.Y. Khodakov, Oil & Gas Science and Technology - Revue de l'IFP, 64 (2008) 11-24.

[85] H. Xiong, M. Moyo, M.A.M. Motchelaho, L.L. Jewell, N.J. Coville, Appl. Catal. A, 388 (2010) 168-178.

[86] J. Gaube, H.F. Klein, Appl. Catal. A, 350 (2008) 126-132.

[87] S. Li, S. Krishnamoorthy, A. Li, G.D. Meitzner, E. Iglesia, J. Catal., 206 (2002) 202-217.

[88] S. Li, A. Li, S. Krishnamoorthy, E. Iglesia, Catal. Lett., 77 (2001) 197-205.

[89] S. Li, G.D. Meitzner, E. Iglesia, J. Phys. Chem. B, 105 (2001) 5743-5750.

[90] H.M. Torres Galvis, A.C.J. Koeken, J.H. Bitter, T. Davidian, M. Ruitenbeek, A.I. Dugulan, K.P. de Jong, J. Catal., 303 (2013) 22-30.

[91] C.-F. Huo, B.-S. Wu, P. Gao, Y. Yang, Y.-W. Li, H. Jiao, Angew. Chem. Int. Ed., 50 (2011) 7403-7406.

[92] J.M. Zowtiak, C.H. Bartholomew, J. Catal., 83 (1983) 107-120.

[93] Y. Ohtsuka, Y. Takahashi, M. Noguchi, T. Arai, S. Takasaki, N. Tsubouchi, Y. Wang, Catal. Today, 89 (2004) 419-429.

[94] A.R. de la Osa, A. de Lucas, L. Sánchez-Silva, J. Díaz-Maroto, J.L. Valverde, P. Sánchez, Fuel, 95 (2012) 587-598.

[95] A.R. de la Osa, A. De Lucas, J. Díaz-Maroto, A. Romero, J.L. Valverde, P. Sánchez, Catal. Today, 187 (2012) 173-182.

[96] A.R. de la Osa, A. De Lucas, A. Romero, J.L. Valverde, P. Sánchez, Catal. Today, 176 (2011) 298-302.

[97] B. Sun, K. Xu, L. Nguyen, M. Qiao, F. Tao, ChemCatChem, 4 (2012) 1498-1511.

[98] K.-S. Ha, G. Kwak, K.-W. Jun, J. Hwang, J. Lee, Chem. Commun., 49 (2013) 5141-5143.

[99] G. Yu, B. Sun, Y. Pei, S. Xie, S. Yan, M. Qiao, K. Fan, X. Zhang, B. Zong, J. Am. Chem. Soc., 132 (2009) 935-937.

[100] Y. Yang, L. Jia, B. Hou, D. Li, J. Wang, Y. Sun, J. Phys. Chem. C, 118 (2014) 268-277.

[101] Y. Yang, L. Jia, B. Hou, D. Li, J. Wang, Y. Sun, ChemCatChem, 6 (2014) 319-327.

[102] E. Iglesia, S.L. Soled, R.A. Fiato, G.H. Via, Dispersion, support, and bimetallic effects in Fischer-Tropsch synthesis on cobalt catalysts, in: H.E. Curry-Hyde, R.F. Howe (Eds.) Stud. Surf. Sci. Catal., Elsevier, 1994, pp. 433-442.

[103] J. Kang, S. Zhang, Q. Zhang, Y. Wang, Angew. Chem. Int. Ed., 48 (2009) 2565-2568.

[104] J.M.G. Carballo, J. Yang, A. Holmen, S. García-Rodríguez, S. Rojas, M. Ojeda, J.L.G. Fierro, J. Catal., 284 (2011) 102-108.

[105] Q.H. Zhang, J.C. Kang, Y. Wang, ChemCatChem, 2 (2010) 1030-1058.

[106] C. Xing, G. Yang, D. Wang, C. Zeng, Y. Jin, R. Yang, Y. Suehiro, N. Tsubaki, Catal. Today, 215 (2013) 24-28.

[107] Q. Tang, Q. Zhang, P. Wang, Y. Wang, H. Wan, Chem. Mater., 16 (2004) 1967-1976.

[108] X. Li, K. Asami, M. Luo, K. Michiki, N. Tsubaki, K. Fujimoto, Catal. Today, 84 (2003) 59-65.

[109] E.W. Kuipers, C. Scheper, J.H. Wilson, I.H. Vinkenburg, H. Oosterbeek, J. Catal., 158 (1996) 288-300.

[110] C.L. Bianchi, V. Ragaini, J. Catal., 168 (1997) 70-74.

[111] E.W. Kuipers, I.H. Vinkenburg, H. Oosterbeek, J. Catal., 152 (1995) 137-146.

[112] W. Böhringer, A. Kotsiopoulos, M. de Boer, C. Knottenbelt, J.C.Q. Fletcher, Selective Fischer-Tropsch wax hydrocracking-opportunity for improvement of overall gas-to-liquids processing, in: B.H. Davis, M.L. Occelli (Eds.) Stud. Surf. Sci. Catal., Elsevier, 2007, pp. 345-365.

[113] G. Henrici-Olivé, S. Olivé, Angew. Chem. Int. Ed., 15 (1976) 136-141.

[114] D.S. Lafyatis, H.C. Foley, Chem. Eng. Sci., 45 (1990) 2567-2574.

[115] G.H. Yang, H. Kawata, Q.H. Lin, J.Y. Wang, Y.Z. Jin, C.Y. Zeng, Y. Yoneyama, N. Tsubaki, Chem. Sci., 4 (2013) 3958-3964.

[116] A. Martínez, G. Prieto, Top. Catal., 52 (2009) 75-90.

[117] K. Asami, A. Iwasa, N. Igarashi, S. Takemiya, K. Yamamoto, K. Fujimoto, Catal. Today, 215 (2013) 80-85.

[118] N. Tsubaki, Y. Yoneyama, K. Michiki, K. Fujimoto, Catal. Commum., 4 (2003) 108-111.

[119] Z.-W. Liu, X. Li, K. Asami, K. Fujimoto, Catal. Commum., 6 (2005) 503-506.

[120] Z.-W. Liu, X. Li, K. Asami, K. Fujimoto, Catal. Today, 104 (2005) 41-47.

[121] G. Yang, J. He, Y. Yoneyama, Y. Tan, Y. Han, N. Tsubaki, Appl. Catal. A, 329 (2007) 99-105.

[122] J. Bao, J. He, Y. Zhang, Y. Yoneyama, N. Tsubaki, Angew. Chem. Int. Ed., 47 (2008) 353-356.

[123] X. Li, J. He, M. Meng, Y. Yoneyama, N. Tsubaki, J. Catal., 265 (2009) 26-34.

[124] X.G. Li, C. Liu, J. Sun, H. Xian, Y.S. Tan, Z. Jiang, A. Taguchi, M. Inoue, Y. Yoneyama, T. Abe, N. Tsubaki, Scientific Reports, 3 (2013).

[125] J. Sun, X.G. Li, A. Taguchi, T. Abe, W.Q. Niu, P. Lu, Y. Yoneyarna, N. Tsubaki, ACS catal., 4 (2014) 1-8.

[126] A. Corma, Chem. Rev., 95 (1995) 559-614.

[127] J. Cejka, A. Corma, S. Zones, Zeolites and catalysis: synthesis, reactions and applications, John Wiley & Sons, 2010.

[128] J. Weitkamp, M. Hunger, Chapter 22 Acid and base catalysis on zeolites, in: H.v.B.A.C. Jiří Čejka, S. Ferdi (Eds.) Stud. Surf. Sci. Catal., Elsevier, 2007, pp. 787-835.

[129] S. Davis, G. Somorjai, D. King, D. Woodruff, The Chemical Physics of Solid Surfaces and Heterogeneous Catalysis, Elsevier, Amsterdam, 1982.

[130] M. Rigutto, Cracking and Hydrocracking, in: Zeolites and Catalysis, Wiley-VCH Verlag GmbH & Co. KGaA, 2010, pp. 547-584.

[131] S. Sartipi, M. Makkee, F. Kapteijn, J. Gascon, Catal. Sci. Technol., 4 (2014) 893-907.

[132] J. Weitkamp, Solid State Ionics, 131 (2000) 175-188.

[133] X. Meng, F.-S. Xiao, Chem. Rev., 114 (2013) 1521-1543.

[134] K. Li, J. Valla, J. Garcia-Martinez, ChemCatChem, 6 (2014) 46-66.

[135] L.-H. Chen, X.-Y. Li, J.C. Rooke, Y.-H. Zhang, X.-Y. Yang, Y. Tang, F.-S. Xiao, B.-L. Su, J. Mater. Chem., 22 (2012) 17381-17403.

[136] A. Corma, J. Catal., 216 (2003) 298-312.

[137] K. Li, J. Valla, J. Garcia-Martinez, ChemCatChem, 6 (2013) 46-66.

[138] D. Verboekend, J. Pérez-Ramírez, ChemSusChem, 7 (2014) 653-764.

[139] R. Chal, C. Gérardin, M. Bulut, S. van Donk, ChemCatChem, 3 (2011) 67-81.

[140] X. Meng, F. Nawaz, F.-S. Xiao, Nano Today, 4 (2009) 292-301.

[141] J. Perez-Ramirez, C.H. Christensen, K. Egeblad, C.H. Christensen, J.C. Groen, Chem. Soc. Rev., 37 (2008) 2530-2542.

[142] A. Inayat, I. Knoke, E. Spiecker, W. Schwieger, Angew. Chem. Int. Ed., 51 (2012) 1962-1965.

[143] C. Fernandez, I. Stan, J.-P. Gilson, K. Thomas, A. Vicente, A. Bonilla, J. Pérez-Ramírez, Chem. Eur. J., 16 (2010) 6224-6233.

[144] Z.X. Yang, Y.D. Xia, R. Mokaya, Adv. Mater., 16 (2004) 727-732.

[145] M. Hartmann, Angew. Chem. Int. Ed., 43 (2004) 5880-5882.

[146] P.A. Jacobs, M. Dusselier, B.F. Sels, Angew. Chem. Int. Ed., 53 (2014) 8621-8626.

[147] M.S. Holm, E. Taarning, K. Egeblad, C.H. Christensen, Catal. Today, 168 (2011) 3-16.

[148] Y. Tao, H. Kanoh, L. Abrams, K. Kaneko, Chem. Rev., 106 (2006) 896-910.

[149] D.P. Serrano, J.M. Escola, P. Pizarro, Chem. Soc. Rev., 42 (2013) 4004-4035.

[150] K. Na, M. Choi, R. Ryoo, Microporous Mesoporous Mater., 166 (2013) 3-19.

[151] V. Valtchev, G. Majano, S. Mintova, J. Perez-Ramirez, Chem. Soc. Rev., 42 (2013) 263-290.

[152] Z.L. Hua, J. Zhou, J.L. Shi, Chem. Commun., 47 (2011) 10536-10547.

[153] J.C. Groen, L.A. Peffer, J.A. Moulijn, J. Perez-Ramirez, Chemistry, 11 (2005) 4983-4994.

[154] J.C. Groen, J.A. Moulijn, J. Pérez-Ramírez, Microporous Mesoporous Mater., 87 (2005) 153-161.

[155] J.C. Groen, J.C. Jansen, J.A. Moulijn, J. Pérez-Ramírez, J. Phys. Chem. B, 108 (2004) 13062-13065.

[156] A. Pereira, J. González-Carballo, F. Pérez-Alonso, S. Rojas, J. Fierro, M.d. Rangel, Top. Catal., 54 (2011) 179-189.

[157] J.C. Kang, K. Cheng, L. Zhang, Q.H. Zhang, J.S. Ding, W.Q. Hua, Y.C. Lou, Q.G. Zhai, Y. Wang, Angew. Chem. Int. Ed., 50 (2011) 5200-5203.

[158] S. Sartipi, J.E. van Dijk, J. Gascon, F. Kapteijn, Appl. Catal. A, 456 (2013) 11-22.

[159] S. Sartipi, K. Parashar, M.J. Valero-Romero, V.P. Santos, B. van der Linden, M. Makkee, F. Kapteijn, J.

Gascon, J. Catal., 305 (2013) 179-190.

[160] S. Sartipi, K. Parashar, M. Makkee, J. Gascon, F. Kapteijn, Catal. Sci. Technol., 3 (2013) 572-575.

[161] S. Sartipi, M. Alberts, M.J. Meijerink, T.C. Keller, J. Perez-Ramirez, J. Gascon, F. Kapteijn, ChemSusChem, 6 (2013) 1646-1650.

[162] M. Janardanarao, Ind. Eng. Chem. Res., 29 (1990) 1735-1753.

[163] M.E. Dry, T. Shingles, L.J. Boshoff, G.J. Oosthuizen, J. Catal., 15 (1969) 190-199.

[164] M.E. Dry, T. Shingles, C.S. van H. Botha, J. Catal., 17 (1970) 341-346.

[165] M.M. McClory, R.D. Gonzalez, J. Catal., 89 (1984) 392-403.

[166] W. Ngantsoue-Hoc, Y. Zhang, R.J. O'Brien, M. Luo, B.H. Davis, Appl. Catal. A, 236 (2002) 77-89.

[167] J.P. den Breejen, J.R.A. Sietsma, H. Friedrich, J.H. Bitter, K.P. de Jong, J. Catal., 270 (2010) 146-152.

[168] J.R. Sietsma, J.D. Meeldijk, J.P. den Breejen, M. Versluijs-Helder, A.J. van Dillen, P.E. de Jongh, K.P. de Jong, Angew. Chem. Int. Ed., 46 (2007) 4547-4549.

[169] A. Martinez, J. Rollan, M. Arribas, H. Cerqueira, A. Costa, E. Saguiar, J. Catal., 249 (2007) 162-173.

[170] Y. Li, T. Wang, C. Wu, Y. Lv, N. Tsubaki, Energ. Fuel, 22 (2008) 1897-1901.

[171] G. Ertl, H. Knözinger, F. Schüth, J. Weitkamp, Handbook of Heterogeneous Catalysis II, Wiley-VCH Verlag GmbH Co, 2008.

[172] A.Y. Khodakov, A. Griboval-Constant, R. Bechara, V.L. Zholobenko, J. Catal., 206 (2002) 230-241.

[173] Y. Wang, M. Noguchi, Y. Takahashi, Y. Ohtsuka, Catal. Today, 68 (2001) 3-9.

[174] Ø. Borg, S. Eri, E.A. Blekkan, S. Storsæter, H. Wigum, E. Rytter, A. Holmen, J. Catal., 248 (2007) 89-100.

[175] A.Y. Khodakov, V.L. Zholobenko, R. Bechara, D. Durand, Microporous Mesoporous Mater., 79 (2005) 29-39.

[176] R.M.M. Abbaslou, J. Soltan, A.K. Dalai, Appl. Catal. A, 379 (2010) 129-134.

[177] D.J. Kim, B.C. Dunn, F. Huggins, G.P. Huffman, M. Kang, J.E. Yie, E.M. Eyring, Energ. Fuel, 20 (2006) 2608-2611.

[178] P.A. Chernavskii, V.I. Zaikovskii, G.V. Pankina, A.Y. Khodakov, ChemCatChem, 5 (2013) 1758-1761.

[179] S. Abelló, D. Montané, ChemSusChem, 4 (2011) 1538-1556.

[180] X. An, B.-s. Wu, H.-J. Wan, T.-Z. Li, Z.-C. Tao, H.-W. Xiang, Y.-W. Li, Catal. Commum., 8 (2007) 1957-1962.

[181] M.C. Ribeiro, G. Jacobs, B.H. Davis, D.C. Cronauer, A.J. Kropf, C.L. Marshall, J. Phys. Chem. C, 114 (2010) 7895-7903.

[182] M. Saglam, Ind. Eng. Chem. Res., 28 (1989) 150-154.

[183] T.C. Bromfield, N.J. Coville, Appl. Catal. A, 186 (1999) 297-307.

[184] J. Abbott, N.J. Clark, B.G. Baker, Applied Catalysis, 26 (1986) 141-153.

[185] J.-B. Li, H.-F. Ma, H.-T. Zhang, Q.-W. Sun, W.-Y. Ying, D.-Y. Fang, Fuel Process. Technol., 125 (2014) 119-124.

Chapter 2. Experimental

2.1 Catalyst preparation

2.1.1 Preparation of mesoporous beta zeolite

H-beta zeolite with a Si/Al ratio of 27 was purchased from Nankai University Catalyst Co. The meso-beta was prepared by treating the H-beta using NaOH aqueous solutions (Figure 2-1). Typically, H-beta powders (4.0 g) were added into NaOH aqueous solutions (100 mL) with different concentrations in a range of 0.05-0.7 mol dm^{-3} (M). Then, the suspension was heated to 343 K and stirred for 1 h. After cooled down to room temperature, the solid was recovered by filtration, followed by washing thoroughly with deionized water. The recovered solid sample was dried at 373 K for 8 h and calcined in air at 573 K for 3 h. The sample thus obtained is denoted as meso-beta-*x* M, where *x* is the concentration of NaOH. Our inductively coupled plasma mass spectrometry (ICP-MS) analysis suggested that Na^+ ions were exchanged into the cationic sites in the meso-beta. Thus, the meso-beta-*x*M samples were further exchanged into their NH_4^+ forms by adding the meso-beta-*x*M powders into $NH_4{\cdot}NO_3$ aqueous solution (1.0 M). After the ion-exchange, the solid product was obtained by filtration, followed by washing, drying and calcination at 823 K for 6 h. The obtained sample was denoted as H-meso-beta-*x*M, where *x* is the concentration of NaOH used for H-beta zeolite treatment.

Figure 2-1. Diagram of introduction of mesopores into the microporous zeolite by desilication

2.1.2 Preparation of mesoporous ZSM-5 zeolite

ZSM-5 was synthesized by the hydrothermal method according to a recipe reported by Ryoo and co-workers [1]. Typically, 2.0 g sodium aluminate, 28.0 g tetrapropylammonium bromide (TPABr) and 8.0 g NaOH were first dissolved in 1350 g H_2O, and the mixture was

stirred vigorously for 2 h. Then, 85.7 g tetraethylorthosilicate (TEOS) was added into the mixture. After being stirred for another 2 h at room temperature, the obtained homogeneous mixture was transferred into a Teflon tube, which was placed in a stainless-steel autoclave. The hydrothermal synthesis was carried out at 443 K with a rotation speed of 50 rpm for 3 days. The solid product was obtained by centrifugation, followed by washing with deionized water and drying at 373 K in air. The powdery sample was calcined at 823 K in air for 6 h to obtain Na-ZSM-5.

The mesoporous ZSM-5 was prepared by treating the Na-ZSM-5 using NaOH aqueous solutions with different concentrations (desilication treatment). Typically, 4.0 g Na-ZSM-5 powder was added into 40 mL NaOH aqueous solutions of different concentrations in a range of 0.1-1.2 mol dm^{-3} (M), the suspension was then heated to 343 K and stirred at 343 K for 1 h. After being cooled to room temperature, the solid was recovered by filtration, followed by washing thoroughly with deionized water. The recovered solid sample was further dried at 393 K for 12 h. The Na-type samples were exchanged into their H-type forms by the typical ion-exchange method using a 1.0 mol dm^{-3} $NH_4{\cdot}NO_3$ aqueous solution. The exchanging procedure may be performed for several times to alter the H^+-exchange degree. The obtained sample was thoroughly washed, followed by calcination in air at 823 K for 6 h. The ZSM-5 samples with different H^+-exchange degrees were prepared by a similar ion-exchange technique.

2.1.3 Preparation of silica supports with different pore diameters

Five periodic mesoporous silicas and two commercial silicas were used as catalytic supports. The silicas are labeled as Si*x*, where *x* indicates the average silica pore size in nm. The pore sizes in mesoporous silicas are displayed in Table 1. The Si2.8 sample (MCM-41 type) was synthesized using a procedure reported in Ref [2]. Synthesis of this material started with mixing 1 g of 28% $NH_4{\cdot}OH$ solution and 21 g of 25% solution of cetyltrimethylammonium chloride (CTMACl). Then 5.3 g tetramethylammonium hydroxide pentahydrate (TMAOH), 5.6 g of fumed silica and 11.4 g of deionized water were added to the solution. The mixture was stirred for 30 min, then, kept at 353 K for 48 h. The resulting gel was filtered and washed with water and ethanol. The final product was dried at 353 K for 24 h and then carefully calcined in flowing nitrogen for 5 hours at 773 K and in flowing air 823 K with a ramp 1 K min^{-1}.

The Si5.2, Si7.2, Si7.7 and Si9.2 samples (SBA-15 type) with different pore sizes were prepared using triblock copolymer P123 ($EO_{20}PO_{70}EO_{20}$, *Mn* ca. 5800, Aldrich, 43546-5) as a

soft template. The pore sizes of these silicas were varied by tuning the hydrothermal temperature, concentration of HCl and addition of swelling agent [2-4]. For the synthesis of Si5.2, Si7.2 and Si7.7 silicas, firstly 6 g of P123 copolymer was dispersed in 45 g of water and 180 g of 2 M HCl under stirring at 313 K. After complete dissolving P123, 12.75 g of tetraethylorthosilicate (TEOS) were added to the solution. The mixture was kept at 313 K under stirring for 24 h to obtain a uniform solution. The solution was transferred into a hermetically closed polypropylene flask and kept in an oven for 48 h at 323 K (Si5.2), 353 K (Si7.2) and 373 K (Si7.7) respectively. The gel was washed with distilled water, dried at 353 K for 24 h, and subsequently calcined with a flow of air at 823 K for 6 h. The rate of temperature ramping was 1 K min^{-1}. To synthesize Si9.2 silica, dimethylformamide (DMF) was used as swelling agent. Firstly, 90 g of DMF, 180 g of water, and 180 g of 4 M HCl were mixed in a glass flask under stirring. Then 12 g of P123 was dispersed in the resulting solution under stirring at 313 K. After complete dissolving of P123, 24 g of TEOS were added. The mixture was kept at 313 K under stirring for 24 h to obtain a uniform solution. Then the solution was transferred into a hermetically closed polypropylene flask and kept in an oven at 373 K for 48 h. The gel was washed, dried and calcined using the same procedure as for other SBA-15 type silicas. Si17.5 and Si50 samples with larger pores were commercial silicas: CARIACT Q-10 and Aerosil 200.

2.1.4 Preparation of carbon supports

The synthesis of CMK-3 (Figure 2-2) was carried out according to Ref. [5]. Briefly, 5 g of SBA-15 was added to a solution obtained by dissolving 6.25 g of sucrose and 0.7 g of H_2SO_4 in 25 g of H_2O. The mixture was transferred to a drying oven for 6 h at 373 K, and followed by increasing the oven temperature to 433 K for 6 h. After dissolving additional 4 g of sucrose, 0.45 g of H_2SO_4 and 25 g of H_2O, the mixture was treated again at 373 K and 433 K using the same drying oven. The carbonization was completed by pyrolysis with heating to typically 1173 K under N_2 flow. The obtained carbon-silica composite was washed twice with 1 M NaOH solution (solid-to-liquid ratio 1:100) at 368 K to remove the silica template. The template-free carbon material was filtered, washed with deionized water and dried at 393 K overnight. The synthesized CMK-3 was treated with 1 M nitric acid solution at 323 K for 2 h to remove residual sodium.

Multi-wall carbon nanotubes (CNT, purity ≥ 95%, outer diameter 20 - 30 nm) prepared by chemical vapor deposition (CVD) were purchased from the Chengdu Limited Company of Organic Chemistry (CCOC) in China. Before using, raw CNTs were refluxed for 16 h in

concentrated HNO_3 (65 wt. %) at 393 K in an oil bath to to remove amorphous carbon and the remaining Ni catalyst. Then, the mixture was filtered and washed with distilled water thoroughly until neutral pH was reached, followed by drying at 373 K overnight.

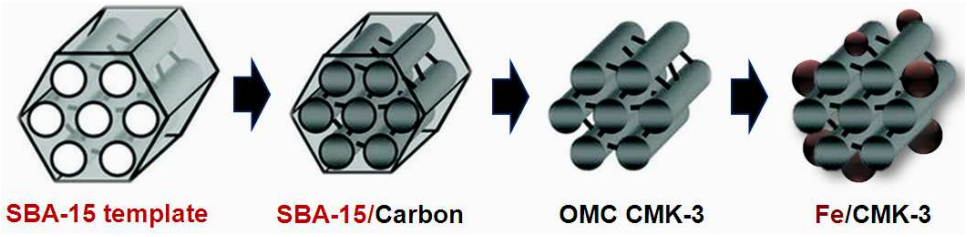

Figure 2-2. Synthesis procedure of ordered mesoporous carbon and supported iron catalysts

2.1.5 Preparation of supported Ru catalysts

The supported Ru catalysts were prepared by an impregnation method. Briefly, the meso-beta-*x*M or H-meso-beta-*x*M sample was added into a $RuCl_3$ aqueous solution, and the suspension was stirred for 8 h, followed by resting for 15 h. After evaporation to dryness at 343 K, the solid product was further dried at 323 K in vacuum overnight, followed by calcination in air at 573 K for 3 h. The catalyst was finally reduced in H_2 gas flow at 573 K for 3 h. The loading of Ru in each catalyst was fixed at 3.0 wt%.

2.1.6 Preparation of supported Co catalysts

The supported Co catalysts were prepared by an impregnation method with a fixed loading of 8.0 wt% Co. Briefly, a stoichiometric amount of $Co(NO_3)_2$ aqueous solution was added into 2.0 g zeolite support under stirring. After evaporation to dryness at 343 K, the solid $Co(NO_3)_2$/zeolite composite was carefully treated under a flow of 5 vol% NO/Ar gas flow at 673 K for 3 h to obtain homogeneously distributed Co nanoparticles [6, 7]. The catalyst was then reduced in H_2 gas flow at 673 K for 6 h before reaction.

2.1.7 Preparation of supported Fe catalysts

The supported iron catalysts were prepared by incipient wetness impregnation of silicas with aqueous solutions of hydrous iron nitrate ($Fe(NO_3)_3 \cdot 9 H_2O$). The dosage of aqueous solution was based on the total pore volume calculated by N_2 physical adsorption. The concentrations of the impregnating solutions were calculated to obtain 10 wt. % irons in the final catalysts. The catalysts are labeled as *y*FeSi*x*, where *y* indicates iron content (in wt. %) in the catalyst and *x* stands for support pore size (in nm). After impregnation the catalysts were dried overnight in an oven at 373 K. Then they were calcined in air flow at 673 K for 6 h with

a 1 K min^{-1} temperature ramping. The 20FeSi17.5 catalyst was obtained using two consecutive impregnations. The catalyst was calcined at 673 K in air flow between the impregnations.

The Fe/SiO_2, Fe/Al_2O_3, Fe/CNT, Fe/CMK-3 catalysts were also prepared by incipient wetness impregnation of the relevant support with aqueous solutions of hydrous iron nitrate ($Fe(NO_3)_3 \cdot 9H_2O$). The concentrations of the impregnating solutions were calculated to obtain 10 wt. % iron in the final catalysts. After impregnation the catalysts were dried overnight in an oven at 393 K. Then they were calcined in air (Fe/SiO_2, Fe/Al_2O_3) or N_2 flow (Fe/CNT, Fe/CMK-3) at 673 K for 6 h with 1 K min^{-1} temperature ramping.

The sodium promoted catalysts was prepared by subsequent impregnation of calcined catalyst with aqueous solution of Na_2CO_3. The catalysts have been subsequently calcined in N_2 flow at 673 K for 6 h. The amount of Na in the samples was calculated to have the molar ratio of Na to Fe 0.1, 0.3 and 0.5. The samples are labeled as $Fe/SiO_2(x)$, where *x* indicates the molar ratio of Na to Fe.

2.2 Evaluation of Catalytic Performance

2.2.1 Equipment for evaluation of Ru and Co catalysts

FT synthesis was performed in a fixed-bed stainless steel reactor (Figure 2-3) with an inner diameter of 7.0 mm. The catalyst (typically 0.50 g) was first placed in the middle of the reactor between quartz wool plugs. The Co catalyst was pretreated in pure H_2 gas flow (flow rate = 60 mL min^{-1}) at 673 K (for Ru catalysts at 573 K) prior to reaction. After the reactor was cooled to 373 K, a syngas (flow rate = 20 mL min^{-1}) with a H_2/CO ratio of 1/1 was introduced into the reactor. The pressure of the syngas was typically regulated to 2.0 MPa. Argon with a concentration of 4.0 vol% in the CO was used as an internal standard for the calculation of CO conversion. The reaction was started by raising the temperature to the desired reaction temperature (Co catalysts at 513 K and Ru catalysts at 533 K). The products were analyzed by gas chromatography. The selectivity was calculated on a molar carbon basis. Carbon balances were all about 95-100%, and catalytic performances typically after 12 h of reaction were used for discussion.

A TDX-01 packed column is connected to a TCD detector to separate Ar, CH_4, CO and CO_2 gas. In order to analyze all the hydrocarbons on line, a dypass line from the reactor to the GC oven is heated to 533K to evaporate all the hydrocarbon products, and the split and

pressure reduction of reaction gas is carried out by a needle valve. The separation and analysis of hydrocarbons is conducted by a Pona capillary column linked to a FID detector. Most of the long-chain hydrocarbons are collected in the cold trap.

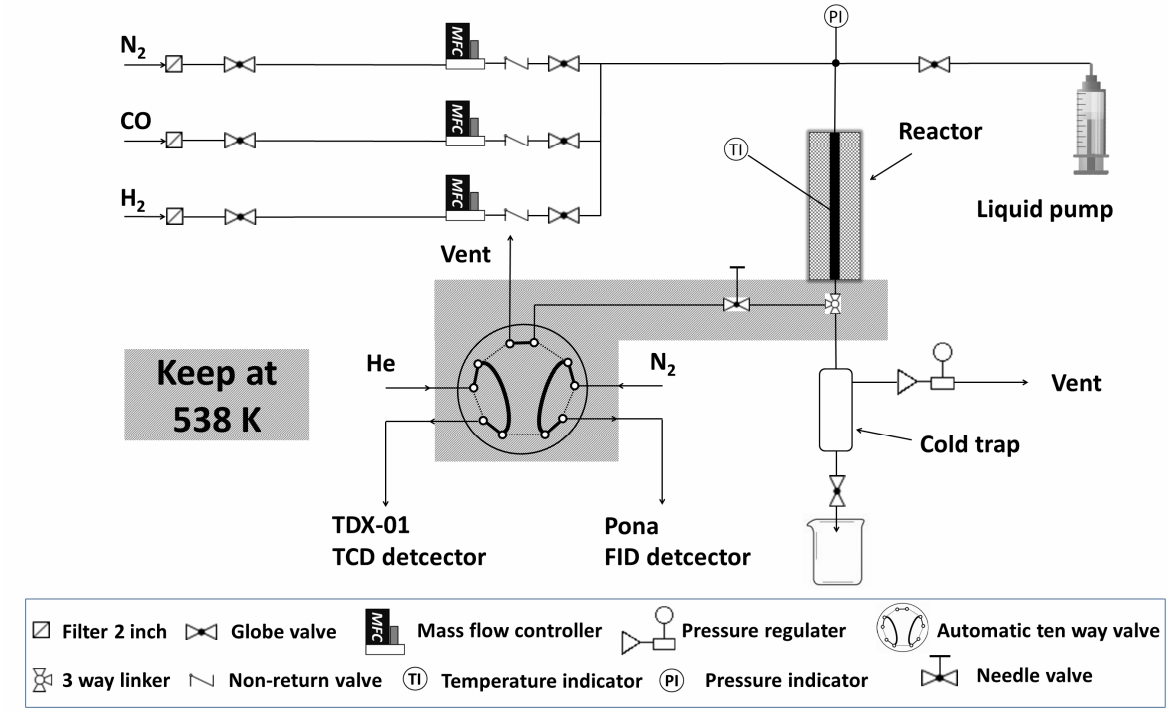

Figure 2-3. Schematic diagram of device for Fischer-Tropsch synthesis and *n*-hexadecane hydrocracking.

2.2.2 Equipment for evaluation of *n*-hexadecane hydrocracking

Hydrocracking of *n*-hexadecane is conducted on the same equipment for FT reaction in section 2.2.1. The Co catalyst was pretreated in pure H_2 gas flow (flow rate = 60 mL min^{-1}) at 673 K (for Ru catalysts at 573 K) prior to reaction. After the reactor was cooled to 373 K, high pressure H_2 (40 - 60 mL min^{-1}) was introduced into the reactor. The pressure was typically set to 2.0 MPa. When the temperature was raised to set point, *n*-hexadecane was introduced by a Lab Alliance Series III pump. Analysis of hydrocarbons was processed with a FID detector connected to a Pona capillary column.

2.2.3 Equipment for catalytic evaluation of Fe catalysts

Carbon monoxide hydrogenation was carried out on the REALCAT platform in a Flowrence® high-throughput unit (Avantium, Figure 2-4) equipped with 16 parallel milli-fixed-bed reactors (d_{in} = 2 mm) [8] operating at a total pressure of 20 bars, 573 K,

H_2/CO= 2.1 molar ratio and GHSV in the range 8.4 to 33.8 L g^{-1} h^{-1}. The FT tests have been conducted in the same unit at 573 K, 20 bars and H_2 flow with GHSV = 0.75 L g^{-1} h^{-1}. The catalyst loading was 50 mg per reactor. Prior to the catalytic test all the samples were activated in a flow of CO at atmospheric pressure during 10 h at 623 K for 10 h. During the activation step, the temperature ramp was 3 K min^{-1}. After the activation, the catalysts were cooled down to 453 K and a flow of premixed syngas was gradually introduced through the catalysts. When pressure attained 20 bar, the temperature was slowly increased to 573 K. Gaseous reaction products were analyzed by on-line gas chromatography. Analysis of permanent gases was performed using a Molecular Sieve column and a thermal conductivity detector. Carbon dioxide and C_1-C_4 hydrocarbons were separated in a PPQ column and analyzed by a thermoconductivity detector. C_5-C_{12} hydrocarbons were analyzed using CP-Sil5 column and a flame-ionization detector. High-molecular-weight products were collected at atmospheric pressure in vials heated at 353 K. The carbon monoxide contained 5% of helium, which was used as an internal standard for calculating carbon monoxide conversion. The reaction rates were defined as the number of moles of CO converted per hour per mole of catalyst (mol mol_{Fe}^{-1} h^{-1}). The product selectivity (S) was reported as the percentage of CO converted into a given product and is expressed on carbon basis.

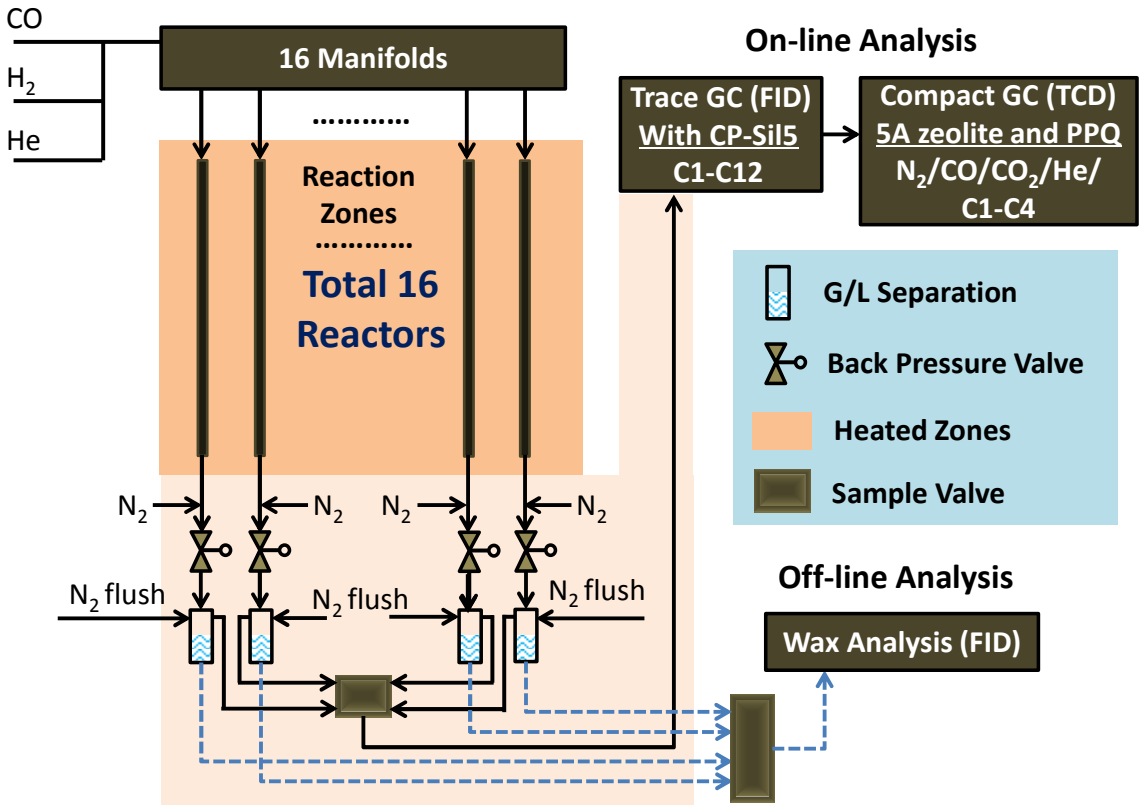

Figure 2-4. Avantium's parallel fixed bed 16-reactors systems

2.3 Analysis of Reaction Products

Hereinafter, *A* means the area of peak exported from GC，*f* means calibration factor，*n* means moles of product (based on carbon atom moles)，*j* means carbon number and *S* means selectivity. Before reaction, the area ratio of CO/Ar (or CO/He) is firstly calculated, so the CO conversion during reaction can be calculated using Equation 2-1.

$$CO_{(Conv.)\%} = (1 - \frac{A_{initialAr} / A_{reactionAr}}{A_{initialCO} / A_{reactionCO}}) * 100\% \qquad \text{(Equation 2-1)}$$

The inlet rate of internal standard gas (Ar or He) is controlled by MFC. So the generation rate of CH_4 and CO_2 can be calculated by Equation 2-2 and Equation 2-3 respectively, and there selectivity can be also calculated by Equation 2-4 and Equation 2-5.

$$n_{CH_4} = \frac{A_{CH_4} / f_{CH_4}}{A_{Ar} / f_{Ar}} * n_{Ar} \qquad \text{(Equation 2-2)}$$

$$n_{CO_2} = \frac{A_{CO_2} / f_{CO_2}}{A_{Ar} / f_{Ar}} * n_{Ar} \qquad \text{(Equation 2-3)}$$

$$S_{CO_2} = \frac{n_{CO_2}}{n_{CO} * CO_{(conv.)\%}} * 100\% \qquad \text{(Equation 2-4)}$$

$$S_{CH_4} = \frac{n_{CH_4}}{n_{CO} * CO_{(conv.)\%} - n_{CO_2}} * 100\% \qquad \text{(Equation 2-5)}$$

FID is a carbon counting device [9]. Correlated with CH_4, the generation rate and selectivity of other hydrocarbons can be calculated by Equation 2-6 and Equation 2-7 respectively.

$$n_{C_j} = \frac{A_{Cj}}{A_{CH_4}} * n_{CH_4} \qquad \text{(Equation 2-6)}$$

$$S_{Cj} = \frac{n_{Cj}}{n_{CO} * CO_{(conv.)\%} - n_{CO_2}} * 100\% \qquad \text{(Equation 2-7)}$$

Carbon balance was calculated by Equation 2-8.

$$C_{balance} = \frac{n_{CO_2} + \sum_{j=1}^{max} n_{Cj}}{n_{CO} \cdot CO_{(conv.)\%}} * 100\% \qquad \text{(Equation 2-8)}$$

For the experiment of *n*-hexadecane hydrocracking, the selectivity of product and cracking conversion are calculated by Equation 2-9 and Equation 2-10.

$$S_{C_j} = \frac{A_{C_j}}{\sum_{j=1}^{15} A_{C_j}} * 100\% \qquad \text{(Equation 2-9)}$$

$$C_{16\,(conv.)\%} = \frac{\sum_{j=1}^{15} A_{C_j}}{\sum_{j=1}^{16} A_{C_j}} * 100\% \qquad \text{(Equation 2-10)}$$

2.4 Catalyst Characterization

2.4.1 X-ray diffraction

Powder X-ray diffraction patterns were recorded by a Siemens D5000 diffractometer using Cu($K\alpha$) (λ = 0.1538 nm) radiation at room temperature, 0.02° step size and 2 s step time. The average crystallite size of Fe_2O_3 Fe_3O_4 and Fe_xC_y were calculated according to Scherrer's equation [10]. Prior to the characterization of activated samples, a very small amount of O_2 was introduced in the flowing N_2 (1% O_2 in N_2) for passivation of the samples before they were removed out from the reactor at room temperature. Crystallite phases were determined by comparing the diffraction patterns with those in the standard powder XRD files (JCPDS) published by the International Center for Diffraction Data.

The relative crystallinity of zeolitic samples was calculated by comparing the areas of feature diffraction peaks with respect to the parent H-beta and H-ZSM-5 zeolite [11].

2.4.2 Transmission electron microscopy images

Transmission electron microscopy (TEM) images of the samples were obtained on a FEI Tecnai G^2 20 S-Twin microscope. The samples were prepared by directly dipping a copper 400 microscope grids covered with carbon film into ultrasonic suspension of the powder in ethanol. The metal particle histograms obtained using more than 150 detected iron particles from the TEM images.

2.4.3 Hydrogen temperature-programmed reduction

The reducibility of the catalysts was studied by hydrogen temperature-programmed reduction (H_2-TPR). The H_2-TPR was carried out on AutoChem II 2920 apparatus (Figure 2-5) from Micromeritics using 0.05 g of the sample in 5 vol. % H_2/Ar stream (50 $cm^3\,min^{-1}$). The temperature was increased from room temperature to 1173 K at a rate of 10 K min^{-1}. The consumption of H_2 was followed by a TCD detector.

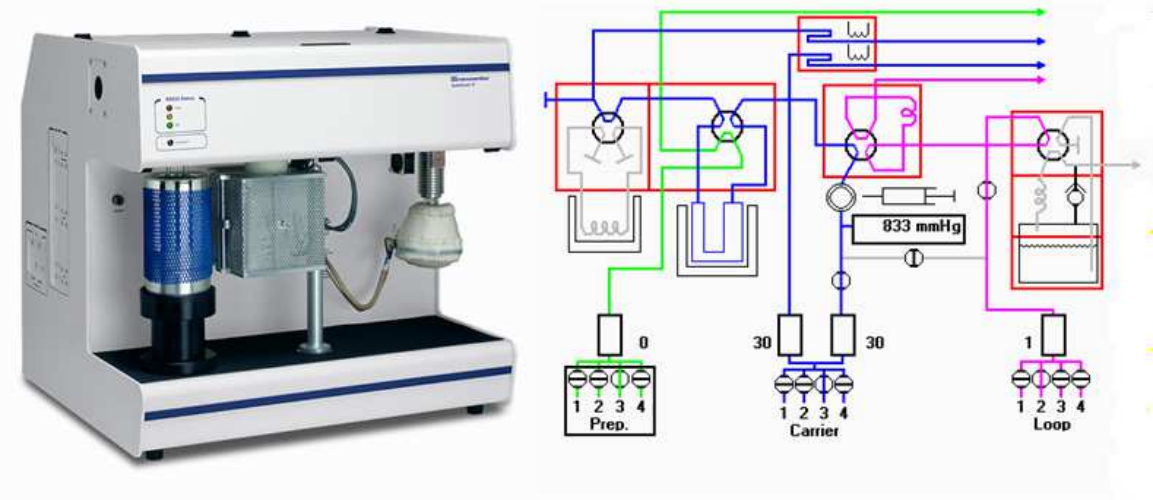

Figure 2-5. Picture of Micromeritics AutoChem II 2920 apparatus and the gas-route chart.

2.4.4 Temperature-programmed desorption of CO_2

For TPD of CO_2 has been conducted over Micromeritics AutoChem II 2920 instrument connected to a ThermoStar GSD301 T2 mass spectrometer. 100 mg of the catalyst after CO pretreatment has been loaded in a quartz reactor and pretreated with a He flow at 623 K for 60 min. The adsorption of CO_2 was performed with 10% CO_2/He for 60 min at 373 K. After purging with pure He, raising the temperature from 373 K to 1073 K with a 10 K min^{-1} ramping. CO_2 was detected with MS using the signal m/e = 44.

2.4.5 Temperature-programmed desorption of NH_3

NH_3-TPD measurements were performed by a Micromeritics AutoChemII 2920 instrument. Typically, the sample was pretreated in a quartz reactor with an O_2-He gas (20 vol% O_2) at 673 K for 1 h, followed by purge with high-purity Helium. The adsorption of NH_3 was performed at 373 K in an NH_3-He mixture (10 vol% NH3) for 1 h, and TPD was performed in Helium flow by raising the temperature to 1073 K at a rate of 10 K min^{-1}.

2.4.6 Temperature-programmed oxidation

Temperature-programmed oxidation (TPO) measurements were also performed on the Micromeritics AutoChem2920 II instrument. The catalyst after catalytic reactions was first pretreated in pure He gas flow at 673 K for 0.5 h. Then, TPO was performed by switching the He flowto an O_2-He (1 vol.%O_2) flow after the temperature was decreased to 373 K. The temperature was raised to 1073 K at a rate of 10 K min^{-1}, and the formed CO_2 was detected by the mass spectrometer with signals of m/e =44.

2.4.7 Pulse oxidation

The reduction degree of Co catalysts was measured by the pulse oxidation method. Typically, the calcined sample was placed in the same apparatus as used for the H_2-TPR experiments. After reduction with pure H_2 at 673 K for 6 h, the gas was switched into pure He and the sample was kept in He at 673 K for 1 h. Calibrated pulses of O_2-He (20 vol% O_2) were then added into the continuous He flow until no further consumption of O_2 was detected by the thermal conductivity detector located downstream of the reactor. The amount of O_2 consumed was calculated from the known pulse volume, temperature, pressure, and the number of pulses. The extent of reduction was calculated by assuming the stoichiometric reoxidation of Co^0 to Co_3O_4 [12].

2.4.8 Surface area and pore size distribution

The BET surface area and pore size distribution in mesoporous silicas were measured using N_2 adsorption-desorption at 77 K. Prior to the experiments, the samples were outgassed at 523 K for 3 h. The isotherms were measured using a Micrometrics ASAP 2010 system. The total pore volume (TPV) was calculated from the amount of vapor adsorbed at a relative pressure close to unity assuming that the pores are filled with the condensate in liquid state. The pore size distribution curves were calculated from the desorption branches of the isotherms using Barrett–Joyner–Halenda (BJH) formula [13].

2.4.9 In situ magnetic characterization

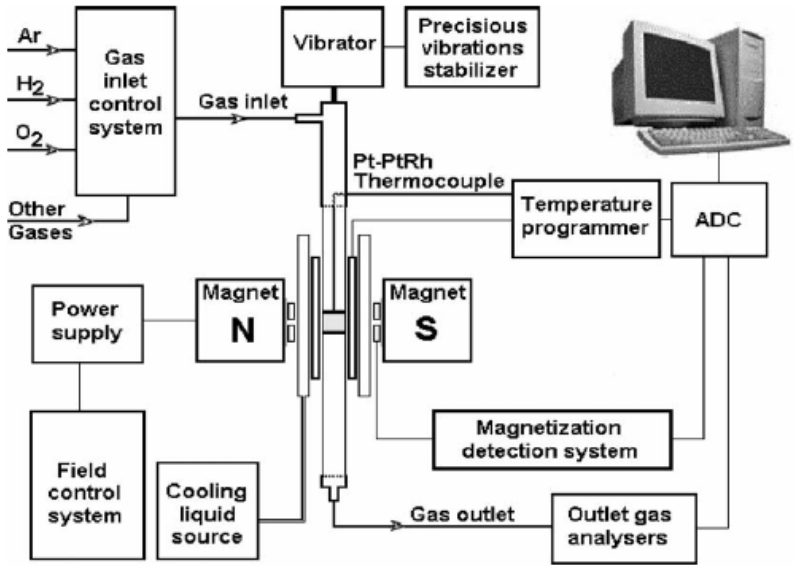

Figure 2-6. Experimental setup for in situ magnetization measurements.

The magnetic properties of catalysts were investigated in situ using a Foner vibrating-sample magnetometer [14, 15] with 20 mg catalyst loading (Figure 2-6). The magnetometer was calibrated by using 1 mg of pure metallic Fe before each experiment. First, under the 15 mL min^{-1} feed of pure CO, the sample was heated to 200 °C with a 6.6 °C min^{-1} ramping and kept for 10 min, then sequentially heated to 350 °C with a 4.7 °C min^{-1} ramping and kept for 120 min. After activation, the CO flow was switched to Ar to remove any CO that had adsorbed onto the catalysts and the sample was cooled to the room temperature. During the whole process of heat treatment, the curve of magnetization was recorded by the magnetometer in the magnetic field of 3 KOe. This magnetic field might be insufficient to reach saturation magnetization in particular for smaller superparamagnetic iron particles. Our estimation gives incertitude of 10 °C in the calculation of the Curie temperature if the saturation magnetization has not been completely achieved. In addition, the CO_2 signal was recorded by a selective IR detector or using a mass spectrometer.

The magnetic method is particularly suitable for investigation of the formation and evolution of different iron phases in the supported catalysts. Several iron phases have paramagnetic, ferromagnetic, antiferromagnetic or ferrimagnetic properties. The magnetic properties of iron compounds are briefly discussed below. Further information about magnetism and magnetic method is available from dedicated publications [14-21].

Ferromagnetism corresponds to parallel coupling of magnetic moments in the solids and results in a very high magnetic susceptibility. Antiferromagnetics are materials with antiparallel equal magnetic moments in different layers. As a result, the magnetic moments cancel and the antiferromagnetic sample does not have any significant magnetic susceptibility. Ferrimagnetics are solids with non-equal antiparallel magnetic moments. The magnetic moment in this case does not cancel and the solid has a magnetic moment corresponding to the direction of the most important magnetic moment in the layer. The magnetic phenomena are temperature dependent. Curie's temperature corresponds to the loss of ferromagnetism or ferrimagnetism; the resulting solid becomes paramagnetic at higher temperatures. The antiferromagnetics becomes paramagnetic at temperatures higher than the Neel temperature.

The magnetic properties, Curie and Neel temperatures of iron compounds are summarized in Table 2-1. Hematite (α-Fe_2O_3) is an antiferromagnetics below its Neel temperature (682 °C). It becomes paramagnetic at higher temperatures. The Morin transition of hematite (T= -13°C) corresponds to the reorganization of the magnetic structure, which may show very weak ferromagnetism above this temperature. Maghemite (γ-Fe_2O_3) and magnetite (Fe_3O_4) are ferrimagnetic. Maghemite is not stable at the reaction temperatures. In

the reducing atmosphere during heating, maghemite can readily convert to magnetite. Metallic iron and iron carbides are ferromagnetic.

Table 2-1. Magnetic properties of iron compounds.

Compound	Properties (room temperature)	Curie or Neel temperatures
α-Fe_2O_3 (hematite)	Antiferromagnetic with very week ferromagnetisms	682 °C
γ-Fe_2O_3 (maghemite)	Ferrimagnetic	470 to 695 °C (unstable from 250°C)
Fe_3O_4 (magnetite)	Ferrimagnetic	585 °C
FeO (wustite)	Paramagnetic (antiferromagnetic below Neel temperature)	-73 °C
Metallic Fe	Ferromagnetic	770 °C
χ-Fe_5C_2 (Hägg carbide)	Ferromagnetic	205-256 °C
Hexagonal ε-Fe_2C	Ferromagnetic	380 °C
Pseudo-hexagonal ε'-$Fe_{2.2}C$	Ferromagnetic	450 °C
Orthorhombic θ-Fe_3C (cementite)	Ferromagnetic	208 °C

2.4.10 Mössbauer spectrometry

Samples after reaction were characterized by transmission Mössbauer spectrometry (TMS). TMS allows identification and quantification of iron based phases. Mössbauer spectra were recorded at room temperature, in the ±12 mm s^{-1} range, using a 1GBq source of 57Co in rhodium matrix, Mössbauer MR360 constant acceleration driving unit and DFG1200 digital function generator, a NaI (Tl) scintillation detector, a 1024 multichannel analyser. The experimental Mössbauer spectra were analysed using a least square computer fit assuming Lorentzian peak shapes, α-Fe as reference. Hyperfine parameters such as hyperfine field (HF), isomer shift (IS) or quadrupole splitting (QS), which are the characteristics of each iron environment, were calculated with respect to α-Fe spectrum reference. These hyperfine parameters were compared to whose of Fe_3C [22, 23], χ-Fe_5C_2 [24, 25], ε-$Fe_{2.2}C$ [22, 23], Fe_xO_y [23], Fe_2O_3, Fe_3O_4 [22, 23].

2.4.11 H_2 chemisorption measurements

H_2 chemisorption measurements were carried out with a Micromeritics ASAP 2020 C instrument to calculate the Co dispersion *D* (%). Before each measurement, the sample was reduced for 6 h in flowing H_2 at 673 K at a heating rate of 5 K min^{-1}. After reduction, the samples were evacuated at that temperature for 30 min to desorb any H_2. Then, the temperature was cooled down to 423 K for 1 h. The H_2-adsorption isotherms and Co dispersion were measured at 423 K, using the classical method recommended by Reuel and Bartholomew [25, 26]. The H/Co ratios at zero pressure were found by extrapolating the linear part of the isotherm. Calculations were made using the total amount of

adsorbed hydrogen corrected with reduction degree measured by O_2 pulse oxidation and a stoichiometry of one hydrogen atom per cobalt surface atom. Thus, $D = 1.179X/Wf$, where X denotes total H_2 uptake in micromoles per gram of catalyst measured at 423 K, W denotes weight percentage of cobalt, and f denotes fraction of cobalt reduced to the metal determined from O_2 pulse oxidation. Average crystallite diameters (in nanometer) were calculated from D (%) assuming spherical metal crystallites of uniform diameter d with a site density of 14.6 atom nm^{-2} for supported cobalt crystallites and 11.2 atoms nm^{-2} for unsupported cobalt crystallites. Thus for supported cobalt catalysts, $d = 6.59\ s/D$ (%) = $96/D$ (%), where s denotes site density in atoms nm^{-2} and D (%) denotes percentage dispersion [25, 6].

2.4.12 Infrared spectroscopy analysis

Fourier transform infrared (FT-IR) studies of adsorbed pyridine were performed with a Nicolet 6700 instrument equipped with an MCT detector (Figure 2-7). The sample was pressed into a self-supported wafer and placed in an in-situ IR cell. After pretreatment under vacuum at 673 K for 30 min, the sample was cooled to 423 K, then, pyridine was adsorbed at 423 K on the sample for a sufficient time. FT-IR spectra were recorded after gaseous or weakly adsorbed pyridine molecules were removed by evacuation at 423 K.

Ex-situ IR spectra of silica and alumina supports were recorded with a Nicolet Protégé 460 FT-IR spectrometer at 4 cm^{-1} optical resolution. Prior to the measurements, the catalysts were pressed with KBr in the discs.

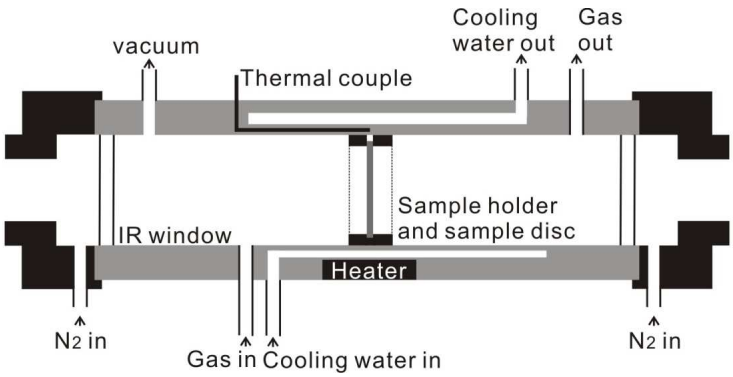

Figure 2-7. Schematic diagram of high temperature in situ IR cell.

2.4.13 Elemental analysis

Zeolitic samples were firstly digested with 1 mL of HF acid in a Teflon vessel. Then, the vessel was heated to 423 K to evaporate the silicon in the form of SiF_4. The residual solid was further dissolve with 1mL of concentrated HNO_3 solution, and diluted with 4 wt% HCl aqueous solution in the volumetric flask. ICP-OES analyses were performed on a Thermo

Electron IRIS Intrepid II XSP instrument to obtain the Al^{3+} content. Before making the solution, the zeolitic samples were calcined at 823 K for 6 h. The constitution of zeolite can be roughly considered as $xSiO_2 \cdot yAl_2O_3$, so based on Al content, Si content can be calculated metrically.

2.4.14 ^{27}Al MAS NMR

^{27}Al MAS NMR experiments were conducted on a Varian Infinity plus AS400 spectrometer (Varian Inc.) operated with frequency at 104.26 MHz, pulse width at 0.5 μs, radiofrequency field strength at 50 G, pulse delay at 0.5 s, spinning rate at 7 kHz, and with 85,000 scans. The samples used for ^{27}Al MAS NMR measurements did not undergo hydration preliminarily.

2.5 Reference

[1] M. Choi, H.S. Cho, R. Srivastava, C. Venkatesan, D.H. Choi, R. Ryoo, Nat Mater, 5 (2006) 718-723.

[2] A.Y. Khodakov, A. Griboval-Constant, R. Bechara, V.L. Zholobenko, J. Catal., 206 (2002) 230-241.

[3] D. Zhao, J. Feng, Qisheng Huo, Nicholas Melosh, Glenn H. Fredrickson, Bradley F. Chmelka, G.D. Stucky*, Science, 279 (1998) 548-552.

[4] A. Nossov, E. Haddad, F. Guenneau, A. Galarneau, F. Di Renzo, F. Fajula, A. Gédéon, J. Phys. Chem. B, 107 (2003) 12456-12460.

[5] S. Jun, S.H. Joo, R. Ryoo, M. Kruk, M. Jaroniec, Z. Liu, T. Ohsuna, O. Terasaki, J. Am. Chem. Soc., 122 (2000) 10712-10713.

[6] J.R. Sietsma, J.D. Meeldijk, J.P. den Breejen, M. Versluijs-Helder, A.J. van Dillen, P.E. de Jongh, K.P. de Jong, Angew. Chem. Int. Ed., 46 (2007) 4547-4549.

[7] M. Wolters, P. Munnik, J.H. Bitter, P.E. de Jongh, K.P. de Jong, J. Phys. Chem. C, 115 (2011) 3332-3339.

[8] http://www.avantium.com/flowrence/

[9] T. Holm, J. Chromatogr. A, 842 (1999) 221-227.

[10] P. Scherrer, Phys., 2 (1918) 98-100.

[11] M.A. Camblor, A. Corma, S. Valencia, Microporous Mesoporous Mater., 25 (1998) 59-74.

[12] S. Storsæter, B. Tøtdal, J.C. Walmsley, B.S. Tanem, A. Holmen, J. Catal., 236 (2005) 139-152.

[13] S. van Donk, A.H. Janssen, J.H. Bitter, K.P. de Jong, Catal. Rev., 45 (2003) 297-319.

[14] P.A. Chernavskii, A.Y. Khodakov, G.V. Pankina, J.S. Girardon, E. Quinet, Appl. Catal. A, 306 (2006) 108-119.

[15] P.A. Chernavskii, J.A. Dalmon, N.S. Perov, A.Y. Khodakov, Oil & Gas Science and Technology - Revue de l'IFP, 64 (2009) 25-48.

[16] P.A. Chernavskii, B.S. Lunin, R.A. Zakharyan, G.V. Pankina, N.S. Perov, Instrum. Exp. Tech., 57 (2014) 78-81.

[17] R.F. Butler, R.F. Butler, Paleomagnetism: magnetic domains to geologic terranes, Blackwell Scientific Publications Boston, 1992.

[18] P. Selwood, Chemisorption and magnetization, Elsevier, 2012.

[19] J.T. Richardson, J. Appl. Phys., 49 (1978) 1781-1786.

[20] B. Imelik, J.C. Védrine, Catalyst characterization: physical techniques for solid materials, Springer, 1994.

[21] P.A. Chernavskii, A.Y. Khodakov, G.V. Pankina, J.S. Girardon, E. Quinet, Appl. Catal. A, 306 (2006) 108-119.

[22] E. de Smit, B.M. Weckhuysen, Chem. Soc. Rev., 37 (2008) 2758-2781.

[23] B. David, O. Schneeweiss, M. Mashlan, E. Šantavá, I. Morjan, J. Magn. Magn. Mater., 316 (2007) 422-425.

[24] F.E. Huggins, S. Bali, G.P. Huffman, E.M. Eyring, Spectrochimca Acta A Mol. Biomol. Spectrosc., 76 (2010) 74-83.

[25] J.M. Zowtiak, C.H. Bartholomew, J. Catal., 83 (1983) 107-120.

[26] R.C. Reuel, C.H. Bartholomew, J. Catal., 85 (1984) 63-77.

Chapter 3. Mesoporous Beta Zeolite-Supported Ruthenium Nanoparticles for Selective Conversion of Synthesis Gas to C_5-C_{11} Isoparaffins

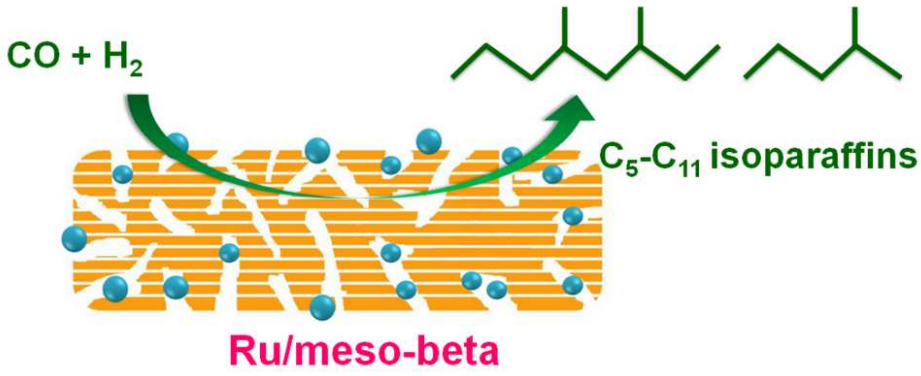

Abstract: Mesoporous beta (meso-beta) zeolites prepared by post-treatment of H-beta zeolite with NaOH aqueous solution were studied as supports of Ru catalysts for Fischer-Tropsch (FT) synthesis. The size and volume of the mesopores increased with the concentration of NaOH. A further ion-exchange of the meso-beta with $NH_4{\cdot}NO_3$ followed by calcination, forming H-meso-beta, could recover the Brønsted acidity. The use of H-meso-beta instead of H-beta as the support for FT synthesis decreased the selectivities to CH_4 and heavier hydrocarbons (C_{12}^+) and increased that to C_5-C_{11} hydrocarbons. The C_5-C_{11} selectivity depended on the concentration of NaOH used for meso-beta preparation. Under an optimum NaOH concentration, a C_5-C_{11} selectivity of 67%, significantly higher than the maximum expected from Anderson-Schulz-Flory distribution (~45%), was attained with a ratio of isoparaffins to *n*-paraffins being 3.9. The mesoporosity and unique acidity of the meso-beta probably contribute to the selective hydrocracking of the primary heavier hydrocarbons formed on Ru nanoparticles into gasoline-range liquid fuels.

This Chapter is based on the following publication:

Kang Cheng, Jincan Kang, Shuiwang Huang, Zhenya You, Qinghong Zhang,* Jiansheng Ding, Weiqi Hua, Yinchuan Lou, Weiping Deng, Ye Wang*, *ACS Catalysis* 2 (**2012**) 441-449.

3.1 Introduction

Hierarchical zeolites containing both micropores and mesopores (Figure 3-1) have attracted much attention as a new type of promising catalytic materials in recent years [1-10]. These materials combine the advantages of the conventional microporous zeolites, which possess acidic catalytic functions and shape-selective features and are stable at high temperatures because of the crystalline structures, and the mesoporous materials with efficient mass transport [11-13]. Mesoporous zeolites have demonstrated improved performances in several catalytic reactions, particularly the acid-catalyzed reactions. For examples, the activity and selectivity for the alkylation of benzene to ethylbenzene or cumene were increased by using mesoporous ZSM-5 or mesoporous mordenite instead of conventional H-ZSM-5 and mordenite [14-16]. Mesoporous Y or mesoporous ZSM-5 zeolites exhibited improved product distributions or enhanced activity and stability for the hydrocracking of heavy hydrocarbons [17-19]. Mesoporous beta zeolite-supported Pd showed higher catalytic performances in the deep hydrogenation of aromatics [20]. The presence of mesopores in ZSM-5 suppressed the catalyst deactivation in the conversion of methanol to hydrocarbons [21].

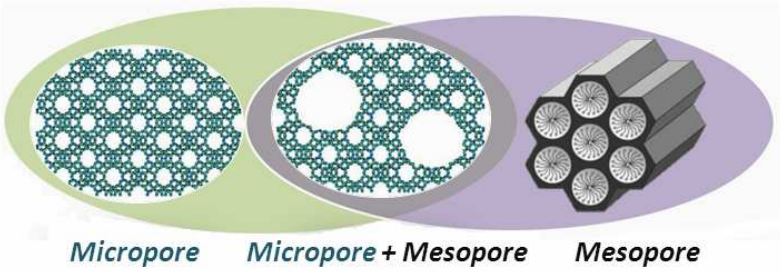

Figure 3-1. Schematic diagram of mesoporous zeolite (from left to right: microporous zeolite, mesoporous zeolite and ordered mesoporous material).

Fischer-Tropsch (FT) synthesis, i.e., the conversion of synthesis gas (syngas, $CO + H_2$) to hydrocarbons, is a crucial step in the indirect transformation of non-petroleum carbon resources such as natural gas, coal and biomass into fuels such as gasoline and diesel or chemicals such as lower olefins. Because of the global demand for a decreased dependence on petroleum, FT synthesis has received renewed interests in recent years [22-27].

One of biggest challenges in FT synthesis is the selectivity control. Over most conventional FT catalysts, the products follow the Anderson-Schulz-Flory (ASF) distribution, and such a distribution is unselective for middle-distillate products [27, 28]. For example, the maximum selectivities to C_5-C_{11} (gasoline-range) and C_{12}-C_{20} (diesel-range) hydrocarbons are

~45% and ~30%, respectively. The development of new type of catalysts with higher selectivity to middle-distillate products is a challenging research target [27, 29, 30]. It is known that the combination of an acid catalyst, typically a zeolite, with a conventional FT catalyst or an FT active metal into a bifunctional catalyst system may increase the selectivity to gasoline-range hydrocarbons [31-33]. Over such a bifunctional catalyst system, the primary linear hydrocarbons formed on the FT active metal may undergo several secondary reactions (e.g., isomerization of the linear hydrocarbons, hydrocracking of heavier hydrocarbons, and oligomerizations of light olefins) on the acid site. In the bifunctional catalyst system, the acidic zeolite can be packed in a separate reactor or a separate layer in the downstream of the FT catalyst [31, 32, 34], and can also be mixed with the conventional FT catalyst to form a hybrid catalyst [31, 32, 34-36]. To further improve the efficiency of the bifunctional hybrid catalyst, Tsubaki and co-workers [37-41] developed an intriguing core-shell structured catalyst system containing a conventional FT catalyst (e.g., Co/SiO_2 or Co/Al_2O_3) as the core and a zeolite membrane as the shell, completely suppressing the formation of C_{12}^+ hydrocarbons. However, the selectivity of CH_4 over these bifunctional catalyst systems is usually high, exceeding 13% in most cases. This is believed to arise from the slow transportation of the products inside the long micropores of zeolites, where the acid sites are located, and the strong acidity of the H-form zeolites. The high selectivities to CH_4 and light (C_2-C_4) alkanes resulting from the over-cracking are highly undesirable for FT synthesis.

It is expected that the use of mesoporous zeolite to replace the conventional microporous zeolite may avoid the over-cracking because of the improved mass transport, decreasing the selectivities to CH_4 and C_2-C_4 light alkanes. However, there has been no report on the utilization of mesoporous zeolites for FT synthesis before our work. In a recent communication [42], we have demonstrated for the first time that a mesoporous ZSM-5-supported Ru catalyst can catalyze the conversion of syngas to C_5-C_{11} hydrocarbons with a very high selectivity (~80%). H-beta is also efficient for the secondary reactions when it is combined with a conventional FT catalyst [39, 43]. The acid strength of H-beta is weaker than that of H-ZSM-5 [44], but H-beta zeolite is better for isomerization reaction [45, 46], which may further increase the selectivity of isoparaffins in FT reaction. The studies on the mesoporous beta zeolite are quite limited as compared to the mesoporous ZSM-5 zeolite [1-10, 20, 47]. Here, we report our detailed studies on the characterizations of the mesoporous beta (meso-beta) zeolite prepared by desilication of H-beta in alkaline medium and the utilization of the meso-beta as the support of Ru catalysts for FT synthesis. The effects of the mesoporosity and the acidity of the meso-beta on catalytic performances, particularly the

product selectivity, for FT synthesis will be discussed to gain insights into the key to the rational design of new FT catalysts with controlled product selectivities.

3.2 Result and Discussion

3.2.1 Structure of Mesoporous Beta Zeolites

Only a few papers have been devoted to studying the mesoporous beta zeolite prepared by alkaline-treatment method [47], although there exist many reports on the alkaline-treated hierarchical ZSM-5 [2, 3, 5, 6, 10]. The XRD patterns for our H-meso-beta samples prepared by desilication method with different concentrations of NaOH aqueous solutions at 343 K are shown in Figure 3-2. The comparison of the XRD patterns for series of samples confirmed that the crystalline structure of beta zeolite was sustained for these samples prepared with suitable concentrations of NaOH. When the concentration of NaOH exceeded 0.15 M, the intensities of the two diffraction peaks at 2θ□ of 7.7º and 22.4º, which are characteristic of the crystalline beta zeolite, decreased significantly, implying the partial collapse of the crystalline structure under the treatment with higher concentrations of NaOH. Groen et al. [47] found the damage in crystalline structure of beta zeolite at higher temperatures (≥ 338 K) at a fixed concentration of NaOH (0.2 M).

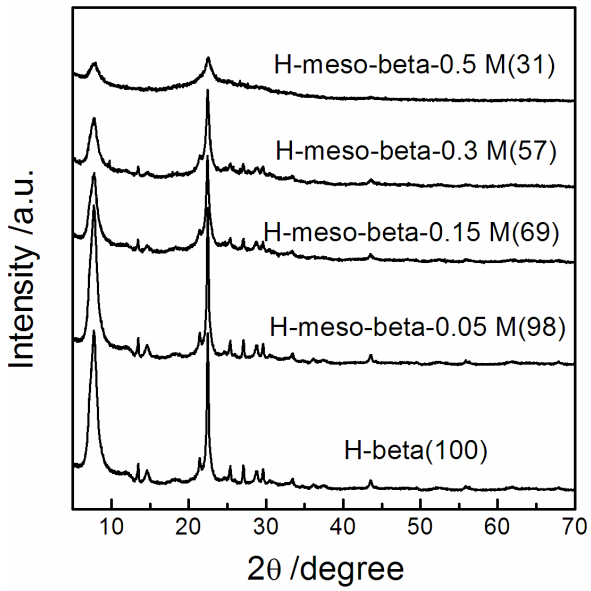

Figure 3-2. XRD patterns for series of H-meso-beta samples treated with different concentration of NaOH solution, the number in the parentheses after each sample denotes the relative crystallinity (%) compared with H-beta.

The porous properties of the samples were studied by Ar physisorption at 87 K. Figure 3-3 shows the adsorption-desorption isotherms of meso-beta samples together with H-beta zeolite. The H-beta exhibits the type-I isotherm, which is typical of microporous zeolites [9]. The pore size distribution for this sample in the microporous region evaluated by the HK method showed a maximum at 0.67 nm (Figure 3-4a), which is typical for the beta zeolite. The treatment of H-beta with NaOH aqueous solutions caused the appearance of hysteresis loop (Figure 3-3), indicating the generation of mesopores.

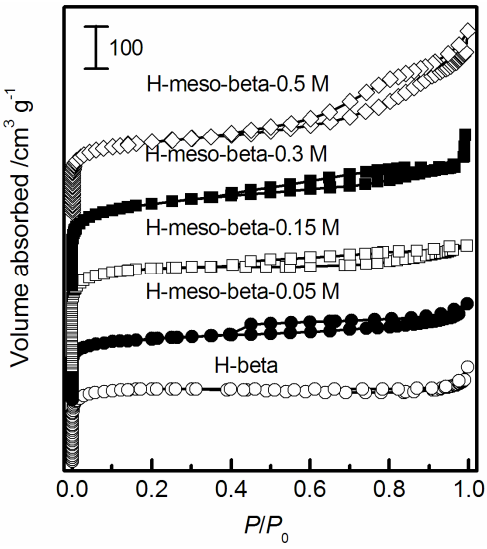

Figure 3-3. Ar adsorption-desorption isotherms for the H-meso-beta samples as well as H-beta.

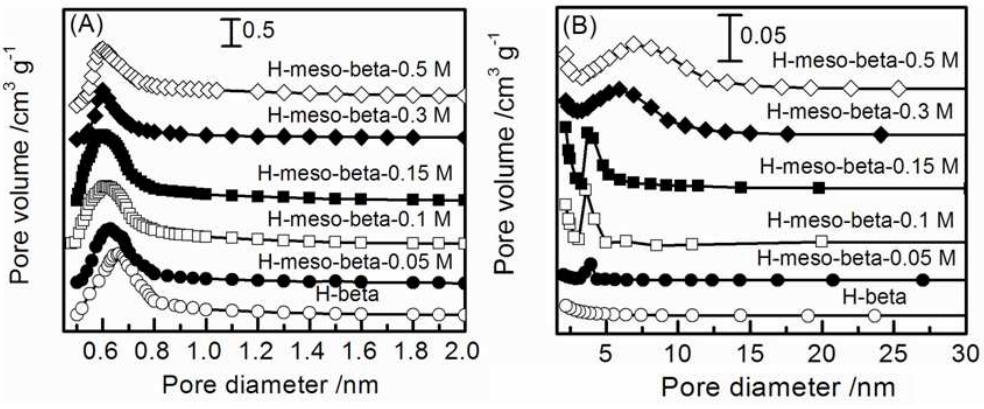

Figure 3-4. Pore size distribution for H-meso-beta samples as well as H-beta: (a) microporous region by HK method and (b) mesoporous region by BJH method.

According to the analysis by the BJH method, the pore diameter in the mesoporous region for the meso-beta sample had a narrow distribution when the concentration of NaOH did not exceed 0.15 M (Figure 3-4b). For the H-meso-beta-0.30 M and the H-meso-beta-0.50

M samples, the pore diameter distribution became relatively broader. The mean diameter of mesopores depended on the concentration of NaOH used for H-meso-beta preparation; the higher concentration of NaOH resulted in the larger size of mesopores. The pore diameters and the pore volumes in the microporous and mesoporous regions for meso-beta samples are summarized in Table 3-1. With increasing the concentration of NaOH used for the preparation of meso-beta samples, the pore volume in the microporous region (V_{micro}) decreased and that in the mesoporous region (V_{meso}) increased significantly. These results suggest that the alkaline treatment is effective for generating the mesoporosity in the beta zeolite, forming hierarchical mesoporous beta zeolites.

Table 3-1. Textural properties of H-meso-beta samples prepared by desilication.

Samples	Si/Al ratio[a]	S_{BET}[b] ($m^2\ g^{-1}$)	S_{meso}[c] ($m^2\ g^{-1}$)	V_{micro}[d] ($cm^3 g^{-1}$)	V_{meso}[e] ($cm^3\ g^{-1}$)	D_{micro}[f] (nm)	D_{meso}[g] (nm)
H-beta	27	626	20	0.21	0.005	0.64	-
H-meso-beta-0.05 M	24	599	53	0.20	0.033	0.60	3.4
H-meso-beta-0.1 M	22	683	121	0.17	0.10	0.62	4.1
H-meso-beta-0.15 M	21	671	170	0.15	0.12	0.61	4.4
H-meso-beta-0.3 M	20	642	302	0.13	0.32	0.60	5.2
H-meso-beta-0.5 M	19	575	213	0.12	0.41	0.60	7.4

[a] Si/Al molar ratio measured by ICP-OES. [b] BET surface area. [c] Mesoporous surface area evaluated by the t-plot method. [d] Pore volume for micropores evaluated by the *t*-plot method. [e] Pore volume for mesopores evaluated by the BJH method. [f] Mean pore diameter for micropores estimated by the HK method. [g] Mean pore diameter for mesopores evaluated by the BJH method.

TEM was further used to investigate the mesoporosity of our H-meso-beta samples. Figure 3-5 presents TEM images of the meso-beta zeolites prepared using different concentrations of NaOH. These TEM images further evidenced the generation of mesopores in the crystalline beta zeolite for the meso-beta samples. The collapse of the zeolite crystal under a higher concentration of NaOH solution (particularly 0.7 M) could also be observed from the TEM images.

It is accepted that the alkaline treatment resulted in the desilication rather dealumination from the framework of zeolites [2, 5, 6, 10, 47]. Our ICP-MS measurements reveal that the

Si/Al ratio in the meso-beta sample is lower than that in the parent beta zeolite (Table 3-1), confirming that silicon atoms have mainly been removed from the framework of beta zeolite during the treatment by NaOH aqueous solutions.

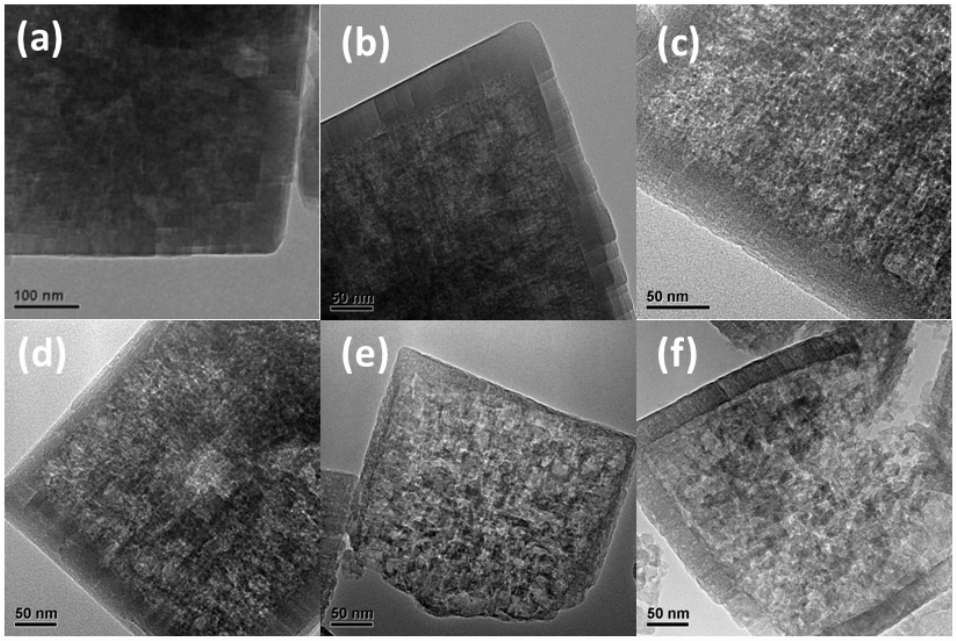

Figure 3-5. TEM images for H-meso-beta-*x*M samples: (a) none, (b) 0.05M, (c) 0.1M, (d) 0.15M, (e) 0.3M, (f) 0.5M.

3.2.2 Acidity of Mesoporous Beta Zeolites

In aluminosilicate-type zeolites, silicon atom is at the 4+ oxidation state at tetrahedral positions on the framework while the coordinating oxygen atoms are in the oxidation state -2. Globally this leads to neutral $SiO_{4/2}$ tetrahedra. Upon substitution of silicon atoms by aluminum atoms with a 3^+ charge in the framework, the formal charge on the corresponding tetrahedra changes from neutral to 1^-. These negative framework charges are balanced by extra-framework metal cations or hydroxyl protons forming weak Lewis acids site or strong Brønsted acid sites, respectively [46, 48]. These hydroxyl groups are commonly donated structural or bridging OH groups, where the Brønsted acid sites comes from. The Brønsted acid sites can transform into Lewis acid sites by dehydration reaction (Figure 3-6).

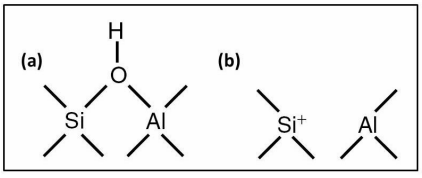

Figure 3-6. Schematic representation of different types of acid sites in zeolite.

The acidities of both the meso-beta and the H-meso-beta series of samples were investigated by NH_3-TPD. Figure 3-7 shows that the parent H-beta exhibits two NH_3 desorption peaks at ~463 and ~630 K. The H-type zeolite usually exhibits two NH_3 desorption peaks; the lower-temperature peak at <500 K may arise from the weakly held (probably hydrogen-bonded) NH_3 molecules, while the higher-temperature peak can be assigned to the desorption of NH_3 molecules chemisorbed on the Brønsted acid sites [49, 50]. As shown in Figure 3-7, when NaOH concentration is not more than 0.15 M, the NH_3-TPD peaks of H-meso-beta is similar with the H-beta, suggesting that the type and amount of acid sites is similar. Further increasing the NaOH concentration causes a larger low-temperature peak and a smaller high temperature peak. The reason is that high concentrated NaOH solution makes zeolite structure collapse [51]. So the NH_3 desorption peak at low temperature increased. The collapse of framework also reduces the number of the framework aluminum in beta zeolite (decreasing Brønsted acid sites), so that the NH_3 desorption peak at high temperature decreases.

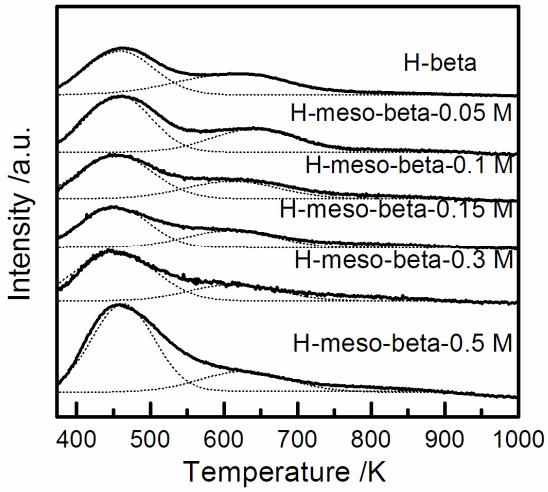

Figure 3-7. NH_3-TPD profiles for H-meso-beta-*x*M samples prepared by desilication.

For the H-meso-beta series of samples, our ICP-MS analysis uncovered that the Na/Al ratio was about 0.1, indicating that ~90% of Na^+ residual cations were exchanged into protons. In general, Figure 3-7 shows that the H-meso-beta series of samples display a NH_3 desorption peak at >615 K, which is close to that observed for the H-beta and can be ascribed to the Brønsted acid sites. This observation indicates that the H-meso-beta series of samples possess strong Brønsted acidity.

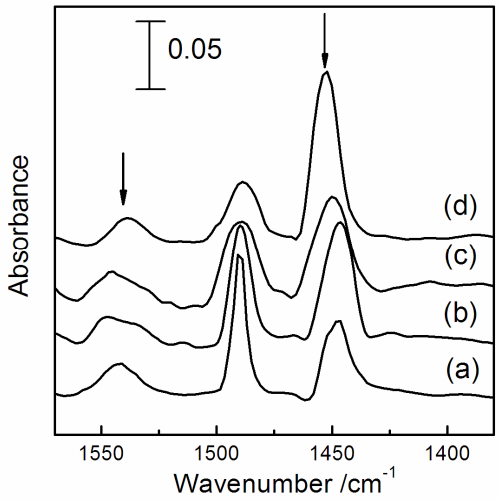

Figure 3-8. Pyridine-adsorbed FT-IR spectra:(a) H-beta, (b) H-meso-beta-0.05 M, (c) H-meso-beta-0.15 M, and (d) H-meso-beta-0.3 M.

To gain further information about the nature of the acidity in these samples, we have performed FT-IR studies of adsorbed pyridine for both H-meso-beta series of samples. Figure 3-8 shows that there are three distinct preaks in the selected range. The band at 1455 cm^{-1} could be attributed to the Lewis acidity, and the band at 1543^{-1} is attributable to the Brønsted acid sites [50]. The IR band at 1490 cm^{-1} could stem from both Brønsted acid and Lewis acid sites [50]. Brønsted acid sites are supposed to be active sites for isomerization and cracking [48, 52].

3.2.3 Characterizations of Mesoporous Beta Zeolite-Supported Ru Catalysts

Ru is in its oxidic state after calcination in air [53]. Figure 3-9 shows the H_2-TPR profiles for the calcined Ru catalysts loaded on typical H-meso-beta samples before H_2 reduction. All these supported Ru samples displayed a single reduction peak at 455-464 K. The effect of the mesoporosity of the support on the reduction behavior was insignificant. We have calculated the degree of reduction of Ru species for each catalyst by quantifying the H_2-TPR result. The degrees of reduction of RuO_2 to metallic Ru evaluated from H_2-TPR for the Ru/H-meso-beta samples are summarized in Table 3-2. In most cases, the degree of reduction exceeded 85% at 573 K, which has been employed for the reduction of catalyst during the catalyst preparation. Thus, metallic Ru particles are the predominant Ru species over all our catalysts after H_2 reduction. There is no H_2 consumption peak at high temperature, which indicates the easier reductive behavior of Ru catalysts compared with Co or Fe catalysts supported on alumina or silicas.

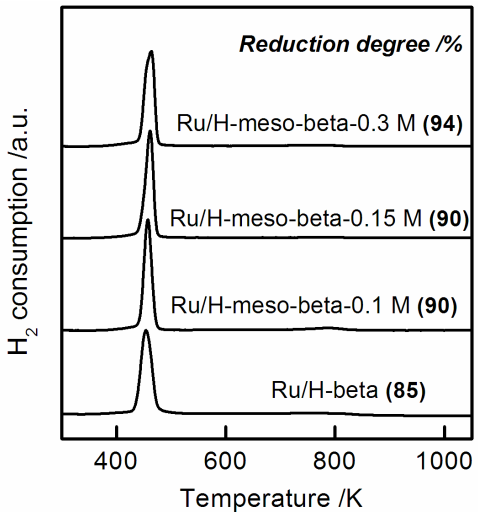

Figure 3-9. H_2-TPR profiles for the Ru/H-meso-beta-*x*M samples after calcination, the number in the parentheses after each sample denotes the reduction degree (%).

The mean size of Ru particles over each sample was measured by TEM. Figures 3-10 shows the typical TEM images for Ru catalysts loaded on typical H-meso-beta samples. The Ru particle size distributions derived by counting ~200 Ru nanoparticles in these samples are also displayed in Figures 3-10 and table 3-2. Over most catalysts, the Ru particles were distributed in the range of 4-12 nm, and the maxima are located in 6-8 nm. The mean sizes of Ru nanoparticles over these catalysts were similar at 5.5-7.3 nm (Table 3-2).

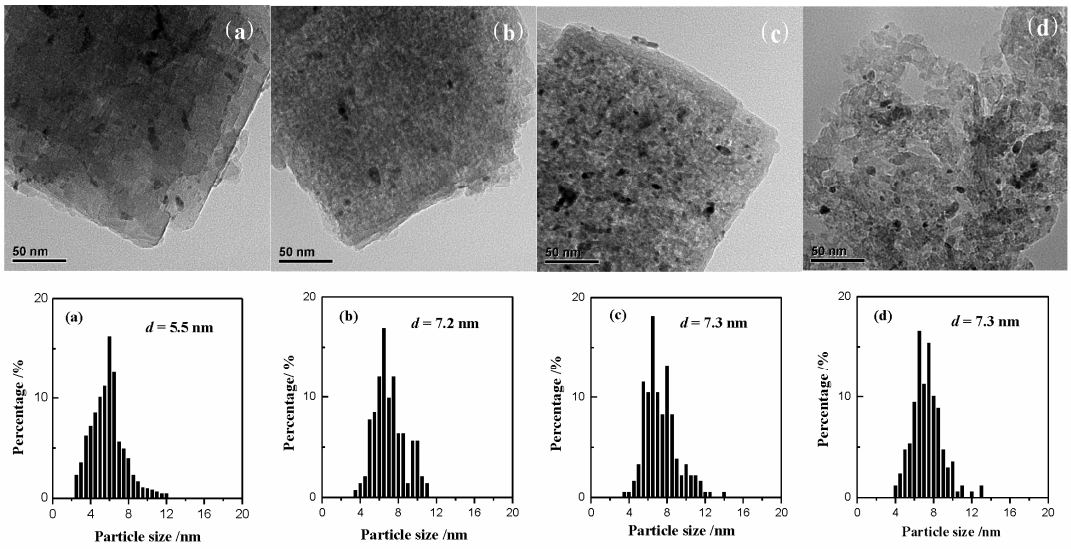

Figure 3-10. TEM micrographs: (a) Ru/H-beta, (b) Ru/H-meso-beta-0.15 M, (c) Ru/H-meso-beta-0.3 M, and (d) Ru/H-meso-beta-0.5 M.

We have also measured the dispersion of Ru nanoparticles over the H-meso-beta series

of samples as well as H-beta by the H_2-O_2 titration method [54], and the results are summarized in Table 3-2. The values of Ru dispersions over these catalysts were also quite similar (0.19-0.26). From the values of Ru dispersion, the mean size (d) of Ru particles can be roughly estimated by using the following relationship: d (nm) = 1.32/D, where D is the dispersion of Ru particles [55]. The mean sizes of Ru nanoparticles estimated from the values of Ru dispersions for these catalysts are also listed in table 3-2. The mean sizes of Ru obtained from Ru dispersion and those from TEM are consistent with each other.

Table 3-2. Properties of Ru/meso-beta and Ru/H-meso-beta Catalysts

Catalyst	reduction degree at 573 K[a] (%)	mean Ru size[b] (nm)	Ru dispersion[c]	mean Ru size[d] (nm)
Ru/H-beta	83	5.5	0.26	5.1
Ru/H-meso-beta-0.05 M	96	n.d.	0.25	5.3
Ru/H-meso-beta-0.1 M	90	6.9	0.23	5.7
Ru/H-meso-beta-0.15 M	90	7.2	0.22	6.0
Ru/H-meso-beta-0.3 M	94	7.3	0.19	6.9
Ru/H-meso-beta-0.5 M	86	7.2	0.22	6.0

[a] Calculated from H2-TPR. [b] Evaluated from TEM images. [c] Measured from H2-O2 titration. [d] Calculated from the following relationship: particle size (nm) = 1.32/dispersion.[55]

3.2.4 Catalytic Behaviors of H-meso-beta Supported Ru Catalysts for FT Synthesis

In the present work, we have selected Ru as the active metal for FT synthesis. In spite of the higher price of Ru as compared to Co and Fe, Ru-based catalysts are suitable for fundamental research to obtain clear-cut information about the effect of the support because Ru precursors can be easily reduced to Ru^0 and the size of Ru^0 particles can be easily controlled over different supports.

Before discussing the catalytic behaviors of H-meso-beta-supported Ru catalysts, we have compared the performances of Ru nanoparticles loaded on several types of microporous zeolites as well as on conventional metal oxide supports. As shown in Table 3-3, the distribution of products was rather broad, and considerable amounts of heavier ($C_{\geqslant 12}$) hydrocarbons were produced over metal oxide-supported Ru catalysts. The employment of a H-form zeolite as the support decreased the selectivity to $C_{\geqslant 12}$ and increased that to C_5-C_{11} hydrocarbons, the gasoline-range liquid fuels. The ratio of isoparaffins to *n*-paraffins in the

range of C_5-C_{11} (denoted as C_{iso}/C_n), an indicator of the quality of gasoline, also increased over the zeolite-supported Ru catalysts. This can be attributed to the secondary reactions, including hydrocracking and isomerization of the primary hydrocarbons, over the acid sites in the H-form zeolites [31, 32]. However, the selectivity to CH_4 or C_2-C_4 (mainly alkanes) also became significantly higher over these zeolite-supported catalysts as compared to those over the Ru/SiO_2 and Ru/Al_2O_3 catalysts. Among these catalysts, the Ru/H-beta exhibited the highest selectivity to C_5-C_{11} and a relative higher C_{iso}/C_n value.

Table 3-3. Catalytic Performances of Ru Loaded on Several Microporous Zeolites as Well as Metal Oxides for FT Synthesis[a]

catalyst[b]	CO conv. (%)	hydrocarbon selectivity (%)				C_{iso}/C_n[c]
		CH_4	C_{2-4}	C_{5-11}	$C_{\geq 12}$	
Ru/SiO_2	32	6.8	10	25	57	0.42
Ru/Al_2O_3	40	3.1	6.8	22	68	0.53
Ru/TiO_2	20	14	36	26	25	1.1
Ru/H-mordenite (12)	31	11	18	52	19	1.8
Ru/H-beta (27)	24	14	21	58	6.9	3.3
Ru/H-MCM-22 (30)	22	10	35	54	0	4.1
Ru/H-ZSM-5 (26)	25	15	37	47	0.7	2.7

[a] Reaction conditions: W = 0.5 g, H_2/CO = 1/1, P = 2 MPa, F = 20 cm^3/min, T = 533 K, time on stream = 12 h. [b] Ru loading is 3.0 wt% in each catalyst; the number in the parenthesis denotes the Si/Al ratio. [c] The molar ratio of isoparaffins to *n*-paraffins in the range of C_5-C_{11}.

Although it is still difficult to rationalize the differences in catalytic behaviors among Ru catalysts loaded on different zeolites with different porous structures, it seems that the acidity is a key factor in determining the product distribution. The NH_3-TPD profiles for the microporous zeolites listed in Table 3-3 are shown in Figure 3-11. All these zeolites exhibited two NH_3 desorption peaks except for H-mordenite, which displayed a broad peak. As described previously, the higher-temperature peak is attributable to the Brønsted acidity in the H-form zeolite. Thus, the strength of the acidity of these zeolites increases in the following sequence: H-mordenite < H-beta ≈ H-MCM-22 < H-ZSM-5. With increasing the strength of

the acidity, the selectivity to C_{12}^+ decreases, but the selectivity to C_5-C_{11} arrives at a maximum over the Ru catalyst loaded on H-beta with a medium strength of acidity. The tendency in Table 3-3 indicates that the stronger acidity of zeolite may cause over-cracking, leading to higher selectivity to lighter (i.e., C_1-C_4) hydrocarbons.

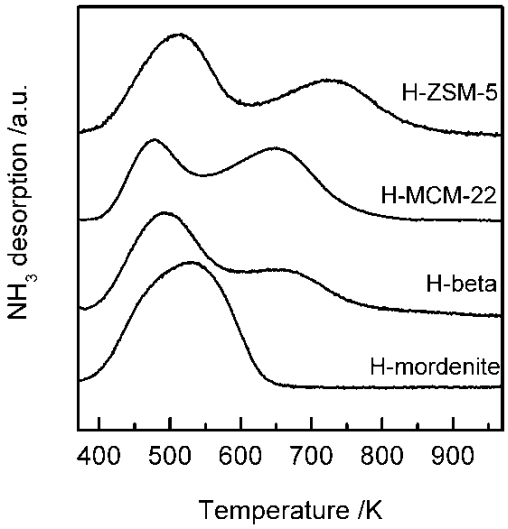

Figure 3-11. NH3-TPD profiles for several zeolites.

Figure 3-12 shows the catalytic performances of Ru catalysts loaded on H-meso-beta samples prepared by treating H-beta with different concentrations of NaOH, followed by NH_4^+ exchanging and calcination. The use of H-meso-beta instead of H-beta (NaOH concentration = 0 M in Figure 11) as the support of Ru decreased the selectivity of CH_4. For examples, the selectivity of CH_4 decreased from 14% over the Ru/H-beta to 11% and 7.9% over the Ru/H-meso-beta-0.1 M and the Ru/H-meso-beta-0.15 M catalysts, respectively. The selectivity to C_{12}^+ also declined when the H-meso-beta-0.1 M and the H-meso-beta-0.15 M were used. A further increase in the concentration of NaOH to 0.3 M increased the selectivity to C_{12}^+ again. Thus, the highest selectivity to C_5-C_{11} hydrocarbons for this series of catalysts was attained over the Ru/H-meso-beta-0.15 M catalyst (67%). CO conversion increased gradually with increasing the concentration of NaOH used for H-meso-beta preparation (Figure 3-12b). The C_{iso}/C_n ratio for Ru/H-meso-beta-0.15 catalyst could reach as high as 3.9, which is significantly higher than other reports [39, 40, 56]. Our characterizations have clarified that the reduction degree of Ru species and the mean sizes of Ru particle are similar over these catalysts (Table 3-2). Moreover, the acidities of the H-meso-beta series of samples were also similar and were comparable to the H-beta (Figures 3-7 and 3-8). Thus, these results

allow us to consider that the differences in catalytic behaviors among the catalysts in Figure 3-12 mainly result from the difference in the mesoporosity of the support. We propose that the mesoporosity in the H-meso-beta can enhance the mass transport, contributing to the higher CO conversion and the lower CH_4 selectivity. The presence of mesoporosity can also enhance the accessibility of primary products, i.e., the linear hydrocarbons, formed on Ru nanoparticles to the acid sites. This resulted in the decrease in the selectivity of C_{12}^+ by using H-meso-beta-0.1 M and H-meso-beta-0.15 M to replace H-beta (Figure 3-12a).

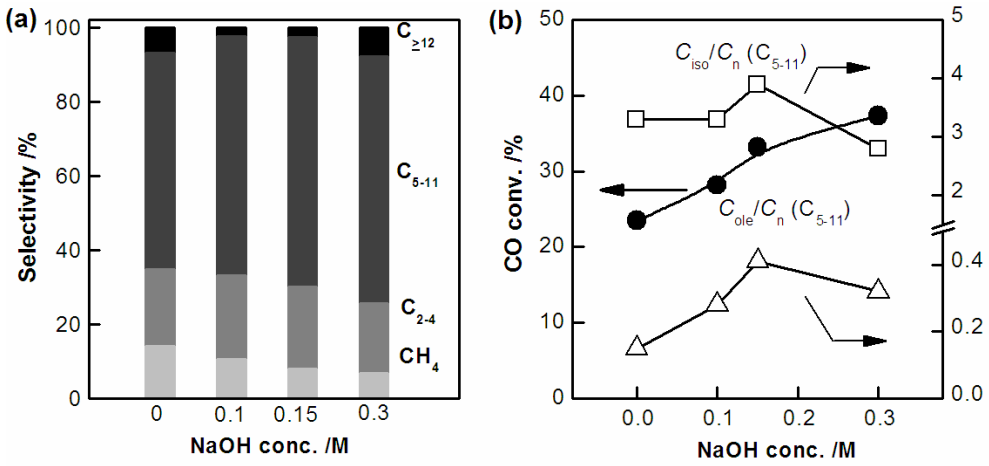

Figure 3-12 Catalytic performances of the Ru/H-meso-beta-xM catalysts: (a) product selectivity; (b) CO conversion, C_{iso}/C_n, and C_{ole}/C_n in C_{5-11}. Reaction conditions: W = 0.5 g, H_2/CO = 1/1, P = 2 MPa, F =20 cm3/min, T = 533 K, time on stream =12 h.

3.2.5 Performance of *n*-hexadecane hydrocarcking over Ru/H-meso-beta catalysts

In order to verify whether the Ru/H-meso-beta-*x*M catalysts can crack $C_{\geqslant 12}$ products, we performed *n*-hexadecane hydrocracking. Although it is already reported that the molecular sieve can promoted secondary cracking reaction to increase the gasoline fraction in FT product, there is no direct experimental proof to confirm this hypothesis. In this section, hydrocracking of *n*-hexadecane was conducted over Ru/H-meso-beta-*x*M bifunctional catalyst, with the same temperature and pressure used for FT reaction. As shown in Table 3-4, under the selected reaction conditions, *n*-hexadecane was almost completely cracked over Ru/H-meso-beta-*x*M catalyst. C_2-C_4 and C_5-C_{11} hydrocarbons are the main cracking product. The C_2-C_4 selectivity over Ru/H-beta catalyst is slightly higher, which may be caused by successive cracking of long-chain hydrocarbons [57]. Ru/H-meso-beta-0.15M catalyst possesses the highest C_5-C_{11} selectivity, which is consistent with its FT performance. There are almost no C_{12}-C_{15} hydrocarbons in the cracking products over these three catalysts, and

C_5-C_{11} hydrocarbons consist of mainly isoparaffins. We note that the hydrocracking reaction did not produce CH_4, which is consistent with carbocation mechanism catalyzed by Brønsted acid sites [58]. Ru/H-beta (no mesopores) catalyst shows higher CH_4 selectivity in FT reaction. Low methane selectivity was observed on the same catalyst in n-hexadecane hydrocracking. Vervloet et al. [59, 60] reported the diffusion rate of H_2 and CO in the microporous zeolite pore. Hydrogen diffuses faster than CO, then, the localized high concentration of H_2 would promote the direct hydrogenation of CH_x into CH_4. Apparently this does not occur during n-hexadecane hydrocracking.

Table 3-4. Catalytic behaviors of Ru/H-meso-beta-*x*M catalysts with different porous structures for hydrocracking of *n*-hexadecane.[a]

Catalyst	*n*-$C_{16}H_{34}$ conv. / %	Hydrocarbon selectivity / (mol%)				C_{iso}/C_n in C_{5-11}
		CH_4	C_{2-4}	C_{5-11}	C_{12-15}	
Ru/H-beta	97.8	0.5	31.1	65.9	2.5	3.6
Ru/H-meso-beta-0.15M	100	0.6	30.3	69.1	0	3.8
Ru/H-meso-beta-0.3M	95.7	0.9	28.2	65.9	5.0	3.2

[a] Reaction conditions: catalyst 0.5 g, feed of *n*-hexadecane 0.045 ml/min^{-1}, flow rate of H_2 30mL min^{-1}, P = 2 Mpa, T = 533 K, time on stream 12 h.

3.3 Conclusion

Two series of mesoporous beta zeolites were successfully prepared by a simple alkaline post-treatment method. The size and volume of mesopores depended on the concentration of NaOH used for post-treatment. The higher concentration of NaOH led to the generation of mesopores with larger sizes and volumes, but the crystalline structure of beta zeolite underwent partial collapse under treatment in NaOH aqueous solutions with higher concentrations. The H-meso-beta series of samples after ion-exchange with NH_4^+ followed by calcination displayed Brønsted acidity similar to that of H-beta. Ru/H-beta showed relatively higher selectivity to C_5-C_{11} hydrocarbons as compared to Ru/H-mordenite, Ru/H-MCM-22, and Ru/H-ZSM-5 possibly because of the medium-strength Brønsted acidity of H-beta zeolite. The use of H-meso-beta prepared using a proper concentration of NaOH ($\leqslant$0.15 M) instead of H-beta as the support of Ru decreased the selectivities to both CH_4 and heavier hydrocarbons (C_{12}^+) and increased that to C_5-C_{11} hydrocarbons. CO conversion was also

increased, and the ratio of isoparaffins to *n*-paraffins kept at > 3. A 67% selectivity to C_5-C_{11} hydrocarbons with a ratio of isoparaffins to *n*-paraffins being 3.9 could be attained over the Ru/H-meso-beta-0.15 M catalyst. The mesoporosity and the unique acidity of the H-meso-beta sample are proposed to contribute to the selective hydrocracking of heavier hydrocarbons to C_5-C_{11} hydrocarbons.

3.4 Reference

[1] M. Hartmann, Angew. Chem. Int. Ed., 43 (2004) 5880-5882.

[2] J. Perez-Ramirez, C.H. Christensen, K. Egeblad, C.H. Christensen, J.C. Groen, Chem. Soc. Rev., 37 (2008) 2530-2542.

[3] W. Schmidt, ChemCatChem, 1 (2009) 53-67.

[4] X. Meng, F. Nawaz, F.-S. Xiao, Nano Today, 4 (2009) 292-301.

[5] R. Chal, C. Gérardin, M. Bulut, S. van Donk, ChemCatChem, 3 (2011) 67-81.

[6] D. Verboekend, J. Perez-Ramirez, Catal. Sci. Technol., 1 (2011) 879-890.

[7] H. Chen, J. Wydra, X. Zhang, P.S. Lee, Z. Wang, W. Fan, M. Tsapatsis, J. Am. Chem. Soc., 133 (2011) 12390-12393.

[8] K. Zhu, J. Sun, J. Liu, L. Wang, H. Wan, J. Hu, Y. Wang, C.H.F. Peden, Z. Nie, ACS catal., 1 (2011) 682-690.

[9] S. van Donk, A.H. Janssen, J.H. Bitter, K.P. de Jong, Catal. Rev., 45 (2003) 297-319.

[10] J.C. Groen, J.A. Moulijn, J. Pérez-Ramírez, J. Mater. Chem., 16 (2006) 2121.

[11] D. Verboekend, J. Pérez-Ramírez, ChemSusChem, 7 (2014) 653-764.

[12] P.A. Jacobs, M. Dusselier, B.F. Sels, Angew. Chem. Int. Ed., 53 (2014) 8621-8626.

[13] K. Li, J. Valla, J. Garcia-Martinez, ChemCatChem, 6 (2013) 46-66.

[14] C.H. Christensen, K. Johannsen, I. Schmidt, C.H. Christensen, J. Am. Chem. Soc., 125 (2003) 13370-13371.

[15] J.C. Groen, T. Sano, J.A. Moulijn, J. Pérez-Ramírez, J. Catal., 251 (2007) 21-27.

[16] A.N.C. van Laak, S.L. Sagala, J. Zečević, H. Friedrich, P.E. de Jongh, K.P. de Jong, J. Catal., 276 (2010) 170-180.

[17] K.P. DeJong, J. Zečević, H. Friedrich, P.E. de Jongh, M. Bulut, S. van Donk, R. Kenmogne, A. Finiels, V. Hulea, F. Fajula, Angew. Chem. Int. Ed., 49 (2010) 10074-10078.

[18] Z. Qin, B. Shen, X. Gao, F. Lin, B. Wang, C. Xu, J. Catal., 278 (2011) 266-275.

[19] J. Zhou, Z. Hua, Z. Liu, W. Wu, Y. Zhu, J. Shi, ACS catal., 1 (2011) 287-291.

[20] T. Tang, C. Yin, L. Wang, Y. Ji, F.-S. Xiao, J. Catal., 249 (2007) 111-115.

[21] J. Kim, M. Choi, R. Ryoo, J. Catal., 269 (2010) 219-228.

[22] A.Y. Khodakov, W. Chu, P. Fongarland, Chem. Rev., 107 (2007) 1692-1744.

[23] B.H. Davis, Ind. Eng. Chem. Res., 46 (2007) 8938-8945.

[24] X. Hao, G. Dong, Y. Yang, Y. Xu, Y. Li, Chem. Eng. Technol., 30 (2007) 1157-1165.

[25] E. van Steen, M. Claeys, Chem. Eng. Technol., 31 (2008) 655-666.

[26] E. de Smit, B.M. Weckhuysen, Chem. Soc. Rev., 37 (2008) 2758-2781.

[27] Q. Zhang, J. Kang, Y. Wang, ChemCatChem, 2 (2010) 1030-1058.

[28] R. Luque, A.R. de la Osa, J.M. Campelo, A.A. Romero, J.L. Valverde, P. Sanchez, Energy Environ. Sci., 5 (2012) 5186-5202.

[29] J. Kang, S. Zhang, Q. Zhang, Y. Wang, Angew. Chem. Int. Ed., 48 (2009) 2565-2568.

[30] G. Yu, B. Sun, Y. Pei, S. Xie, S. Yan, M. Qiao, K. Fan, X. Zhang, B. Zong, J. Am. Chem. Soc., 132 (2009) 935-937.

[31] A. Martínez, G. Prieto, Top. Catal., 52 (2009) 75-90.

[32] B. Sun, M. Qiao, K. Fan, J. Ulrich, F.F. Tao, ChemCatChem, 3 (2011) 542-550.

[33] A. Shamsi, V.U.S. Rao, R.J. Gormley, R.T. Obermyer, R.R. Schehl, J.M. Stencel, Ind. Eng. Chem. Prod. Res. Dev., 23 (1984) 513-519.

[34] N. Tsubaki, Y. Yoneyama, K. Michiki, K. Fujimoto, Catal. Commum., 4 (2003) 108-111.

[35] A. Martinez, J. Rollan, M. Arribas, H. Cerqueira, A. Costa, E. Saguiar, J. Catal., 249 (2007) 162-173.

[36] T.-S. Zhao, J. Chang, Y. Yoneyama, N. Tsubaki, Ind. Eng. Chem. Res., 44 (2005) 769-775.

[37] J. He, Y. Yoneyama, B. Xu, N. Nishiyama, N. Tsubaki, Langmuir, 21 (2005) 1699-1702.

[38] J. He, Z. Liu, Y. Yoneyama, N. Nishiyama, N. Tsubaki, Chem. Eur. J., 12 (2006) 8296-8304.

[39] J. Bao, J. He, Y. Zhang, Y. Yoneyama, N. Tsubaki, Angew. Chem. Int. Ed., 47 (2008) 353-356.

[40] X. Li, J. He, M. Meng, Y. Yoneyama, N. Tsubaki, J. Catal., 265 (2009) 26-34.

[41] G.H. Yang, C. Xing, W. Hirohama, Y.Z. Jin, C.Y. Zeng, Y. Suehiro, T.J. Wang, Y. Yoneyama, N. Tsubaki, Catal. Today, 215 (2013) 29-35.

[42] J.C. Kang, K. Cheng, L. Zhang, Q.H. Zhang, J.S. Ding, W.Q. Hua, Y.C. Lou, Q.G. Zhai, Y. Wang, Angew. Chem. Int. Ed., 50 (2011) 5200-5203.

[43] X.G. Li, J.J. He, M. Meng, Y. Yoneyama, N. Tsubaki, J. Catal., 265 (2009) 26-34.

[44] A. Auroux, Top. Catal., 19 (2002) 205-213.

[45] A. Corma, V. Gonzàlez-Alfaro, A.V. Orchillès, Appl. Catal. A, 129 (1995) 203-215.

[46] J. Cejka, A. Corma, S. Zones, Zeolites and catalysis: synthesis, reactions and applications, John Wiley & Sons, 2010.

[47] J.C. Groen, S. Abelló, L.A. Villaescusa, J. Pérez-Ramírez, Microporous Mesoporous Mater., 114 (2008) 93-102.

[48] A. Corma, Chem. Rev., 95 (1995) 559-614.

[49] M.A. Camblor, A. Corma, S. Valencia, Microporous Mesoporous Mater., 25 (1998) 59-74.

[50] N. Katada, H. Igi, J.-H. Kim, M. Niwa, J. Phys. Chem. B, 101 (1997) 5969-5977.

[51] J.-B. Koo, N. Jiang, S. Saravanamurugan, M. Bejblová, Z. Musilová, J. Čejka, S.-E. Park, J. Catal., 276 (2010) 327-334.

[52] W.O. Haag, R.M. Dessau, R.M. Lago, Kinetics and Mechanism of Paraffin Cracking with Zeolite Catalysts, in: S.N. Tomoyuki lnui, T. Takashi (Eds.) Stud. Surf. Sci. Catal., Elsevier, 1991, pp. 255-265.

[53] J. Sun, X.G. Li, A. Taguchi, T. Abe, W.Q. Niu, P. Lu, Y. Yoneyarna, N. Tsubaki, ACS catal., 4 (2014) 1-8.

[54] K.C. Taylor, J. Catal., 38 (1975) 299-306.

[55] C. Fernandez, I. Stan, J.-P. Gilson, K. Thomas, A. Vicente, A. Bonilla, J. Pérez-Ramírez, Chem. Eur. J., 16 (2010) 6224-6233.

[56] X. Li, X. Feng, Q. Ge, K. Fujimoto, Fuel, 87 (2008) 534-538.

[57] J. Weitkamp, ChemCatChem, 4 (2012) 292-306.

[58] A. Corma, J. Planelles, J. Sánchez-Marín, F. Tomás, J. Catal., 93 (1985) 30-37.

[59] D. Vervloet, F. Kapteijn, J. Nijenhuis, J.R. van Ommen, Catal. Sci. Technol., 2 (2012) 1221-1233.

[60] S. Sartipi, K. Parashar, M. Makkee, J. Gascon, F. Kapteijn, Catal. Sci. Technol., 3 (2013) 572-575.

Chapter 4. Selective Transformation of Syngas into Gasoline-Range Hydrocarbons over Mesoporous H-ZSM-5-Supported Cobalt Nanoparticles

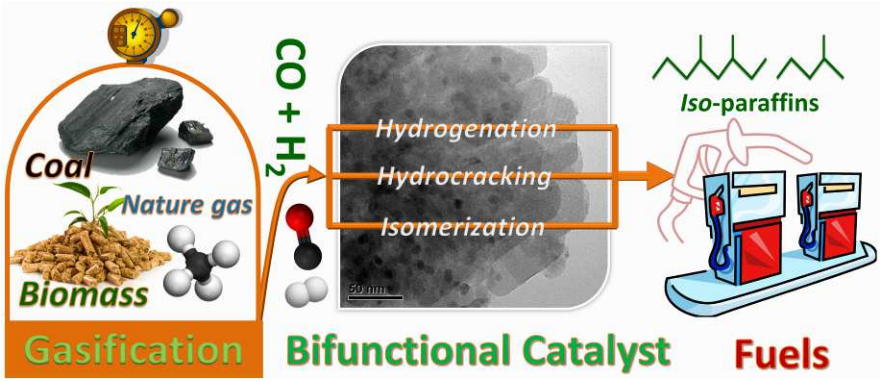

Abstract: We have demonstrated that bifunctional Fischer-Tropsch (FT) catalysts, which couple the uniform-sized Co nanoparticles for CO hydrogenation and the mesoporous zeolites for hydrocracking/isomerization reactions, are promising for the direct production of gasoline-range (C_{5-11}) hydrocarbons from syngas. Our results reveal that the strong Brønsted acidity functions for the hydrocracking/isomerization of the heavier hydrocarbons formed on Co nanoparticles, while the mesoporosity contributes to suppressing the formation of lighter (C_{1-4}) hydrocarbons. The selectivity of C_{5-11} hydrocarbons could reach ~70% with a ratio of isoparaffins to n-paraffins of ~2.3 over our catalyst, markedly higher than the maximum value (~45%) expected from the Anderson-Schulz-Flory distribution. Using *n*-hexadecane as a model molecule, we have clarified that both the acidity and mesoporosity play key roles in controlling the hydrocracking reactions, contributing to the improved product selectivity in FT synthesis.

This Chapter is based on the following publication:

Kang Cheng, Lei Zhang, Jincan Kang, Xiaobo Peng, Qinghong Zhang,* and Ye Wang,* *Chem. Eur. J.*, (**2014**), DOI: 10.1002/chem.201405277. (inside cover paper)

4.1 Introduction

The products of FT synthesis usually follow the Anderson-Schulz-Flory (ASF) distribution over conventional catalysts [13]. Such product distributions are broad and unselective towards the middle-distillate products, which are generally the desired products such as gasoline (C_{5-11}), diesel (C_{10-20}), and jet fuels (C_{8-16}). For example, according to the ASF distribution, the maximum selectivity of gasoline-range hydrocarbons is ~45%. In the current FT technology, the widely distributed hydrocarbon products must be further refined in the second stage by hydrotreating (including hydrocracking and isomerization) to produce high-quality fuels [14, 15]. As compared to this high-cost and energy-consuming two-stage process, the direct production of liquid fuels without the high-pressure H_2 plants for hydrotreatment would make the FT process more competitive. However, the selectivity control for the production of narrowly distributed middle-distillate products is one of the most difficult challenges in FT synthesis.

How to improve the selectivity to $C_{\geqslant 5}$ hydrocarbons is the main focus in most of the recent studies concerning FT product selectivities [7-11, 16]. The development of FT catalysts that can directly break the ASF distribution is an attractive but difficult challenge and has recently become a hot research direction [17-20]. In particular, the construction of bifunctional FT catalysts containing a component for CO hydrogenation to $C_{\geqslant 5}$ hydrocarbons (primary reaction) and that for hydrocracking/isomerization (secondary reaction) to produce middle-distillate hydrocarbons has attracted much attention in recent years [16, 21].

Hierarchical zeolites containing both micropores and mesopores, which combine the advantages of crystalline zeolites (possessing strong acidity and high stability) and amorphous mesoporous materials (possessing efficient mass transportation), have attracted much attention in catalysis in recent years [38-43]. In particular, hierarchical zeolites have shown improved catalytic performances in many acid-catalyzed reactions involving larger molecules such as the hydrocracking of heavier hydrocarbons. The introduction of hierarchical porosity could not only enhance the activity and stability but also may improve the product selectivity during the hydrocracking reactions. For example, de Jong et al. demonstrated that, as compared to the conventional microporous Y zeolite, a hierarchical Y zeolite-supported Pt catalyst can provide higher selectivity toward middle-distillate hydrocarbons including kerosene and diesel, while the selectivity toward lighter hydrocarbons becomes lower during the hydrocracking of squalane (branched C_{30} alkane) [44]. A previous study in our group shows that Ru nanoparticles supported on carbon nanotubes (CNTs) show excellent selectivity

for C_{10-20} hydrocarbons [21]. The acidic groups on the surface of CNTs may play a key role in the mild hydrocracking of $C_{\geq 21}$ products into diesel-range hydrocarbons. Summarizing the available researches, we consider that combining secondary hydrocracking reaction can tune the selelctivity of liquid fuels in FT reaction (Figure 4-1). Certainly, we expect that the hierarchical zeolites would be suitable for the construction of bifunctional FT catalysts with controllable secondary reactions.

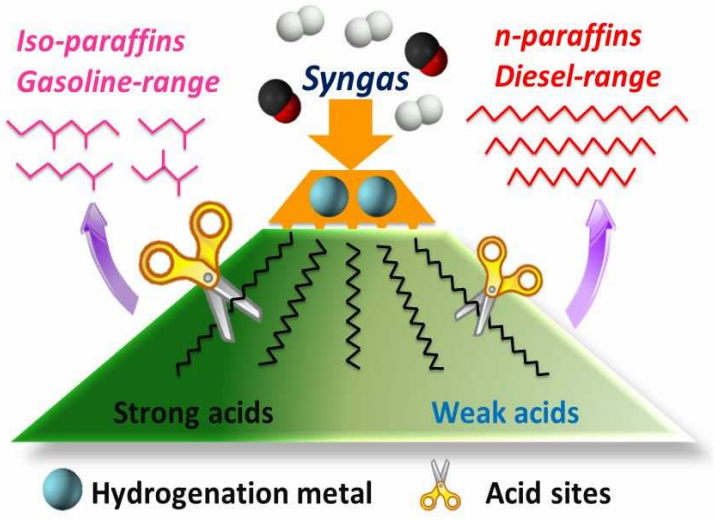

Figure 4-1. Concept of designing bifunctional catalysts for gasoline-range and diesel-range hydrocarbons from syngas.

So far, only limited studies have utilized mesoporous zeolites for FT synthesis [45-52]. In our previous work, we investigated the catalytic performances of Ru nanoparticles loaded on mesoporous ZSM-5 and mesoporous beta zeolites, and found that the selectivities toward C_{5-11} hydrocarbons over these catalysts could reach 70-80%, which were much higher than those over other bifunctional catalysts reported to date [45, 46]. However, the high cost and the low availability of Ru would hinder its industrial-scale application. Recently, Kapteijn and co-workers reported a series of studies on the use of mesoporous zeolite-supported cobalt catalysts for FT synthesis. They obtained an encouraging C_{5-11} selectivity of ~60%, which was higher than that expected from the ASF distribution [48-52]. However, the selectivity to CH_4 was still unfavorably high (~15%) [19]. Deeper fundamental studies on the effects of mesoporosity and acidity as well as the state and size of Co nanoparticles on product selectivity are needed.

Herein, we present our comprehensive studies on the fabrication and utilization of mesoporous ZSM-5 with tunable mesopores sizes and acidities for FT synthesis. In our work,

we attempt to prepare bifunctional catalysts containing uniform-sized Co nanoparticles and mesoporous ZSM-5 with changeable mesopores sizes or acidities to disentangle the effects of different factors. In addition to FT synthesis, the hydrocracking of *n*-hexadecane, a model molecule of heavier hydrocarbons, will also be investigated to provide deeper insights into the formations of different-range products over the bifunctional catalysts.

4.2 Results and Discussion

4.2.1 Support effect of Co-based catalysts for FT synthesis

This section examines the performance of cobalt catalysts supported on various supports for FT reaction. It was reported that the support not only determined the number of active site, but also influenced selectivity of FT products [30, 53]. The supports can be generally categorized into three classes: (1) oxide supports SiO_2 and γ-Al_2O_3, (2) Silicalite-1 with micro-porous structure and mesoporous silica materials SBA-15, (3) molecular sieves with different topologies. Due to different chemical composition and crystal structure, these materials show different acidic properties.

Table 4-1. Catalytic performances of various supported Co catalysts for FT synthesis.[a]

catalyst	CO conv. /%	Hydrocarbon Selectivity (%)					C_{iso}/C_n in C_{5-11}
		CH_4	C_{2-4}	C_{5-11}	C_{12-20}	$C_{\geq 21}$	
Co/SiO_2	43.7	6.5	9.6	25.8	29.2	28.9	0.1
Co/γ-Al_2O_3	22.2	9.5	21.4	42.9	21.6	4.6	0.3
Co/Silicalite-1	43.4	11.6	13.0	31.3	33.0	11.2	0.6
Co/SBA-15	40.9	7.1	15.7	44.2	29.3	3.7	0.2
Co/NaY	20.5	9.5	12.4	42.9	31.3	3.9	0.6
Co/HY	23.7	9.4	14.8	43.4	29.3	3.0	1.0
Co/USY	17.5	8.6	16.0	43.2	29.0	3.3	1.0
Co/H-MCM-22	38.7	14.8	17.8	48.5	18.6	0.3	2.1
Co/H-beta(25)[b]	25.9	23.8	22.9	49.4	4.6	0.1	2.2
Co/H-ZSM-5(18) [b]	17.2	20.4	23.2	50.7	5.6	0.1	1.9

[a]Reaction condition: catalysts, W = 0.5 g, H_2/CO = 1/1, P = 2 MPa, F = 20 mL min^{-1}, T = 513 K, time on stream = 12 h. [b] the value in the parentheses is Si/Al ratio.

Silicalite-1 and SBA-15 are considered as a weak acid or acid-free support [43]. As showed in Table 4-1, catalysts using SiO_2 and Silicalite-1 as supports dispaly high activity and wider distribution of hydrocarbon products, close to the ASF distribution, with high selectivity towards C_{12-20} and $C_{\geqslant 21}$ hydrocarbons. The γ-Al_2O_3 supported catalyst shows lower CO conversion, probably due to the generation of aluminate during thermal treatment (strong interaction between Co and γ-Al_2O_3) which is very hard to reduce [7]. The product distribution of Co/γ-Al_2O_3 is also wider but with higher C_{2-4} and C_{5-11} selectivity compared to Co/SiO_2, presumably caused by the weak acidity of γ-Al_2O_3 material. When using SBA-15 as the support, catalyst shows high selectivity towards C_{5-11} and C_{12-20} middle distillates. Ohtsuka et al. [54] also observed that Co catalysts supported on SBA-15 or MCM-41 showed high selectivity of C_{10-20} hydrocarbons in FT reaction.

It is interesting that when using molecular sieves as supports, the product distribution shifts to middle distillates, especially the C_{5-11} hydrocarbons. Co catalysts supported on Y-type zeolites with intermediate acidic strength (NaY, HY and USY) produce mainly C_{5-11} and C_{12-20} hydrocarbons. While using stronger acidic molecular sieves as supports, the selectivity of C_{5-11} hydrocarbons increases to 49.4% and 50.7% for Co/H-beta and Co/H-ZSM-5, respectively, which exceeds the maximum 45% calculated from the ASF distribution. In addition, the ratio of *iso*-paraffin to *n*-paraffin in C_{5-11} hydrocarbons for molecular sieves supported catalysts is higher than for weaker acidic or non-acidic catalysts. In general, FT product distribution is strongly affected by the acidities of support. Strong acidic molecular sieve supported catalysts can produce mainly C_{5-11} hydrocarbons with branched chains. However, these acidic catalysts also produce CH_4 and C_{2-4} hydrocarbons which are not desired in FT synthesis. Suppressing the generation of light hydrocarbons is challenging in this area.

NH_3-TPD profiles for every supports are showed in Figure 4-2. Higher desorption temperature represents the stronger acidic strength, and the amount of acidic sites is proportional to the area of corresponding peaks. As shown in Figure 4-2, SiO_2 and SBA-15 materials are non-acidic, and NH_3 desorption peaks of Silicalite-1 and γ-Al_2O_3 are lower and smaller. NaY, HY and USY show larger peak area in low temperature. H-MCM-22, H-beta (25) and H-ZSM-5 (18) obviously has two distinct peaks, and the high temperature peak is caused by Brønsted acid sites [55]. A. Auroux[56] considered that Brønsted acidity in molecular sieves is caused by framework alumina. According to the adsorption strength of of NH_3, a scale of acidic order was given: Silicalite-1 < NaY < HY (2.4) < H-beta (10) < H-ZSM-5 (14) < USY [56]. This order is consistent with our NH_3-TPD results. The only

difference is USY zeolite which may be caused by the different Si/Al ratio of USY zeolite or different preparation method [57].

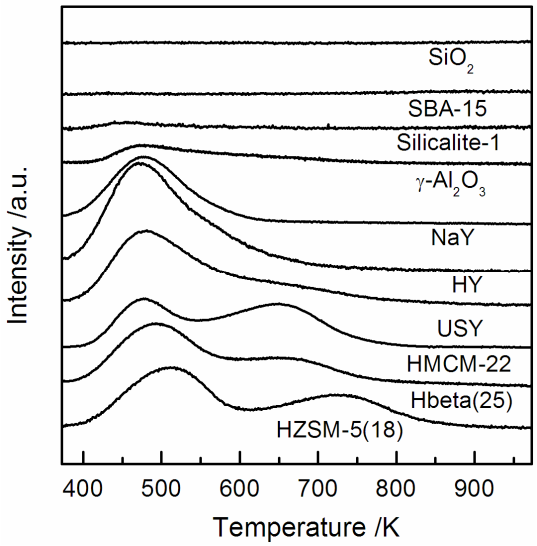

Figure 4-2. NH_3-TPD profiles for different supports.

4.2.2 Structural properties of mesoporous ZSM-5

The mesoporous ZSM-5 samples with different mesopores sizes have been synthesized by post-treatment of the crystalline Na-ZSM-5 with a Si/Al ratio of 18 using NaOH aqueous solutions with different concentrations at 343 K, followed by ion-exchange to transform the Na-form to H-form samples. The proton-exchanged samples are denoted as H-meso-ZSM-5-*x* M, where *x* represents the concentration of NaOH aqueous solution used for post-treatment.

Figure 4-3 shows the typical transmission electron microscopy (TEM) images of the H-meso-ZSM-5 samples thus obtained. The ZSM-5 crystals synthesized in our laboratory possessed sheet-like morphology, which may be beneficial to the mass transportation [58]. Figure 4-3 clearly shows that the post-treatment using NaOH aqueous solutions with concentrations $\geqslant$ 0.3 M can lead to the generation of mesopores over the ZSM-5 crystals. The size of mesopores became larger upon an increase in the concentration of NaOH. From the high-resolution TEM (HRTEM) images (insets in Figure 4-3), we could observe the crystalline fringes in H-ZSM-5, indicating the high crystallinity of this sample. The crystalline fringes could also be seen in the H-meso-ZSM-5-*x*M series of samples but were interrupted by the mesopores, in particular for the sample prepared using a higher concentration of NaOH. This observation suggests that the crystalline structure of ZSM-5 can be sustained after the post-treatment, but the generated mesopores may shorten the length of the ordered structure.

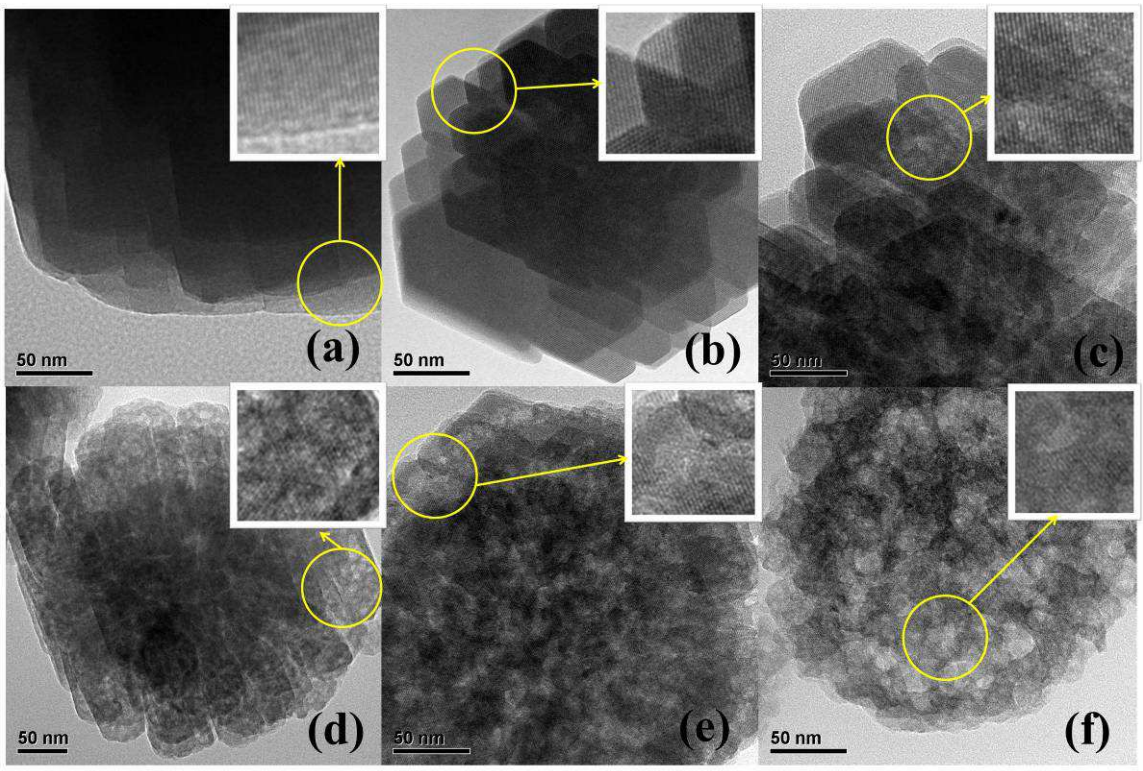

Figure 4-3. TEM micrographs: a) H-ZSM-5, b) H-meso-ZSM-5-0.1 M, c) H-meso-ZSM-5-0.3 M, d) H-meso-ZSM-5-0.5 M, e) H-meso-ZSM-5-0.8 M, and f) H-meso-ZSM-5-1.2 M. The insets are the HRTEM images in the selected area.

We also investigated the change in the crystalline structure after the post-treatment by X-ray diffraction (XRD) in Figure 4-4. The result revealed that all the diffraction peaks belonging to crystalline ZSM-5 could be observed for the H-meso-ZSM-5, but the intensities of the peaks decreased significantly when the concentration of NaOH used for post-treatment exceeded 0.5 M. This suggests that the crystalline structure has been sustained for the H-meso-ZSM-5-*x*M samples although the long-ordered regularity decreases when *x* exceeds 0.5. This agrees well with the above TEM results.

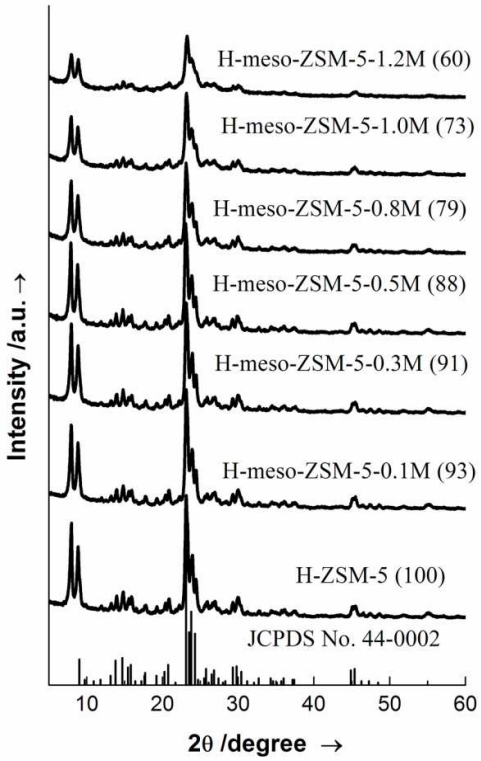

Figure 4-4. XRD patterns of the H-meso-ZSM-5-*x*M series of samples. The number in the parentheses after each sample denotes the relative crystallinity with respect to H-ZSM-5.

The pore structure was further characterized by Ar physisorption technique. The Ar adsorption-desorption isotherms (Figure 4-5) show that the H-ZSM-5 exhibits the type I isotherm, which is typical of microporous zeolites [59]. The treatment of H-ZSM-5 with NaOH aqueous solutions changed the isotherms from type I gradually into type IV and a hysteresis loop appeared, indicating the generation of mesopores [59].

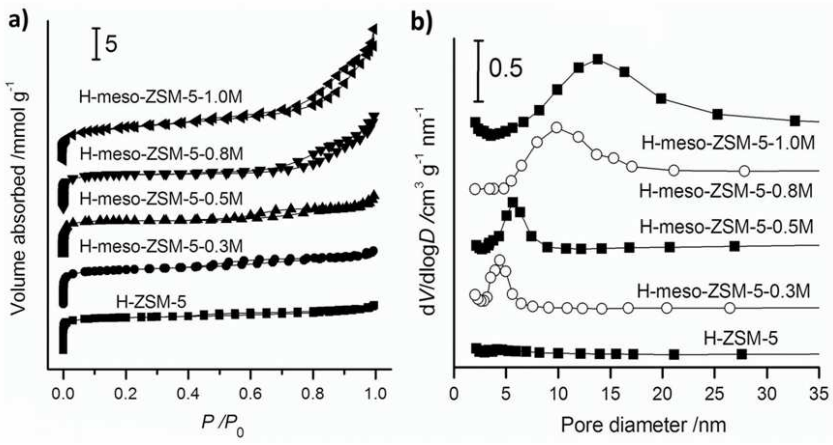

Figure 4-5. a) Argon adsorption-desorption isotherms and b) pore size distributions evaluated by the BJH method for the H-meso-ZSM-5-x M samples.

By using the Barrett-Joyner-Halenda (BJH) method, we have evaluated the pore-diameter distributions in mesoporous region for the H-meso-ZSM-5-*x*M samples. Relatively narrow pore-diameter distributions were observed for the samples with $x \leqslant 0.5$ (Figure 4-5b). The size of mesopores depended on the concentration of NaOH; the higher concentration of NaOH resulted in the larger size of mesopores. The surface areas and pore volumes of the H-meso-ZSM-5-*x*M samples were also evaluated from the Ar physisorption. With an increase in the concentration of NaOH used for post-treatment, the micropore surface area and micropore volume, which were estimated by the t-plot method [60], decreased, whereas the mesopores surface area and mesopores volume estimated by the BJH method increased (Table 4-2). This indicates that some micropores have been transformed into mesopores [61]. Our inductively coupled plasma-optical emission spectroscopy (ICP-OES) measurements revealed that the Si/Al ratio in the H-meso-ZSM-5 samples became lower than that in the parent ZSM-5 (Table 4-2). This suggests that the Si atoms have been removed from the framework of ZSM-5 zeolite during the treatment by NaOH aqueous solutions and the desilication is mainly responsible for the generation of mesopores in the microporous ZSM-5 crystals.

Table 4-2. Textural properties of H-ZSM-5 and H-meso-ZSM-5-*x* M series of samples.

H-meso-ZSM-5-*x*M	Si/Al ratio[a]	S_{BET}[b] [$m^2\ g^{-1}$]	S_{micro}[c] [$m^2\ g^{-1}$]	S_{meso}[d] [$m^2\ g^{-1}$]	V_{total}[e] [$cm^3\ g^{-1}$]	V_{micro}[c] [$cm^3 g^{-1}$]	V_{meso}[d] [$cm^3\ g^{-1}$]	D_{micro}[f] [nm]	D_{meso}[g] [nm]
0	18	354	304	29	0.18	0.13	0.04	0.49	-
0.3	14	358	262	98	0.22	0.11	0.12	0.50	4.5
0.5	14	383	252	153	0.29	0.11	0.19	0.50	5.8
0.8	12	387	225	168	0.40	0.09	0.32	0.50	9.9
1.0	10	372	128	252	0.50	0.05	0.45	0.48	13.8

[a] measured from ICP-OES. [b] BET surface area. [c] S_{micro} and V_{micro} denote micropore surface area and micropore volume, respectively, evaluated by the *t*-plot method. [d] S_{meso} and V_{meso} denote mesopores surface area and mesopores volume, respectively, evaluated by the BJH method. [e] Total pore volume. [f] Mean diameter of micropores evaluated by the HK method. [g] Mean diameter of mesopores evaluated by the BJH method.

4.2.3 Acidities of mesoporous ZSM-5

The acid properties of the H-meso-ZSM-5-x M samples were investigated by the ammonia temperature-programmed desorption (NH_3-TPD). Figure 4-6a shows that the H-meso-ZSM-5 samples exhibit two NH_3 desorption peaks at ~500 K and ~750 K. The

lower-temperature and higher-temperature desorption peaks could be ascribed to the hydrogen-bonded NH_3 molecules and the NH_3 molecules chemisorbed on the Brønsted acid sites, respectively [62, 63].

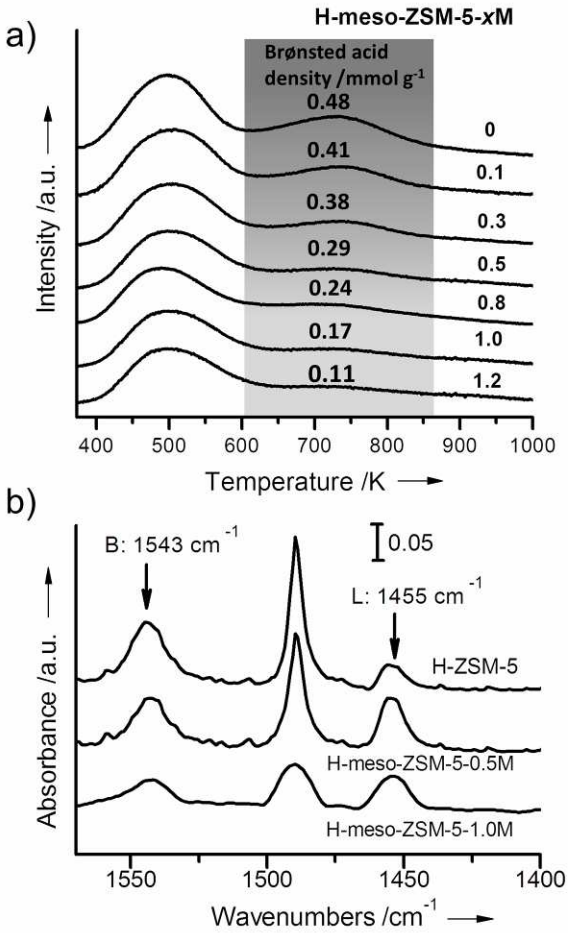

Figure 4-6. a) NH_3-TPD profiles and b) pyridine-adsorbed FT-IR spectra for the H-meso-ZSM-5-*x*M samples prepared by post-treatment of ZSM-5 with different concentrations of NaOH solution.

It is generally accepted that the Brønsted acid site plays a predominant role in the hydrocracking and isomerization reactions, which may involve the carbocation intermediates [64, 65]. Thus, we have estimated the density of Brønsted acid sites over the H-meso-ZSM-5 samples. The density of Brønsted acid sites decreased gradually with increasing the mesopores size or the concentration of NaOH used for post-treatment (Figure 4-6a). Our ICP-OES analysis confirmed that almost no Na^+ remained in the H-meso-ZSM-5 samples, indicating that almost all the Na^+ cations were exchanged into protons. The decrease in the density of Brønsted acid sites may be related to the change of a part of framework Al into

extra-framework Al species during the desilication process [62]. This was confirmed by our ^{27}Al magic-angle spinning nuclear magnetic resonance (^{27}Al MAS NMR) spectroscopic study. ^{27}Al MAS NMR spectra of the HZSM-5 H-meso-ZSM-5-*x*M samples are shown in Figure 4-7. For all the samples, there are two bands: one is centered at 55 ppm and the other is at 0 ppm. The former is attributed to the framework aluminum and the latter is associated with the non-framework aluminum [66]. For H-meso-ZSM-5-*x*M samples, the intensity of the band corresponding to the non-framework aluminum increased due to partial collapse of ZSM-5 structure.

The quantification of Figure 4-6a suggests that approximately 60% of Brønsted acid sites are sustained after the treatment using a 0.5 M NaOH aqueous solution. Pyridine-adsorbed Fourier-transform infrared (FT-IR) spectroscopic studies were performed to gain further information on the acid property of the H-meso-ZSM-5 samples. Figure 4-6b shows that the H-meso-ZSM-5 samples exhibit IR bands at 1455 cm^{-1} and 1543 cm^{-1}, which can be ascribed to the Lewis and the Brønsted acid sites, respectively [67-69]. The IR band observed at 1490 cm^{-1} resulted from both Brønsted and Lewis acid sites over these catalysts. As compared to that for H-ZSM-5, the intensity of the band at 1543 cm^{-1} for the H-meso-ZSM-5 became lower, while that at 1455 cm^{-1} became higher. This corresponds well to the NH_3-TPD result and also suggests that a part of framework Al atoms have migrated to the extra-framework position, leading to the decrease in the density of Brønsted acid sites and the simultaneous increase in the density of Lewis acid sites.

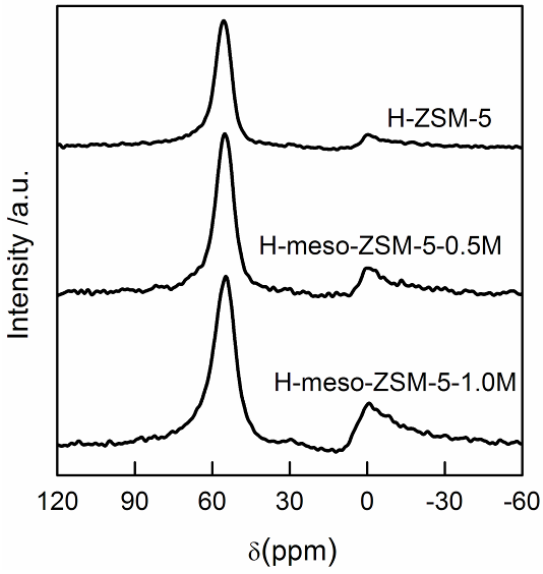

Figure 4-7. ^{27}Al MAS NMR spectra for the H-meso-ZSM-5-x M series of samples.

4.2.4 Preparation of zeolites with different Brønsted acid densities

To gain insights into the effect of acidity without considering the influence of porous properties, we have prepared a series of mesoporous ZSM-5 samples by treating microporous ZSM-5 with a 0.5 M NaOH aqueous solution (denoted as meso-ZSM-5-0.5M) but with different H^+-exchanging degrees and thus different acidities. NH_3-TPD results showed that the intensity of the desorption peak at ~750 K belonging to the Brønsted acid sites increased with an increase in the H^+-exchanging degree (Figure 4-8a), confirming the increase in the density of Brønsted acid sites (Table 4-3). This was further supported by the pyridine-adsorbed FT-IR studies. The IR band at 1543 cm^{-1} ascribed to the Brønsted acid sites increased with an increase in the H^+-exchanging degree (Figure 4-8b). An IR band at 1444 cm^{-1} was observed for the sample with Na^+ remaining at the cation-exchange site due to the interaction of pyridine with Na^+, which is a weak Lewis acid. For comparison, we have also prepared microporous ZSM-5 with different H^+-exchanging degrees. From the NH_3-TPD results (Figure 4-9), we have evaluated the densities of Brønsted acid sites for these samples and the results are also displayed in Table 4-3.

Table 4-3. Density of Brønsted acid sites over ZSM-5 and mesoporous ZSM-5 samples with different H^+-exchanging degrees

Sample	H^+-exchanging degree [%]	Density of Brønsted acid sites[a] [mmol g^{-1}]
meso-ZSM-5-0.5 M	0	0
meso-ZSM-5-0.5 M	6.9	0.02
meso-ZSM-5-0.5 M	48	0.14
meso-ZSM-5-0.5 M	62	0.18
meso-ZSM-5-0.5 M	100	0.29
ZSM-5	0	0
ZSM-5	10	0.05
ZSM-5	33	0.16
ZSM-5	60	0.29
ZSM-5	100	0.48

[a] Evaluated from NH_3-TPD.

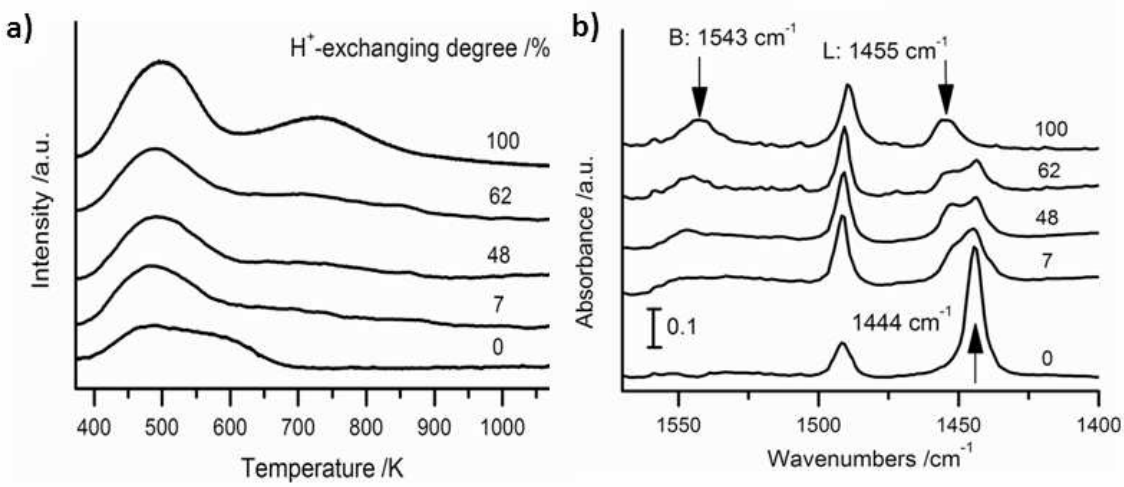

Figure 4-8. a) NH_3-TPD profiles and b) pyridine-adsorbed FT-IR spectra for the meso-ZSM-5-0.5 M samples with different H^+-exchanging degrees.

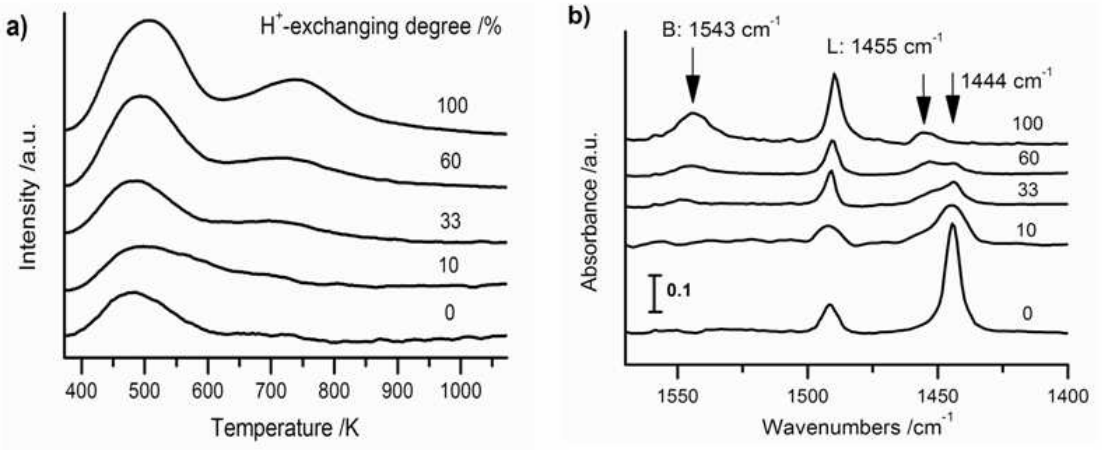

Figure 4-9. a) NH_3-TPD profiles and b) pyridine-adsorbed FT-IR spectra for ZSM-5 samples with different H^+-exchanging degrees.

4.2.5 Preparation of Co nanoparticles loaded on ZSM-5 and mesoporous ZSM-5

It is well known that metallic Co is the active phase for FT synthesis [7-12]. The size of Co particles is a key parameter determining the catalytic performance of supported Co catalysts. It is accepted that Co nanoparticles with a mean diameter of 6-10 nm are favorable for the production of C$\geqslant$5 hydrocarbon in FT synthesis [70]. In the case of using a microporous zeolite as the support, it is difficult to disperse the Co particles in such a size range because the surface area of a zeolite is mostly limited inside the micropores [50]. Thus, we have first investigated the possibility to prepare ZSM-5-supported Co particles with narrow size distributions.

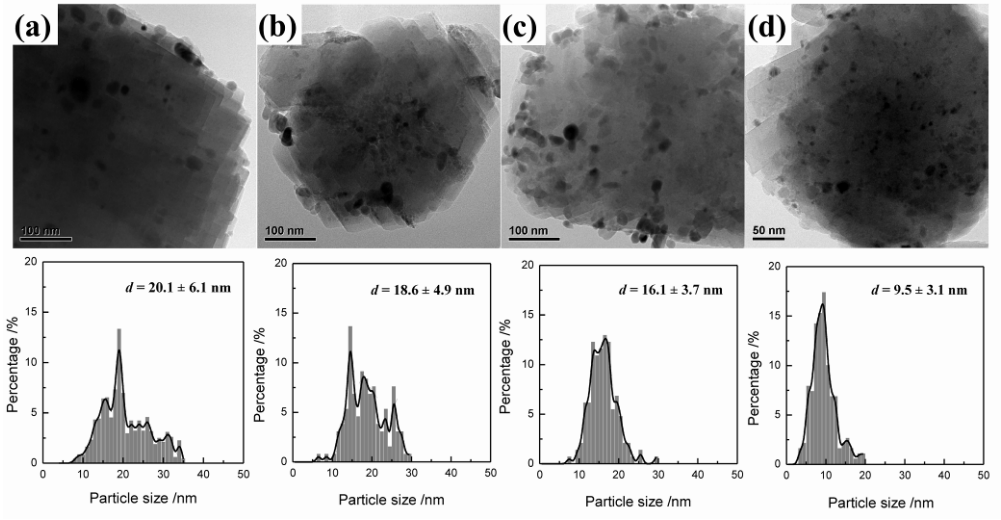

Figure 4-10. TEM micrographs and the corresponding Co particle size distributions for the Co/H-ZSM-5 prepared by thermal treatment of the $Co(NO_3)_2$/H-ZSM-5 composite under different atmospheres. (a) stagnant air at 673 K, (b) flowing air at 673 K, (c) 5% NO/Ar at 673 K, (d) 5% NO/Ar at 573 K.

We prepared H-ZSM-5-supported Co catalysts by a simple impregnation method using $Co(NO_3)_2$ as the precursor. We found that the control of the atmosphere for the subsequent thermal treatment is crucial for obtaining Co nanoparticles with narrow size distributions. The thermal treatment of the $Co(NO_3)_2$/H-ZSM-5 composite in stagnant air or air flow resulted in inhomogeneous supported Co particles. On the other hand, the thermal treatment in NO/Ar flow led to the relatively homogeneous size distribution of Co nanoparticles (Figure 4-10). The mean size of Co particles also became smaller (9.5 nm) by adopting the thermal treatment in NO/Ar flow at 573 K. Our observation is in agreement with that reported by the Utrecht group [71, 72], who demonstrated that the impregnation of $Ni(NO_3)_2$ or $Co(NO_3)_2$ into mesoporous SiO_2, followed by thermal treatment in a gas flow containing NO, led to the formation of uniform-sized Ni or Co nanoparticles. The controlled thermal decomposition of nitrates under NO was proposed to be responsible for the narrow size distribution.

We adopted the same thermal treatment under NO/Ar for the preparation of mesoporous ZSM-5-supported Co catalysts. Co nanoparticles were dispersed in these samples relatively homogeneously (Figure 4-11). The size distributions of Co particles in these catalysts derived by counting more than 200 Co particles were narrow (Table 4-4). It is of interest that the mean sizes of Co particles in the H-meso-ZSM-5-*x*M samples with different mesopores sizes are quite similar, locating in a range of 7.7-10.5 nm. The mean size of Co particles in such a range is believed to be beneficial for FT synthesis [70].

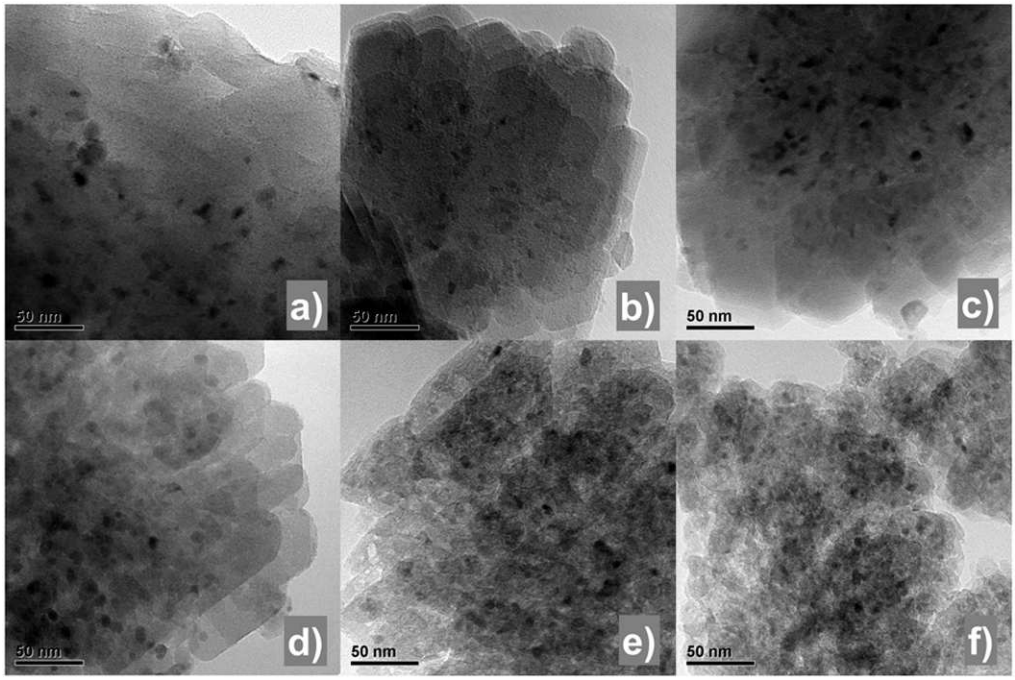

Figure 4-11. TEM micrographs of Co nanoparticles loaded on H-meso-ZSM-5-x M series of catalysts. a) Co/H-ZSM-5, b) Co/H-meso-ZSM-5-0.1 M, c) Co/H-meso-ZSM-5-0.3 M, d) Co/H-meso-ZSM-5-0.5 M, e) Co/H-meso-ZSM-5-0.8 M, f) Co/H-meso-ZSM-5-1.2 M.

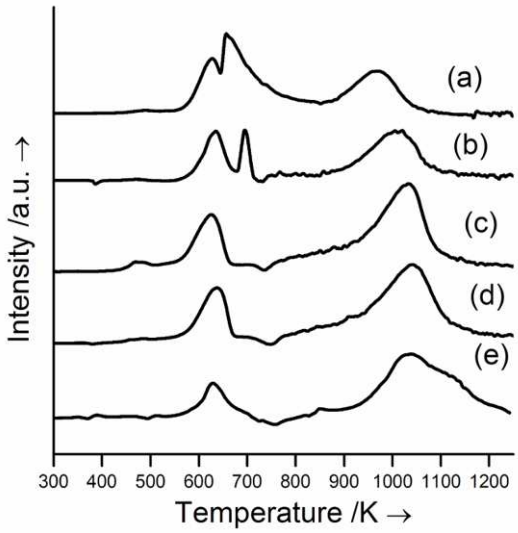

Figure 4-12. H_2-TPR profiles for the Co/H-meso-ZSM-5-*x* M sample before H_2 reduction. (a) Co/H-ZSM-5, (b) Co/H-meso-ZSM-5-0.1 M, (c) Co/H-meso-ZSM-5-0.3 M, (d) Co/H-meso-ZSM-5-0.5 M and (e) Co/H-meso-ZSM-5-1.0 M.

The reduction degree of Co species and cobalt dispersion over the Co/H-meso-ZSM-5 samples were characterized by the pulse oxidation and the H_2 chemisorption techniques. As displayed in Table 4-4, the reduction degree of Co species decreased as the concentration of

NaOH used for post-treatment or the mesopores size increased. Our studies already indicated that a small part of framework Al species moved to extra-framework positions during the NaOH treatment or desilication process (Figure 4-7). The cobalt precursors would strongly interact with these extra-framework Al species, and thus became difficult to be reduced. The decrease in the reducibility was also confirmed by the H_2-temperature-programmed reduction (H_2-TPR) results, which showed that the fraction of the high-temperature reduction peak (>900 K) increased with increasing the concentration of NaOH for post-treatment (Figure 4-12). The retardation of the reduction due to the strong interaction between Co species and Al species was also observed by other groups and was proposed to be due to the formation of cobalt aluminate species [73].

We have evaluated the Co dispersion by measuring the amount of H_2 chemisorption on our catalysts. The Co dispersions for these catalysts were quite similar, located in a range of 0.074-0.099. From the value of Co dispersion, we also estimated the size of Co particles by using a simple reciprocal relationship between the particle size and the dispersion for spherical particles, Co size = 0.96/dispersion. The results displayed in Table 4-4 further suggest that the sizes of Co particles in the Co/H-meso-ZSM-5-*x*M series of catalysts are quite similar.

Table 4-4. Properties of cobalt species over the Co/H-meso-ZSM-5-*x* M series of catalysts

Sample	Mean Co size[a] [nm]	Reduction degree[b] [%]	Co dispersion[c]	Co size[d] [nm]
Co/H-ZSM-5	9.5±3.1	75.2	0.074	12.9
Co/H-meso-ZSM-5-0.1 M	10.5±2.5	63.8	0.081	11.9
Co/H-meso-ZSM-5-0.3 M	8.1±2.0	59.5	0.081	10.8
Co/H-meso-ZSM-5-0.5 M	8.4±1.8	50.5	0.099	9.7
Co/H-meso-ZSM-5-0.8 M	8.7±1.8	43.9	0.094	10.2
Co/H-meso-ZSM-5-1.0 M	7.8±2.2	42.7	0.093	10.3
Co/H-meso-ZSM-5-1.2 M	7.7±2.0	38.1	0.097	9.9

[a] Obtained from TEM. [b] Evaluated by the pulse oxidation method. [c] Measured by the H_2 chemisorption method. [d] Estimated by the equation: Co size = 0.96 /dispersion.

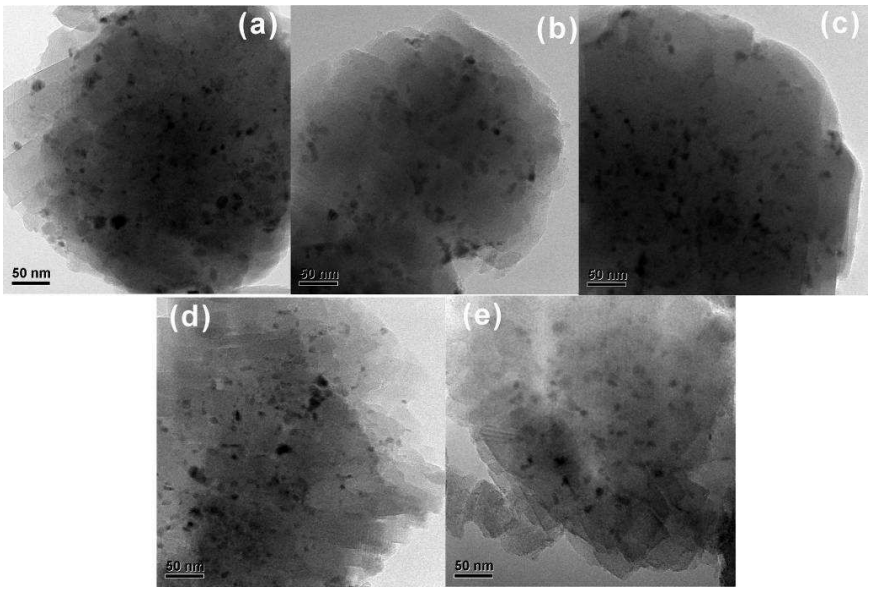

Figure 4-13. TEM micrographs and the corresponding Co particle size distributions for the Co/ZSM-5 catalysts with different H^+-exchanging degrees. H^+-exchanging degree: (a) 100%, (b) 60%, (c) 33%, (d) 10%, (e) 0.

We also loaded Co nanoparticles onto the ZSM-5 and meso-ZSM-5-0.5 M samples with different H^+-exchanging degrees. For these catalysts, the mean sizes of Co particles estimated from TEM measurements were quite similar in a range of 8.4-10.5 nm (Table 4-5, Figures 4-13 and 4-14), which were suitable for FT synthesis.

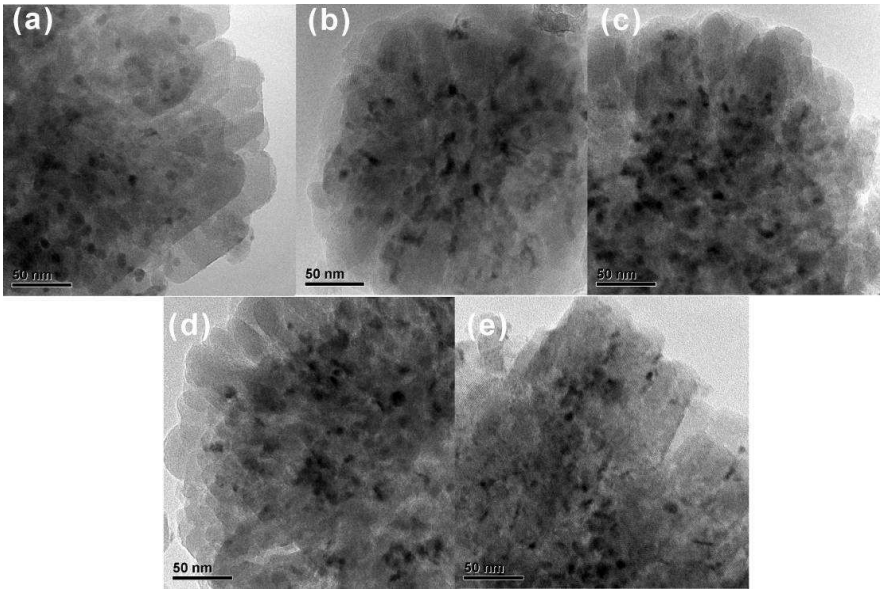

Figure 4-14. TEM micrographs and the corresponding Co particle size distributions for the Co/meso-ZSM-5-0.5 M catalysts with different H^+-exchanging degrees. H^+-exchanging degree: (a) 100%, (b) 62%, (c) 48%, (d) 6.9%, (e) 0.

The reduction degrees of Co species for the Co/ZSM-5 series of catalysts were 75-88%, while those for the Co/meso-ZSM-5-0.5 M series of catalysts were 50-66%. The lower reduction degrees of Co species in the latter series of catalysts are probably due to the strong interaction of Co species with the extra-framework Al species existing in these catalysts. It is quite interesting that the reduction degree of Co species and the Co particle size do not depend on the H^+-exchanging degree or the content of Na^+ in the catalysts. It was reported that the presence of alkali metal ions in the Co-based catalysts may decrease the reducibility of Co species because of the strong interaction of Co species with the alkali metal ions, and thus the alkali metal ion may work as a poison of Co catalysts for FT synthesis [7, 9]. Over our catalysts, the interaction between Co species and Na^+ should be weak because Na^+ ions are located in the cation-exchange positions inside the small micropores, whereas Co species responsible for FT synthesis should be mostly located outside the small micropores.

Table 4-5. Properties of cobalt species over the Co/ZSM-5 series and the Co/meso-ZSM-5-0.5 M series of catalysts with different H^+-exchanging degrees.

Sample	H^+-exchanging degree [%]	Reduction degree[a] [%]	Mean Co size[b] [nm]
Co/ZSM-5	0	88	9.1±1.8
Co/ZSM-5	10	85	9.3±2.4
Co/ZSM-5	34	83	10±1.7
Co/ZSM-5	60	80	10±2.4
Co/ZSM-5	100	75	9.5±3.1
Co/meso-ZSM-5-0.5 M	0	64	9.0±2.4
Co/meso-ZSM-5-0.5 M	6.9	66	8.8±2.1
Co/meso-ZSM-5-0.5 M	48	49	9.4±1.4
Co/meso-ZSM-5-0.5 M	62	50	10.5±2.1
Co/meso-ZSM-5-0.5 M	100	51	8.4±1.8

[a] Evaluated by the pulse oxidation method. [b] Obtained from TEM measurements.

4.2.6 Catalytic behaviors of Co/ZSM-5 and Co/meso-ZSM-5 for FT synthesis

First, we compared the catalytic performances of the Co/H-ZSM-5 catalysts prepared by thermally treating the $Co(NO_3)_2$/H-ZSM-5 composite under different atmospheres. As compared to that by thermal treatment under stagnant air or air flow, the catalyst prepared by

thermal treatment under NO/Ar flow provided significantly higher CO conversions (Table 4-6). The combination of this observation with the TEM result (Figure 4-10) indicates that the catalysts with narrowly distributed and smaller sizes of Co particles possess higher CO conversion activities. Nevertheless, the product selectivities over these catalysts were quite similar; the selectivities to $C_{\geqslant 21}$ and C_{12-20} hydrocarbons were lower and those to C_{5-11} hydrocarbons were ~50%, slightly higher than the maximum value expected from the ASF distribution (~45%). It can be expected that $C_{\geqslant 12}$ hydrocarbons undergo hydrocracking reactions, increasing the C_{5-11} selectivity over these catalysts. However, the selectivity to lighter (C_{1-4}) hydrocarbons, which were unfavorable in FT synthesis, was too high over the Co/H-ZSM-5 catalysts. The CH_4 and C_{2-4} selectivities were 20-22% and 21-23%, respectively. These results indicate that the size of Co particles over the H-ZSM-5 in the range of 9.5-20 nm can affect the CO conversion but does not significantly affect the product selectivity.

Table 4-6. Catalytic performances of Co/H-ZSM-5 prepared by thermal treatment of $Co(NO_3)_2$/H-ZSM-5 composite under different atmospheres[a]

Atmosphere for thermal treatment	CO conv./%	Hydrocarbon selectivity /%					C_{iso}/C_n in C_{5-11}
		CH_4	C_{2-4}	C_{5-11}	C_{12-20}	C_{21}^+	
Stagnant air at 673 K	17	20	23	51	5.6	0.1	1.9
Air flow at 673 K	23	20	21	51	6.8	0.7	1.9
5% NO/Ar flow at 673 K	32	20	22	49	8.0	0.9	1.7
5% NO/Ar flow at 573 K	31	22	22	50	5.9	0.2	1.8

[a] Reaction conditions: catalyst, 0.5 g; H_2/CO = 1.0; temperature, 513 K; pressure, 2 MPa; total flow rate, 20 mL min^{-1}; time on stream, 12 h, Carbon balance is 95-100%.

Then, we investigated the catalytic performances of Co nanoparticles loaded on the H-meso-ZSM-5-*x*M series of samples with different sizes of mesopores. The mean sizes of Co nanoparticles over these catalysts were similar (7.7-10.5 nm). Figure 4-15 shows that the introduction of mesopores significantly changes the product distributions; the selectivity to the lighter (C_{1-4}) hydrocarbons decreased and that to C_{5-11} hydrocarbons increased significantly by using the H-meso-ZSM-5 (x = 0.1-1.2 in Figure 4-15) to replace H-ZSM-5 (x = 0). For example, the selectivity to CH_4 decreased from 22% over the Co/H-ZSM-5 to 7.7% over the Co/H-meso-ZSM-5-0.5 M (x = 0.5) catalyst and the C_{5-11} selectivity increased from 50% to 70% at the same time. The selectivity to C_{2-4} hydrocarbons also decreased from 22%

to 15%, while that to heavier ($C_{\geqslant 12}$) hydrocarbons kept low (<8%). A further increase in *x* value (NaOH concentration) increased the selectivity to heavier hydrocarbons possibly because of the decreased acidity (Figure 4-6). Thus, the highest selectivity to C_{5-11} hydrocarbons for this series of catalysts was attained over the Co/H-meso-ZSM-5-0.5 M catalyst. The ratio of isoparaffins to *n*-paraffins in C_{5-11} hydrocarbons, denoted as C_{iso}/C_n, over this catalyst was 2.3. It is of interest that the Co/H-meso-ZSM-5-0.5 M catalyst also exhibits a higher CO conversion than the Co/H-ZSM-5 likely because of the enhanced mass transportation in the catalyst with mesopores. The further increase in the *x* value rather decreased the CO conversion possibly due to the decrease in the reduction degree of Co species.

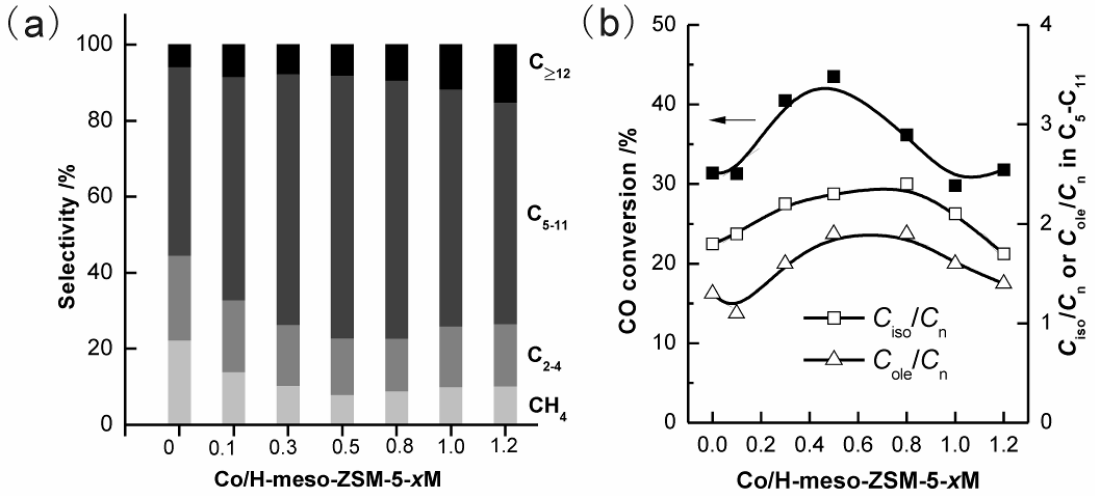

Figure 4-15. Catalytic performances of the Co/H-meso-ZSM-5 series of catalysts for FT synthesis. a) product selectivity. b) CO conversion and C_{iso}/C_n. Reaction conditions: W = 0.5 g, H_2/CO = 1/1, P = 2 MPa, F = 20 mL min^{-1}, T = 513 K, time on stream = 12 h.

It is noteworthy that, although the C_{5-11} selectivity of 70% obtained in this work is lower than that obtained over the mesoporous zeolite-supported Ru catalysts in our previous work [45, 46], this value is better than the Co-based bifunctional catalysts reported to date [17-20]. We have examined the stability of the Co/H-meso-ZSM-5-0.5 M catalyst. CO conversion and C_{5-11} selectivity only decreased slightly with prolonging the time on stream (Figure 4-16). The CO conversion of 36% and C_{5-11} selectivity of 65% could be obtained after 107 h of reaction. These results suggest that our mesoporous ZSM-5-supported Co catalyst is promising for the selective synthesis of C_{5-11} hydrocarbons from syngas.

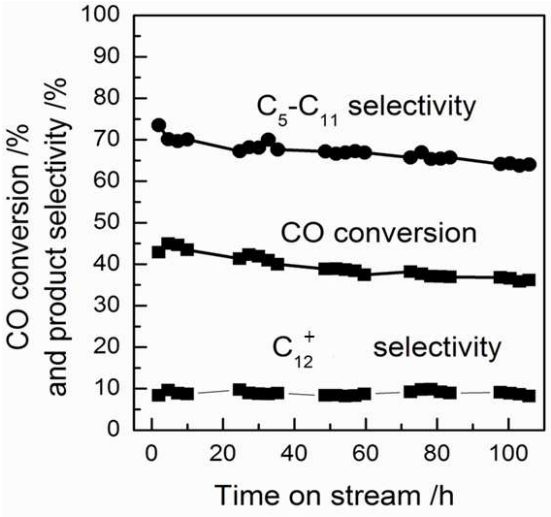

Figure 4-16. Changes of catalytic performances with time on stream over the Co/H-meso-ZSM-5-0.5 M catalyst.

It is of fundamental importance to clarify the key factors determining the catalytic behaviors, in particular the product selectivity, for a bifunctional catalyst. As described above, we have clarified that the mean sizes of Co particles over our catalysts are in the range of 7.7-10.5 nm. In such a range, we could exclude the influence of the size of Co particles on the product selectivity. The result in Figure 4-15 suggests that the presence of mesopores remarkably increases the selectivity to C_{5-11} hydrocarbons by suppressing the formation of CH_4 and C_{2-4} alkanes. However, as displayed in Figure 4-6, the density of the strong Brønsted acidity of the H-meso-ZSM-5-*x*M samples gradually decreased accompanying with the presence of mesopores. The decrease in acidity may suppress the over-cracking of heavier hydrocarbons, resulting in the decrease in the selectivity to lighter hydrocarbons. Thus, it is necessary to unravel the contribution of the presence of mesoporosity or the decreased acidity to suppressing the formation of the lighter hydrocarbons.

4.2.7 Catalyst deactivation

Deactivation is an important problem for Co catalysts. The main reasons of deactivation include poisoning of active sites, sintering, carbon deposition, carbonization, oxidation of metallic cobalt, strong interaction between cobalt and supports, reconstruction of catalyst and so on [74-77]. A. Martínez et al. [78] studied the deactivation behavior of Co/zeolite catalysts in FT reaction systematically. It was found that carbon deposition on catalysts surface cause lower catalytic activity and *iso*-paraffin content. The amount of carbon deposition increases in the following order HZSM-5 < HMOR < HBeta < USY. For Co/HZSM-5 catalyst with

narrow micropores, the catalyst pores contain mostly long-chain hydrocarbons. For cobalt catalysts supported on molecular sieve supports with larger micropores, carbon deposition mainly consists of aromatic hydrocarbons with dual ring and triple ring. Carbon deposition can cover Brønsted acidic sites, but also can be eliminated due to subsequent hydrogenation reaction. So over Co/HZSM-5 catalysts, 80% of Brønsted acid sites are still available after reaction [78].

The TEM mapping images for Co/H-meso-ZSM-5-0.5M catalyst after reaction of 107 h is shown in Figure 4-17. It is clear that there is no cobalt agglomerates observed. The statistics of Co nanoparticles shows that the average cobalt particle size increases from 8.4 ± 1.8 nm (fresh) to 9.6 ± 2.7 nm (after reaction). As FT reaction is a strongly exothermic reaction, Co nanoparticles are prone to reconstruct or agglomerate, which is a major cause of catalyst deactivation. The dark-field TEM images and mapping of cobalt elements also confirmed that Co nanoparticles are well dispersed in the H-meso-ZSM-5-0.5M crystallites. ZSM-5 zeolite consists of Si, Al and O elements. It is also clear that the three elements are well dispersed without enrichment.

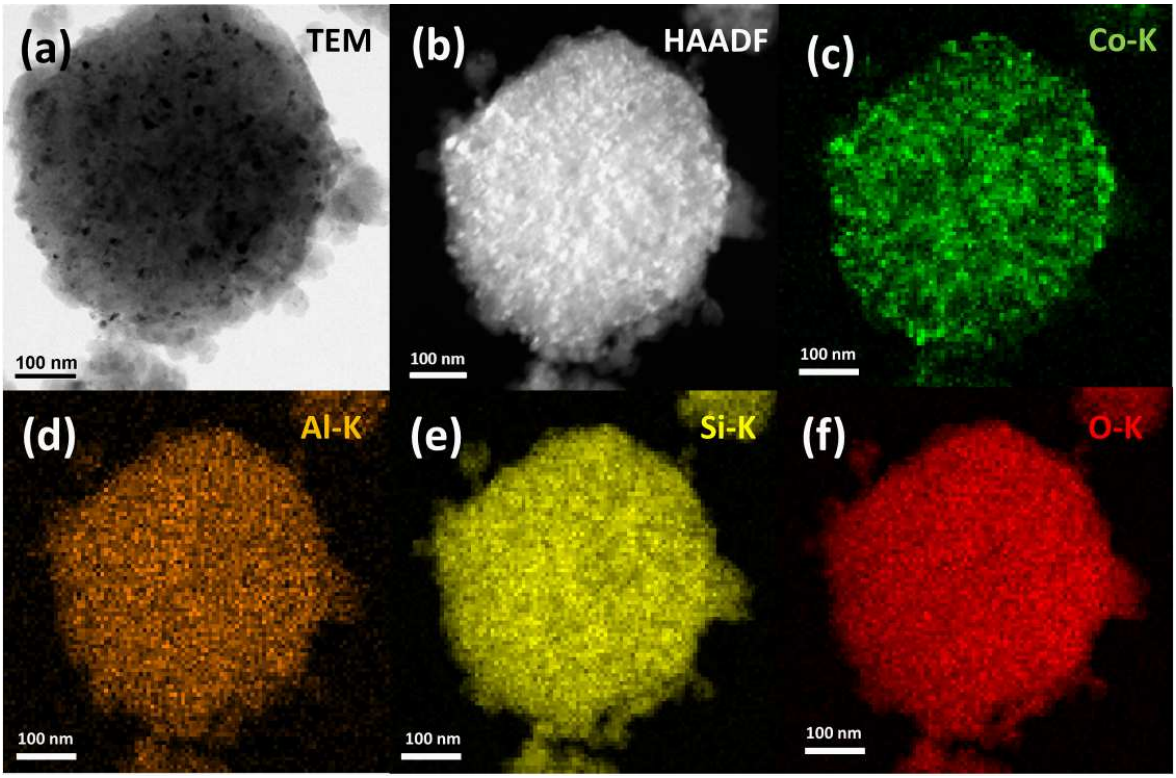

Figure 4-17. Micrographs of Co/H-meso-ZSM-5-0.5M catalyst after reaction for 107 h: (a) TEM image, (b) HAADF-TEM image, (c, d, e, f) TEM-EDX images of cobalt, aluminum, silicon and oxygen, respectively.

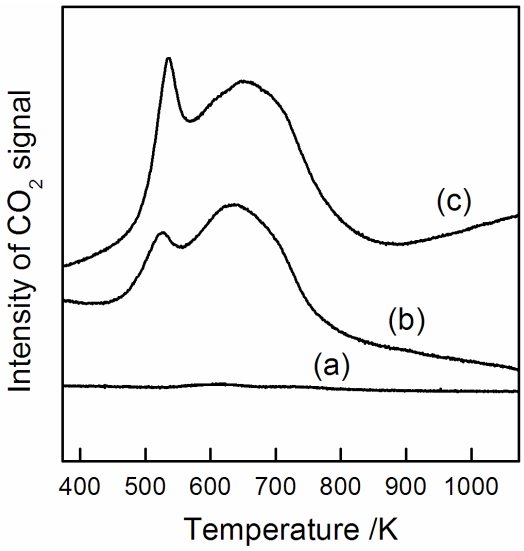

Figure 4-18. O_2-TPO profiles recorded by mass spectrum for Co/H-meso-ZSM-5-0.5M catalys: (a) fresh and after reaction for (b) 12 h and (c) 107 h.

O_2-TPO technique can be used to analyze carbon deposits on the surface of the catalyst [79]. Figure 4-18 shows that there is no carbon contamination on catalyst surface (no CO_2 signal) for fresh Co/H-meso-ZSM-5-0.5M catalyst. While for the catalysts after 107 h and 12 h reaction, two obvious CO_2 peaks are observed in the range of 400 – 800 K, and the 107 h signal is stronger. Low temperature CO_2 signal may be caused by the combustion of adsorbed carbon on the surface of metallic cobalt particles. Metallic nanoparticles could catalyze the combustion reaction. High temperature signal may come from the aromatic hydrocarbons or waxes in the pores of molecular sieve [80, 81]. The TEM and the O_2-TPO results show that the main reasons for catalyst deactivation include cobalt sintering and carbon deposition.

4.2.8 The effect of Brønsted acid densities on hydrocarbon selectivity

To disentangle the roles of the decreased acidity and the enhanced mesoporosity in improving the C_{5-11} selectivity over the mesoporous H-ZSM-5-supported Co catalysts, we have investigated the catalytic behaviors of ZSM-5 and meso-ZSM-5-0.5 M catalysts with different H^+-exchange degrees or different densities of Brønsted acid sites.

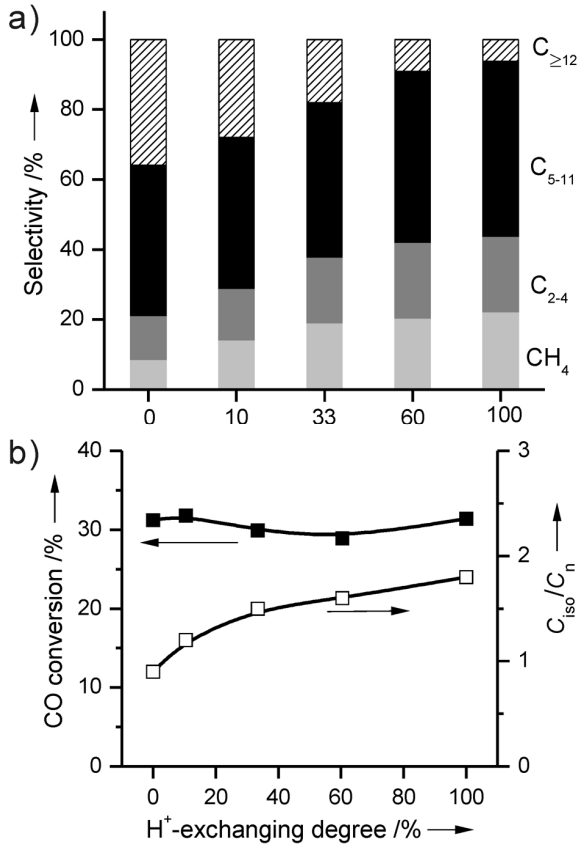

Figure 4-19. Catalytic performances of the Co/ZSM-5 catalysts with different H^+-exchanging degrees for FT synthesis. a) Product selectivity. b) CO conversion and C_{iso}/C_n.

Figure 4-19 shows that, upon decreasing the H^+-exchange degree or the density of Brønsted acidity, the selectivity to CH_4 and C_{2-4} hydrocarbons can really be decreased to some extent, but the selectivity to C_{5-11} hydrocarbons cannot be increased significantly. Actually, Figure 4-19 shows that the C_{5-11} selectivity varies between 40-50% with changing the H^+-exchange degree. Instead, the selectivity to $C_{\geqslant 12}$ hydrocarbons increased significantly with decreasing the H^+-exchanging degree. The CO conversion was kept at ~30%, whereas the ratio of *n*-paraffins to *iso*-paraffins decreased from 1.8 to 0.9 with decreasing the H^+-exchanging degree from 100% to 0. All these results suggest that the decrease in the density of Brønsted acid sites can suppress the hydrocracking and isomerization reactions as expected. However, the selectivity to C_{5-11} hydrocarbons cannot be enhanced by systematically regulating the acidity of the Co/ZSM-5 series of catalysts without mesopores.

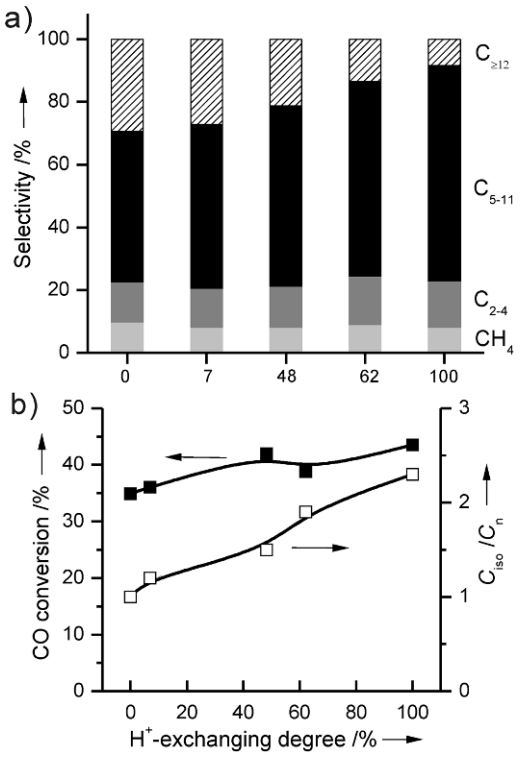

Figure 4-20. Catalytic performances of the Co/meso-ZSM-5-0.5 M catalysts with different H^+-exchange degrees for FT synthesis. a) Product selectivity. b) CO conversion and C_{iso}/C_n.

Figure 4-20 displays the catalytic behaviors of the Co/meso-ZSM-5-0.5 M series of catalysts with the same mesopores size (~6 nm) but different H^+-exchange degrees or acidities. CO conversion changed only slightly over this series of catalysts. It is of interest that the selectivities to CH_4 and C_{2-4} hydrocarbons do not vary significantly for this series of catalysts with different acidities. The increase in the H^+-exchanging degree or the density of Brønsted acid sites increased the C_{5-11} selectivity at the expense of $C_{\geqslant 12}$ selectivity. The ratio of *iso*-paraffins to *n*-paraffins increased from 1.0 to 2.3 with increasing the H^+-exchanging degree from 0 to 100%. In other words, in the presence of mesopores, the increase in the density of Brønsted acid sites enhanced the hydrocracking and isomerization of heavier hydrocarbons selectively into C_{5-11} hydrocarbons without forming additional CH_4 and C_{2-4} alkanes. On the other hand, the increase in the Brønsted acidity for the Co/ZSM-5 series of catalysts without mesopores by increasing the H^+-exchanging degree caused the significant increase in the CH_4 and C_{2-4} selectivities but not the C_{5-11} selectivity (Figure 4-19). These results clearly indicate that the presence of mesoporosity mainly contributes to the high C_{5-11} selectivity of the Co/H-meso-ZSM-5 catalysts.

4.2.9 Catalytic behaviors of *n*-hexadecane hydrocracking

The results described above indicate that the mesoporosity plays a key role in suppressing the formation of lighter hydrocarbons and enhancing the C_{5-11} selectivity. To understand deeply the roles of the acidity and the mesoporosity, we have performed the hydrocracking reactions using *n*-hexadecane as a model molecule of heavier ($C_{\geqslant 12}$) hydrocarbons under the reaction conditions similar to those used for FT synthesis. For both the Co/ZSM-5 and Co/meso-ZSM-5 series of catalysts, the hydrocracking reaction could take place and conversion of *n*-$C_{16}H_{34}$ increased with increasing the H^+-exchanging degree or the density of Brønsted acid sites (Table 4-7). At the same time, the ratio of *iso*-paraffins to *n*-paraffins in C_{5-11} hydrocarbons (C_{iso}/C_n) increased significantly from 0.1 or 0.2 to 0.8 or 1.4. These observations confirm that the Brønsted acid sites play crucial roles in the hydrocracking and isomerization reactions.

It should be noted that the product selectivity also depended on the density of Brønsted acidity. For the catalysts with higher densities of Brønsted acidity (the H^+-exchanging degree $\geqslant$ 33% for Co/ZSM-5 and $\geqslant$ 48% for Co/meso-ZSM-5-0.5 M), the major products were C_{2-11} hydrocarbons, whereas C_{12-15} hydrocarbons and CH_4 were formed with higher selectivities over the catalysts with lower densities of Brønsted acidity. We believe that this is because of the different reaction mechanisms. For the solid acid-supported metal catalysts, it is generally accepted that the hydrocracking reaction follows the bifunctional sequential mechanism [36, 83]. In brief, n-alkane (here *n*-$C_{16}H_{34}$) undergoes dehydrogenation on metal sites over a bifunctional catalyst, and then the olefinic products could be adsorbed on Brønsted acid sites, forming carbocations, which would undergo isomerization and C-C bond scission to provide shorter branched and linear paraffins as the final products [36, 83, 84]. On the other hand, over the supported metal catalysts with less or no acidity, the reaction may follow the metal-catalyzed hydrogenolysis mechanism [36, 85, 86]. The C-C cleavage during the metal-catalyzed hydrogenolysis of paraffins usually occurs at the terminal C-C bond, producing CH_4 and the remaining moiety. This can explain the higher selectivities of CH_4 and C_{12-15} hydrocarbons during the conversion of *n*-$C_{16}H_{34}$ over the catalysts with smaller or no Brønsted acid sites. Nevertheless, the conversions of *n*-$C_{16}H_{34}$ over the catalysts with lower densities of Brønsted acid sites were lower. This indicates that the hydrogenolysis activity is not as high as the hydrocracking activity catalyzed by the bifunctional catalyst. Thus, the effect of the hydrogenolysis on the product selectivity in FT synthesis should not be very significant. Actually, the selectivity of CH_4 over the Co/meso-ZSM-5-0.5 M catalyst with a

H^+-exchange degree of 0 (Co/pure Na^+-form mesoporous zeolite) showed a slightly higher CH_4 selectivity than the corresponding catalyst with a higher H^+-exchange degree (Figure 4-20a).

Figure 4-21 shows the product distributions of *n*-hexadecane hydrocracking for Co/H-ZSM-5, Co-H-meso-ZSM-5-0.5M and Co-H-meso-ZSM-5-1.5M, respectively. It is interesting that the product distributions for three catalysts are different. There are more C_{3-5} hydrocarbons in the cracking product of Co/H-ZSM-5, which may be caused by secondary cracking of long-chain hydrocarbons in the long and narrow micropores [36, 44]. The distribution shifts to middle distillates when mesopores are introduced. High content of *iso*-paraffins was also observed in these acidic catalysts.

Table 4-7. Hydrocracking of n-hexadecane over Co/ZSM-5 and Co/meso-ZSM-5-0.5 M series of catalysts with different H^+-exchanging degrees.[a]

Catalyst[b]	*n*-$C_{16}H_{34}$ conv. [%]	Hydrocarbon selectivity [%]				C_{iso}/C_n
		CH_4	C_{2-4}	C_{5-11}	C_{12-15}	
Co/ZSM-5 (0)	3.6	8.4	19	31	42	0.1
Co/ZSM-5 (10)	17	7.6	20	37	35	0.2
Co/ZSM-5 (33)	33	1.3	37	53	9.0	0.5
Co/ZSM-5 (60)	53	0	42	57	1.6	0.5
Co/ZSM-5 (100)	73	0.5	41	57	2.2	0.8
Co/meso-ZSM-5-0.5 M (0)	7.5	17	2.7	3.6	77	0.2
Co/meso-ZSM-5-0.5 M (6.9)	12	6.6	22	30	42	0.2
Co/meso-ZSM-5-0.5 M (48)	56	2.1	29	50	18	0.9
Co/meso-ZSM-5-0.5 M (62)	66	1.3	29	54	16	1.0
Co/meso-ZSM-5-0.5 M (100)	79	1.1	25	67	7.0	1.4

[a] Reaction conditions: catalyst, 0.50 g; H_2/*n*-$C_{16}H_{34}$ (molar ratio) = 50, $F(H_2)$ = 60 mL min^{-1}; P = 2 MPa; T = 513 K. [b] The number in the parenthesis denotes the H^+-exchanging degree.

A significant point in our work is that, we found that the presence of mesoporosity could alter the product distributions in the hydrocracking of *n*-$C_{16}H_{34}$ over the Brønsted acidity-bearing bifunctional catalysts. As displayed in Table 4-7, for the Co/ZSM-5 series of catalysts, upon increasing the density of Brønsted acid sites, the selectivity to C_2–C_4 hydrocarbons increased to 41-42%. The highest C_{5-11} selectivity for this series of catalyst was

limited to ~57%. On the other hand, for the Co/meso-ZSM-5-0.5 M series of catalysts, with increasing the density of Brønsted acid sites, the C_{2-4} selectivity was not higher than 30%, and thus, the C_{5-11} selectivity could reach ~70%. The hierarchical porous system is proposed to accelerate the mass transportation of the hydrocracking products from the micropores and this can suppress the formation of lighter hydrocarbons, contributing to the enhancement in the selectivity to middle-distillate (C_{5-11}) products. This conclusion is essentially in agreement with that reported by de Jong et al. for the hydrocracking of squalane [44]. However, our present work further extends this idea of selectivity tuning to FT synthesis.

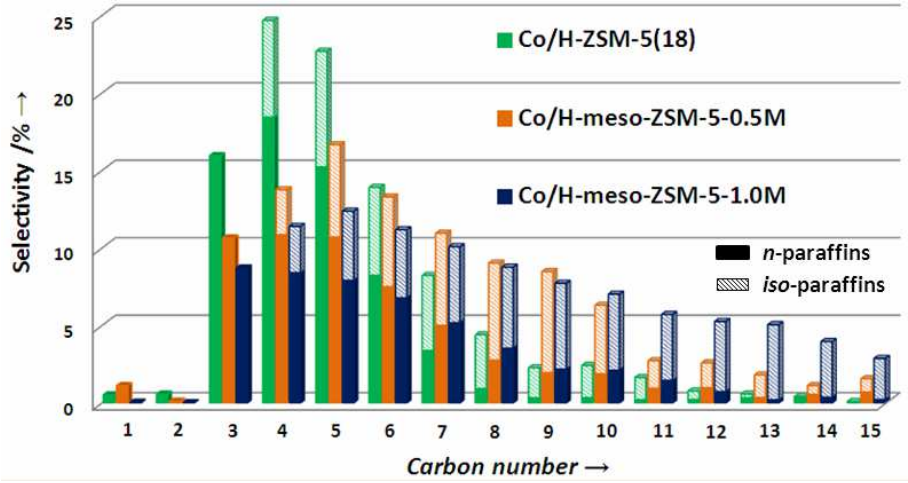

Figure 4-21 Product distribution of *n*-hexadecane hydrocracking for Co/H-meso-ZSM-5-*x*M treated with different concentration of NaOH solution (*n*-$C_{16}H_{36}$ conversion is 73 - 83%).

4.3 Discussion on the roles of acidity and mesoporosity

We found that the use of H-meso-ZSM-5 instead of traditional microporous H-ZSM-5 significantly suppressed the formation of unfavorable C_{1-4} hydrocarbons. Our work has clarified that, while the Brønsted acid sites are responsible for the hydrocracking of primary heavier hydrocarbons, the mesoporous structure of H-meso-ZSM-5 contributes to suppressing the formation of CH_4 and C_{2-4} hydrocarbons, leading to the high C_{5-11} selectivity. Here, we briefly discuss the roles of mesoporosity and acidity in tuning the product selectivity in FT synthesis.

First, our results obtained from the hydrocracking of *n*-$C_{16}H_{34}$ indicate that the diffusion limitation due to the long microporous channel of H-ZSM-5 may cause the repeated hydrocracking, leading to the higher C_{2-4} selectivity over the Co/H-ZSM-5 catalyst. The use of H-meso-ZSM-5-supported Co catalyst significantly decreased the C_{2-4} selectivity and

enhanced the C_{5-11} selectivity in the hydrocracking of *n*-$C_{16}H_{34}$ by accelerating the mass transportation. These results allow us to conclude that the lower C_{2-4} selectivity over the Co/H-meso-ZSM-5 catalyst in the FT synthesis is caused by the suppressed over-cracking of the primary heavier hydrocarbons formed on Co nanoparticles.

Second, it should be noted that the Co/H-ZSM-5 showed much higher CH_4 selectivity than the Co/H-meso-ZSM-5 catalyst. However, almost no CH_4 was produced in the hydrocracking of *n*-hexadecane over both catalysts. Sartipi et al. reported that the hydrocracking of n-hexane did not produce CH_4 over Co catalysts loaded on H-ZSM-5 and mesoporous H-ZSM-5 [49]. Therefore, we propose that CH_4 is mainly formed by the direct hydrogenation of CO or the C1 intermediates over our catalysts. It is known that a higher CH_4 selectivity may be obtained over a catalyst containing small Co particles or Co species with lower reducibility [70, 87]. However, the mean sizes of Co nanoparticles in our catalysts with and without mesopores were similar (7.7-10.5 nm), and the H_2 chemisorption measurements also indicated similar mean sizes of Co nanoparticles in these catalysts. Thus, we speculate that it is not the difference in Co particles but other factors may cause the difference in CH_4 selectivity.

Many studies have demonstrated that the small pores of support may increase CH_4 selectivity and proposed that the higher CH_4 selectivity results from the higher H_2/CO ratio in the vicinity of the active metal due to the diffusion limitation by the small pores, since the transportation of CO is much lower than that of H_2 [7-12, 48-51, 88, 89]. The mesoporous structure of the Co/H-meso-ZSM-5 catalyst could prevent the locally higher H_2/CO ratio on Co surfaces due to the enhanced mass transportation. Moreover, we speculate that the Brønsted acid sites near the Co particles may also play a role in the formation of CH_4, especially for the Co/H-ZSM-5 catalyst with the diffusion limitation, since both the Co/Na-ZSM-5 and the Co/H-meso-ZSM-5 catalysts exhibit lower CH_4 selectivities. Several studies have reported the enhancement of hydrogenation reactions in the presence of strong Brønsted acidity [90, 91]. The Brønsted acid site might promote the hydrogenation of the C1 intermediates into CH_4 by decreasing the energy barriers [91]. Thus, the enhanced mass transportation and the decreased density of Brønsted acid sites for the Co/H-meso-ZSM-5 catalyst may both contribute to the lower CH_4 selectivity. Further experimental and computational studies are still needed to clarify the detailed mechanism for the formation of CH_4 over the zeolite-based catalysts.

4.4 Conclusions

A series of mesoporous ZSM-5 samples with tunable mesopores sizes were successfully synthesized by a simple alkaline desilication method. The size and volume of mesopores increased with increasing the concentration of NaOH used for desilication, while the crystalline structure of ZSM-5 could be sustained under controlled concentrations of NaOH. A part of Al species were removed from the framework to extra-framework positions, and this decreased the Brønsted acidity of the H^+-form samples. The density of Brønsted acid sites could be regulated by changing the H^+-exchanging degree. While the conventional thermal treatment of the $Co(NO_3)_2$/H-ZSM-5 composite in stagnant or flow air caused the formation of inhomogeneous Co particles, the thermal treatment in NO/Ar gas flow resulted in narrow size distribution of Co particles. Using this thermal treatment method, we obtained uniform-sized Co particles over ZSM-5 and mesoporous ZSM-5 samples with different mesopores sizes or acidities.

We demonstrated that the use of mesoporous H-ZSM-5 instead of the conventional microporous H-ZSM-5 significantly increased the selectivity to C_{5-11} hydrocarbons by suppressing the formation of the lighter (CH_4 and C_{2-4}) hydrocarbons. Through systematic studies using catalysts with tuned mesoporosity and Brønsted acidity, we clarified that the presence of mesoporosity mainly contributed to suppressing the formation of lighter hydrocarbons, while the Brønsted acidity was required for the hydrocracking of heavier ($C_{\geqslant 12}$) hydrocarbons. A 70% selectivity to C_{5-11} hydrocarbons with a ratio of *iso*-paraffins to *n*-paraffins being 2.3 could be attained from syngas over the Co/H-meso-ZSM-5-0.5 M catalyst. Using *n*-hexadecane as a model molecule of heavier hydrocarbons, we confirmed the role of Brønsted acidity in the hydrocracking/isomerization reactions and the role of mesoporosity in determining the product selectivity. Our present work points out that the uniform Co nanoparticles with optimized sizes loaded on mesoporous zeolites with strong Brønsted acidity and tuned mesoporosity are promising catalysts for the production of gasoline-range hydrocarbons from syngas.

4.5 Reference

[1] T. Takeshita, K. Yamaji, Energy Policy, 36 (2008) 2773-2784.

[2] R.C. Baliban, J.A. Elia, C.A. Floudas, Energy Environ. Sci., 6 (2013) 267-287.

[3] R.C. Baliban, J.A. Elia, C.A. Floudas, Ind. Eng. Chem. Res., 52 (2013) 3381-3406.

[4] S.Y. Yang, L. Xiao, S.Y. Yang, A. Kraslawski, Y. Man, Y. Qian, Acs Sustainable Chem. Eng., 2 (2014) 80-87.

[5] P.S. Shuttleworth, M. De bruyn, H.L. Parker, A.J. Hunt, V.L. Budarin, A.S. Matharu, J.H. Clark, Green Chem., 16 (2014) 573-584.

[6] R. Luque, A.R. de la Osa, J.M. Campelo, A.A. Romero, J.L. Valverde, P. Sanchez, Energy Environ. Sci., 5 (2012) 5186-5202.

[7] A.Y. Khodakov, W. Chu, P. Fongarland, Chem. Rev., 107 (2007) 1692-1744.

[8] E. de Smit, B.M. Weckhuysen, Chem. Soc. Rev., 37 (2008) 2758-2781.

[9] Q. Zhang, J. Kang, Y. Wang, ChemCatChem, 2 (2010) 1030-1058.

[10] H. Jahangiri, J. Bennett, P. Mahjoubi, K. Wilson, S. Gu, Catal. Sci. Technol., 5 (2014) 2210-2229.

[11] Y. Liu, O. Ersen, C. Meny, F. Luck, C. Pham-Huu, ChemSusChem, 7 (2014) 1218-1239.

[12] J. Kang, W. Deng, Q. Zhang, Y. Wang, J. Energy. Chem., 22 (2013) 321-328.

[13] G.P. Van Der Laan, A.A.C.M. Beenackers, Catal. Rev., 41 (1999) 255-318.

[14] A. de Klerk, Green Chem., 10 (2008) 1249-1279.

[15] A.d. Klerk, Energy Environ. Sci., 4 (2011) 1177-1205.

[16] Q. Zhang, W. Deng, Y. Wang, J. Energy. Chem., 22 (2013) 27-38.

[17] A. Martínez, G. Prieto, Top. Catal., 52 (2009) 75-90.

[18] B. Sun, M. Qiao, K. Fan, J. Ulrich, F.F. Tao, ChemCatChem, 3 (2011) 542-550.

[19] S. Sartipi, M. Makkee, F. Kapteijn, J. Gascon, Catal. Sci. Technol., 4 (2014) 893-907.

[20] Q. Zhang, K. Cheng, J. Kang, W. Deng, Y. Wang, ChemSusChem, 7 (2014) 1251-1264.

[21] J. Kang, S. Zhang, Q. Zhang, Y. Wang, Angew. Chem. Int. Ed., 48 (2009) 2565-2568.

[22] J. He, Z. Liu, Y. Yoneyama, N. Nishiyama, N. Tsubaki, Chem. Eur. J., 12 (2006) 8296-8304.

[23] J. Bao, J. He, Y. Zhang, Y. Yoneyama, N. Tsubaki, Angew. Chem. Int. Ed., 47 (2008) 353-356.

[24] X.G. Li, J.J. He, M. Meng, Y. Yoneyama, N. Tsubaki, J. Catal., 265 (2009) 26-34.

[25] J. Bao, G.H. Yang, C. Okada, Y. Yoneyama, N. Tsubaki, Appl. Catal. A, 394 (2011) 195-200.

[26] G.H. Yang, C. Xing, W. Hirohama, Y.Z. Jin, C.Y. Zeng, Y. Suehiro, T.J. Wang, Y. Yoneyama, N. Tsubaki, Catal. Today, 215 (2013) 29-35.

[27] Q.H. Lin, G.H. Yang, X.N. Li, Y. Yoneyama, H.L. Wan, N. Tsubaki, Chemcatchem, 5 (2013) 3101-3106.

[28] B. Sun, G. Yu, J. Lin, K. Xu, Y. Pei, S. Yan, M. Qiao, K. Fan, X. Zhang, B. Zong, Catal. Sci. Technol., 2 (2012) 1625-1629.

[29] J.-Y. Liu, J.-F. Chen, Y. Zhang, Catal. Sci. Technol., 3 (2013) 2559.

[30] S. Bessell, Appl. Catal. A, 96 (1993) 253-268.

[31] S. Bessell, Appl. Catal. A, 126 (1995) 235-244.

[32] S.-J. Jong, S. Cheng, Appl. Catal. A, 126 (1995) 51-66.

[33] C. Kibby, K. Jothimurugesan, T. Das, H.S. Lacheen, T. Rea, R.J. Saxton, Catal. Today, 215 (2013) 131-141.

[34] B. Li, B. Sun, X. Qian, W. Li, Z. Wu, Z. Sun, M. Qiao, M. Duke, D. Zhao, J. Am. Chem. Soc., 135 (2013) 1181-1184.

[35] J. Sun, X.G. Li, A. Taguchi, T. Abe, W.Q. Niu, P. Lu, Y. Yoneyarna, N. Tsubaki, ACS catal., 4 (2014) 1-8.

[36] J. Weitkamp, ChemCatChem, 4 (2012) 292-306.

[37] A. Baiker, H. Blaser, G. Ertl, H. Knözinger, J. Weitkamp, Handbook of Heterogeneous Catalysis II, 1997.

[38] M. Hartmann, Angew. Chem. Int. Ed., 43 (2004) 5880-5882.

[39] J.C. Groen, J.A. Moulijn, J. Pérez-Ramírez, J. Mater. Chem., 16 (2006) 2121.

[40] J. Perez-Ramirez, C.H. Christensen, K. Egeblad, C.H. Christensen, J.C. Groen, Chem. Soc. Rev., 37 (2008) 2530-2542.

[41] W. Schmidt, ChemCatChem, 1 (2009) 53-67.

[42] R. Chal, C. Gérardin, M. Bulut, S. van Donk, ChemCatChem, 3 (2011) 67-81.

[43] L.-H. Chen, X.-Y. Li, J.C. Rooke, Y.-H. Zhang, X.-Y. Yang, Y. Tang, F.-S. Xiao, B.-L. Su, J. Mater. Chem., 22 (2012) 17381-17403.

[44] K.P. de Jong, J. Zečević, H. Friedrich, P.E. de Jongh, M. Bulut, S. van Donk, R. Kenmogne, A. Finiels, V. Hulea, F. Fajula, Angew. Chem. Int. Ed., 49 (2010) 10074-10078.

[45] J.C. Kang, K. Cheng, L. Zhang, Q.H. Zhang, J.S. Ding, W.Q. Hua, Y.C. Lou, Q.G. Zhai, Y. Wang, Angew. Chem. Int. Ed., 50 (2011) 5200-5203.

[46] K. Cheng, J. Kang, S. Huang, Z. You, Q. Zhang, J. Ding, W. Hua, Y. Lou, W. Deng, Y. Wang, ACS catal., 2 (2012) 441-449.

[47] A. Pereira, J. González-Carballo, F. Pérez-Alonso, S. Rojas, J. Fierro, M.d. Rangel, Top. Catal., 54 (2011) 179-189.

[48] S. Sartipi, M. Alberts, M.J. Meijerink, T.C. Keller, J. Perez-Ramirez, J. Gascon, F. Kapteijn, ChemSusChem, 6 (2013) 1646-1650.

[49] S. Sartipi, K. Parashar, M. Makkee, J. Gascon, F. Kapteijn, Catal. Sci. Technol., 3 (2013) 572-575.

[50] S. Sartipi, K. Parashar, M.J. Valero-Romero, V.P. Santos, B. van der Linden, M. Makkee, F. Kapteijn, J. Gascon, J. Catal., 305 (2013) 179-190.

[51] S. Sartipi, J.E. van Dijk, J. Gascon, F. Kapteijn, Appl. Catal. A, 456 (2013) 11-22.

[52] S. Sartipi, M. Alberts, V.P. Santos, M. Nasalevich, J. Gascon, F. Kapteijn, ChemCatChem, 6 (2014) 142-151.

[53] G. Jacobs, T.K. Das, Y. Zhang, J. Li, G. Racoillet, B.H. Davis, Appl. Catal. A, 233 (2002) 263-281.

[54] Y. Ohtsuka, Y. Takahashi, M. Noguchi, T. Arai, S. Takasaki, N. Tsubouchi, Y. Wang, Catal. Today, 89 (2004) 419-429.

[55] N. Katada, H. Igi, J.-H. Kim, J. Phys. Chem. B, 101 (1997) 5969-5977.

[56] A. Auroux, Top. Catal., 19 (2002) 205-213.

[57] L.-X. Dai, K. Koyama, M. Miyamoto, T. Tatsumi, Appl. Catal. A, 189 (1999) 237-242.

[58] L. Tosheva, V.P. Valtchev, Chem. Mater., 17 (2005) 2494-2513.

[59] R. Pierotti, J. Rouquerol, Pure Appl. Chem., 57 (1985) 603-619.

[60] R.W. Cranston, F.A. Inkley, 17 The Determination of Pore Structures from Nitrogen Adsorption Isotherms, in: F. Adalbert (Ed.) Adv. Catal., Academic Press, 1957, pp. 143-154.

[61] C. Fernandez, I. Stan, J.-P. Gilson, K. Thomas, A. Vicente, A. Bonilla, J. Pérez-Ramírez, Chem. Eur. J., 16 (2010) 6224-6233.

[62] J.C. Groen, J.A. Moulijn, J. Pérez-Ramírez, Microporous Mesoporous Mater., 87 (2005) 153-161.

[63] N. Katada, H. Igi, J.-H. Kim, M. Niwa, J. Phys. Chem. B, 101 (1997) 5969-5977.

[64] A. Corma, A. Martinez, S. Pergher, S. Peratello, C. Perego, G. Bellusi, Appl. Catal. A, 152 (1997) 107-125.

[65] M. Steijns, G. Froment, P. Jacobs, J. Uytterhaeven, J. Weitkamp, Ind. Eng. Chem. Prod. Res. Dev., 20 (1981) 654-660.

[66] L. Su, L. Liu, J. Zhuang, H. Wang, Y. Li, W. Shen, Y. Xu, X. Bao, Catal. Lett., 91 (2003) 155-167.

[67] J.-B. Koo, N. Jiang, S. Saravanamurugan, M. Bejblová, Z. Musilová, J. Čejka, S.-E. Park, J. Catal., 276 (2010) 327-334.

[68] G.L. Woolery, G.H. Kuehl, H.C. Timken, A.W. Chester, J.C. Vartuli, Zeolites, 19 (1997) 288-296.

[69] D.P. Serrano, R.A. García, G. Vicente, M. Linares, D. Procházková, J. Čejka, J. Catal., 279 (2011) 366-380.

[70] G.L. Bezemer, J.H. Bitter, H.P.C.E. Kuipers, H. Oosterbeek, J.E. Holewijn, X. Xu, F. Kapteijn, A.J. van Dillen, K.P. de Jong, J. Am. Chem. Soc., 128 (2006) 3956-3964.

[71] J.R. Sietsma, J.D. Meeldijk, J.P. den Breejen, M. Versluijs-Helder, A.J. van Dillen, P.E. de Jongh, K.P. de Jong, Angew. Chem. Int. Ed., 46 (2007) 4547-4549.

[72] M. Wolters, P. Munnik, J.H. Bitter, P.E. de Jongh, K.P. de Jong, J. Phys. Chem. C, 115 (2011) 3332-3339.

[73] Y. Zhao, J. Li, Y. Zhang, S. Chen, K. Liew, ChemCatChem, 4 (2012) 1926-1929.

[74] N.E. Tsakoumis, M. Rønning, Ø. Borg, E. Rytter, A. Holmen, Catal. Today, 154 (2010) 162-182.

[75] A. Martinez, J. Rollan, M. Arribas, H. Cerqueira, A. Costa, E. Saguiar, J. Catal., 249 (2007) 162-173.

[76] G. Jacobs, P.M. Patterson, Y. Zhang, T. Das, J. Li, B.H. Davis, Appl. Catal. A, 233 (2002) 215-226.

[77] D. Peña, A. Griboval-Constant, F. Diehl, V. Lecocq, A.Y. Khodakov, ChemCatChem, 5 (2013) 728-731.

[78] A. Martínez, J. Rollán, M.A. Arribas, H.S. Cerqueira, A.F. Costa, E.F. S.-Aguiar, J. Catal., 249 (2007) 162-173.

[79] Q. Zhang, Y. Tan, C. Yang, H. Xie, Y. Han, J. Ind. Eng. Chem., 19 (2013) 975-980.

[80] J.M. Ortega, A.G. Gayubo, A.T. Aguayo, P.L. Benito, J. Bilbao, Ind. Eng. Chem. Res., 36 (1997) 60-66.

[81] T. Xu, H. Song, W. Deng, Q. Zhang, Y. Wang, Chin. J. Catal., 34 (2013) 2047-2056.

[82] N.E. Tsakoumis, M. Rønning, Ø. Borg, E. Rytter, A. Holmen, Catal. Today, 154 (2010) 162-182.

[83] J.W. Thybaut, C.S. Laxmi Narasimhan, J.F. Denayer, G.V. Baron, P.A. Jacobs, J.A. Martens, G.B. Marin, Ind. Eng. Chem. Res., 44 (2005) 5159-5169.

[84] F. Regali, M. Boutonnet, S. Järås, Catal. Today, 214 (2013) 12-18.

[85] J.H. Sinfelt, Specificity in Catalytic Hydrogenolysis by Metals, in: H.P. D.D. Eley, B.W. Paul (Eds.) Adv. Catal., Academic Press, 1973, pp. 91-119.

[86] A. Soualah, J.L. Lemberton, L. Pinard, M. Chater, P. Magnoux, K. Moljord, Appl. Catal. A, 336 (2008) 23-28.

[87] A.Y. Khodakov, A. Griboval-Constant, R. Bechara, V.L. Zholobenko, J. Catal., 206 (2002) 230-241.

[88] J.A. Lapszewicz, H.J. Loeh, J.R. Chipperfield, J. Chem. Soc., Chem. Comm., (1993) 913-914.

[89] D. Vervloet, F. Kapteijn, J. Nijenhuis, J.R. van Ommen, Catal. Sci. Technol., 2 (2012) 1221-1233.

[90] Y.W. Chen, H.T. Wang, J.G. Goodwin Jr, J. Catal., 85 (1984) 499-508.

[91] S. Senger, L. Radom, J. Am. Chem. Soc., 122 (2000) 2613-2620.

Chapter 5. Pore Size Effects in High Temperature Fischer-Tropsch Synthesis over Supported Iron Catalysts

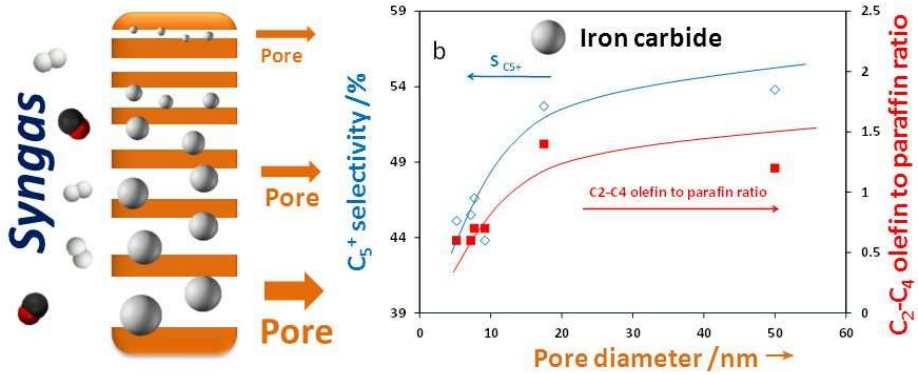

Abstract: This chapter addresses the effect of support pore sizes on the structure and performance of iron catalysts supported by mesoporous silicas in high temperature Fischer-Tropsch synthesis. A combination of characterization techniques showed that the size of supported iron particles was controlled by silica pore sizes. The larger iron particles were localized in large pore supports.

Iron carbidization with carbon monoxide resulted in preferential formation of Hägg iron carbide (χ-Fe_5C_2). The extent of iron carbidization was strongly affected by silica pore diameters. Larger iron oxide crystallites in large pore supports were much easier to carbidize than smaller iron oxide counterparts in small pore supports. Higher Fischer-Tropsch reaction rates, higher olefin and C_5^+ selectivity were observed over iron catalysts supported by large pore catalysts. High dispersion of iron oxide in small pore silicas was not favorable for carbon monoxide hydrogenation because of poor iron carbidization and reducibility. Higher concentration of iron carbide active phase results in better catalytic performance of iron catalysts supported by large pore silicas in Fischer-Tropsch synthesis.

This Chapter is based on the following publication:

K. Cheng, M. Virginie, V. V. Ordomsky, C. Cordier, P. A. Chernavskii, M. I. Ivantsov, S. Paul, Y. Wang and A. Y. Khodakov,* *J. Catal.*, (**2014**) DOI: 10.1016/j.jcat.2014.12.007.

5.1 Introduction

Light olefins are important intermediates in chemical and petrochemical industries for manufacturing polymers, plastics, textiles and solvents [1-3]. In the industry, olefins are currently produced by steam cracking of petroleum fractions or by recovery from fluid catalytic cracking [4]. In these processes, olefins are obtained as by-side products; consequently the selectivity to specific olefins is rather low. Alternatively, light olefins can be obtained using MTO (methanol-to-olefins) or SDTO (syngas via dimethyl ether to olefins) technologies [5-8], which involve conversion of methanol or dimethyl ether into olefins on zeolite catalysts. Methanol and dimethyl ether for these processes are obtained from syngas via the following reactions: $CO + 2H_2 = CH_3OH$ or $2CO + 4H_2 = CH_3\text{-}O\text{-}CH_3+H_2O$. High cost and catalyst deactivation are major drawbacks of MTO or SDTO technologies.

Both cobalt and iron catalysts are used for FT synthesis at industrial scale [9]. Cobalt catalysts usually operate in a narrow temperature range. They are the catalysts of choice for synthesis of middle distillates and long chain hydrocarbons. Iron catalysts are more flexible. They produce paraffins at lower temperature, while olefins and alcohols are major products on iron catalysts at higher temperatures [10]. They have several advantages for olefin synthesis such as higher selectivity, low methanation activity, availability, low price and lower sensitivity to poisons [1]. Iron catalysts could be also efficient for utilization of syngas produced from coal and biomass which have lower hydrogen content ($H_2/CO < 2$). The literature shows a general consensus [1-3] that the activity of iron catalysts in high temperature FT synthesis can be principally attributed to iron carbides. Indeed, under the reaction conditions, iron catalysts undergo “self-organization” [11]; different iron species gradually transform in iron carbides in the presence of carbon monoxide and hydrogen.

Iron can be used for FT synthesis in both bulk and supported catalysts [2]. Bulk iron catalysts however could become mechanically instable under the conditions of catalyst activation [12] or high temperature FT synthesis [2]. The production of fine particles may lead to plugging the reactor equipment and thus could complicate the efficient use of fluidized bed technology for this highly exothermic reaction. Supporting iron species on a porous support leads to better mechanical stability, more efficient use of the active phase, and could result in a higher catalytic activity. The most important role of the support is to maintain highly dispersed iron in carburized state during Fischer-Tropsch synthesis. The supports for iron catalysts are mostly limited to SiO_2, Al_2O_3, TiO_2, carbon materials and mixed SiO_2-Al_2O_3 oxides including zeolites [13]. It is commonly accepted that support chemical composition

may have a strong impact on FT catalytic performance [1]. It could be expected that strong interacting supports could provide better catalysts, because of stabilization of higher iron dispersion. On other hand, strong interaction between iron and support can lead to hardly reducible iron-support mixed compounds (e.g. aluminate or silicate). These mixed iron support compounds are also very difficult to reduce or to carbidize. They do not generate any active sites for high temperature FT synthesis [14-16]. On other hand, weak interacting support (e.g. activated carbon) may exhibit rapid deactivation which can be due to iron sintering, formation of graphitic carbon and other phenomena [17, 18].

In addition to the chemical composition of the support, the support porosity could also affect the catalytic performance of supported iron species. Unfortunately, very few information is available in the literature about the effect of support texture on the structure of supported iron catalysts. Previously, the effect of catalyst pore size on FT synthesis was principally assessed for bulk iron catalysts. Anderson [19] and coworkers in 1950s attributed the influence of pore size on the catalytic activity of fused iron catalysts to mass transport phenomena. More recently, the effect of intra-particle pore-diffusion limitations on the productivity of fused iron catalysts was evaluated by Post [20] and Bukur [21, 22] in a more quantitative manner. Davis [23] and Coville [24] identified and characterized the role of catalyst porosity on mass transfer in FT synthesis over promoted bulk iron catalysts prepared by precipitation. Note that relatively large grains of bulk iron catalysts were used in those works.

MCM-41 and SBA-15 discovered in 1990s are periodic mesoporous silicas with narrow pore size distribution and tunable pore sizes in the range from 2 nm to 30 nm [25-28]. Because of relatively narrow pore size distributions, mesoporous silicas are considered as model supports, which allow evaluation of the effect of pore sizes on the catalytic behavior of supported catalysts. Previously, both mesoporous and commercial silicas were used for evaluation of pore size effects on the structure and catalytic performance of cobalt FT catalysts [29-34]. Important information about influence of support texture on the structure of cobalt species in mesoporous silicas was obtained. Cobalt dispersion, cobalt reducibility in mesoporous silicas and catalytic performance were efficiently controlled by the support pore sizes.

In contrast to the supported cobalt catalysts, very few reports have addressed so far iron FT catalysts supported by silica mesoporous materials. Cano [35] and coworkers studied two silica supported iron catalysts, the first catalyst was supported by SBA-15, the second one was supported by MCM-41. The higher activity of the SBA-15 catalyst with larger iron particles

was attributed to “structural sensitivity” of FT synthesis at nanoscale range. Kim [36] and coworkers observed that catalytic performance of iron catalysts supported by SBA-15 in low temperature FT synthesis depended on the quantity of aluminum present in silica. They suggested that the presence of aluminum might facilitate iron carbide formation.

The present work focuses on influence of support texture on the structure and catalytic performance of iron catalysts for high temperature FT synthesis. The catalysts supported by periodic mesoporous and commercial silica with a broad range of pore diameters from 2 to 50 nm were characterized in this work at different stages of their preparation, activation and reaction using a wide range of techniques: BET, XRD, H_2-TPR, in-situ magnetic measurements, transmission Mössbauer spectroscopy. The catalytic performance of supported iron catalysts was evaluated in fixed bed micro-reactors including a Flowrence high-throughput unit (Avantium®) under typical conditions of high temperature FT synthesis.

5.2 Results and discussion

5.2.1 Support Porosity

Figures 5-1 and 5-2 show the nitrogen adsorption-desorption isotherms and corresponding pore-diameter distributions calculated using BJH method for the mesoporous silicas. The BET surface area, total pore volume and average pore diameter are given in Table 5-1.

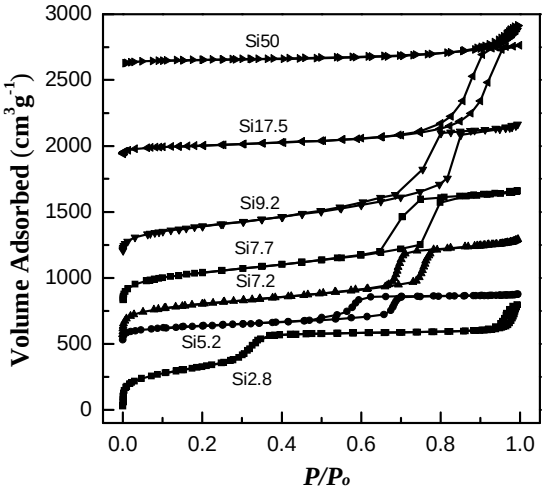

Figure 5-1. Isotherms of nitrogen adsorption-desorption on mesoporous silicas

The Si2.8 sample exhibit an IV-type isotherm according to Brunauer and coworkers [37] without hysteresis and with a sudden increase in adsorption at $P/P_0 = 0.3$. This isotherm corresponds to the filling with nitrogen of narrow mesopores. The Si2.8 silica has a very large

surface area (>1000 m^2 g^{-1}) and relatively narrow mesopores (2.8 nm calculated using the BJH method). The observed isotherms and adsorption properties of the Si2.8 silica are consistent with previous results for MCM-41-type materials [25, 36].

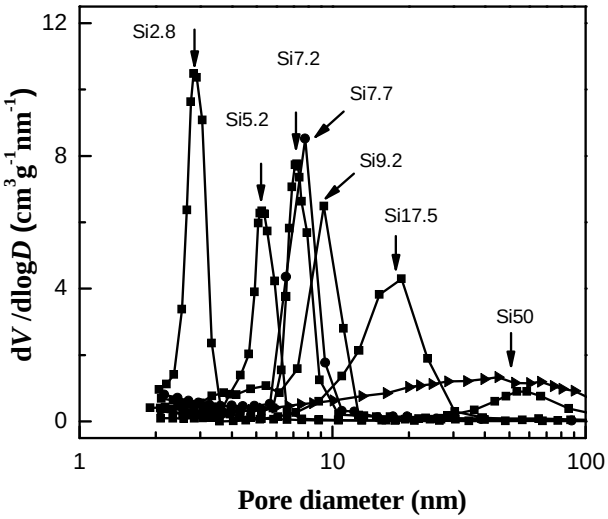

Figure 5-2. BJH pore size distribution curves calculated from nitrogen desorption isotherms for mesoporous silicas

As expected for SBA-15, nitrogen adsorption isotherms of the Si5.2, Si7.2, Si7.7 and Si9.2 silicas are of IV type with H1 type reversible hysteresis [38, 39]. The H1 type hysteresis is usually attributed to filling and emptying of cylinder pores of rather constant cross section [40]. The BET surface of SBA-15 is slightly lower than for MCM-41 and varies between 550 and 1000 m^2 g^{-1}. Very small micropore volume was calculated in these materials using the t-plot method. This suggests that the silicas contain principally mesopores (Table 5-1). The inflection point in desorption curve is related to a diameter in the mesopores range. The BJH pore size distribution curves suggest variation of pore sizes from 2.8 nm to 50 nm as a function of silica synthesis conditions. The BJH curves (Figure 5-2) show very narrow pore size distributions characteristic of SBA-15 materials. They also indicate that the pore size in SBA-15 can be efficiently controlled by the synthesis procedure in the range from 5.2 to 9.2 nm (Table 5-1).

Commercial silicas had much lower surface areas (180-300 m^2 g^{-1}) than MCM-41 and SBA-15 materials. The average pore size was however, much larger: 17.5 and 50 nm for Si17.5 (CARIACT Q-10) and Si50 (Aerosil 200) respectively. Note that the commercial silicas had much broader pore size distribution curves compared to the MCM-41 and SBA-15

periodic mesoporous silicas.

Table 5-1. Adsorption properties of mesoporous silica supports

Sample	S_{BET} [a] [$m^2 g^{-1}$]	S_{micro} [b] [$m^2 g^{-1}$]	S_{exter} [c] [$m^2 g^{-1}$]	V_{total} [d] [$cm^3 g^{-1}$]	V_{micro} [e] [$cm^3 g^{-1}$]	D_{meso} [f] [nm]
Si2.8	1198.0	314.3	883.7	1.23	0	2.8
Si5.2	549.4	181.2	368.2	0.71	0.03	5.2
Si7.2	651.8	177.5	474.3	0.96	0.02	7.2
Si7.7	1045.5	162.9	882.6	1.39	0.06	7.7
Si9.2	884.9	4.9	880．0	1.53	0	9.2
Si17.5	307.1	24.8	282.3	1.31	0.01	17.5
Si50	188.8	39.5	149.3	0.49	0	50

[a] BET surface area.

[b] Micropore area evaluated by the t-plot method.

[c] External Surface area calculated by SBET - Smicro.

[d] Adsorption branch of N_2 at the $P/P_0 = 0.99$ signal point..

[e] Pore volume for micropores evaluated by the t-plot method.

[f] Most probable pore size from the curve of BJH curves.

5.2.2 Iron species in mesoporous silicas

The XRD patterns of calcined iron catalysts supported on different mesoporous silicas are shown in Figure 5-3a. The broad peak observed at $2\theta = 20 - 25°$ corresponds to amorphous silica. All the studied calcined catalysts exhibit the presence of α-Fe_2O_3 (hematite). The magnetic measurements did not detect any magnetization of the calcined samples. The width of the Fe_2O_3 XRD peaks is strongly affected by the pore sizes of silica. The XRD patterns were very broad for the 10FeSi2.8 small pore catalyst. This indicates relatively small size of iron oxide crystallites. An increase in pore sizes silicas results in narrowing XRD peaks and respectively in larger sizes of Fe_2O_3 crystallites. The sizes of Fe_2O_3 crystallites calculated using Scherer equation are displayed in Table 5-2. Figure 5-4 clearly shows a correlation between the pore diameter and Fe_2O_3 crystallites size. The Fe_2O_3 crystallite size increases with an increase in silica pore diameter and larger Fe_2O_3 crystallites are located in larger pore materials. A correlation between ion particle size and pore diameter suggests that the oxide crystallites might be mostly localized in silica pores. Some deviations between the

sizes of iron oxide and catalyst pore diameters can be due to both the non-spherical morphology of iron oxide crystallites and limitations of the XRD. The similar phenomenon was previously observed [29, 33] for silica supported cobalt catalysts prepared using impregnation from the nitrate solutions. Small deviations between the sizes of iron oxide and catalyst pore diameters can be due to both the non-spherical morphology of iron oxide crystallites and limitations of the XRD. The Scherrer equation may overestimate [41] the crystallite size, very small cobalt particles could be missed by XRD because of significant XRD line broadening, while the crystallites may adopt elongated shape inside the silica pores [33].

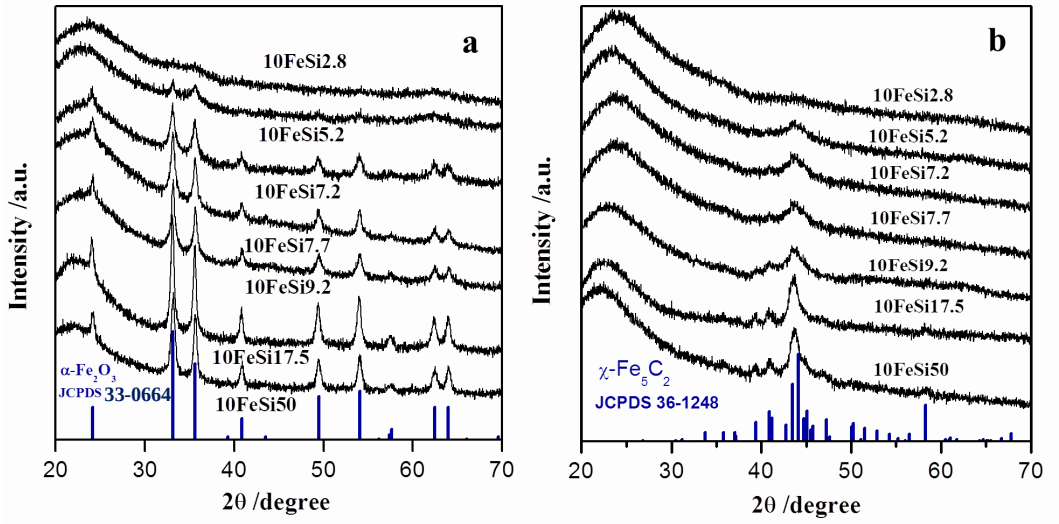

Figure 5-3. XRD patterns of iron catalysts after calcination in air (a) and activation in carbon monoxide (b)

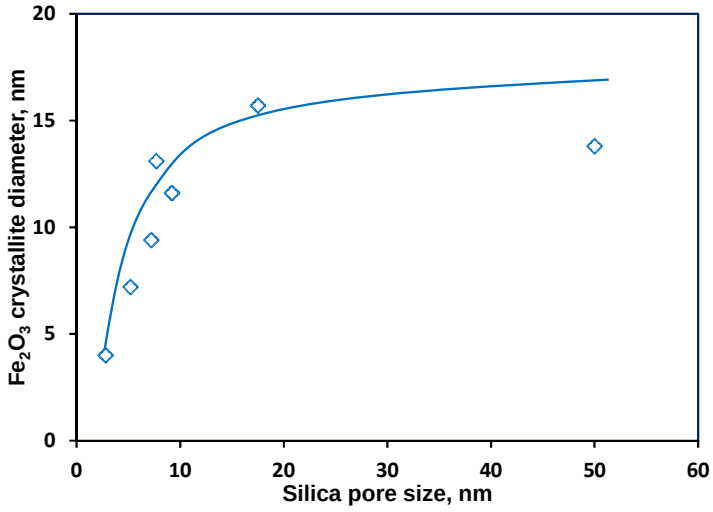

Figure 5-4. Fe_2O_3 crystallite size versus pore diameters in silica supports

Table 5-2. Properties of iron catalysts supported on mesoporous silicas

Sample	Pore size /nm	Fe_2O_3 size from XRD /nm	Iron carbide size after reaction from TEM /nm
10FeSi2.8	2.8	Very small	4.5
10FeSi5.2	5.2	7.2	10.5
10FeSi7.2	7.2	9.4	13.1
10FeSi7.7	7.7	13.1	15.7
10FeSi9.2	9.2	11.6	14.3
10FeSi17.5	17.5	15.7	17.8
10FeSi50	50	13.8	21.9

Figure 5-5 shows H_2-TPR profiles measured on silica supported iron catalysts. The TPR profiles exhibit several hydrogen consumption peaks. For iron catalysts, these TPR peaks can be attributed either to the reduction of different iron species or for the same iron species, these peaks can correspond to different reduction steps: $Fe_2O_3 \rightarrow Fe_3O_4 \rightarrow FeO \rightarrow Fe$.

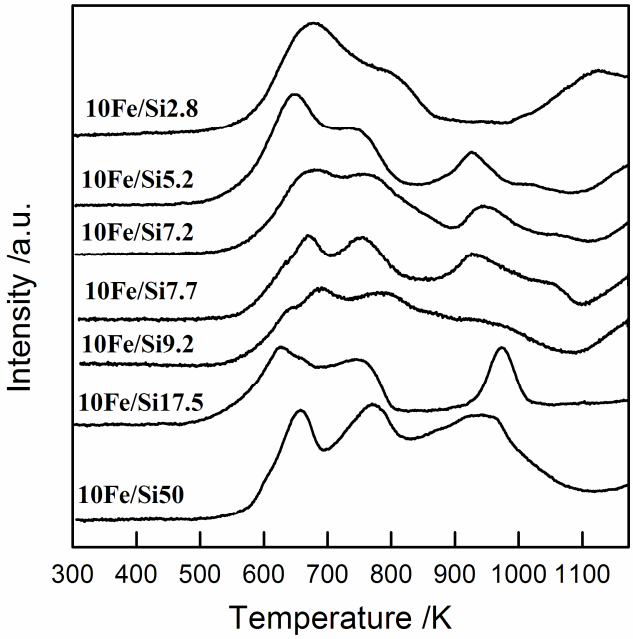

Figure 5-5. H_2-TPR curves of iron catalysts supported on mesoporous silicas

In agreement with previous reports [14, 15], the low temperature peaks at 623 – 653 K was attributed to the reduction of hematite (Fe_2O_3) to magnetite (Fe_3O_4). The formation of metallic iron phase probably corresponds to the TPR peak at 973 K. It was shown earlier [14,

42] that the reduction of magnetite to iron metallic phase via formation of wustite (FeO) occurs at temperature higher than 843 K. In agreement with report [43], a very broad unresolved TPR peak situated at 1173 K could be attributed to the reduction of hardly reducible iron silicate which can form via reaction of small iron oxide particles with silica. Interestingly, the peak area of this high temperature TPR peak and correspondingly the concentration of iron silicate species depend on silica pore size. The fraction of iron silicate is much higher in 10FeSi2.8 with narrow pores than in the large pore catalysts. This can be due to a stronger interaction of smaller iron oxide particles with silica which can facilitate formation of iron silicate [16]. This suggestion is consistent with previous reports about the effect of the metal oxide crystallite sizes on metal silicate formation in other silica supported catalysts. A higher fraction of metal silicate species is usually detected in the silica catalysts containing smaller metal oxide particles. Larger pore catalysts show a less intense peak at 1173 K and a much lower concentration of iron silicate. A very high intensity of the peak at 973 K is also observed in the iron catalysts supported by larger pore silicas which may correspond to the formation of metallic iron. The fraction of metallic ion seems to be lower in smaller pore silicas compared to the large pore catalysts.

Iron catalysts for FT synthesis can be activated either in hydrogen, syngas or carbon monoxide. Our experiments performed with 20FeSi17.5 showed a beneficial effect of activation in carbon monoxide on the catalytic performance compared to the activation in hydrogen; the results are discussed in a greater detail in section 4.5.3. That was the reason why all silica supported catalysts in this paper were activated in carbon monoxide prior to the catalytic tests. The catalysts after activation in pure carbon monoxide were characterized by both in-situ and ex-situ techniques; for ex-situ characterization the catalysts were passivated in 1% O_2 in N_2.

The ex-situ XRD patterns obtained with iron catalysts activated in pure carbon monoxide at 523 K for 10 h are shown in Figures 5-3b and 5-6. The patterns exhibit several peaks at 2θ = 40-50° which correspond to iron carbide species. The intensities of these peaks were more significant on the large pore catalysts, which indicates higher fraction of iron carbides. These peaks were very broad especially in smaller pore silicas. The significant width of these peaks is indicative of smaller sizes of iron carbide crystallites in these supports. This is consistent with XRD data for the calcined catalysts. It can be therefore suggested that carbidization of small iron oxide particles leads to smaller iron carbide crystallites. Thus, iron dispersion in silica supported catalysts is principally affected by silica pore sizes.

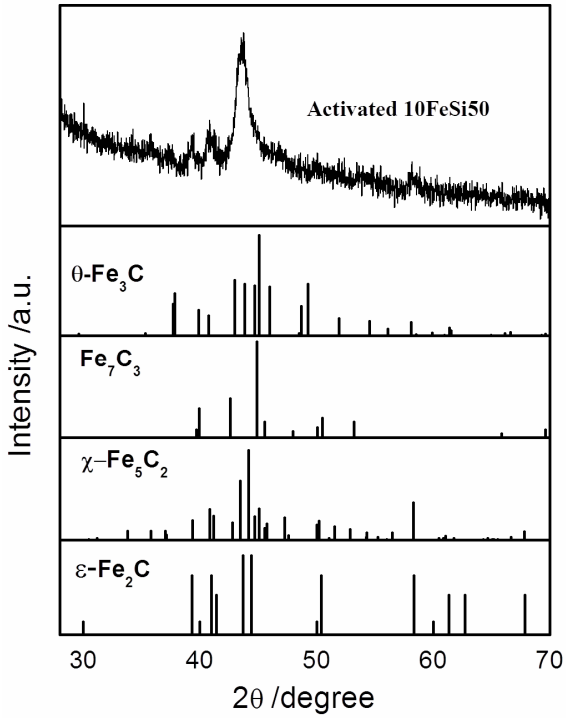

Figure 5-6. XRD patterns of iron carbides in the activated large pore 10FeSi50 catalyst

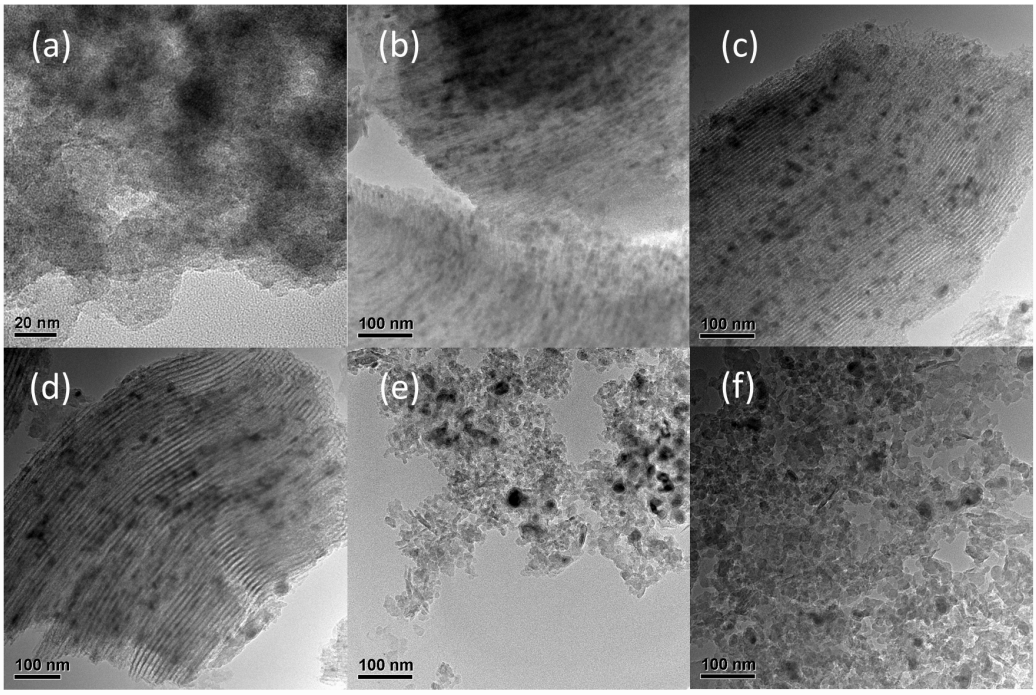

Figure 5-7. TEM images of spent iron catalysts supported on different silicas: 10FeSi2.8 (a), 10FeSi5.2 (b), 10FeSi7.2 (c), 10FeSi9.2 (d), 10FeSi17.5 (e) and 10FeSi50.

The TEM images of carbidized catalysts after catalyst activation and FT catalytic tests are displayed in Figure 5-7. The TEM images confirm the effect of pore size on the

dispersion of iron carbide in spent silica supported catalysts. More dispersed iron carbide species were observed in smaller pore supports. The mean size of iron carbide particles was calculated from TEM data by counting more than 100 particles with a standard deviation. The size of iron carbide particles in the spent catalysts steadily increases from 4.5 nm in 10FeSi2.8 silica to 21.9 nm in 10FeSi50 (Table 5-2) which is in line with the increase in silica pore diameter. Iron particles seem to be protected from sintering during catalyst pretreatments such as carbidization. Moreover, even catalyst exposure to FT reaction conditions did not result in major alternations of iron dispersion. In addition, the porous structure of SBA-15 materials can be clearly seen in the TEM images of the spent catalysts (Figure 5-7). This suggests relative stability of SBA-15 porous matrix in the presence of high temperature and high pressure of syngas and FT reaction products.

5.2.3 Magnetic characterization of iron carbides

The identification of iron carbide phases however could only be performed for larger pore catalysts which exhibit relatively distinct XRD peaks of iron carbide phases (Figure 5-6). A comparison of the XRD peaks of the activated catalyst with iron carbide reference compounds indicates the presence of either χ-Fe_5C_2 or ε-Fe_2C in the activated catalysts (Figure 5-3b). Note that XRD characterization nearly excludes the presence of θ-Fe_3C or Fe_7C_3. Due to a significant broadening of carbide XRD peaks, the unambiguous identification of specific χ-Fe_5C_2 or ε-Fe_2C carbide phases seems rather challenging in smaller pore silicas.

Table 5-3. Magnetic properties of iron catalysts supported on mesoporous silicas

Catalysts	X_{CO} /%	Iron time Yield / 10^{-3} s^{-1}	Magnetization Intensity after activation (emu/g)[a]	Iron carbide size after reaction from TEM /nm
10FeSi2.8	0	0	0.5	4.5
10FeSi9.2	15.4	5.8	5.0	14.3
10FeSi17.5	28.5	10.7	9.3	17.8

[a] The value obtained after the activated samples cooling to 318 K under Ar.

More detailed information about type and concentration of iron carbides in activated silica supported iron catalysts were obtained from in situ magnetic measurements performed under the flow of carbon monoxide. Three catalysts 10FeSi2.8, 10FeSi9.2 and 10FeSi17.5 with gradient catalytic activity (Table 5-3) were tested to obtain the correlation between iron

carbides and catalytic performance in FT synthesis. There was no magnetization observed for 10FeSi2.8 catalyst during CO activation which also shown no catalytic activity in FT synthesis. Figure 5-8 shows variation of magnetization with temperature during catalyst activation in CO for the 10FeSi9.2 and 10FeSi17.5 catalysts. The treatment of supported iron catalysts in carbon monoxide results in an increase in magnetization starting from 473 K. The increase in magnetization also coincides with production of CO_2 which can be probably due to the reduction of iron oxides [44], iron carbidization and carbon monoxide disproportionation:

$3Fe_2O_3 + CO \rightarrow 2Fe_3O_4 + CO_2$,

$5Fe_3O_4 + 32CO \rightarrow 3Fe_5C_2 + 26CO_2$,

$2CO \rightarrow CO_2 + C$.

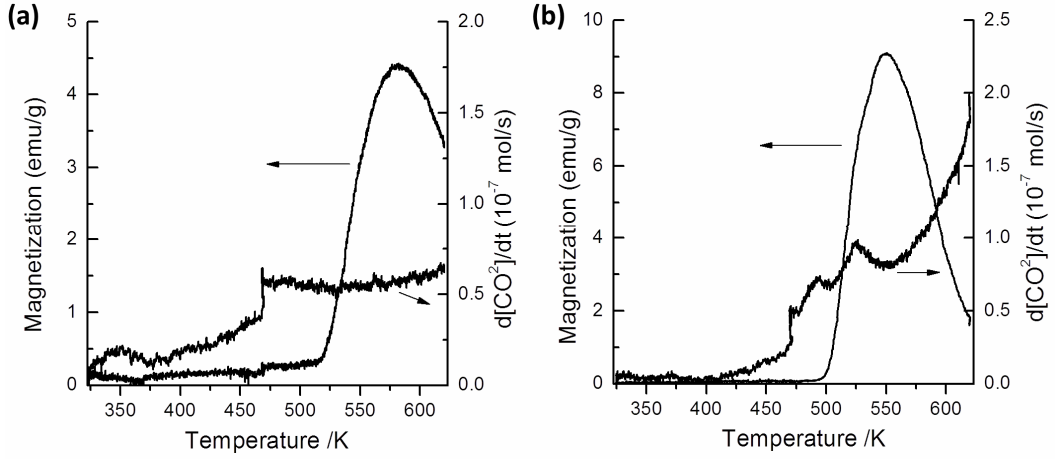

Figure 5-8. Variation of catalyst magnetization and CO_2 formation rate with temperature during the activation in presence of CO over 10FeSi9.2 (a) and 10FeSi17.5 (b).

The magnetization of 10FeSi17.5 decreases however as the temperature reaching 553 K (581 K for 10FeSi9.2 catalyst). The decrease in magnetization at higher temperatures could be due to the disordering of magnetic domains after reaching the Curie temperature for the ferromagnetic phases present in the catalyst. Compared with 10FeSi9.2, the 10FeSi17.5 catalyst displayed higher CO_2 generation rate and intensity of magnetization. The inflection point of magnetization curve of 10FeSi17.5 was also lower than that of 10FeSi9.2 (500 K VS 520 K), which means 10FeSi17.5 catalyst is easier to carbidize. Several iron ferromagnetic compounds may exist in the catalysts: iron carbides, metallic iron and magnetite (Fe_3O_4). The Curie temperature for these compounds is given in Table 5-4. Note that a decrease in

magnetization to zero at temperatures higher than 553 K (581 K for 10FeSi9.2 catalyst) rules out the presence of any noticeable concentrations of metallic iron, magnetite or hexagonal ε-Fe_2C carbide. All these compounds have relatively high Curie temperature. 10FeSi2.8 did not exhibit any measureable magnetization after activation in CO. This suggests very low concentration of all ferromagnetic iron phases in this sample.

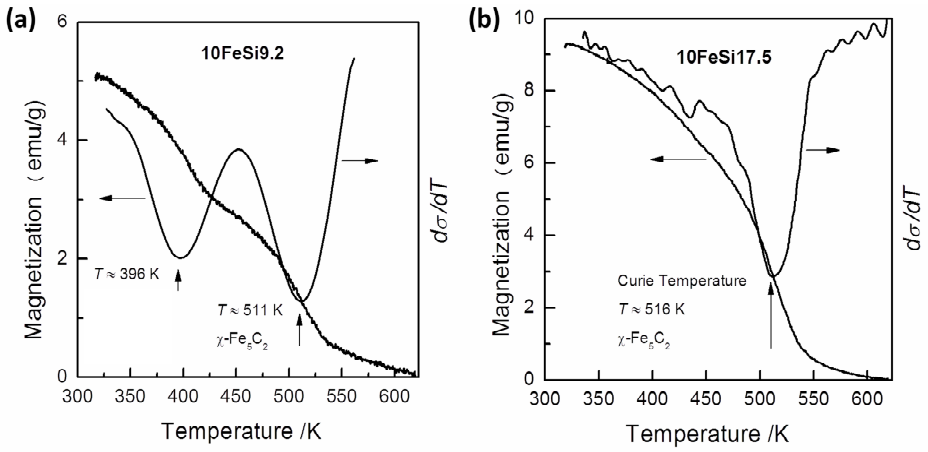

Figure 5-9. Temperature dependence of magnetization (σ) in 10FeSi9.2 (a) and 10FeSi17.5 (b) during cooling. The catalysts which were pretreated with carbon monoxide p=1 atm at 350°C for 2 h.

For a more accurate identification of iron ferromagnetic species using their Curie temperature, the temperature after the catalyst carbidization was decreased with continuous in-situ measurement of the magnetization. The results are shown in Figure 5-9. The Curie temperature was evaluated from the first derivative of the variation of magnetization with temperature. Both 10FeSi9.2 and 10FeSi17.5 catalyst exhibited the presence of Hägg χ-Fe_5C_2 iron carbide, which had the Curie temperature at 511 -516 K. Besides of χ-Fe_5C_2, an additional ferromagnetic phase with the Curie temperature at 396 K was detected in 10FeSi9.2 sample. This phase cannot be attributed to any of iron carbides; indeed, all known iron carbides do not have Curie temperature in this range (Table 2-1). In the present work, this phase was tentatively attributed to non-stoichiometric carbon species containing small amounts of iron atoms. More accurate identification of this phase requires however further investigations.

In addition to the identification of iron ferromagnetic phases, the magnetic method provided important information about concentration of these phases in the activated catalysts. Since iron carbides are the only ferromagnetic phases in the activated silica supported

catalysts, the saturation magnetization can be related to their concentration. Thus, the extent of carbidization can be estimated from the magnetic data. The results shown in Table 5-3 are indicative of higher magnetization of silica supported iron catalysts with larger pores. These catalysts had the same iron content. Higher magnetization observed in larger pore silicas suggests therefore a higher extent of iron carbidization. It appears that carbidization depends on the silica pore sizes. The larger iron oxide particles could be converted into iron carbides easier than smaller counterparts.

Table 5-4. Mössbauer spectra parameters of the spent silica catalysts

Sample	Iron sites	HF /T	IS /mm s^{-1}	QS /mm s^{-1}	Relative area /%	Phase quantification /%
10FeSi9.2	Fe_3C (I)	21.40	0.1618	-0.1182	8.5	Fe_3C: 14.1±2%
	Fe_3C (II)	-	0.2485	0	5.6	χ-Fe_5C_2: 35.9±2%
	χ-Fe_5C_2 (I)	18.16	0.1713	-0.0489	14.7	ε-$Fe_{2.2}C$:10.6±2%
	χ-Fe_5C_2 (II)	21.50	0.2880	0.0552	21.2	Oxides: 39.4±2% (17.9% Fe^{3+} +12.1% Fe_xO_y + 9.4%Fe_3O_4)
	ε-$Fe_{2.2}C$	18.07	0.3037	0.0552	10.6	
	Fe^{3+}	-	0.2919	0.8750	17.9	
	Fe_xO_y	15.46	0.2485	0.0552	12.1	
	Fe_3O_4	48.52	0.5586	0.0708	9.4	
10FeSi17.5	Fe_3C (I)	20.82	0.245	0.020	10.6	Fe_3C: 11.7±2%
	Fe_3C (II)	-	0.359	0	1.1	χ-Fe_5C_2: 58.4±2%
	χ-Fe_5C_2 (I)	18.66	0.207	-0.006	25.7	ε-$Fe_{2.2}C$: 12.7±2%
	χ-Fe_5C_2 (II)	22.09	0.266	0.014	32.7	Oxides: 17.2±2% (11.3% Fe_xO_y + 5.9% Fe_3O_4)
	ε-$Fe_{2.2}C$	17.28	0.150	0.020	12.7	
	Fe_xO_y	13.55	0.367	-0.071	11.3	
	Fe_3O_4	48.23	0.275	-0.449	5.9	

The in situ magnetization data showing influence of silica pore size on iron magnetization are also consistent with the results of Mössbauer spectroscopy. Figure 5-10 displays transmission Mössbauer spectra measured for the 10FeSi9.2 and 10FeSi17.5 catalysts after carbidization. The results of quantitative Mössbauer spectra decomposition are given in Table 5-4. The shape of Mössbauer spectra is rather different for these two samples. For the small pore sample, the Mössbauer spectrum is constituted by contributions mostly

from iron oxides with a smaller fraction of iron carbides, while for larger pore catalysts, the Mössbauer spectroscopy is indicative of higher fraction of carbide species. Interestingly for both catalysts, Mössbauer spectroscopy suggests that χ-Fe_5C_2 is the dominant iron carbide phase among all iron carbides present in the catalyst. The contribution of other iron carbide phases to the Mössbauer spectrum is relatively low. The uncovered preferential formation of Hägg iron carbides during carbidization of supported iron FT catalysts is also consistent with the results of XRD characterization and in particular with the in situ magnetic measurements. This finding is also in agreement with previous reports [3, 12, 14, 22].

Thus, the characterization results suggest that in calcined silica supported iron catalysts, the size of iron oxide crystallites is principally controlled by silica pore sizes; larger crystallites are detected in larger pore catalysts. In addition, smaller pore supports may contain barely reducible iron oxide-silica support mixed compounds (e.g. iron silicate), which were detected in these catalysts by a high temperature peak in H_2-TPR profiles. The pretreatment of silica supported iron catalysts with pure carbon monoxide leads to formation of mostly χ-Fe_5C_2 iron carbide. Similar to iron oxide species, higher iron carbide dispersion is observed in smaller pore silicas. The extent of iron carbidization also depends on silica pore size. Large iron particles can be carbidized to Hägg iron carbide much more easily than smaller iron oxide crystallites in smaller pore supports.

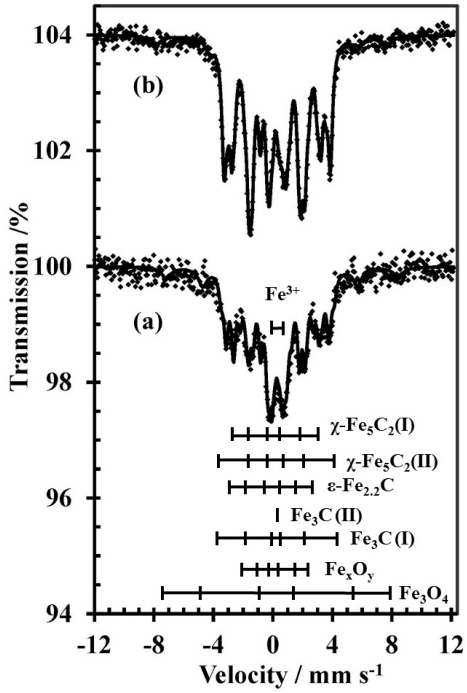

Figure 5-10. Mössbauer spectra of the spent silica supported iron catalysts: (a) 10FeSi9.2 and 10FeSi17.5.

5.2.4 FT performance of iron catalysts supported by mesoporous silicas

Activation procedure is an important step in the design of iron FT catalysts. The activation atmosphere strongly affects both the activity and selectivity of iron FT catalysts. Previous works [22, 44-49] have mostly focuses on the activation of bulk iron catalysts, while much fewer information is available for the supported counterparts. Analysis of the literature data also suggests that the optimized activation procedure could be dependent on catalyst structure and should be optimized for a given catalyst. In order to evaluate the influence of catalyst activation procedure on the catalytic performance of silica supported catalysts, two activation procedures were tested and compared in this work. The first activation procedure involves catalyst activation in hydrogen, while the second one includes catalyst activation in pure carbon monoxide. The catalytic performance results obtained after these two activation procedures are shown in Figure 5-11 and Table 5-5.

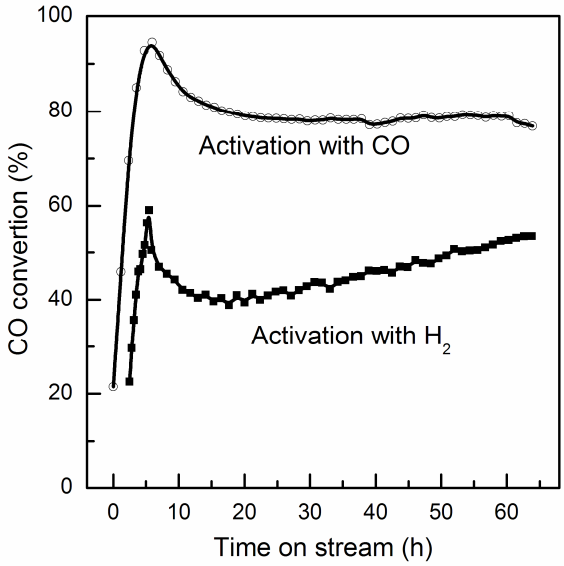

Figure 5-11. Carbon monoxide conversion versus time on-stream for 20FeSi50 catalyst activated in hydrogen and in carbon monoxide

After catalyst activation in carbon monoxide followed by exposure to syngas, a short transient period of about 5 h was observed. Then a relatively high carbon monoxide conversion of 80% was observed and this conversion was stable with time on stream for at least 60 h (GHSV= 3.600 NL g^{-1} h^{-1}). In contrast to activation in carbon monoxide, a much lower carbon monoxide conversion was observed under the same conditions on the catalyst activated in hydrogen (Figure 5-11). Interestingly, for the hydrogen-activated sample, the carbon monoxide conversion gradually increased with time on steam. The observed increase

in the reaction rate can be due to the modification of the catalyst structure which can be assigned to gradual carbidization of iron species. This interpretation is consistent with previous reports by Niemantsverdriet [50, 51] who attributed the low initial activity of iron catalysts activated in hydrogen to a competition between bulk carbidization and hydrocarbon synthesis or a slow activation of the catalyst surface.

Table 5-5. Effect of activation in H_2 and CO on the catalytic performance of 20FeSi50

Activation gas	X_{CO} (%)	CO_2 selec.(%)	CH selectivity (%C mol)				olefin/parafin in C_2-C_4
			CH_4	$C_2^=$-$C_4^=$	C_2-C_4	C_5^+	
CO	76.9	32.1	24.9	25.8	44.0	26.5	1.4
H_2	51.6	29.9	34.8	20.1	42.2	23.0	1.0

Reaction conditions: tubular flow fixed-bed reactor (d_{in} = 8 mm); catalyst, 1.0 g; SiC, 5.0 g, H_2/CO = 2.1; GHSV=3.6 NL $g^{-1}h^{-1}$; *T* = 573 K; *P* = 20 bar; time on stream, 60 h.

Note that catalyst activation of iron catalysts in carbon monoxide seems to lead to a higher FT reaction rate. The FT reaction rates expressed as FTY and selectivity measured after 60 h on stream on the 20FeSi17.5 catalyst activated in pure carbon monoxide and hydrogen are shown in Table 5-6. Though the selectivity for these two experiments can be compared only qualitatively, one can notice slightly higher olefins to paraffins ratio observed after activation in carbon monoxide relative to the activation in hydrogen. Thus, activation in carbon monoxide produces more active silica supported iron catalysts for carbon monoxide hydrogenation than catalyst activation in hydrogen with a possible small effect on the hydrocarbon selectivities.

Catalyst activation in CO was chosen therefore in this work for FT catalytic tests of silica supported iron catalysts using a high throughput Flowrence unit. The results of catalytic tests conducted at GHSV=16.2 NL g^{-1} h^{-1} at 573 K and H_2/CO = 2.1 and total pressure of 20 bar are shown in Table 5-6 and in Figure 5-12. Depending on the catalyst, carbon monoxide conversion varied from 0 to 35%. Figure 5-12 displays a plot of reaction rate expressed as iron time yield (FTY) versus pore size in mesoporous silicas. The FTY reaction rates are strongly affected by the pore size in mesoporous silicas. Very low catalytic performance was observed for the 10FeSi2.8 small pore supported catalyst. Then, the catalytic activity increases as a function of catalyst pore diameter. The general trend is that much higher catalytic activity was observed on larger pores supports.

Table 5-6. Catalytic performance of iron catalysts supported on silicas with different pore sizes.[a]

Catalysts	X_{CO} /%	Iron time Yield /10^{-3} s^{-1}	CO_2 selec. /%	CH selectivity (%C mol)				olef/para in C_2-C_4
				CH_4	$C_2^{=}$-$C_4^{=}$	C_2-C_4	C_5^{+}	
10FeSi2.8	0	0	-	-	-	-	-	-
10FeSi5.2	19.4	6.5	8.5	18.3	13.1	33.9	45.1	0.6
10FeSi7.2	23.2	8.7	9.1	18.0	12.9	33.6	45.5	0.6
10FeSi7.7	25.7	9.6	10.2	18.8	12.9	31.6	46.6	0.7
10FeSi9.2	15.4	5.2	7.4	21.1	13.8	32.4	43.8	0.74
10FeSi17.5	28.5	9.6	11.9	15.3	17.0	29.3	52.7	1.39
10FeSi50	33.8	11.4	13.9	15.5	15.6	28.7	53.8	1.2

[a] Flowrence high throughput unit, H_2/CO = 2.1; GHSV = 16.2 NL $g^{-1}h^{-1}$, T = 573 K, P = 20 bar; time on stream, 60 h.

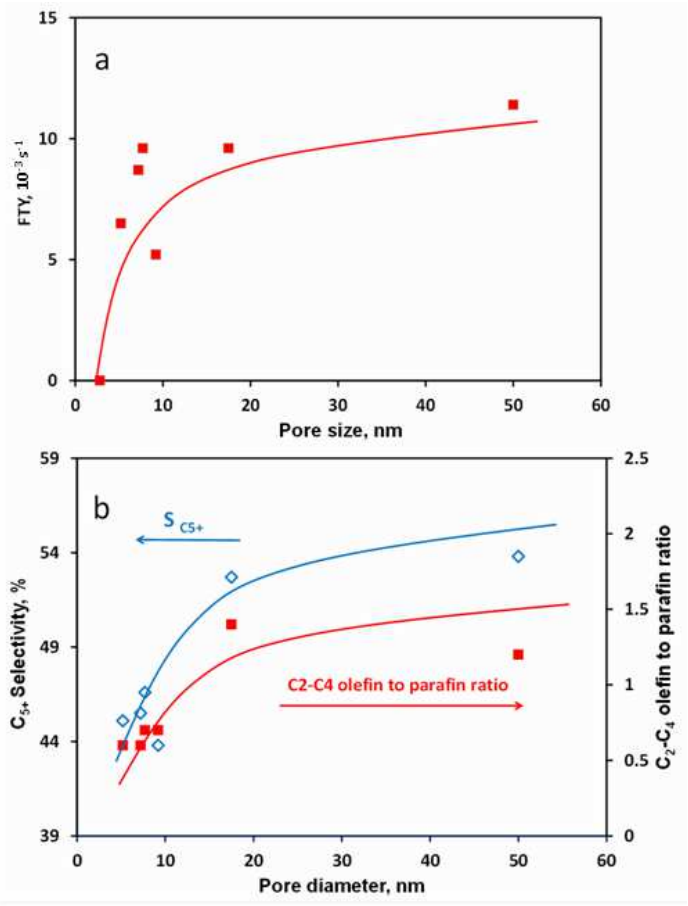

Figure 5-12. Effect of silica pore size on the iron time yields (FTY) (a) and C_2-C_4 olefin to paraffin ratio and C_5^{+} selectivity (b) in FT synthesis.

The reaction selectivity is also affected by the pore size in the supports. Lower methane selectivity and higher C_5^+ selectivities were observed on larger pore supports. An increase in pore size is also beneficial for olefin selectivity. At comparable conversion levels (around 25%), the olefin to paraffin ratio was about 1.2-1.9 in large pore catalysts compared to 0.6-0.7 smaller pore counterparts. The observed different catalytic performance of large pore and small pore iron catalysts can be attributed to the different catalyst structure. The effects of pore size on the catalyst structure and catalytic performance of silica supported iron catalysts are discussed in the following paragraphs.

5.2.5 Discussion of pore size effects on silica supported iron catalysts

The interest in mesoporous silicas as molding agents for metal oxide and metallic nanoparticles is principally due to the silcas high surface area, tunable narrow pore size distribution and chemical stability of these solids. Encapsulation in silica pores often leads to nanoparticles with the particle size distribution which is controlled by the porous structure of silica. This approach can be also used for the design of highly efficient nanoreactors with defined nanoparticle size.

Several routes have been previously explored [52, 53] to prepare catalysts with desired dispersion of the active phase via its molding within the silica matrix. The precursors of nanoparticles can be introduced to the silica pores either during the synthesis of mesoporous solids or using post-synthesis methods such as grafting and impregnation. Each of these preparation routes has its advantages and drawbacks. Simultaneous “single-pot” synthesis of mesoporous matrix and nanoparticles usually ensures uniform nanoparticle distribution inside the porous matrix. At the same time, a strong interaction between silica and nanoparticles during the synthesis could result in mixed metal support compounds (e.g. metal silicates) and thus could reduce the quantity of encapsulated nanoparticles. Grafting is typically used for deposition of relatively small amounts of active phase, whereas the efficient catalysts should contain significant amounts of active phase to ensure high reaction rate and product productivity. Impregnation is a technically simpler technique than grafting for deposition of the active species onto mesoporous solids. In addition, impregnation can introduce more significant amounts of nanoparticles than other techniques. Note however that the particle size distribution can be broad in the impregnated catalyst especially if the catalyst preparation procedure (drying, calcination, activation) has not been properly optimized [54, 55]. In this work, the iron oxide nanoparticles were prepared using impregnation of periodic mesoporous and commercial silicas with iron nitrate solution followed by drying and calcination. Hematite

(α-Fe_2O_3) was the dominant iron phase in the calcined catalysts. The characterization results indicate a strong influence of support pore size on the sizes of supported Fe_2O_3 nanoparticles. A correlation between the size of iron oxide nanoparticles and silica pore is shown Figure 5-4. Iron dispersion was effectively controlled by the support texture; larger iron oxide particles are located in large pore supports, while smaller pore silicas contained mostly small iron oxide crystallites.

The fraction of iron silicate in the iron catalysts is also a function of the support pore diameter. H_2-TPR was indicative of higher concentration of inert iron silicate species in the smaller pore catalysts. Iron silicates cannot be reduced to metallic iron or carbidized into iron carbides under moderate temperatures. The presence of these compounds leads to lower FT reaction rate. Interestingly, encapsulation of iron nanoparticles in silica pore protects them from sintering. Subsequent treatments of the catalysts containing iron oxide nanoparticles in carbon monoxide and in syngas under reaction conditions did not result in any noticeable iron sintering (Figure 5-7). The results are consistent with earlier reports [29-31, 33, 34] for cobalt FT catalysts supported on mesoporous silicas. Cobalt dispersion and reducibility in those catalysts were also strongly influenced by support pore sizes. Larger pore mesoporous silicas favored larger size of cobalt nanoparticles, higher extent reducibility and consequently higher reaction rate in low temperature FT synthesis.

Catalyst activation in carbon monoxide leads to iron carbidization. A higher fraction of Hägg carbide (χ-Fe_5C_2) was detected using a combination of characterization techniques (XRD, Mössbauer spectrometry and in situ magnetic method) in two catalysts with distinct catalytic performance (10FeSi9.2, 10FeSi17.5). Besides Hägg carbide, the activated ion catalysts could also contain non ferromagnetic iron oxides and iron silicate species. Note that the magnetization method did not detect any noticeable concentration of metallic iron or magnetite in the silica supported iron catalysts activated in carbon monoxide. The extent of iron carbidization and fraction of Hägg carbide and thus FT reaction rate are also affected by silica pore dimeters. Higher iron oxide dispersion has been detected in smaller pore catalysts. Interestingly, smaller iron oxide particles and possibly iron silicate species cannot be transformed into iron carbide species using treatment with carbon monoxide or syngas. Despite significant iron dispersion, on the smaller pore catalysts, low concentration of iron carbides leads to lower FT reaction rate. Larger particles in larger pore supports are much easier to carbidize than smaller iron oxide particles. Recently the in-situ magnetic method uncovered dimensional effects in carbidization of iron species in silica supported catalysts [56]. It was found that higher activation energy was required for carbide formation from

smaller iron particles. In addition smaller iron carbide particles were less thermodynamically stable than their larger counterparts. Thus, higher activity of iron catalysts supported by larger pore silicas compared to small pore counterparts could be principally attributed to higher extent of iron carbidization. The catalytic and characterization data of the present work indicate that the catalytic performance of silica supported iron catalysts can be attributed to Hägg carbide (χ-Fe_5C_2). This suggestion is in agreement with previous reports [1-3, 18]. Note however that FT rates and selectivities could be also influenced to some extent by residual iron oxide species which may control the water gas shift reaction and stabilize the supported iron carbide catalyst against oxidation [57].

In supported iron catalysts, the pore size, iron particle size, extent of carbidization and catalytic performance are often inter-connected parameters. Indeed, our results show that silica pore sizes affect both iron dispersion, ease of carbidization and catalytic performance. The literature presents numerous publications [2, 3, 35, 43, 60-64] which relate iron particle size to the reaction rate and hydrocarbon selectivity in high temperature FT synthesis. Most of reports address however either bulk iron catalysts or iron catalysts containing different promoters (K, Mn, S etc). The promotion can also contribute to the modification of catalytic activity and hydrocarbon selectivity in FT synthesis. In chemically promoted catalysts, the particle size effects on the FT catalytic performance may be confonded to some extent to the effects of promoters. Some of supports (e.g. active carbon) and iron precursors may also contain different impurities (sulfur, alkali ions etc.) which may modify the reaction rate and selectivity. Therefore, the intrinsic fundamental information about particle size effect on the catalytic performance of FT catalysts could be possibly obtained using supported iron catalysts which do not contain any promoters or impurities.

Most of previous publications relevant to particle size effects in high temperature FT synthesis have addressed carbon supported iron catalysts. Bartholomew and coworkers [43] showed using a series of carbon supported iron catalysts that both initial and steady state specific activities decrease with decrease in iron particle size. Higher olefin to paraffin ratio was observed on larger ion particles. Similar results for carbon supported catalysts were also obtained by Jung and coworkers [50, 60]. The TOF calculated from FT reaction rate and carbon monoxide adsorption increased with an increase in iron particle size. In fact, most iron supported catalysts investigated by Jung and coworkers [50] had similar overall activity, because the lower TOF of highly dispersed catalysts was compensated by their high specific surface area. The influence of iron particles supported by carbon nanotubes on the FT catalysts performance was studied by Dalai and coworker [61, 62]. Most of iron particles

were localized inside the nanotubes where their diameters were controlled by nanotube pore size. The iron catalysts supported by narrow pore carbon nanotubes showed higher activity and better selectivity to long chain hydrocarbons in FT synthesis compared to the catalyst supported by wide pore nanotubes. In alumina and silica supported catalysts, higher specific activity was also observed for larger iron particles. Park and coworkers [63] showed that the TOF at 673 K calculated from reaction rate and carbon monoxide adsorption increased from 0.02 to 0.16 s^{-1} as iron particle size increased from 2.4 to 6.2 nm in alumina supported catalysts and remained almost constant up to a particle size of 11.5 nm. Higher FT reaction rate was also on larger iron crystallites by Cano and coworkers [31] who compared two silica supported catalysts prepared using MCM-41 and SBA-15 materials. The effects were attributed to the structural sensitivity of FT synthesis on iron species with different particle size. The Utrecht group [3] recently reported different results about particle size dependence of FT catalytic performance on iron catalysts supported by carbon nanofibers. The TOF increased 6-8 fold, as the iron nanoparticle size decreased from 7 to 2 nm. The Hägg iron carbide was supposed to be active phase for FT synthesis in those catalysts. Only very slight influence of the particle size on methane and olefin selectivity was observed [3] with unpromoted carbon supported catalysts, while the presence of trace amounts of sulfur and sodium led to higher methane production in particular over smaller iron carbide nanoparticles. The contradictive catalytic results and uncertainty in evaluation of particle size effect on the FT reaction rate and selectivity on supported iron catalysts can be due to simultaneous presence of several active sites for this reaction, incomplete iron carbidization and possible iron oxidation during the reaction. Simultaneous presence of several reaction active sites and iron phases make calculating TOF rather difficult in particular for smaller iron particles.

Our results show that the overall catalyst reaction rate expressed as iron time yield (FTY) increased with an increase in iron particle size and extent of iron carbidization. This suggests a higher concentration of FT active phase in larger pore catalysts with lower iron dispersion. Note that larger particles can be much easier carbidized than small counterparts. Assuming almost complete iron carbidization in the large pore 10FeSi17.5 catalyst, the calculation of TOF yields 0.19 s^{-1}. The TOF calculated for silica supported iron catalyst is consistent with earlier result of Park [63] for alumina supported iron counterparts with relatively large iron particles (6-12 nm) tested under similar reaction conditions (T = 573 K, P = 20 bar, H_2/CO ~2). Lower activity of smaller pore iron catalysts containing smaller iron particles can be assigned to lower extent of iron carbidization observed in this work. The XRD, in situ magnetic method and Mössbauer spectroscopy showed lower concentrations of iron carbides

in smaller pore catalysts. Note that at similar level of carbon monoxide conversion, larger iron carbide nanoparticles possess more interesting properties in terms of reaction selectivity. An increase in particle size leads to lower methane selectivity, while the olefin to paraffin ratio for lighter C_2-C_4 hydrocarbons is getting higher for larger iron carbide nanoparticles.

5.3 Conclusion

A combination of characterization techniques and catalytic tests indicates a strong impact of pore sizes in mesoporous silicas on the structure of supported iron species and their catalytic performance in high temperature FT synthesis. Smaller pores in mesoporous silicas lead to higher iron dispersion with low extent of carbidization during catalyst activation. An increase in pore size results in larger iron particles which exhibit however higher extent of carbidization. The catalytic performance of iron catalysts supported by mesoporous silicas seems to be attributed to the presence of Hägg iron carbide (χ-Fe_5C_2).

The catalytic performance of iron nanoparticles in the catalysts with different pore size principally correlates with the extent of iron carbidization, while higher dispersion of iron oxide in calcined catalysts supported by smaller pore mesoporous silicas is detrimental for carbon monoxide hydrogenation activity, because of poor iron reducibility and low concentration of iron carbide species these catalysts after activation.

5.4 Reference

[1] H.M. Torres Galvis, K.P. de Jong, ACS Catal., 3 (2013) 2130-2149.

[2] H.M. Torres Galvis, J.H. Bitter, C.B. Khare, M. Ruitenbeek, A.I. Dugulan, K.P. de Jong, Science, 335 (2012) 835-838.

[3] H.M. Torres Galvis, J.H. Bitter, T. Davidian, M. Ruitenbeek, A.I. Dugulan, K.P. de Jong, J. Am. Chem. Soc., 134 (2012) 16207-16215.

[4] A. Corma, F.V. Melo, L. Sauvanaud, F. Ortega, Catal. Today, 107–108 (2005) 699-706.

[5] M. Stöcker, Microporous Mesoporous Mater., 29 (1999) 3-48.

[6] Y. Traa, Chem. Commun., 46 (2010) 2175-2187.

[7] E. Jin, Y. Zhang, L. He, H.G. Harris, B. Teng, M. Fan, Appl. Catal. A, 476 (2014) 158-174.

[8] D. Xiang, S. Yang, X. Liu, Z. Mai, Y. Qian, Chem. Eng. J., 240 (2014) 45-54.

[9] F.G. Botes, J.W. Niemantsverdriet, J. van de Loosdrecht, Catal. Today, 215 (2013) 112-120.

[10] Q.H. Zhang, J.C. Kang, Y. Wang, ChemCatChem, 2 (2010) 1030-1058.

[11] Y. Zhang, J. Bao, S. Nagamori, N. Tsubaki, Appl. Catal. A, 352 (2009) 277-281.

[12] M.D. Shroff, D.S. Kalakkad, K.E. Coulter, S.D. Kohler, M.S. Harrington, N.B. Jackson, A.G. Sault, A.K. Datye, J. Catal., 156 (1995) 185-207.

[13] B. Sun, K. Xu, L. Nguyen, M. Qiao, F. Tao, ChemCatChem, 4 (2012) 1498-1511.

[14] R.P. Mogorosi, N. Fischer, M. Claeys, E. van Steen, J. Catal., 289 (2012) 140-150.

[15] C.-H. Zhang, H.-J. Wan, Y. Yang, H.-W. Xiang, Y.-W. Li, Catal. Commum., 7 (2006) 733-738.

[16] A.F.H. Wielers, A.J.H.M. Kock, C.E.C.A. Hop, J.W. Geus, A.M. van Der Kraan, J. Catal., 117 (1989) 1-18.

[17] A.P.B. Sommen, F. Stoop, K. Van Der Wiele, Applied Catalysis, 14 (1985) 277-288.

[18] E. de Smit, B.M. Weckhuysen, Chem. Soc. Rev., 37 (2008) 2758-2781.

[19] J.F. Shultz, M. Abelson, K.C. Stein, R.B. Anderson, J. Phys. Chem., 63 (1959) 496-500.

[20] M.F.M. Post, A.C. Van't Hoog, J.K. Minderhoud, S.T. Sie, AIChE J., 35 (1989) 1107-1114.

[21] W.H. Zimmerman, J.A. Rossin, D.B. Bukur, Ind. Eng. Chem. Res., 28 (1989) 406-413.

[22] D.B. Bukur, M. Koranne, X. Lang, K.R.P.M. Rao, G.P. Huffman, Appl. Catal. A, 126 (1995) 85-113.

[23] D.R. Milburn, K.V.R. Chary, B.H. Davis, Appl. Catal. A, 144 (1996) 121-132.

[24] T.R. Motjope, H.T. Dlamini, G.R. Hearne, N.J. Coville, Catal. Today, 71 (2002) 335-341.

[25] C.T. Kresge, M.E. Leonowicz, W.J. Roth, J.C. Vartuli, J.S. Beck, Nature, 359 (1992) 710-712.

[26] J.S. Beck, J.C. Vartuli, W.J. Roth, M.E. Leonowicz, C.T. Kresge, K.D. Schmitt, C.T.W. Chu, D.H. Olson, E.W. Sheppard, J. Am. Chem. Soc., 114 (1992) 10834-10843.

[27] Y. Wan, D. Zhao, Chem. Rev., 107 (2007) 2821-2860.

[28] D. Zhao, J. Feng, Qisheng Huo, Nicholas Melosh, Glenn H. Fredrickson, Bradley F. Chmelka, G.D. Stucky*, Science, 279 (1998) 548-552.

[29] A.Y. Khodakov, R. Bechara, A. Griboval-Constant, Appl. Catal. A, 254 (2003) 273-288.

[30] A.Y. Khodakov, R. Bechara, A. Griboval-Constant, Structure and catalytic performance of cobalt Fischer Tropsch catalysts supported by periodic mesoporous silicas, in: G.G. R. Aiello, F. Testa (Eds.) Stud. Surf. Sci. Catal., Elsevier, 2002, pp. 1133-1140.

[31] A.M. Saib, M. Claeys, E. van Steen, Catal. Today, 71 (2002) 395-402.

[32] A. Griboval-Constant, A.Y. Khodakov, R. Bechara, V.L. Zholobenko, Support mesoporosity: a tool for better control of catalytic behavior of cobalt supported Fischer Tropsch catalysts, in: B.M.J.R. F. Rodriguez-Reinoso, K. Unger (Eds.) Stud. Surf. Sci. Catal., Elsevier, 2002, pp. 609-616.

[33] A.Y. Khodakov, A. Griboval-Constant, R. Bechara, V.L. Zholobenko, J. Catal., 206 (2002) 230-241.

[34] A.Y. Khodakov, A. Griboval-Constant, R. Bechara, F. Villain, J. Phys. Chem. B, 105 (2001) 9805-9811.

[35] L.A. Cano, M.V. Cagnoli, N.A. Fellenz, J.F. Bengoa, N.G. Gallegos, A.M. Alvarez, S.G. Marchetti, Appl. Catal. A, 379 (2010) 105-110.

[36] D.J. Kim, B.C. Dunn, F. Huggins, G.P. Huffman, M. Kang, J.E. Yie, E.M. Eyring, Energ. Fuel, 20 (2006) 2608-2611.

[37] S. Brunauer, L.S. Deming, W.E. Deming, E. Teller, J. Am. Chem. Soc., 62 (1940) 1723-1732.

[38] F. Rouquerol, J. Rouquerol, K. Sing, Adsorption by powders and porous solids, Academic Press, London, 1999.

[39] K.S.W. Sing, Pure Appl. Chem., 57 (1985) 603-619.

[40] S. van Donk, A.H. Janssen, J.H. Bitter, K.P. de Jong, Catal. Rev., 45 (2003) 297-319.

[41] P. Ganesan, H.K. Kuo, A. Saavedra, R.J. De Angelis, J. Catal., 52 (1978) 310-320.

[42] H.H.P. Yiu, M.A. Keane, Z.A.D. Lethbridge, M.R. Lees, A.J.E. Haj, J. Dobson, Nanotechnology, 19 (2008) 255606.

[43] K. Yogo, S. Tanaka, T. Ono, T. Mikami, E. Kikuchi, Microporous Mater., 3 (1994) 39-46.

[44] M. Luo, H. Hamdeh, B.H. Davis, Catal. Today, 140 (2009) 127-134.

[45] D.B. Bukur, L. Nowicki, R.K. Manne, X.S. Lang, J. Catal., 155 (1995) 366-375.

[46] D.B. Bukur, L. Nowicki, X. Lang, Catal. Today, 24 (1995) 111-119.

[47] H.W. Pennline, M.F. Zarochak, J.M. Stencel, J.R. Diehl, Ind. Eng. Chem. Res., 26 (1987) 595-601.

[48] R.J. O'Brien, L. Xu, R.L. Spicer, B.H. Davis, Energ. Fuel, 10 (1996) 921-926.

[49] L.A. Cano, M.V. Cagnoli, J.F. Bengoa, A.M. Alvarez, S.G. Marchetti, J. Catal., 278 (2011) 310-320.

[50] J.W. Niemantsverdriet, A.M. Van der Kraan, W.L. Van Dijk, H.S. Van der Baan, J. Phys. Chem., 84 (1980) 3363-3370.

[51] J.W. Niemantsverdriet, A.M. van der Kraan, J. Catal., 72 (1981) 385-388.

[52] F. Schüth, Angew. Chem. Int. Ed., 42 (2003) 3604-3622.

[53] C. Tang, H. Zhang, C. Sun, J. Li, L. Qi, Y. Quan, F. Gao, L. Dong, Catal. Commum., 12 (2011) 1075-1078.

[54] A.Y. Khodakov, Braz. J. Phys., 39 (2009) 171-175.

[55] T. Toupance, M. Kermarec, C. Louis, J. Phys. Chem. B, 104 (2000) 965-972.

[56] P.A. Chernavskii, V.I. Zaikovskii, G.V. Pankina, A.Y. Khodakov, ChemCatChem, 5 (2013) 1758-1761.

[57] P. Thüne, P. Moodley, F. Scheijen, H. Fredriksson, R. Lancee, J. Kropf, J. Miller, J.W. Niemantsverdriet, J. Phys. Chem. C, 116 (2012) 7367-7373.

[58] V.K. Jones, L.R. Neubauer, C.H. Bartholomew, J. Phys. Chem., 90 (1986) 4832-4839.

[59] H.J. Jung, P.L. Walker Jr, A. Vannice, J. Catal., 75 (1982) 416-422.

[60] H.J. Jung, M.A. Vannice, L.N. Mulay, R.M. Stanfield, W.N. Delgass, J. Catal., 76 (1982) 208-224.

[61] R.M.M. Abbaslou, J. Soltan, A.K. Dalai, Appl. Catal. A, 379 (2010) 129-134.

[62] R.M. Malek Abbaslou, A. Tavasoli, A.K. Dalai, Appl. Catal. A, 355 (2009) 33-41.

[63] J.-Y. Park, Y.-J. Lee, P.K. Khanna, K.-W. Jun, J.W. Bae, Y.H. Kim, J. Catal. Mol. Catal. A: Chem., 323

(2010) 84-90.

[64] E. I. Mabaso, E. Van Steen, M. Claeys, DGMK Tagungsbericht, 4 (2006) 93-100.

Chapter 6. Support Effects in High Temperature Fischer-Tropsch Synthesis on Iron Catalysts

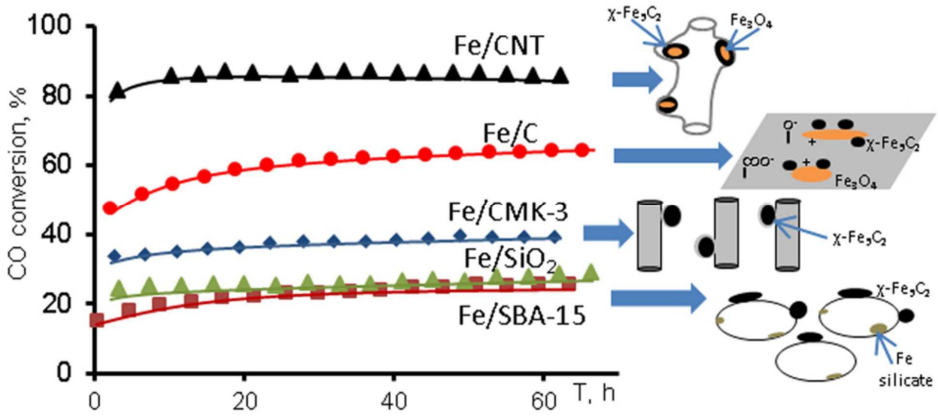

Abstract: This chapter addresses the effects of silica and carbon supports on the structure and catalytic performance of iron catalysts for high temperature Fischer-Tropsch synthesis. Iron phase composition and dispersion in both calcined and activated catalysts were strongly affected by the support. Hematite was the major iron phase in calcined silica supported catalysts, while carbon supported counterparts contain magnetite. Catalyst activation in carbon monoxide leads to carbidisation of iron oxides to principally Hägg iron carbide. Higher Fischer-Tropsch reaction rates were observed on carbon supported iron catalysts compared to silica supported counterparts. The catalytic performance principally depended on iron phase composition rather than on iron dispersion. Iron catalysts supported on carbon nanotubes and activated carbon showed highest activity in Fischer-Tropsch, which could be attributed to the formation of composites of iron carbide and residual magnetite.

This Chapter is based on the following publication:

K. Cheng, V.V. Ordomsky*, M. Virginie, B. Legras, P.A. Chernavskii, V.O. Kazak, C. Cordier, S. Paul, Ye Wang and A.Y. Khodakov*, *Appl.Catal. A*, 488 (**2014**) 66-77.

6.1 Introduction

Silica, alumina and titania are the most common supports for FT catalysts. Carbon materials such as activated carbon, carbon nanotubes, carbon spheres, glassy carbon and carbon nanofibres have also been recently applied for supporting iron catalysts [1-6]. Carbon materials exhibit several advantages as supports. They have high surface area, which could lead to higher iron dispersion. They also have versatile surface chemistry, which makes it possible to add new functional surface groups and to vary their density by activation and post-treatments. The presence of oxygen containing groups in carbon materials allows tuning support acidity, which could affect interaction between the support and Fe species and thus, hydrocarbon selectivity in FT reaction [7]. Close contact between Fe nanoparticles and carbon support may facilitate formation of iron carbide, which is often considered as active phase for FT synthesis [8, 9]. The porous texture and morphology could lead to encapsulation of Fe inside of the carbon support. It was found that the confinement of Fe within carbon nanotubes (CNTs) modified the redox properties of encapsulated iron oxides and led to a significant increase in the activity of iron catalysts for FT synthesis [10, 11]. The catalyst stability towards sintering can be also improved by isolating metal nanoparticles within the carbon matrix.

Most of the previous works have reported characterization and catalytic data obtained with iron catalysts prepared using only one support. This makes difficult a direct comparison between iron catalysts supported on different materials. This chapter is aimed at clarifying this point. In this work, iron catalysts for FT synthesis on carbon supports (active carbon, CMK-3 and carbon nanotubes) at different stages of preparation and activation are compared with silica supported counterparts (amorphous silica and SBA-15). Iron species before and after activation and catalytic reaction have been characterized by a wide range of techniques (X-ray diffraction, FTIR, TEM, in situ magnetic method, transmission Mössbauer spectrometry and XPS) in order to elucidate the correlations between the catalytic performance in FT synthesis and catalyst structure.

6.2 Result and Discussion

6.2.1 Characterization of supports

The textural properties of different supports are displayed in Table 6-1. SBA-15 consists of hexagonal cylindrical pores, which are connected to each other by small micropores in their

walls with surface area of about 1000 m^2/g [12]. The main volume of SBA-15 is presented by the mesoporous volume of 1.39 cm^3/g with diameter of the pores about 7 nm and small micropore volume (0.06 cm^3/g). These textural parameters are consistent with the literature [13]. Commercial amorphous silica (SiO_2) possesses large mesopores formed by volume between globules with a surface area of about 300 m^2/g. CMK-3 was prepared by filling mesopores of SBA-15 template with sucrose with subsequent removal of the template. Thus, CMK-3 is formed by interconnected carbon rods and has a surface very similar to those of SBA-15. The size of the CMK-3 pores is smaller (3.8 nm) in comparison with SBA-15 due to the lower thickness of the SBA-15 walls in comparison with diameter of the mesopores [14]. Activated carbon (AC) has a relatively large surface area (557 m^2/g) with a higher contribution of micropores (Table 6-2). This is the result of the carbonization procedure with formation of graphitic-like sheets joined by random cross-linking [15]. The nanotubes of the acid treated CNT have uniform diameters of about 5 nm. The relatively high surface area (Table 6-1) indicates that nanotubes have open caps.

Table 6-1. Catalysts characterization

Sample	N_2 adsorption over supports					Particle size, nm					Magnetization of calcined catalysts, emu/g
	S_{BET}, m^2/g	S_{mic}, m^2/g	V_{tot}, cm^3/g	V_{mic}, cm^3/g	Pore size, nm	after calcination		after CO treatment		After reaction (TEM)	
						XRD[a]	TEM	XRD	TEM		
Fe/SBA-15	1045	162	1.39	0.06	7.7	9.4(H)	6.1	2	-	14.3	0
Fe/SiO_2	307	25	1.31	0.01	19.5	17.5(H)	14.3	6.1	11.6	14.7	0
$Fe/SiO_2(N_2)$	-	-	-	-	-	5.5(H)	-	-	-	-	0
Fe/CMK-3S	1326	557	1.32	0.12	2.8	3.8(M)	-	1.8	13	-	3.1
Fe/CMK-3L	-	-	-	-	-	15.4(M)	17.1	4.0	-	9.5	12.3
Fe/AC	558	232	0.4	0.07	-	6.7(M)	-	2.1	13.6	-	4.4
Fe/CNT	163	17	0.56	0.01	5	12.3(M)	14	4.1	13.1	14.4	12.2

[a] Based on the diffraction peaks of hematite (H) or magnetite/maghemite (M).

Carbon supports, besides the differences in morphology and textural properties, could also possess different functional groups on their surface. Figure 6-1 shows IR spectra of pure carbon supports. AC, CNT and CMK-3 show a broad band situated in the region of 3300-3600 cm^{-1} corresponding to OH stretching vibrations in partially hydrogen-bonded hydroxyl groups [16]. The sharp band at 1385 cm^{-1} might be assigned to bending in-plane OH vibrations [17]. The intensity of these bands is decreasing as follows: AC>CNT>CMK-3. AC exhibits also other IR bands at 1580, 1460 and 1100 cm^{-1}. The band at 1580 cm^{-1} was

observed earlier and assigned to aromatic ring stretching coupled to conjugated carbonyl groups (C=O) [18]. The band at 1460 cm^{-1} can be attributed to O–H vibrations in carboxyl groups or C–H bending vibrations [19]. The broad band at 1100 cm^{-1} is generally associated with stretching C–O vibrations in methoxyl groups or ethers [17]. Appearance of these bands indicates partial oxidation of AC surface, which could be a result of the preparation of AC by pyrolysis. CNT and especially CMK-3 display significantly lower concentration of surface functional groups in comparison with AC.

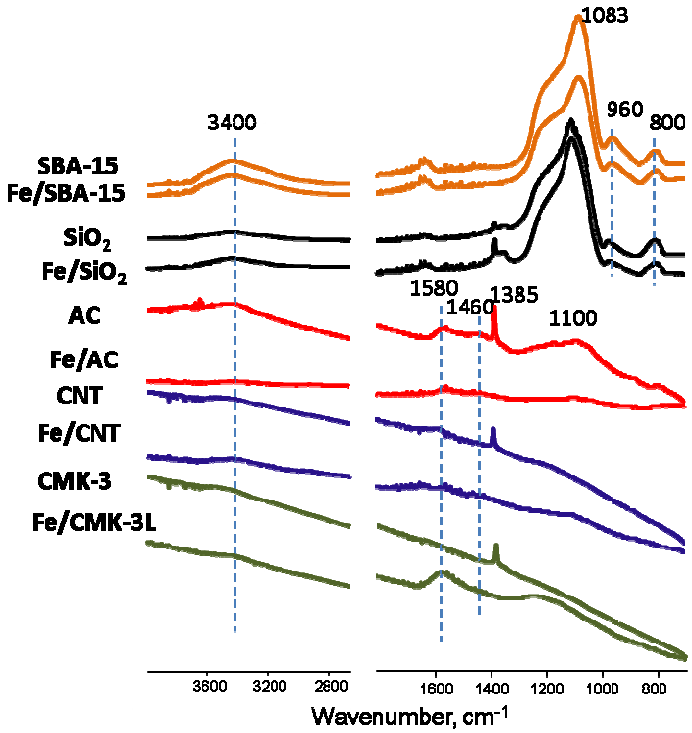

Figure 6-1. IR spectra of carbon supports and supported iron catalysts after calcination.

6.2.2 Calcined catalysts

Iron nitrate was decomposed using calcination in air (for silica supported catalysts) or in nitrogen (for carbon supports). XRD patterns of the calcined catalysts are shown in Figure 6-2. The crystallite size of iron oxides was evaluated from the Scherrer equation [20] (Table 6-2). α-Fe_2O_3 is the main iron phase in Fe/SiO_2 and Fe/SBA-15 calcined in air. Relatively large iron oxide particles of 17.5 nm and 9.4 nm were detected respectively in Fe/SiO_2 and Fe/SBA-15. The iron oxide particle sizes measured by TEM for Fe/SiO_2 and Fe/SBA-15 (14.3 and 6.1 nm, Figure 6-3, Table 6-1) were consistent with XRD. Note that iron nitrate decomposition in air over silica results in formation of hematite phase (α-Fe_2O_3):

$$2\ Fe(NO_3)_3{\cdot}9H_2O = Fe_2O_3 + 6\ NO_2 + 3/2\ O_2 + 18\ H_2O.$$

Interestingly, iron nitrate decomposition in nitrogen also gives hematite similarly to iron nitrate decomposition in air (Fe/SiO_2-N_2, Figure 6-2). No magnetite (Fe_3O_4) was detected in silica supported catalysts (Figure 6-2). The results are consistent with previous reports [5]. At the same time, hematite was not detected in carbon supports after decomposition of iron nitrate in nitrogen. The observed XRD patterns are characteristic of magnetite (Fe_3O_4) and possibly maghemite (γ-Fe_2O_3). Magnetite (Fe_3O_4) and maghemite (γ-Fe_2O_3) possess the same spinel structure and almost identical lattice parameters. Identification of these phases by XRD is rather difficult [21, 22]. An additional broad peak at $2\theta = 43.5°$ was observed in the XRD patterns of Fe/CNT, which corresponds to the graphite layers of multi-walled nanotubes [23]. In Fe/CMK-3L, small amounts of hematite (α-Fe_2O_3) were observed in addition to magnetite. Previously both hematite [8] and magnetite [18] were detected after decomposition of iron nitrate in CNT.

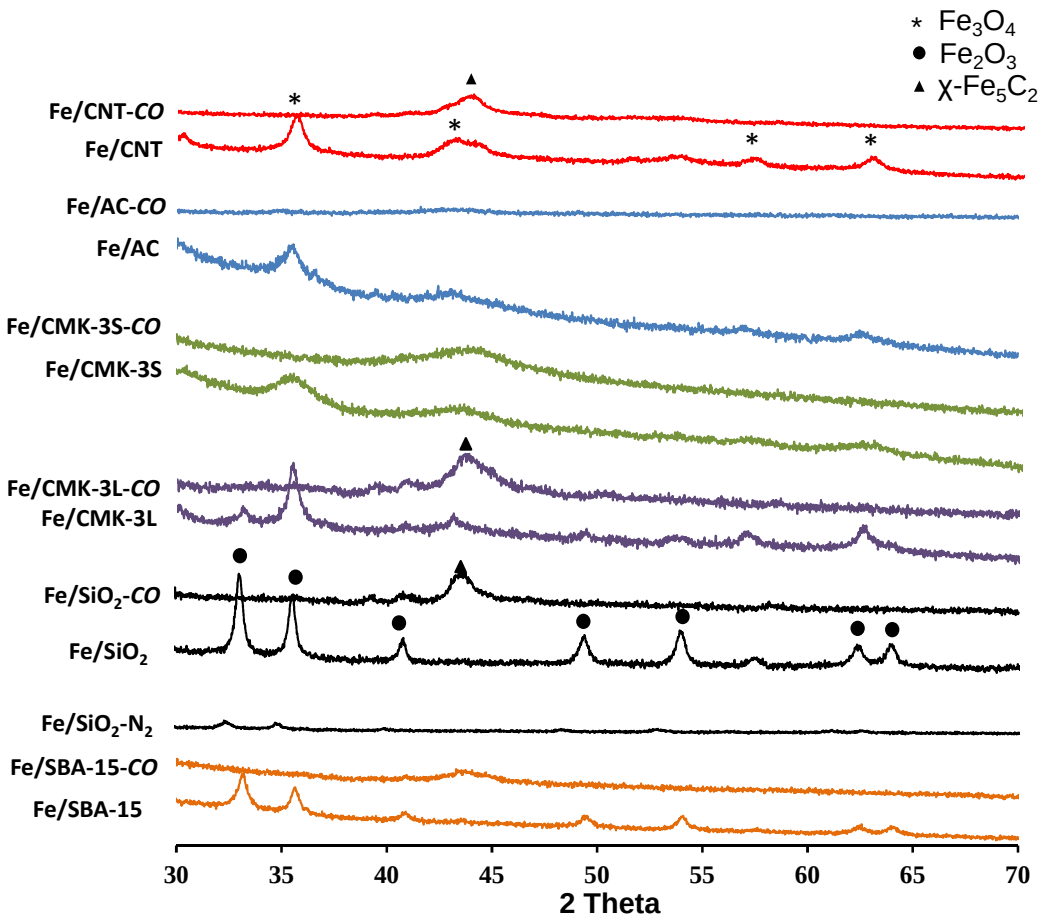

Figure 6-2. XRD patterns of samples after calcination and activation in CO.

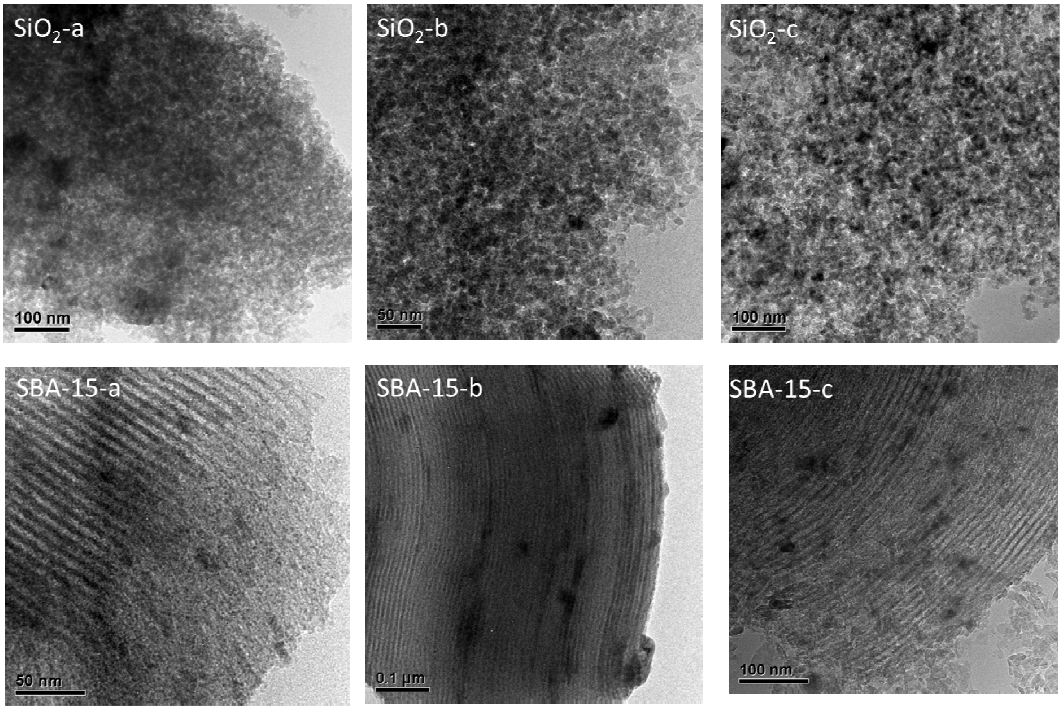

Figure 6-3. TEM images of Fe/SiO_2 and Fe/SBA-15 after calcination in N_2 (a), pretreatment in CO (b) and after reaction (c).

The largest iron oxide particles were observed by both XRD and TEM in CNT (12.3 and 14 nm) and CMK-3L (15.4 and 17.1 nm) prepared by impregnation with aqueous solution of nitrate (Table 6-1, Figure 6-4). Impregnation of CMK-3 with the ethanol solution results in a decrease in the particle size to 3.8 nm. Larger particles size of iron oxide obtained in aqueous impregnation can be due to the hydrophobicity of carbon support, which could lead to a less uniform repartition of iron nitrate during the impregnation and iron oxide agglomeration. Impregnation with ethanol solution results in more uniform support wetting and consequently smaller iron oxide crystallites.

The calcined catalysts were also characterized using the magnetic method [chapter 2]. Table 6-2 shows a significant magnetization of calcined Fe/CNT and Fe/CMK-3L and a lower magnetization of calcined Fe/CMK-3S and Fe/AC. The high initial magnetization at room temperature is probably due to the presence of ferrimagnetic iron oxides (Fe_3O_4 and possibly γ-Fe_2O_3) in calcined Fe/CNT and Fe/CMK-3L. Iron species seem to be well dispersed on the surface of Fe/CMK-3S and Fe/AC (Table 6-1, Figure 6-2). Smaller iron oxide particle size may lead to a distorted structure and a less intense magnetic signal. Earlier, a decrease in the magnetization with the decrease in the size of magnetite nanoparticles (<10 nm) was explained by lower magnetization near the surface of magnetite [24]. Fe/SBA-15, Fe/SiO_2 and Fe/SiO_2-N_2 do not show any significant magnetization. This suggests that ferrimagnetic iron

oxides are not present in these samples (Table 6-1). The magnetization measurements are also consistent with XRD which did not show any noticeable peaks attributed to magnetite in these samples.

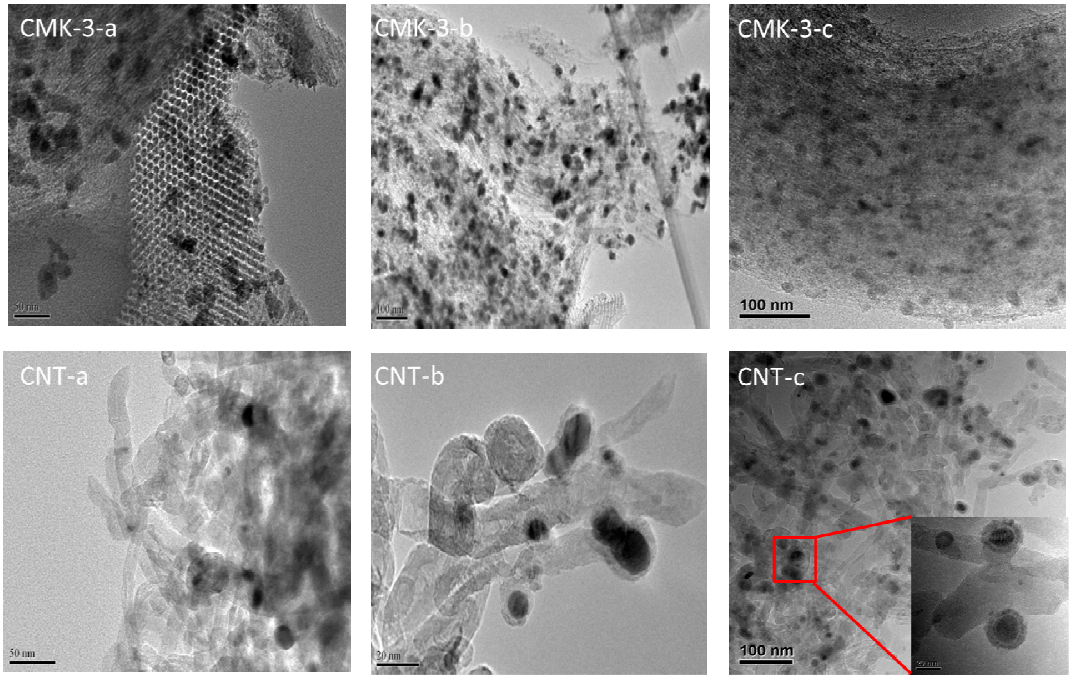

Figure 6-4. TEM images of Fe/CMK-3 and Fe/CNT after calcination in N_2 (a), pretreatment in CO (b) and after reaction (c)

The results of XRD and magnetization show that interaction of iron oxides with carbon supports plays an important role in the genesis of iron surface species. The possible role of carbon support might be related to partial iron reduction during the nitrate decomposition with formation of Fe_3O_4 magnetite phase instead of Fe_2O_3. In this case, carbon support should be partially oxidized by oxygen released during iron nitrate decomposition. In order to confirm oxidation of carbon support during iron nitrate decomposition, Fe/CMK-3L sample after impregnation of CMK-3 with iron nitrate was heated in He flow with CO_2 detection during temperature ramping with a linear rate. Figure 6-5 shows CO_2 formation curves over Fe/CMK-3 and on the pure CMK-3 support. With the Fe containing sample, a broad peak of CO_2 is observed in the range from 100 to 700°C. The amount of produced CO_2 (3.3 mmol/g) corresponds to the amount of Fe in the sample (1.8 mmol/g). Thus, carbon support seems to be partially oxidized by the oxygen released during iron nitrate decomposition. The amount of formed CO_2 is significantly smaller over the pure CMK-3 support. Indeed, CO_2 in this case might be formed only due to the decomposition of carboxylic functional groups on the surface

in helium.

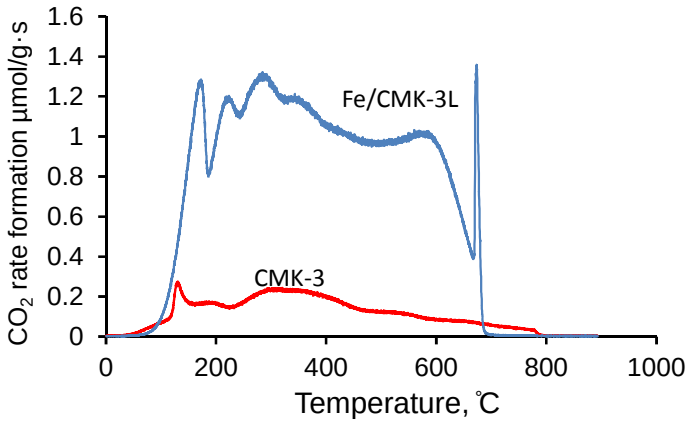

Figure 6-5. CO_2 formation during temperature-programmed decomposition of Fe nitrate over CMK-3 in comparison with pure CMK-3.

The strong interaction between iron species and carbon supports was also observed by FTIR spectroscopy (Figure 6-1). Deposition of iron species results in significant modifications of IR spectra relative to the pure carbon supports. The IR bands at 1580, 1460 and 1100 cm^{-1} which correspond to hydroxyl and carbonyl groups in AC and CNT disappear after iron deposition on these supports. This fact might be explained by a strong interaction of magnetite with the support and neutralization of the surface functional groups by iron species. Note that these bands appear in CMK-3 after iron addition. This might be due to the partial oxidation of CMK-3 by oxygen released during iron nitrate decomposition.

6.2.3 Catalyst activation in CO

The XRD patterns of iron catalysts activated in carbon monoxide are shown in Figure 6-2. Treatment of all catalysts in CO at 350 °C results in the formation of iron carbides with a broad diffraction peak at around 43° (Figure 6-2). This broad peak probably corresponds to the superposition of the most intense diffraction peaks of several iron carbides: most likely χ-Fe_5C_2 and ε-Fe_2C [8]. The size of carbide crystals seems to correlate with the size of oxide phase. The largest particles calculated using the Scherrer equation are observed over Fe/SiO_2, Fe/CMK-3L and Fe/CNT (4-6 nm) and the smallest counterparts (2 nm) over Fe/SBA-15, Fe/AC and Fe/CMK-3S (Table 6-1, Figure 6-2). Note however that much smaller iron carbide particles were observed by XRD after CO treatment in comparison with the oxide precursors (Table 6-1, Figures 6-3 and 6-4), while TEM does not shown any major decrease in iron

particle size after carbidization (Table 6-1). This observed discrepancy can be attributed to the limitations of these two techniques. Indeed, XRD measures only the size of iron carbide ordered crystalline domains, while TEM can detect both iron individual carbide crystallites and crystallite agglomerates.

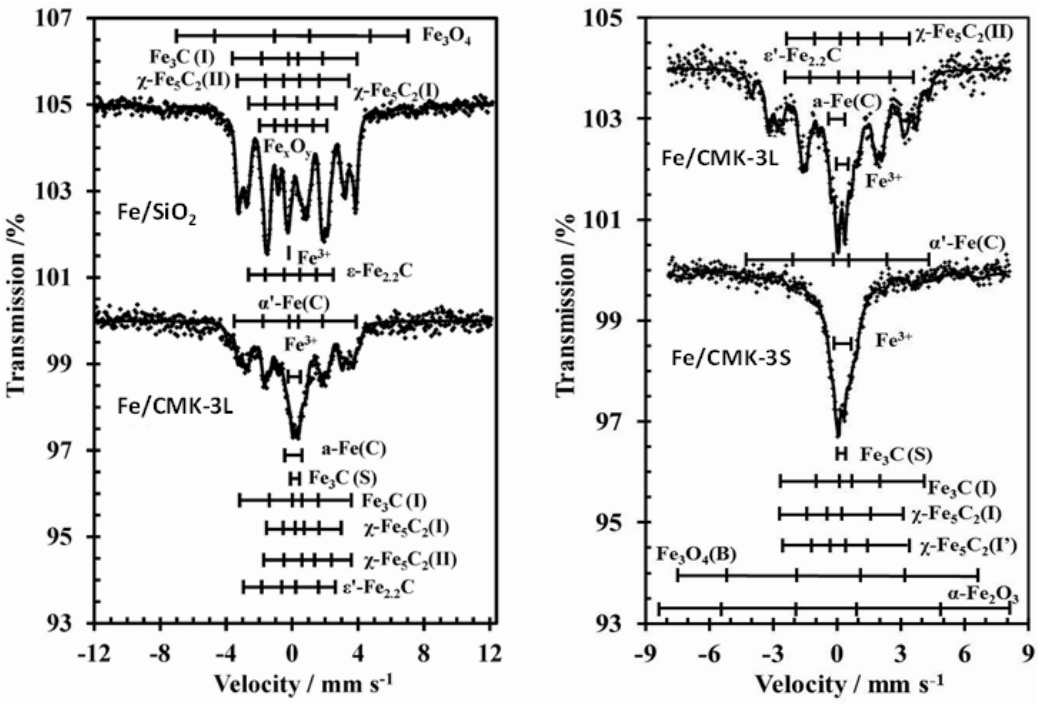

Figure 6-6. Transmission Mössbauer spectra of Fe/SiO_2, Fe/CMK-3L and Fe/CMK-3S activated in CO.

The catalysts activated in CO were also characterized by Mössbauer spectroscopy and XPS. The transmission Mössbauer spectra of the activated Fe/SiO_2, Fe/CMK-3L and Fe/CMK-3S catalysts are shown in Figure 6-6. The calculated Mössbauer parameters are given in Table 6-3. Lower extent of carbidisation was observed on the Fe/SiO_2 catalyst relative to Fe/CMK-3L (Figure 6-6, Tables 6-1 and 6-2) with residual iron oxide contents of 17.2 and 7.7 %, respectively after activation in CO. Both catalysts have similar iron dispersion (Figure 6-6, Tables 6-1 and 6-2). Higher extent of carbidisation has been also observed in the Fe/CMK-3L catalyst containing larger iron particles compared to Fe/CMK-3S (Figure 6-6, Table 6-2). It seems that the extent of carbidisation is affected, on one hand, by the support (carbon CMK-3 versus SiO_2) and, on other hand, by a diameter of iron crystallites. Higher extent of carbidization is observed in carbon supported catalysts compared to silica supported counterparts, while on a given support, larger iron particles could be carbidized easier than smaller ones. Previously, lower stability of smaller iron carbide nanoparticles

compared to larger ones was uncovered using in-situ magnetic method [25]. Interestingly, analysis of the Mössbauer data suggests that χ-Fe_5C_2 is the most abundant carbide in Fe/SiO_2 while Fe_3C is the major phase in Fe/CMK-3L.

Table 6-2. Mössbauer parameters of supported iron catalysts activated in CO.

Sample	Iron sites	HF (T)	IS (mm s^{-1})	QS (mm s^{-1})	Relative area%	Phase quantification (%)
Fe/CMK-3L	α'-Fe(C)	25.96	0.209	-0.0784	9.5	α'-Fe(C): 9.5±2%
	ε'-$Fe_{2.2}C$	18.15	0.311	0.071	11.1	Fe_3C: 35.5±2%
	Fe_3C(I)	21.57	0.245	-0.004	25.8	χ-Fe_5C_2: 29.6±2%
	Fe_3C superpara	-	0.217	0.266	9.7	ε-$Fe_{2.2}C$:11.1±2% a-FeC: 6.6±2%
	χ-Fe_5C_2(I)	15.37	0.280	0.016	8.6	Oxides: 7.7±2%
	χ-Fe_5C_2(II)	18.35	0.187	-0.025	21.0	(7.7% Fe^{3+}(spm))
	a-FeC	-	0.068	0.627	6.6	
	Fe^{3+} (spm)	-	0.319	0.689	7.7	
Fe-CMK-3S	Fe_3C superpara	-	0.205	0.243	19.2	α'-Fe(C): 0±2% Fe_3C: 19.2±2%
	χ-Fe_5C_2 (I')	18.05	0.476	0.204	12.3	χ-Fe_5C_2: 25.2±2%
	χ-Fe_5C_2(I)	10.74	0.358	0.118	12.9	ε-$Fe_{2.2}C$: 0±2%
	α-Fe_2O_3	51.77	0.333	-0.235	10.4	a-FeC: 0±2%
	Fe_3O_4(B)	43.87	0.274	-0.035	11.0	Oxides: 55.6±2%
	Fe^{3+} (spm)	-	0.288	1.191	15.3	(18.9+15.3 +11.0 +10.4)
	Fe^{3+} (spm)	-	0.268	0.666	18.9	
Fe/SiO_2	Fe_3C (I)	20.82	0.245	0.020	10.6	Fe_3C: 11.7±2%
	Fe_3C (II)	-	0.359	0	1.1	χ-Fe_5C_2: 58.4±2%
	χ-Fe_5C_2 (I)	18.66	0.207	-0.006	25.7	ε-$Fe_{2.2}C$: 12.7±2%
	χ-Fe_5C_2 (II)	22.09	0.266	0.014	32.7	Oxides: 17.2±2%
	ε-$Fe_{2.2}C$	17.28	0.150	0.020	12.7	(11.3%Fe_xO_y +
	Fe_xO_y	13.55	0.367	-0.071	11.3	5.9%Fe_3O_4)
	Fe_3O_4	48.23	0.275	-0.449	5.9	

The Fe 2p XPS spectra of the activated catalysts are shown in Figure 6-7. Different iron species in these catalysts were identified using the absolute values of binding energies and Fe (2p3/2) and Fe (2p1/2) orbital splitting [26-28]. The peaks at 710.7 and 724.6 eV in the XPS spectra of Fe/CNT correspond to Fe(2p3/2) and Fe(2p1/2) core level binding energies in Fe_3O_4 species. The activated Fe/SiO_2 and Fe/SBA-15 catalysts contain mostly Fe^{3+} species, which were identified by XPS peaks at 712.0 (Fe (2p3/2)) and 725.4 eV (Fe2p1/2)) [45, 46]. Fe/CNT also exhibits peaks at 707.1 and 720.2 eV. The peaks can be assigned either to metallic iron or iron carbide (F_xC_y). Unfortunately, XPS at Fe 2p energy level did not allow

distinguishing between metallic iron and iron carbide. We assigned the peaks at 707.1 and 720.2 eV to respectively Fe(2p3/2) and Fe(2p1/2) binding energies in iron carbide because the reduction of magnetite to metal iron is less probable under these conditions. Previously, reduction of iron carbide to α-Fe was observed by CO-TPR combined with XRD analysis only at the temperatures higher than 380 °C [29]. Examination of the XPS spectrum of activated Fe/CNT suggests that iron carbide is the dominant iron phase in this catalyst with the presence of residual Fe_3O_4. In the activated Fe/SiO_2 and Fe/SBA-15, the intensity of the peaks at 707.1 and 720.2 eV attributed to iron carbide is much lower than in Fe/CNT. This suggests a lower extent of carbidisation of silica based catalysts relative to Fe/CNT.

The XPS results are also consistent with Mössbauer data, which suggest much easier iron carbidisation in carbon materials in comparison with silica containing smaller nanoparticles. These facts might be explained by strong interaction of iron species with silica support leading to inactive Fe silicate. It is also interesting to note that the concentration of Fe^{3+} species is significantly higher for SBA-15 in comparison with Fe/SiO_2. Larger SBA-15 surface area and smaller size of hematite particles would favor chemical reaction between iron species and silica with formation of iron silicate.

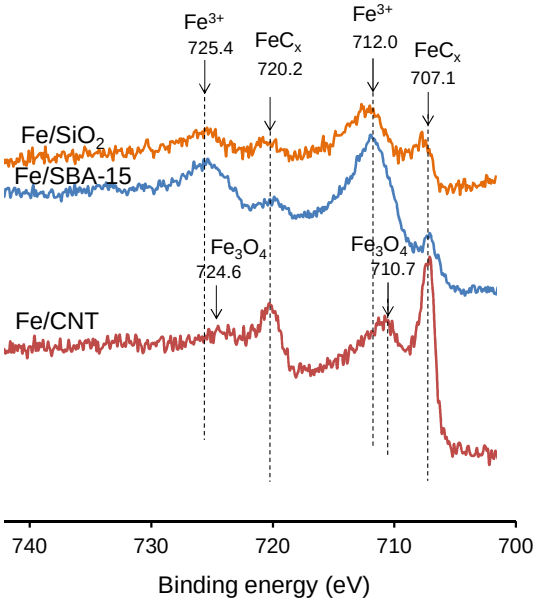

Figure 6-7. Fe 2p XPS spectra of Fe/SiO_2, Fe/SBA-15 and Fe/CNT catalysts activated in CO.

The formation of carbide phases during CO pretreatment was also observed by magnetization (Figure 6-8a). Heating of the catalysts in the atmosphere of CO results in a significant increase in the magnetization of Fe/CMK-3L, Fe/SBA-15, Fe/SiO_2 and Fe/SiO_2-N_2

at 200 ^{o}C with subsequent decrease in the magnetization for all the samples at the temperatures higher than 250 ^{o}C. The increase in the magnetization over Fe/CMK-3L and silica supported samples might be explained by formation of ferromagnetic iron phases. The decrease in the magnetization over Fe/CMK-3L, Fe/CMK-3S, Fe/SiO_2 and Fe/CNT at higher temperatures might be explained by disordering of magnetic domain after attaining the Curie temperature. The monoclinic Hägg χ-Fe_5C_2 has the Curie temperature at 205-256 ^{o}C (Table 6-1). The presence of Hägg carbide in the activated Fe/CNT, Fe/AC and Fe/CMK-3S is in agreement with a sharp decrease in the magnetization at the Curie temperature of this carbide. This suggestion is consistent with previous report [29].

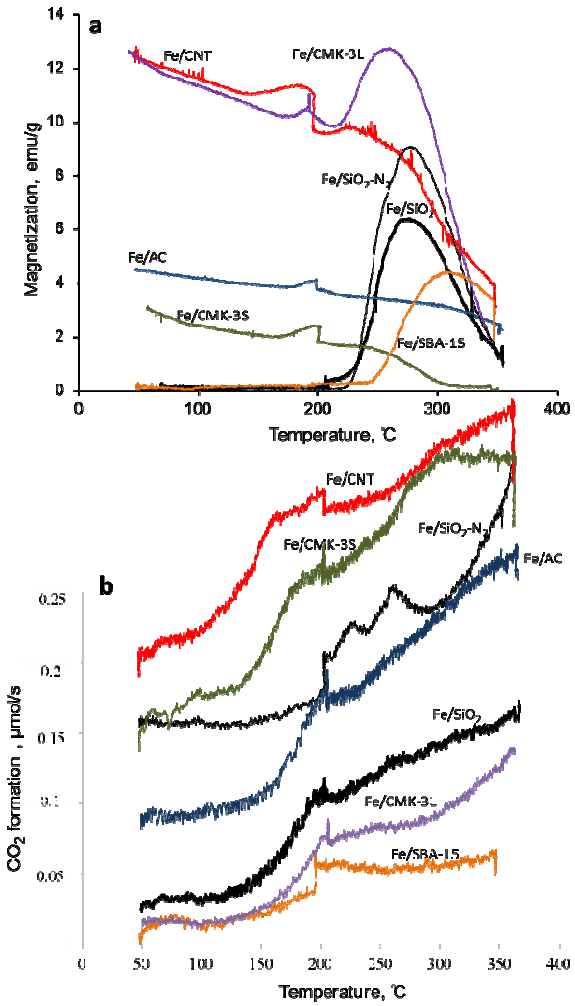

Figure 6-8. Catalyst magnetization (a) and CO_2 formation rates (b) during heating in the flow of CO. The CO_2 formation rates are offset for clarity.

Note that magnetization did not increase significantly over Fe/CNT, Fe/AC and Fe/CMK-3S during CO treatment (Figure 6-8a). This fact might be explained by

transformation of ferrimagnetic oxide phases already presented in the calcined catalysts into ferromagnetic iron carbide during heating in CO. The overall catalyst magnetization can be only very slightly affected by this process.

Analysis of CO_2 formation curves during temperature ramping in CO is in agreement with this assumption (Figure 6-8b). CO_2 forms already starting from 100°C with exponential increase in the rate of formation up to 200 °C. Interestingly, the CO_2 release corresponds to the increase in magnetization for most of catalysts. CO_2 released in this process can be attributed to carbon monoxide disproportionation, which produces on one hand CO_2 and on other hand iron carbides and carbon species. Note that carbon deposition also occurs over 250 °C when iron carbide formation should be already completed.

The magnetization of Fe/SiO_2 and Fe/SBA-15 drops to zero after extended exposure to CO at 350 °C, while Fe/CNT and Fe/AC keep significant residual magnetization at this temperature. This indicates the presence of ferromagnetic species in Fe/CNT and Fe/AC with the Curie temperature higher than that for χ-Fe_5C_2. Possible ferromagnetic phases under these conditions could be magnetite, metallic iron or other iron carbides. Since formation of metallic iron is not expected after treatment in CO at 350 °C, the residual magnetization can be due to either residual magnetite or another form of iron carbide.

The magnetization data are also consistent with XPS results. XPS detected the presence of noticeable amounts of Fe_3O_4 in carbidized Fe/CNT catalysts after activation in CO (Figure 6-7). High stability of Fe_3O_4 in CNT might be tentatively explained by stabilization of dispersed Fe_3O_4 over carbon support. Indeed, Bengoa et al [30] observed stabilization of magnetite with supermagnetic behavior over carbon support with high surface area in comparison with full transformation of magnetite into α-Fe over low surface area glass carbon. The presence of stable magnetite phase in CNT was previously shown by Chen [8] and Abbaslou [23]. Preparation of magnetic CNT composites has attracted a lot of attention because of their potential uses in magnetic data storage and in magnetic force microscopy as nanoprobes [24]. Some of the procedures are based on interaction of magnetite nanoparticles with surface defects and carboxylic defect groups on the CNT surface [25, 26]. Electrostatic interaction may be also responsible for the stabilization of magnetite nanoparticles taking into account the SP2 structure of the CNTs [25, 26].

Figure 6-9 shows variation of magnetization during cooling of the samples after treatment in CO at 350°C. A significant increase in magnetization is observed for most of catalysts when the temperature becomes lower than 250°C. This confirms once again preferential formation of χ-Fe_5C_2 during catalyst activation in CO. Indeed, the Curie

temperature of χ-Fe_5C_2 is in the range 200-250 °C in comparison with the Curie temperature of magnetite and iron at 580 and 770 °C, respectively (Table 2-1) [53]. Higher magnetization at room temperatures was observed on Fe/CMK-3L, Fe/CNT, Fe/SBA-15, Fe/SiO_2 and Fe/SiO_2-N_2 activated in carbon monoxide (Figure 6-7). This is probably due to large concentrations of well-crystallized iron carbide phase in the catalysts. Lower magnetization observed for the Fe/CMK-3S catalyst could be attributed to the lower extent of carbidization. Indeed, Mössbauer spectrometry shows (Figure 6-6) smaller fraction of carbide and higher concentration of Fe^{3+} species in this sample. Fe/AC does not show significant increase in the magnetization during cooling down, although, some concentration of iron carbide can be detected in this catalyst after CO treatment by XRD. Low magnetization might be the result of the formation of highly dispersed carbide phase on the surface of stable magnetite phase. Magnetite in this sample can be stabilized by surface functional groups of the carbon support such as hydroxyls (-OH), carboxyls (-COOH) and carbonyls (C=O) (Figure 1). The strong interaction of Fe with activated carbon with formation of Fe-O-C linkage was proposed earlier by Phillips and co-workers [28].

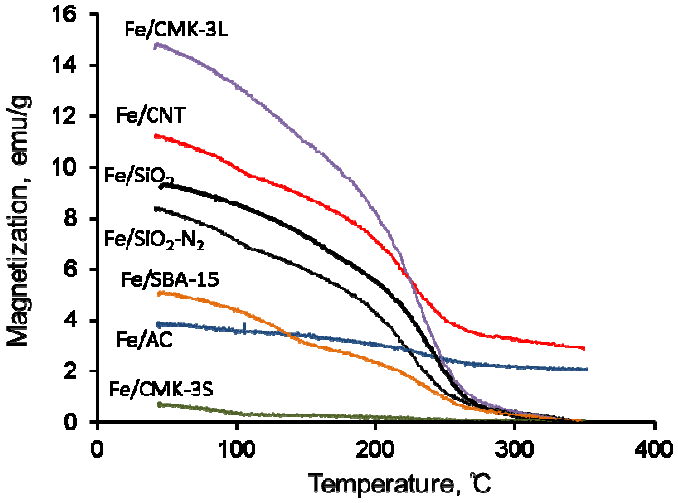

Figure 6-9. Catalyst magnetization during cooling down after CO treatment at 350°C.

TEM has provided further information about interaction between Fe and carbon supports in CNT and CMK-3. Figure 6-4 shows that after the nitrate decomposition, iron oxide particles are observed inside or outside of the carbon nanotubes with their higher fraction located inside of the CNT channels. In contrast to CNT, activation in CO leads to formation of carbon layer on the surface of carbide nanoparticles but without its deep encapsulation into CMK-3 support. Figure 6-4 shows that after the catalytic test the encapsulation of iron

nanoparticles in CNT is even enhanced. At the same time, no encapsulation of iron nanoparticles was observed in the CMK-3 supported catalysts after their exposure to the reaction conditions (Figure 6-4).

Figure 6-10 displays a tentative outline of the evolution of different iron species in silica and carbon supported catalysts during the catalyst synthesis, activation and catalytic test. In silica supported catalysts, impregnation followed by calcination results in preferential formation of α-Fe_2O_3, while decomposition of iron nitrate in carbon materials most probably leads to Fe_3O_4 with possible presence of maghemite phase. Catalyst activation of silica and carbon supported catalysts in carbon monoxide converts iron oxides into iron carbides (presumably χ-Fe_2C_5 carbide). In the case of silica based samples a considerable concentration of iron silicate was detected in the activated catalysts. Smaller iron particles in CMK-3S exhibit lower extent of carbidization. Interestingly, carbon nanotubes and activated carbon can stabilize to some extent magnetite in the presence of carbon monoxide at higher temperatures. This enhanced stability of magnetite which does not completely carbidize in these catalysts could be attributed to both strong interaction between magnetite and carbon support and partial encapsulation of iron oxide nanoparticles in the CNT and active carbon porous structure.

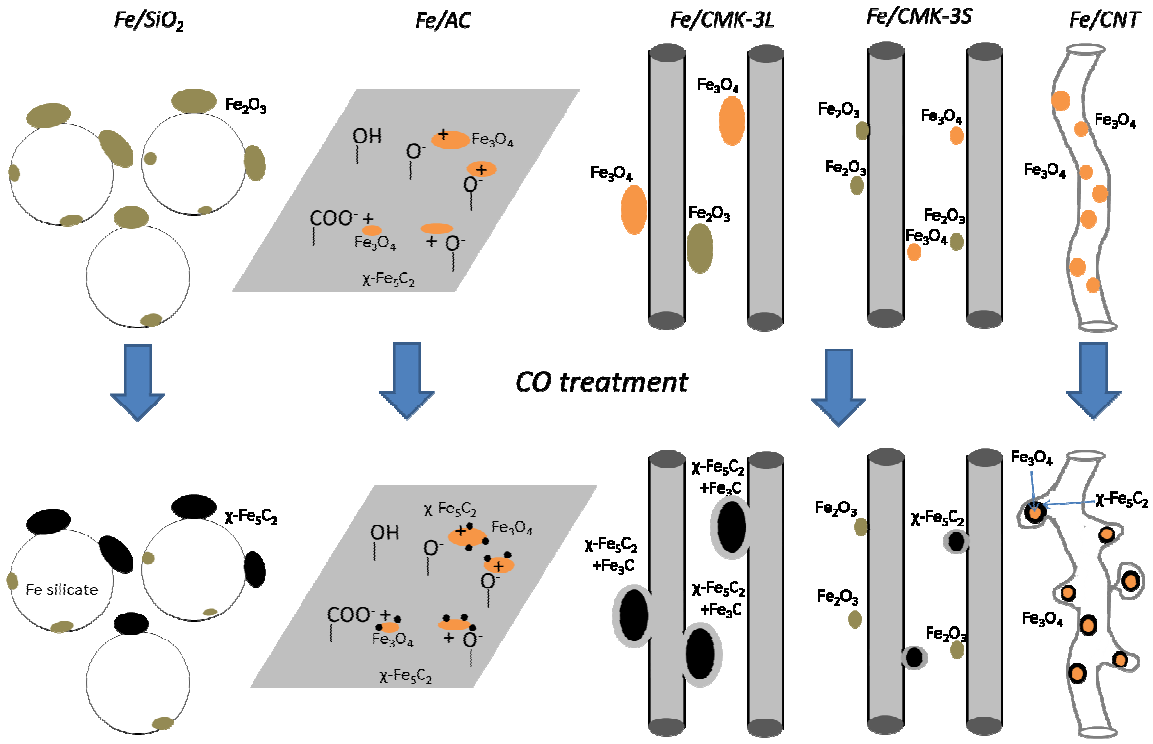

Figure 6-10. Iron species on different supports before and after CO activation.

6.3 FT performance over carbon and silica supported Fe catalysts

The catalytic data are shown in Figures 6-11 and Table 6-3. Methane, light olefins, light paraffins, C_5^+ hydrocarbons and carbon dioxide were the main products of FT synthesis on iron catalysts under these conditions. Silica supported catalysts showed lower activity in comparison with carbon-based counterparts. The catalytic activities of Fe/SBA-15 and Fe/SiO_2 with larger pores are rather similar (iron time yield of 35-39 mol_{CO} mol_{Fe}^{-1} h^{-1}). Iron nitrate decomposition in nitrogen instead of air did not affect the iron time yield to any noticeable extent in the Fe/SiO_2 catalyst (Table 6-3). Lower activity of silica supported catalysts relative to carbon supported counterparts could be due to a more difficult iron carbidization. Indeed, XPS and Mössbauer spectrometry showed higher fractions of inert iron silicate.in silica-based catalysts.

Table 6-3. Catalytic properties of catalysts after CO and H_2 pretreatment (P = 2 MPa, H_2/CO = 2.1, $GHSV$ = 16 L h^{-1} g_{cat}^{-1}, T = 300 °C)

Test	Catalysts	X_{CO},%	Iron time yield, mol_{CO} /mol_{Fe}·h	S_{CO2} ,%	Product distribution, (% C_{at}, CO_2 free)				C_2-C_4 Olefin/ Paraffin
					CH_4	C_2-C_4 olefins	C_2-C_4 paraffins	C_{5+}	
1	Fe/SBA-15	25.7	35.5	10.2	21.0	14.3	20.9	43.8	0.7
2	Fe/SiO_2	28.5	39.4	13.5	12.8	20.6	12.5	54.1	1.6
3	Fe/SiO_2[a]	38.8	26.8	19.1	14.6	20.2	17.4	47.8	1.1
4	Fe/SiO_2 -N_2	24.4	33.7	11.7	13.5	19.4	14.6	52.5	1.3
5	Fe/CMK-3S	49.7	68.6	21.5	12.7	15.5	23.5	48.3	0.7
6	Fe/CMK-3S[b]	27.4	75.7	15.4	12.1	15.4	17.7	54.7	0.9
7	Fe/CMK-3L	38.5	53.2	19.1	15.3	18.3	22.4	44.0	0.8
8	Fe/AC	64.0	88.4	34.1	7.8	21.2	17.3	53.7	1.2
9	Fe/AC[b]	37.6	103.9	20.8	12.2	18.0	19.5	50.3	0.9
10	Fe/CNT	85.4	117.9	30.0	8.7	20.7	14.7	55.9	1.4
11	Fe/CNT[b]	31.7	87.6	16.2	22.2	15.7	26.9	35.3	0.6

[a] GHSV was changed to 8 L h^{-1} g_{cat}^{-1}

[b] GHSV was changed to 32 L h^{-1} g_{cat}^{-1}

The activity of carbon supported samples decreases from CNT to CMK-3 in the following sequence: Fe/CNT>Fe/AC>Fe/CMK-3S>Fe/CMK-3L. Under *iso*-GHSV conditions (GHSV=16 L h^{-1} g^{-1}), Fe/CNT exhibits CO conversion of 85 % (Table 6-3). Fe/AC shows a slightly lower carbon monoxide conversion (60 %). Carbon monoxide conversion over Fe/CMK-3S with smaller iron particles was slightly higher than on Fe/CMK-3L containing less dispersed iron species (Tables 6-1 and 6-3). However the increase in FT reaction rate on

Fe/CMK-3S relative to Fe/CMK-3L was much smaller than could be expected from the iron particle sizes. The lower-than-expected activity of Fe/CMK-3S might be explained by low extent of carbidization of smaller iron nanoparticles compared to larger counterparts observed by Mössbauer spectrometry (Figure 6-6, Table 6-2).

Note that Fe/AC and Fe/CMK-3 catalysts show a slight increase in carbon monoxide conversion with time on stream (Figure 6-11). Iron catalysts could undergo "self-organization" during FT synthesis. The self-organization of iron catalysts principally consists of optimization of iron carbide phase composition and could lead to some enhancement in FT reaction rate. Interestingly, no major sintering was observed by TEM after catalytic tests (Figure 6-4, Table 6-1). The effects of catalytic support on the catalytic performance of iron catalysts in FT synthesis can be interpreted in terms of different iron phase composition rather than in terms of different iron dispersion. Indeed, the catalysts also did not show any significant dependence of the catalytic activity on the size of the oxide or carbide particles. For example, Fe/CNT and Fe/SiO_2 have similar iron particle sizes (Table 6-1), but exhibit rather different FT reaction rates (Table 6-3).

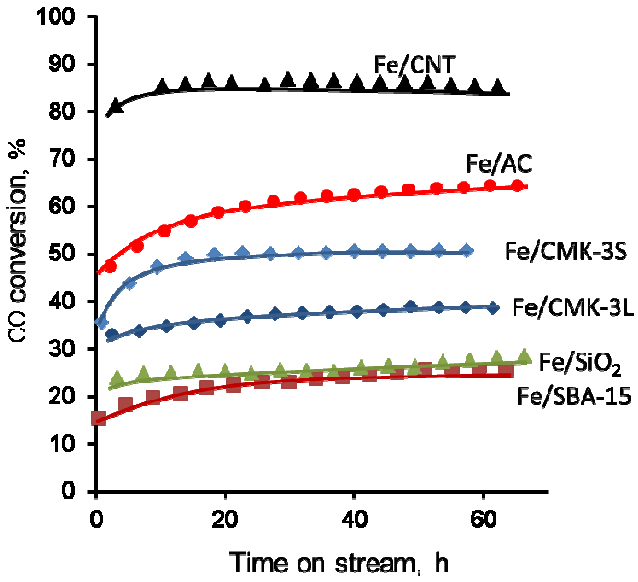

Figure 6-11. Catalytic activity of iron catalysts (P =2 MPa, H_2/CO = 2.1, $GHSV$ = 16 L h^{-1} g_{cat}^{-1}, T = 300°C)

Interestingly, the highest activity is observed over Fe/CNT and Fe/AC samples. Both catalysts exhibit residual magnetization at 350 °C. This suggests possible presence in these catalysts of residual Fe_3O_4 species. The high activity of CNT was explained earlier by Bao and coworkers [8] by a confinement effect of iron particles in the CNT channels. Thus, it was

shown that the confinement of iron inside of the CNT with unique electronic properties significantly modified the catalytic performance and led to more active, selective and stable FT catalysts [29, 30]. The higher activity of small carbide "nodules" forming shell on the surface of the core magnetite phase was proposed as an efficient catalytic system on silica supported catalysts [31-33]. Our results suggest that magnetite itself is inactive in FT synthesis. Indeed, the catalytic tests conducted with the catalysts containing only magnetite phase (without CO treatment) showed zero activity in FT synthesis. However, the composite of magnetite–carbide with highly active defected carbide phase could be involved in FT reaction. The higher activity over Fe/CNT and Fe/AC might be explained by formation of these iron carbide-magnetite composites.

Table 6-3 also displays carbon monoxide conversion data obtained on Fe/SiO_2, Fe/AC, Fe/CMK-3S and Fe/CNT at different GHSV. The methane and CO_2 selectivities were plotted as functions of carbon monoxide conversion on these catalysts (Figure 6-12). Higher carbon monoxide conversion leads to higher CO_2 and lower methane selectivities. Increase in the CO_2 selectivity at higher CO conversion might be explained by higher contribution of the WGS reaction due to increase in the amount of water. Note that some amounts of CO_2 can be also produced by Boudouard reaction, which is thermodynamically favorable under the reaction conditions. In agreement with previous report [34], lower methane selectivity can be explained by suppression of methanation in the presence of higher water pressures at high CO conversion level. The relation between C_2-C_4 olefin to paraffin ratio and carbon monoxide conversion for silica and carbon supported catalysts is displayed in Figure 6-12b. For all studied catalysts the ratio is in the range of 0.6 to 1.4 with slight increase with an increase in CO conversion. All the studied catalysts (with exception for Fe/SiO_2) show similar relations between methane, carbon dioxide selectivities and olefin to paraffin ratio on one hand, and on other hand, carbon monoxide conversion. This suggests the presence of similar active phases for carbon monoxide hydrogenation, which could be probably associated to χ-iron carbide/magnetite composites. Silica supported catalysts showed higher olefin to paraffin ratio than carbon–supported counterparts (Figure 6-12b). A higher fraction of Fe^{3+} species of iron silicate was identified in silica supported catalysts by XPS and Mossbauer spectrometry. Though the observed selectivity deviations on silica supported catalysts probably require further investigations, interaction of iron carbides with Fe^{3+} ions (instead of magnetite) could modify the electronic properties of active sites (similar to alkali metals) and could result in partial suppression of the hydrogenation activity.

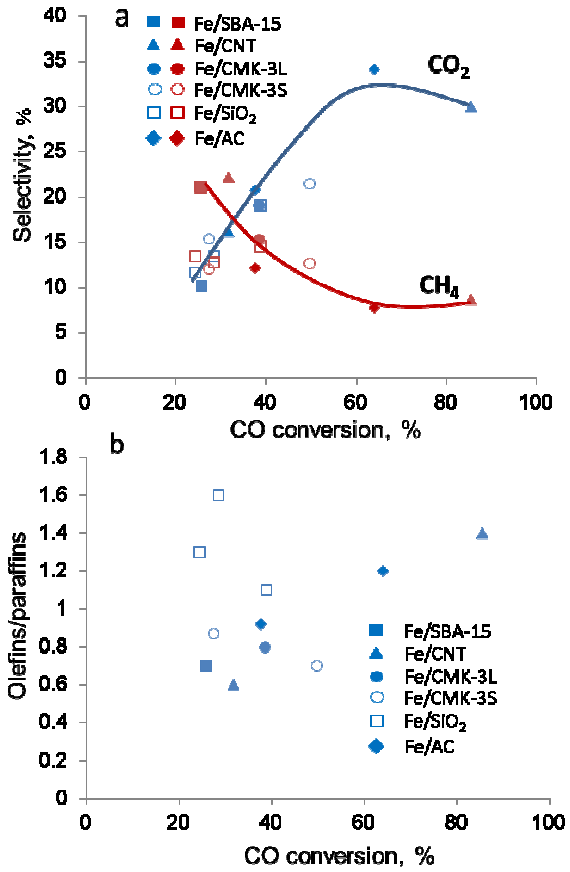

Figure 6-12. Selectivity to methane and CO_2 (a) and C_2-C_4 olefin to paraffin ratio (b) as functions of CO conversion (P = 2 MPa, H_2/CO = 2.1, $GHSV$ = 16 L h^{-1} g_{cat}^{-1}, T = 300 °C)

6.4 Conclusions

Silica and carbon supported iron catalysts show the presence of different iron species at different catalyst preparation and activation stages. The chemical composition and texture of the support affect iron particle size, iron carbidization, catalyst phase composition and finally catalytic performance in carbon monoxide hydrogenation. After iron nitrate decomposition, α-Fe_2O_3 was a dominant phase in the silica supported catalysts, while the carbon materials contain magnetite/maghemite. Catalyst activation in carbon monoxide results in conversion of iron oxides into mostly χ-Fe_2C_5 carbide. The extent of carbidization seems to be higher in carbon than in silica supported catalysts.

The catalytic performance iron species on different supports principally depends on iron phase composition rather than on iron dispersion. Higher activity was observed on the catalysts supported by carbon nanotubes and active carbon, which show the presence of iron carbide-magnetite composites.

6.5 Reference

[1] H.M. Torres Galvis, J.H. Bitter, T. Davidian, M. Ruitenbeek, A.I. Dugulan, K.P. de Jong, J. Am. Chem. Soc., 134 (2012) 16207-16215.

[2] H.M. Torres Galvis, J.H. Bitter, C.B. Khare, M. Ruitenbeek, A.I. Dugulan, K.P. de Jong, Science, 335 (2012) 835-838.

[3] H.M. Torres Galvis, A.C.J. Koeken, J.H. Bitter, T. Davidian, M. Ruitenbeek, A.I. Dugulan, K.P. de Jong, Catal. Today, 215 (2013) 95-102.

[4] H.M. Torres Galvis, A.C.J. Koeken, J.H. Bitter, T. Davidian, M. Ruitenbeek, A.I. Dugulan, K.P. de Jong, J. Catal., 303 (2013) 22-30.

[5] J.-D. Xu, K.-T. Zhu, X.-F. Weng, W.-Z. Weng, C.-J. Huang, H.-L. Wan, Catal. Today, 215 (2013) 86-94.

[6] Z. Yang, X. Pan, J. Wang, X. Bao, Catal. Today, 186 (2012) 121-127.

[7] J. Kang, S. Zhang, Q. Zhang, Y. Wang, Angew. Chem. Int. Ed., 48 (2009) 2565-2568.

[8] W. Chen, Z. Fan, X. Pan, X. Bao, J. Am. Chem. Soc., 130 (2008) 9414-9419.

[9] G. Yu, B. Sun, Y. Pei, S. Xie, S. Yan, M. Qiao, K. Fan, X. Zhang, B. Zong, J. Am. Chem. Soc., 132 (2010) 935-937.

[10] R.M.M. Abbaslou, A. Tavassoli, J. Soltan, A.K. Dalai, Appl. Catal. A, 367 (2009) 47-52.

[11] J. Lu, L. Yang, B. Xu, Q. Wu, D. Zhang, S. Yuan, Y. Zhai, X. Wang, Y. Fan, Z. Hu, ACS catal., 4 (2014) 613-621.

[12] A.Y. Khodakov, A. Griboval-Constant, R. Bechara, V.L. Zholobenko, J. Catal., 206 (2002) 230-241.

[13] V.K. Saini, M. Andrade, M.L. Pinto, A.P. Carvalho, J. Pires, Sep. Purif. Technol., 75 (2010) 366-376.

[14] W. Dai, M. Zheng, Y. Zhao, S. Liao, G. Ji, J. Cao, Nanoscale research letters, 5 (2010) 103-107.

[15] R.J. Dombrowski, D.R. Hyduke, C.M. Lastoskie, Langmuir, 16 (2000) 5041-5050.

[16] J. Zawadzki, Carbon, 18 (1980) 281-285.

[17] A. Macías-García, C. Valenzuela-Calahorro, V. Gómez-Serrano, A. Espínosa-Mansilla, Carbon, 31 (1993) 1249-1255.

[18] C. Moreno-Castilla, M.V. López-Ramón, F. Carrasco-Marín, Carbon, 38 (2000) 1995-2001.

[19] S. Biniak, G. Szymański, J. Siedlewski, A. Świątkowski, Carbon, 35 (1997) 1799-1810.

[20] P. Scherrer, Phys., 2 (1918) 98-100.

[21] H. Itoh, T. Sugimoto, J. Colloid Interface Sci., 265 (2003) 283-295.

[22] W. Kim, C.-Y. Suh, S.-W. Cho, K.-M. Roh, H. Kwon, K. Song, I.-J. Shon, Talanta, 94 (2012) 348-352.

[23] R.M. Malek Abbaslou, J. Soltan, A.K. Dalai, Fuel, 90 (2011) 1139-1144.

[24] Z. Sun, Z. Liu, Y. Wang, B. Han, J. Du, J. Zhang, J. Mater. Chem., 15 (2005) 4497-4501.

[25] M.N. Tchoul, W.T. Ford, G. Lolli, D.E. Resasco, S. Arepalli, Chem. Mater., 19 (2007) 5765-5772.

[26] D. Shi, J.P. Cheng, F. Liu, X.B. Zhang, J. Alloy. Compd., 502 (2010) 365-370.

[27] C.P. Hunt, B.M. Moskowitz, S.K. Banerjee, Magnetic Properties of Rocks and Minerals, in: Rock Physics & Phase Relations, American Geophysical Union, 2013, pp. 189-204.

[28] A.A. Chen, M.A. Vannice, J. Phillips, J. Phys. Chem., 91 (1987) 6257-6269.

[29] R. Haddon, Science, 261 (1993) 1545-1550.

[30] D. Ugarte, A. Chatelain, W. De Heer, Science, 274 (1996) 1897-1899.

[31] L.A. Cano, M.V. Cagnoli, J.F. Bengoa, A.M. Alvarez, S.G. Marchetti, J. Catal., 278 (2011) 310-320.

[32] S. Li, W. Ding, G.D. Meitzner, E. Iglesia, J. Phys. Chem. B, 106 (2002) 85-91.

[33] J. Xu, C.H. Bartholomew, J. Phys. Chem. B, 109 (2005) 2392-2403.

[34] C.N. Satterfield, R.T. Hanlon, S.E. Tung, Z.M. Zou, G.C. Papaefthymiou, Ind. Eng. Chem. Prod. Res. Dev., 25 (1986) 407-414.

Chapter 7. The effect of Na addition over different supports in high temperature Fischer-Tropsch synthesis on iron catalysts

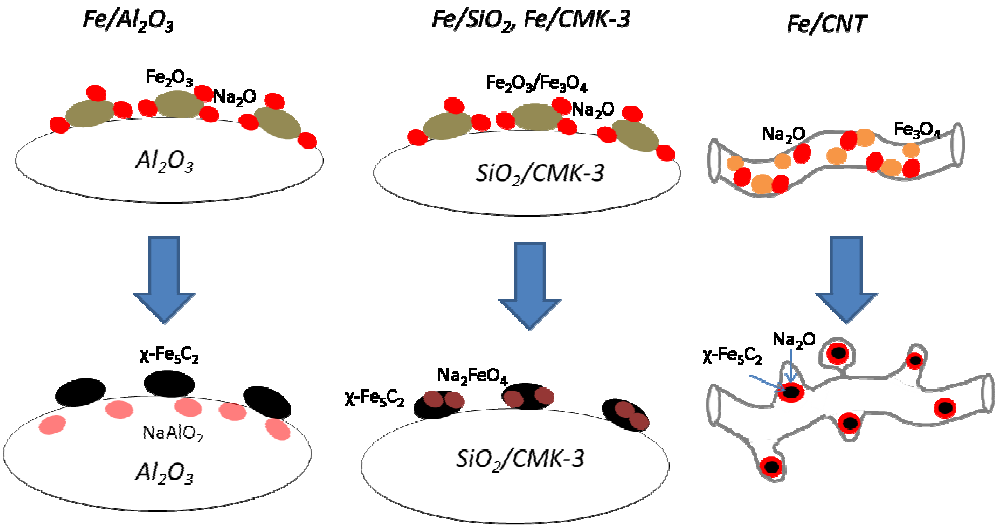

Abstract: The effect of sodium addition over different types of supports with iron has been studied in high temperature Fischer-Tropsch synthesis. The interaction of Na with the catalysts depends strongly on the amount of added Na and type of the support. In the case of alumina, the effect of Na over catalytic properties is weak due to the strong interaction with support. Over silica and CMK-3 iron oxide interacts with Na with formation of inactive mixed oxides but with partial suppression of hydrogenation activity and high olefin/paraffin ratio over rest carbide. The strong interaction of CNT with Fe results in formation of stable carbide but with strong effect of Na which results in the high contribution of olefins for short and long chain hydrocarbons. Excessive Na addition results in a decline in CO conversion.

This Chapter is based on the following publication:

K. Cheng, V. V. Ordomsky,* B. Legras, M. Virginie, S. Paul, Y. Wang and A. Y. Khodakov,* *Appl. Catal. A*, (**2014**) in preparation.

7.1 Introduction

The FT selectivity to light olefins over pure Fe based catalyst is not high enough to be interesting for industrial implementation [1]. The use of promoters is necessary for Fe catalysts in order to increase the selectivity towards desired products in FTS [2]. Different types of promoters have been proposed in the literature to increase the selectivity to olefins like sodium [3, 4], potassium [2], zinc [5], copper [5], vanadium [6], and sulfur [7, 8]. Sodium has been found to be one of the most effective promoters. Addition of it leads to significant increase of the olefin to paraffin ratio, WGS activity and decrease methane selectivity [3, 4, 9]. The effect of sodium is usually explained by decrease of the strength of C-O bonds in the presence of Na increasing the coverage of dissociated CO on the surface [4, 8, 10, 11]. High carburization of the surface results in the suppression of the secondary hydrogenation of olefins and increase of the chain growth probability with suppression of the methanation. The effect has been shown to have an optimum with increase of the concentration of the sodium [4, 11, 12]. The higher concentration of Na had detrimental effect inhibiting carbidisation of Fe which results in decrease of the activity and formation of short chain hydrocarbons [12].

The research over Fe based catalysts is mainly has been focused on the bulk Fe catalysts promoted by metals due to the easy preparation and low cost of this type of catalysts [13]. However, these catalysts cannot be as efficient as supported catalysts due to the lower dispersion and low homogeneity of the catalytic sites. Recently, significant progress has been reported by the Utrecht group [14, 15] in the development of new efficient iron catalysts promoted by sodium and sulfur for efficient synthesis of light olefins with high activity and selectivity over catalysts with weak interaction between iron and supports. The authors have used α-alumina or carbon nanofiber supports. However, it is still not clear what is the role of support in the effect of promoter over iron catalyst and why some supports show high efficiency during application of promoters and others do not.

In Chapter 6 we studied the effect of supports over state of Fe active sites during high temperature FT synthesis. This work is directed on the continuation of this work with the main focus on the interaction between sodium as promoter with support and iron. We have studied most common types of supports used in industry like silica, alumina in comparison with new inert carbon supports CMK-3 and CNT.

7.2 Results and discussion

7.2.1 Structure and surface groups of catalysts

The textural properties of used supports are displayed in Figure 7-1 and Table 7-1. All the four samples showed hysteresis loop which indicates mesopores [16]. Commercial amorphous silica (SiO_2) possesses large mesopores formed by volume between globules with the surface area of about 300 $m^2\ g^{-1}$. γ-Al_2O_3 has lower surface area (186 $m^2\ g^{-1}$). CMK-3 is formed by interconnected carbon rods and has a surface very similar to those of SBA-15 (1326 $m^2\ g^{-1}$) with the centralized pore size about 3.8 nm. The nanotubes of the acid treated CNT have uniform diameters of about 7 nm. The relatively high surface area (163 $m^2\ g^{-1}$) indicates that nanotubes have open caps due to acid treatment [17].

Table 7-1. N_2 Physical Adsorption-desorption and XRD catalyst characterization

Samples	N_2 adsorption over supports					Iron oxide[a] or carbide diameter (XRD) with different Na/Fe ratio, nm		
	S_{BET}, $m^2\ g^{-1}$	S_{mic}, $m^2\ g^{-1}$	V_{tot}, $cm^3\ g^{-1}$	V_{mic}, $cm^3\ g^{-1}$	Pore size, nm	0	0.1	0.5
Fe/SiO_2	307	25	1.31	0.01	17.5	13.7 (6.7)	13.9 (4.8)	13.9(4.0)
Fe/CMK-3	1326	557	1.32	0.12	3.8	6.1 (4.0)	6.6 (5.0)	6.8 (4.4)
Fe/Al_2O_3	186	5	0.51	0.0	11.0		-	-
Fe/CNT	163	17	0.56	0.01	7	16.3(6.1)	20.3(4.1)	18.0(4.6)

[a] Based on the diffraction peaks of hematite (H) or magnetite (M)

Iron nitrate was decomposed using calcination in air (for silica and alumina supported catalysts) or in nitrogen (for carbon supports). Silica and alumina are active supports with functional groups on the surface which might result in the interaction with supported metals. The possible interaction of metals with silica and alumina supports has been studied by FTIR spectroscopy (Figure 7-2). The silica is characterized by the following set of bands: 3440, 1387, 1350, 1109 and 808 cm^{-1}. Absorption bands at 1109 and 808 cm^{-1} might be assigned to Si-O-Si asymmetric stretching and bending vibrations, respectively [18]. The bands at 1387 and 1350 cm^{-1} correspond to carbonate or carboxylate surface species formed due to adsorption of atmospheric CO_2 (symmetric stretching) [19]. The band at 3440 cm^{-1} corresponds to stretching of silanol groups [20]. Strong interaction of Na with the silica could result in the formation of sodium silicates which would be visible by the characteristic bands [21]. However, the spectra of Fe impregnated and Na treated catalysts do not show any

significant changes in the spectra in comparison with the parent silica except slight increase of the hydroxyl groups and adsorbed CO_2. This fact might be explained by low interaction of Na with silica with possible formation of single or mixed oxides on the surface.

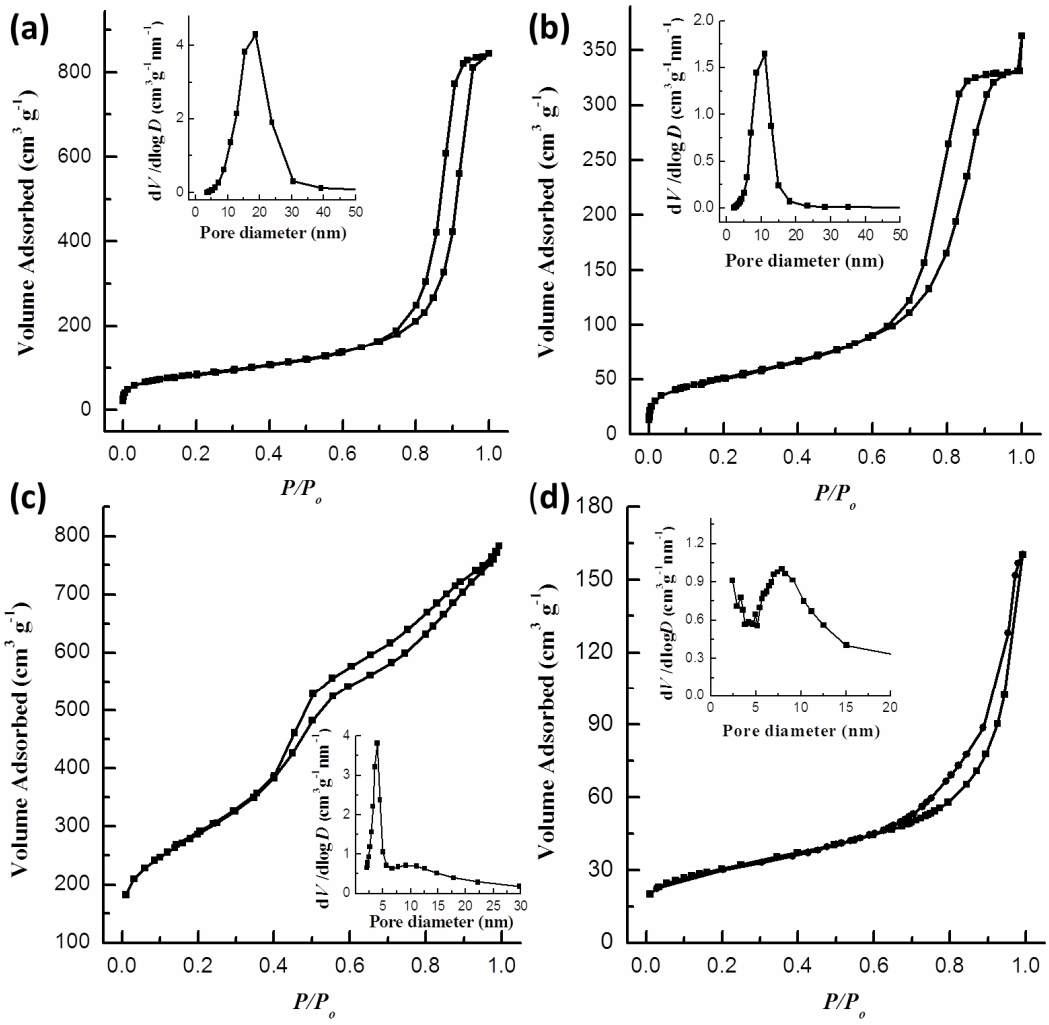

Figure 7-1. N_2 adsorption-desorption isotherms and distribution of pore size for SiO_2 (a), Al_2O_3 (b), CMK-3 (c) and CNT (d).

Parent alumina infrared spectrum has only bands at 3440, 1387 and 1350 cm^{-1} related to hydroxyl groups and adsorbed CO_2. Presence of Fe and Na results in significant changes in the spectra in comparison with silica. Indeed the new broad band appears at 1090 cm^{-1} which might be assigned according to the literature to symmetric stretching bands of carbonates [22]. This might be result of the strong interaction of Fe with alumina with formation of Fe-O-Al bonds and basic OH groups which interacts with CO_2. The presence of Na leads to appearance of additional bands at 1078, 984 and 884 cm^{-1} which might be explained by carbonates formed over sodium aluminate and ferrite.

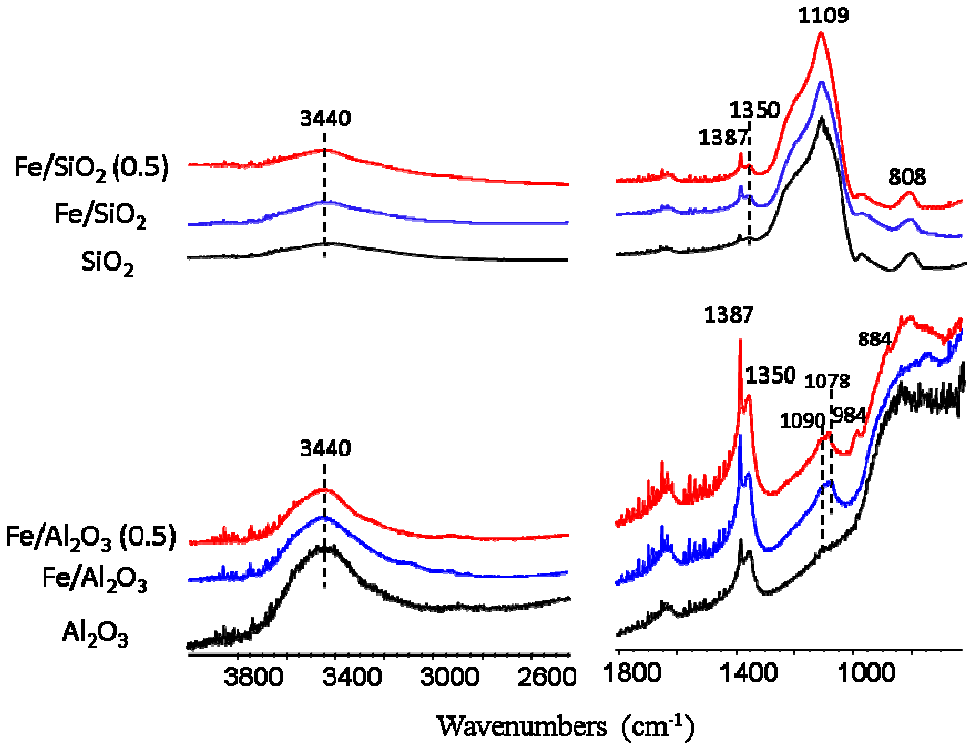

Figure 7-2. IR spectra of silica, alumina and catalysts on their basis

7.2.2 Activation with CO

XRD patterns of the calcined catalysts are shown in Figure 7-3. The crystallite size of iron oxides was evaluated from the Scherrer equation (Table 7-1). Fe_2O_3 is the main iron phase in calcined Fe/SiO_2 with relatively large oxide particles (13.9 nm). In the case of alumina only very weak bands of Fe_2O_3 is observed which might be explained by strong interaction with alumina observed by FTIR (Figure 7-2). At the same time, decomposition of iron nitrate over CNT in nitrogen selectively results in formation of magnetite (Fe_3O_4) with sizes of nanoparticles about 16 nm. For iron catalysts supported on CMK-3, very weak and broad magnetite peaks are observed. CMK-3 has large surface area (1326 m^2 g^{-1}) and abundant oxhydryl groups which are beneficial for metal dispersion [23].

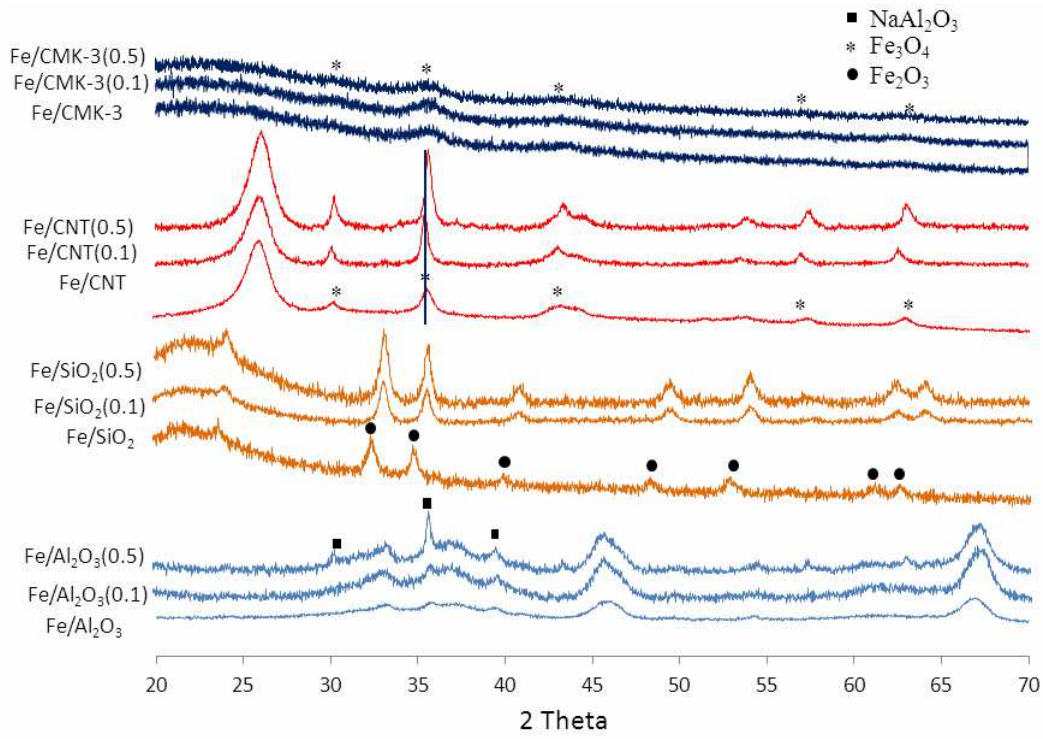

Figure 7-3. XRD patterns of samples before CO treatment.

Presence of sodium does not lead to significant changes in the sizes of oxide nanoparticles (Table 7-1) but leads to other changes of the spectra. Treatment of alumina based catalysts with sodium results in the appearance of the peaks at 30.2, 35.6 and 39.4° assigned to sodium aluminate [14] which support FTIR results. In the case of silica samples presence of sodium results in shift of hematite peaks for about 2° to higher 2θ angles. It might indicate on the incorporation of sodium in the framework of hematite which should result in the structural deformation of the lattice [15]. It is interesting to note that shift happens already after addition of 0.1 Na/Fe. Addition of sodium in the case of CNT does not lead to changes in the XRD spectra (Figure 7-3).

The XRD patterns of iron catalysts activated in carbon monoxide are shown in Figure 7-4. Treatment of catalysts in CO at 623 K results in the formation of iron carbide with a broad diffraction peak at around 43° (Figure 7-4). This broad peak probably corresponds to the superposition of the most intense diffraction peaks of several iron carbides: most likely χ-Fe_5C_2 and ε-Fe_2C [24]. Note however that a significant decrease in the absolute sizes of carbide particles in comparison with the oxide counterparts is observed by XRD after CO treatment over CNT and CMK-3 (Table 7-1), while TEM does not show any major decrease in iron particle size after carbidization (Figure 7-5). This observed discrepancy can be attributed to the limitations of these two techniques. Indeed, XRD measures only the size of

single iron carbide crystallites, while TEM detects both iron individual carbide crystallites and crystallite agglomerates. Large peaks of alumina support hinders peak of carbide over alumina.The size of carbide nanoparticles decreases with increase of the amount of added sodium over Fe/CNT and Fe/SiO_2.

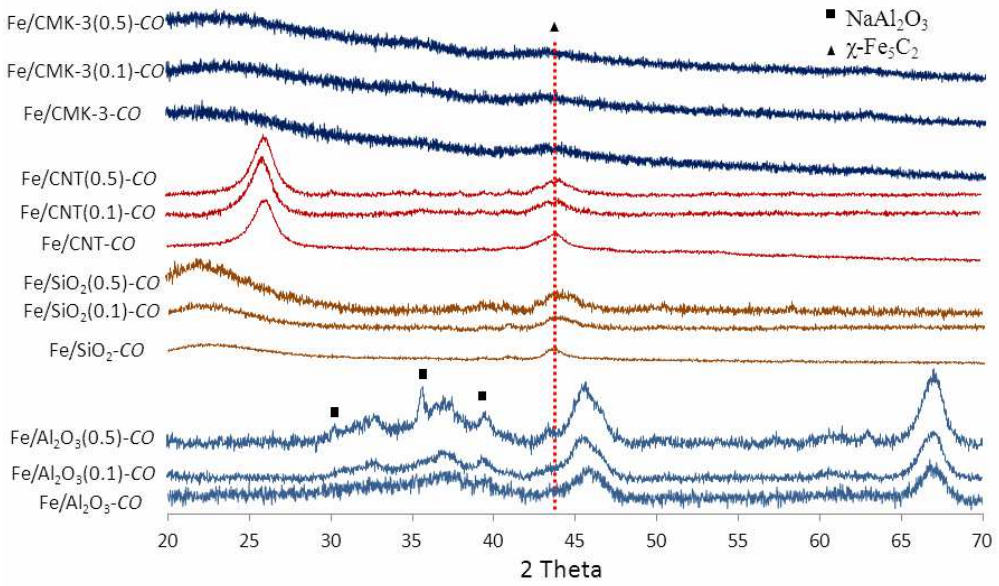

Figure 7-4. XRD patterns of samples after CO treatment.

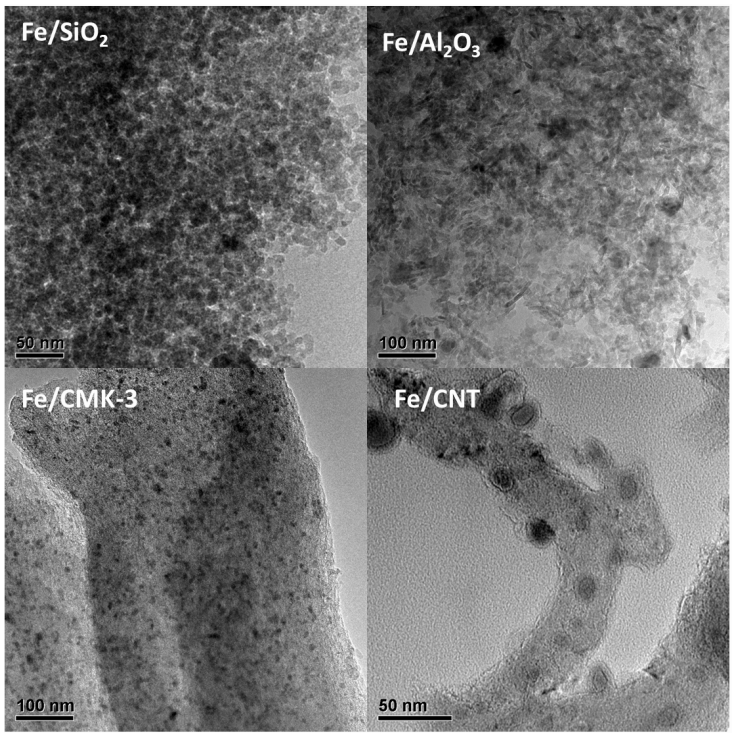

Figure 7-5. TEM images of Fe/SiO_2, Fe/Al_2O_3, Fe/CMK-3 and Fe/CNT after pretreatment with CO at 623 K for 10 h.

7.2.3 Effect of Na introduction on the basicity of catalysts

The interaction between sodium, iron and support should result in the different basicity of the catalysts which has been studied by TPD of CO_2 (Figure 7-6). The intensity of weak, medium, strong and very strong catalyst basic sites are estimated from the area under their TPD curves for the temperature range of 373–523, 523–673, 673–923, and >923 K respectively [25]. The results show that carbon based catalysts possess strong basicity due to the presence of sodium over the catalyst. It means that besides possible interaction of sodium with iron part of impregnated sodium still possesses strong basic properties. In the case of silica support adsorption of CO_2 is significantly smaller in comparison with carbon supports. This fact might be explained taking into account XRD and FTIR results by strong interaction of sodium with iron with formation of mixed oxides less basic in comparison with sodium oxide. Alumina is a support with basic properties due to the presence of surface basic hydroxyls groups [26] which might form carbonates with high temperature of decomposition (Figure 7-6). It makes difficult to conclude about effect of Na. The peak over 1000 K is probably assigned to residual Na_2CO_3 [27].

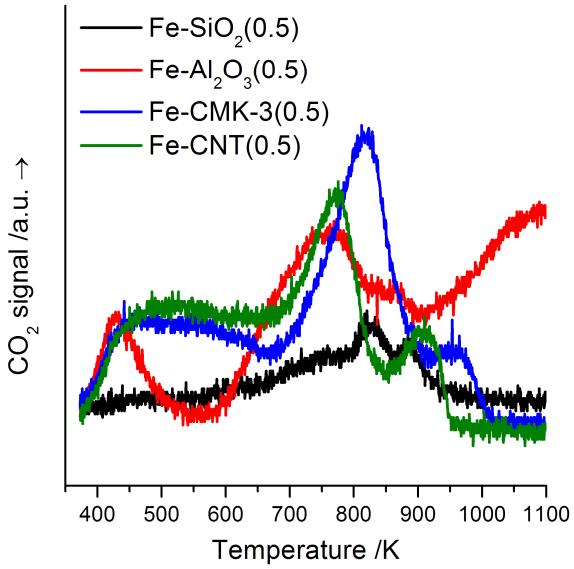

Figure 7-6. TPD of CO_2 over Na promoted catalysts.

7.2.4 Effect of Na introduction on the activity of iron carbides

All these methods like XRD, FTIR, TPD of CO_2, however, do not give direct information about how Na effect on iron carbide. This information might give the method which relates to transformation of carbide like its hydrogenation into methane. This method

has been used earlier for determination of the amount of carbide but analysis of the rate of methane formation might give important information about the activity of carbide in FT synthesis [28, 29]. In order to have information as close as it is possible to reaction conditions the hydrogenation has been conducted at 573 K and 20 bars after CO pretreatment. Figure 7-7 showed that Fe/CNT has the highest initial rate of methane formation with fast decrease in time. It is interesting to note that in the case of silica supported catalyst the rate is almost two times lower but it goes through the maximum. It means that carbide in silica is less accessible or reactive for hydrogenation in comparison with CNT. In the case of alumina the curve is similar to silica based catalysts but without maximum indicating also on the low activity of carbide for hydrogenation. The effect of sodium on the hydrogenation activity was different for different supports. Thus, in the case of CNT the activity decreases in the presence of sodium which means strong interaction of sodium with carbide. At the same time, addition of sodium totally suppresses initial hydrogenation activity of carbide over silica leaving only high time peak. It means that sodium deactivates reactive carbides which support the earlier statement about possible formation of mixed oxides in this case. It is interesting to note that addition of sodium almost does not change hydrogenation activity over alumina. It lies in the line with XRD and FTIR results about preferential sodium interaction with support which should not affect the state of carbide in this case.

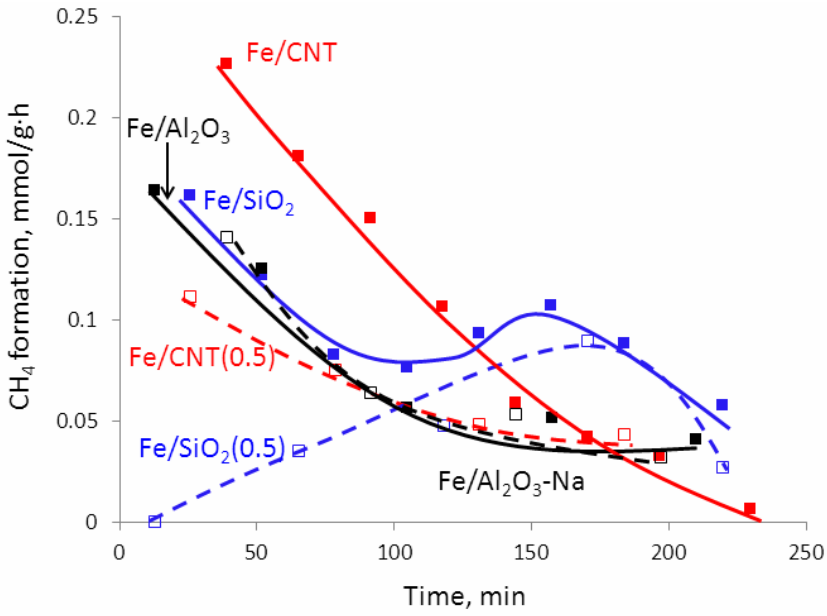

Figure 7-7. Hydrogenation of carbides of sodium promoted and parent catalysts

7.2.5 Fischer-Tropsch synthesis

The catalytic activities and selectivities in Fischer-Tropsch synthesis over catalysts are shown in Figures 7-8 to 7-16 and Table 7-2. Methane, light olefins, light paraffins, C_5^+ hydrocarbons and carbon dioxide were the main products of FT synthesis on iron catalysts under these conditions. Silica based catalyst shows lowest activity in comparison with carbon-based and alumina materials. The low activity of Fe/SiO_2 was explained earlier by formation of inactive silicates and lower degree of Fe carbidization [in chapter 4]. It results in the formation of less reactive carbide which might be observed by low initial rate of hydrogenation of carbide by hydrogen in comparison with Fe/CNT (Figure 7-7). Fe/CNT shows the highest activity (76 %) in comparison with silica, alumina and CMK-3 catalysts. There are several possible reasons of the high activity of Fe/CNT. Bao and coworkers [24] have explained it by confinement effect of iron particles in the CNT channels which results in the different electronic properties of carbides. The other possible reason might be in formation of magnetite-carbide composite with highly defected carbide phase on the surface of magnetite particles stabilized by CNT [2]. In any case it leads to the formation of highly reactive carbide which is easily hydrogenated into methane (Figure 7-7). The low activity of Fe over other carbon based support CMK-3 has been explained by low degree of interaction between carbon and Fe in this case which does not lead to stabilization of magnetite [30]. The catalysts show stable activity during the test (Figure 7-8) with some increase of the activity for Fe/CNT and Fe/Al_2O_3. This effect might be explained by self-organization of iron catalysts at the reaction conditions with modification of iron carbide composition.

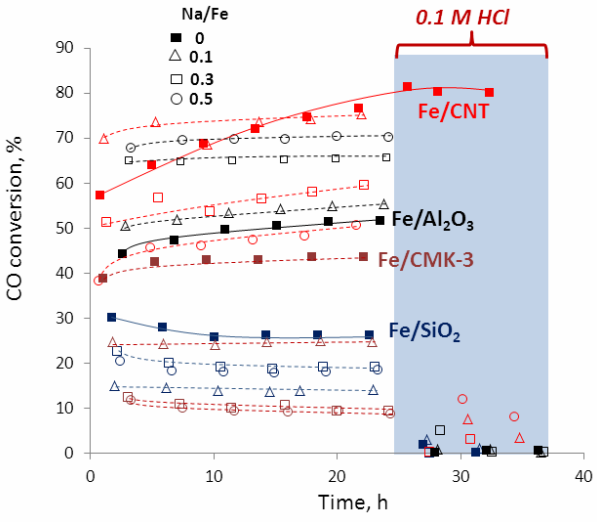

Figure 7-8. Catalytic activity of every iron catalysts (P = 2 MPa, H_2/CO=2.1, GHSV=16 L h^{-1} g^{-1}, T = 573 K)

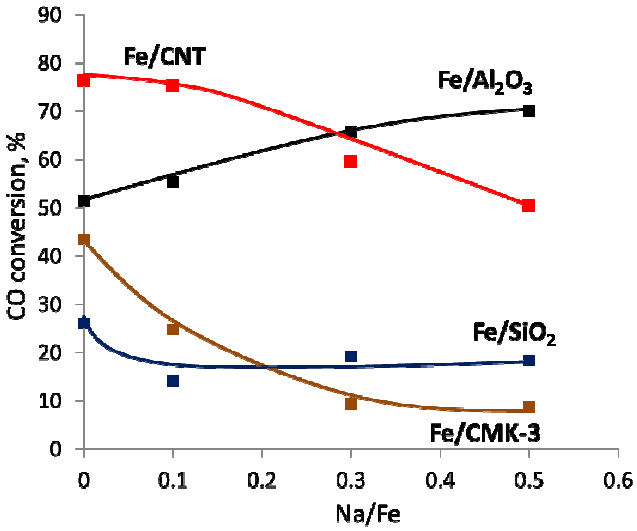

Figure 7-9. CO conversion depending on Na/Fe ratio (P = 2 MPa, H_2/CO=2.1, GHSV=16 L h^{-1} g^{-1}, T = 573 K)

Table 7-2. Catalytic properties of catalysts after CO pretreatment (P = 2 MPa, H_2/CO=2.1, GHSV=16 L h^{-1} g^{-1}, T = 573 K)

Catalysts	X_{CO},%	ITY, [a]	S_{CO2}, %	Product distribution, (% C, CO_2 free)				Olefin/ Parafin C_2-C_4	Olefin/ Parafin C_5-C_{12}
				CH_4	C_2-C_4 olefins	C_2-C_4 paraffins	C_{5+}		
Fe/CNT	76.4	39.9	26.9	9.6	17.9	14.2	58.3	1.3	0.7
Fe/CNT(0.1)	75.3	39.3	39.4	3.4	18.1	3.3	75.2	5.5	4.5
Fe/CNT(0.3)	59.6	31.1	38.0	3.4	16.7	3.0	76.9	5.6	4.9
Fe/CNT(0.5)	50.6	26.4	37.7	3.8	17.0	3.0	76.2	5.7	4.9
Fe/SiO_2	26.1	13.6	12.5	10.2	19.5	10.5	59.8	1.9	1.1
Fe/SiO_2(0.1)	14.2	7.4	13.3	7.1	18.3	4.2	70.4	4.4	2.6
Fe/SiO_2(0.3)	19.2	10	17.7	5.4	19.2	3.3	72.1	5.9	4.2
Fe/SiO_2(0.5)	18.5	9.7	17.9	4.9	19.4	3.2	72.5	6.1	4.7
Fe/Al_2O_3	51.4	26.8	18.7	8.2	16.8	10.8	64.2	1.6	0.6
Fe/Al_2O_3(0.1)	55.3	28.9	20.7	7.4	16.5	11.8	64.3	1.4	0.7
Fe/Al_2O_3(0.3)	65.7	34.3	25.5	5.7	15.9	8.5	69.9	1.9	0.9
Fe/Al_2O_3(0.5)	70.1	36.6	31.8	5.1	18.2	7.1	69.6	2.6	1.5
Fe/CMK-3	42.3	22.1	18.4	10.1	16.1	18.9	54.9	0.9	0.3
Fe/CMK-3(0.1)	24.5	12.8	25.2	5.6	23.7	4.4	66.3	5.4	3.2
Fe/CMK-3(0.3)	10.9	5.7	20.7	4.2	14.4	2.5	78.9	5.8	5.2
Fe/CMK-3(0.5)	10.1	5.3	21.2	4.8	24.1	3.5	67.6	6.9	5.8

[a] ITY represents moles of CO converted per mol of Fe per hour (mol_{CO} mol_{Fe}^{-1} h^{-1}).

Presence of Na results in the significant changes in the activity of the catalysts depending on the sodium content (Figure 7-8 and 7-9). The activity decreases for the catalysts Fe/CNT, Fe/CMK-3 and Fe/SiO_2. The effect of the ratio 0.1 Na/Fe is already significant over Fe/CMK-3 and Fe/SiO_2. It is interesting to note that in comparison with all other catalysts activity of Fe/Al_2O_3 increases with increase of the amount of sodium.

Besides activity the other most important parameter during modification of Fe catalysts is the ratio of light olefins to paraffins. Table 7-2 shows selectivities to olefins and paraffins with their ratio for all catalysts. The selectivity to C_2-C_4 olefins varies in the range 15-24 % and for C_2-C_4 paraffins 3-19 % with the ratio in the range 1 to 7. It might be observed that addition of Na leads to significant suppression of paraffins formation. However, the catalysts show different activity and in order to have correct comparison of selectivities the catalysts have been tested at different space velocities.

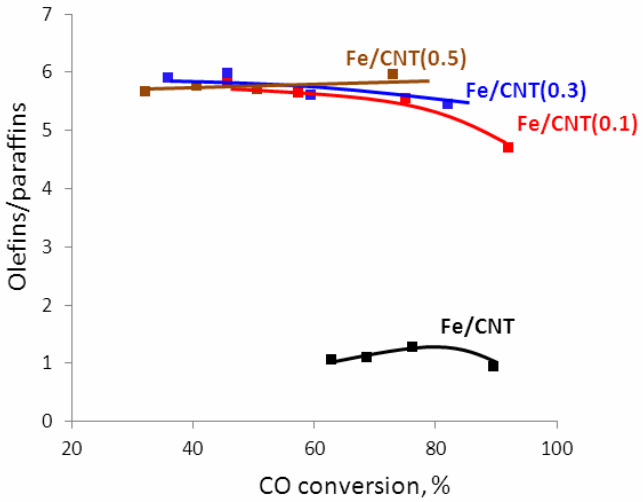

Figure 7-10. Olefins to paraffins ratio in C_2-C_4 range depending on CO conversion over Fe/CNT catalysts.

Figure 7-10 shows olefins to paraffins ratios for (C_2-C_4 range) Fe/CNT at the different conversion of CO. It might be observed that on the parent Fe/CNT the ratio increases with increase of the conversion of CO from 1.0 to 1.3 possibly due to decrease of the partial pressure of H_2. Decrease of the ratio at the high conversion might be explained by decrease of the coverage of the active sites by CO which results in rapid increase of the hydrogenation activity over catalysts without and in the presence of sodium. Addition of sodium results in significant suppression of paraffins formation with the ratio of olefins to paraffins about 6. It is interesting to note that the ratio of olefins to paraffins for the different amount of sodium is

almost the same for the different conversions of CO. The formation of paraffins might have two main reasons: secondary hydrogenation of olefins and direct formation of paraffins over iron carbides. In the case of the first reason of paraffins formation the selectivity to olefins should increase in the same value like decrease of the selectivity to paraffins.

Figure 7-11 shows comparison of the selectivities to olefins and paraffins for hydrocarbons in the range C_3-C_{12} with increase of the sodium content over Fe/CNT catalyst at the similar conversions. The situation is changing with increase of the chain length. In the case of light hydrocarbons (C_3-C_6) the selectivities to olefins and paraffins decrease with addition of sodium. It indicates on the parallel mechanism of the formation of olefins and paraffins over carbides. Long chain hydrocarbons show different mechanism with gradual increase of the selectivity to olefins with decrease of the selectivity to paraffins indicating on the secondary hydrogenation of the formed olefins. This fact might be explained by synthesis of short and long chain hydrocarbons over different sites.

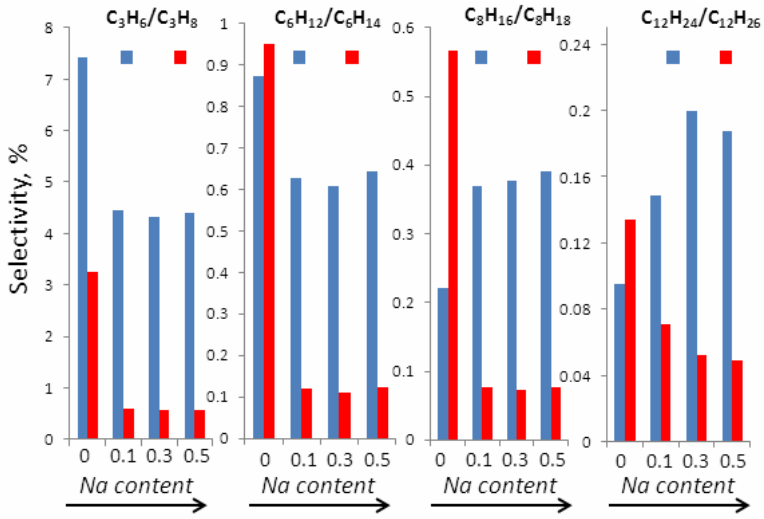

Figure 7-11. Comparison of the selectivities to olefins and paraffins in C_3-C_{12} range over Fe/CNT with different Na/Fe ratios.

Figure 7-12 shows the olefins/paraffins ratio depending on the conversion of CO at the same space velocity. It might be observed that there are 3 different situations depending on the type of the catalysts. In the case of Fe/CNT addition of small amount of Na leads to increase of the ratio to the maximum value 6 which does not change at the higher amount of sodium. In the case of CMK-3 and SiO_2, addition of sodium results in the strong deactivation of the catalysts with simultaneous linear increase of the ratio of olefins to paraffins. The maximum ratio at the highest amount of sodium corresponds to the ratios over sodium treated

Fe/CNT catalysts. In the case of alumina based systems addition of sodium results besides slight increase of the conversion to the low increase of the ratio till 2.5.

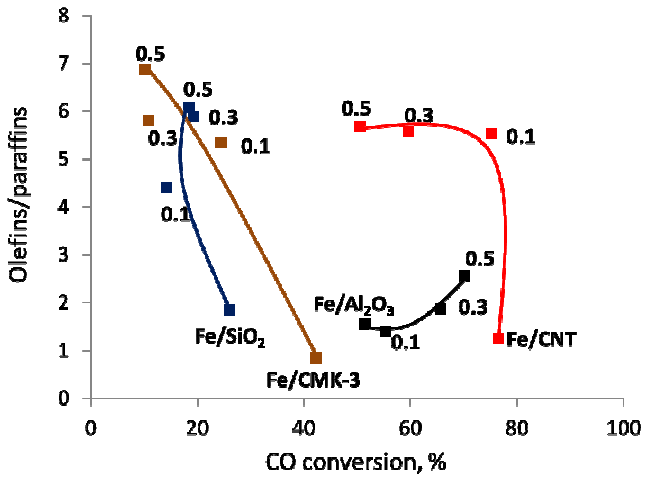

Figure 7-12. Olefins to paraffins ratio in C_2-C_4 range depending on CO conversion over catalysts.

These results might be explained by physicochemical analysis of the catalysts. Indeed, impregnation of sodium to Fe supported over alumina results according to FTIR and XRD mainly in the interaction of Na with alumina (Figure 7-2 and 7-3) with similar reactivity of carbide (Figure 7-7). Increase of the activity might be due to partial displacement of Fe interacting with alumina by sodium. Finally, sodium does not modify significantly the properties of carbide on the surface which results in the similar selectivities to olefins and paraffins.

Decrease of the activity over Fe/SiO_2 might be easily explained by partial interaction of Fe with sodium which is supported by the XRD, TPD of CO_2 and hydrogenation tests. The lower reactivity of silica support in comparison with alumina results in the promotion of the interaction of sodium with Fe with formation of the mixed oxide which should not be reactive in FT synthesis. Increase of the amount of sodium results in the gradual deactivation of the catalysts due to interaction with the higher amount of Fe on the surface. Increase of the selectivity to olefins might be provided by those carbide sites which do not interact directly with sodium but are in the close proximity to the formed mixed oxides. The similar situation has been observed over the catalyst on the basis of high surface area carbon support CMK-3.

The strong suppression of the paraffins formation over Fe/CNT without significant loss of activity might be explained by modification of the carbide properties by sodium but

without its deactivation by formation of mixed oxide. Indeed, results of XRD analysis show preservation of carbide after addition of sodium. TPD of CO_2 shows presence of pure Na_2O on the surface. Hydrogenation of carbide indicates just on the decrease of the carbide reactivity possibly due to modification of its electronic state. Thus, CNT strongly stabilizes the iron carbide inside of the nanotubes without its strong deactivation in the presence of sodium.

The stability of carbides has been checked by addition at the end of test flow of low concentrated HCl aqueous solution (0.1 M) (Figure 7-8). The results show that all the catalysts have been fast deactivated due to formation of iron chloride. The only stable catalyst which did not show any deactivation was Fe supported over CNT. This fact indicates on high stability of the carbide in CNT to transformation into chloride. It explains high stability of carbides in Fe/CNT to interaction with Na with formation of mixed oxides. It is interesting to note that in comparison with parent Fe/CNT the catalysts deactivate fast after sodium modification. This fact might be explained by the presence of sodium on the surface of carbides which should transform into chloride and block access to carbide.

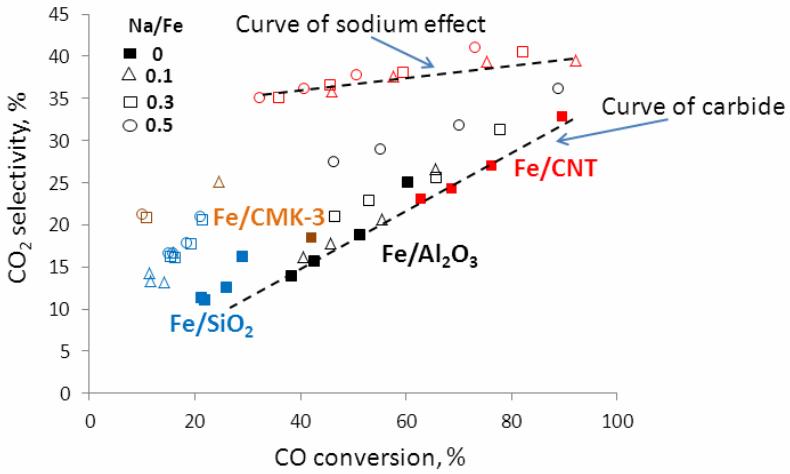

Figure 7-13. CO_2 selectivity depending on CO conversion over parent and sodium promoted catalysts.

The CO_2 and methane selectivities are plotted as functions of carbon monoxide conversion on the catalysts (Figure 7-13 and 7-14). Higher carbon monoxide conversion leads to higher CO_2 selectivities over the catalysts without sodium. The selectivity to CO_2 increases from 10 % at 20 % CO conversion till 30 % at 90 % CO conversion. The curve is general for all the catalysts. Increase in the CO_2 selectivity at higher CO conversion might be explained by higher contribution of the WGS reaction due to increase in the amount of water.

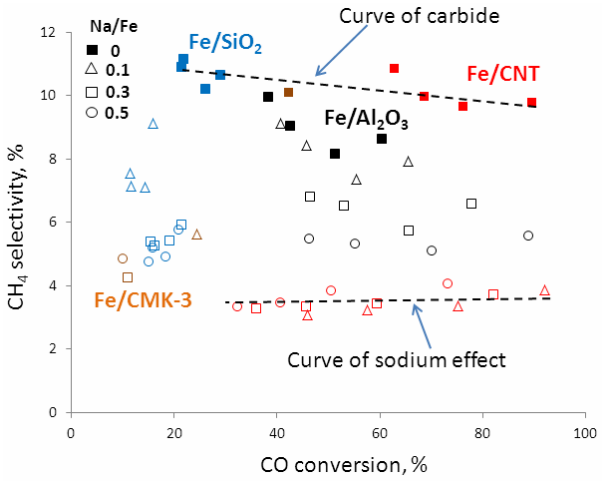

Figure 7-14. CH_4 selectivity depending on CO conversion over parent and sodium promoted catalysts.

Addition of sodium results in increase of the selectivity to CO_2, due to the promotion of WGS reaction by basic sites [3, 31]. The highest effect is observed in the case of Fe/CNT catalysts. It is interesting to note that there is almost no difference between different catalysts with different amount of Na. Thus, even small amount of Na gives high basicity to the catalyst due to the non-active support and stable iron carbide. The angle of the selectivity curve for Na promoted Fe/CNT catalysts is significantly smaller. Indeed the selectivity increase only from 35 to 40 % for the same range of conversions. It means that almost all formed water participates in the WGS with formation of CO_2 which is result of high basicity and accessibility of the sodium.

Figure 7-14 shows methane selectivity depending on the conversion of CO. The selectivity to methane is in the range 10 to 3 %. The highest selectivity is observed over parent catalysts without sodium. The selectivity slightly decreases with increase of CO conversion which might be explained by suppression of methanation in the presence of higher water pressures at high CO conversion. The selectivity to methane decreases with increase of the amount of sodium for all catalysts as opposed to CO_2 selectivity. The effect is the result of the suppression of the hydrogenation activity of Fe in the presence of sodium. The maximum effect is again observed over Fe/CNT with the lowest selectivity to methane (3 %). The effect in this case is similar for all concentrations of sodium and does not change with increase of CO conversion.

Thus, the effect of sodium appears for all light hydrocarbons and might be predicted knowing the type of support. However, analysis of the products shows that the selectivity to C_5^+ products is comparable with the amount of light products and contributes 50-80 % of the

total amount of hydrocarbons on the carbon basis (Table 7-2). It is important to understand the distribution between olefins and paraffins in these products. Figure 7-15 shows the olefins to paraffins ratio for C_5-C_{12} hydrocarbons for parent and sodium promoted catalysts. It might be observed that the ratio of olefins to paraffins decreases with increase of the carbon numbers over all catalysts. The contribution of olefins for the long chain hydrocarbons for sodium promoted catalysts decreases in the row: Fe/CNT>Fe/SiO_2>Fe/CMK-3>Fe/Al_2O_3. The ratio of olefins to paraffins also decreases for the parent catalysts. Thus, this is general effect of FT synthesis over Fe based catalysts and sodium just enhances it suppressing hydrogenation. Due to the fact that paraffins formation for long chain hydrocarbon is mainly secondary process of olefins hydrogenation (Figure 7-11) this effect might be explained by higher probability of hydrogenation with increase of the chain length. Indeed, increase of the chain length should facilitate adsorption and thus hydrogenation of olefins. The high ratio of olefins to paraffins over Fe/CNT(0.5) is the result of the strong modification of carbide by sodium.

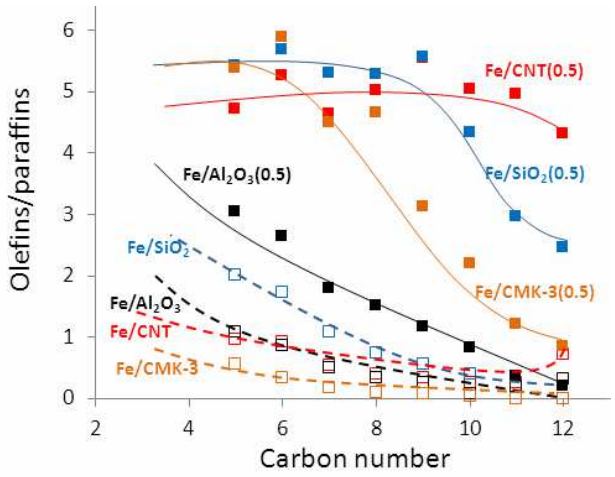

Figure 7-15. Olefins to paraffins ratio for C_5–C_{12} hydrocarbons depending on carbon number

Besides analysis of the gas phase hydrocarbons liquid products have been collected and analyzed. Figure 7-16 shows the distribution of paraffins and olefins before and after modification by sodium. The wax after catalysis over parent samples contains only paraffins which have two peaks with the maximum at 15 and 25 carbon atoms. The first peak might be result of the partial cracking due to the quite high temperature of the reaction. It explains also the highest contribution of this peak over alumina based catalyst which should possess much higher acidity in comparison with other supports. Addition of sodium results in the appearance of significant amount of olefins which is comparable with paraffins only in the case of Fe/CNT(0.5). The olefins form the peak with the maximum at 20 carbon atoms and

the peak of paraffins shifts to the heavier hydrocarbons. For silica the contribution of hydrocarbons almost does not change and for alumina the contribution of first peak decreases probably due to the deactivation of acid sites.

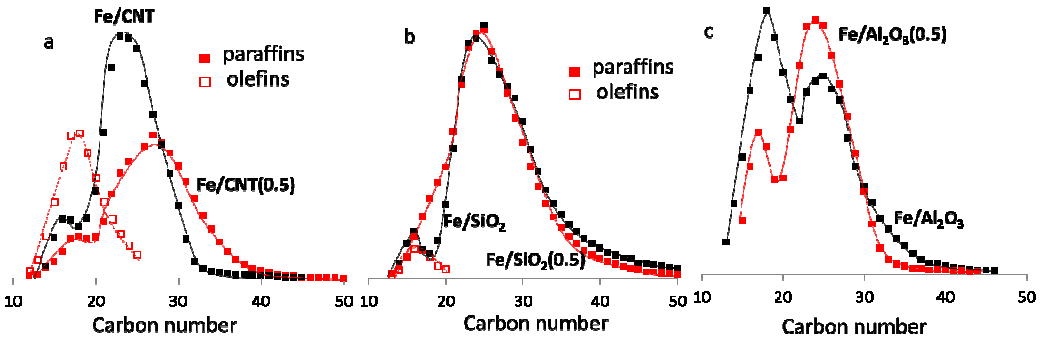

Figure 7-16. Distribution of olefins and paraffins in the wax for parent catalysts and promoted with Na.

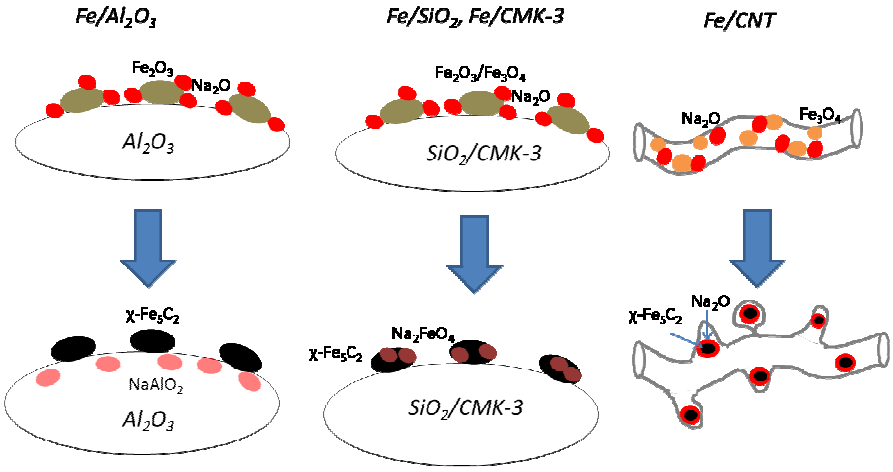

Figure 7-17. The effect of Na on Fe based catalysts over different supports.

Figure 7-17 displays an outline of the evolution of different iron species over supported catalysts after addition of sodium. In the case of active support like alumina impregnation of Fe with sodium with activation in CO results in the preferential formation sodium aluminate and separate iron carbide with weak interaction between them. In the case of more inert supports like silica and CMK-3 impregnation of sodium results in the strong interaction between Fe and Na with formation of mixed oxides inactive in FT synthesis. The effect of Na might be related mostly due to presence of mixed oxide in the close proximity to carbide particle. In the case of CNT iron carbide is strongly stabilized by CNT with effect of sodium

over the surface of carbide particles. It leads to the highest selectivity to olefins for the whole range of products, CO_2 and the lowest selectivity to methane.

7.3 Conclusion

Silica and carbon supported iron catalysts show the presence of different iron species at different catalyst preparation and activation stages. After iron nitrate decomposition, Fe_2O_3 was a dominant phase in the silica supported catalysts, while magnetite was the main phase in carbon materials. Catalyst activation in carbon monoxide results in conversion of both Fe_2O_3 and Fe_3O_4 into mostly χ-Fe_2C_5 carbide. The extent of carbidization seems to be higher in carbon supported catalysts.

Lower catalytic performance of silica supported catalysts in high temperature FT synthesis was due to lower extent of their carbidisation. Higher activity was observed on the catalysts supported by carbon nanotubes and active carbon, which is probably due to the interaction between residual magnetite and iron carbide. Silica and carbon supported catalysts did not show any noticeable differences in selectivity.

7.4 Reference

[1] H.M. Torres Galvis, K.P. de Jong, ACS catal., 3 (2013) 2130-2149.

[2] S. Li, S. Krishnamoorthy, A. Li, G.D. Meitzner, E. Iglesia, J. Catal., 206 (2002) 202-217.

[3] X. An, B.-s. Wu, H.-J. Wan, T.-Z. Li, Z.-C. Tao, H.-W. Xiang, Y.-W. Li, Catal. Commum., 8 (2007) 1957-1962.

[4] M.C. Ribeiro, G. Jacobs, B.H. Davis, D.C. Cronauer, A.J. Kropf, C.L. Marshall, J. Phys. Chem. C, 114 (2010) 7895-7903.

[5] S. Li, A. Li, S. Krishnamoorthy, E. Iglesia, Catal. Lett., 77 (2001) 197-205.

[6] M. Saglam, Ind. Eng. Chem. Res., 28 (1989) 150-154.

[7] T.C. Bromfield, N.J. Coville, Appl. Catal. A, 186 (1999) 297-307.

[8] H.M. Torres Galvis, A.C.J. Koeken, J.H. Bitter, T. Davidian, M. Ruitenbeek, A.I. Dugulan, K.P. de Jong, J. Catal., 303 (2013) 22-30.

[9] J. Abbott, N.J. Clark, B.G. Baker, Applied Catalysis, 26 (1986) 141-153.

[10] J. Gaube, H.F. Klein, Appl. Catal. A, 350 (2008) 126-132.

[11] J.-B. Li, H.-F. Ma, H.-T. Zhang, Q.-W. Sun, W.-Y. Ying, D.-Y. Fang, Fuel Process. Technol., 125 (2014) 119-124.

[12] X. An, B. Wu, W. Hou, H. Wan, Z. Tao, T. Li, Z. Zhang, H. Xiang, Y. Li, B. Xu, F. Yi, J. Catal. Mol. Catal. A: Chem., 263 (2007) 266-272.

[13] G. Ertl, H. Knözinger, F. Schüth, J. Weitkamp, Handbook of Heterogeneous Catalysis II, Wiley-VCH Verlag GmbH Co, 2008.

[14] H.M. Torres Galvis, J.H. Bitter, C.B. Khare, M. Ruitenbeek, A.I. Dugulan, K.P. de Jong, Science, 335 (2012) 835-838.

[15] H.M. Torres Galvis, J.H. Bitter, T. Davidian, M. Ruitenbeek, A.I. Dugulan, K.P. de Jong, J. Am. Chem. Soc., 134 (2012) 16207-16215.

[16] S. van Donk, A.H. Janssen, J.H. Bitter, K.P. de Jong, Catal. Rev., 45 (2003) 297-319.

[17] W. Chen, X. Pan, X. Bao, J. Am. Chem. Soc., 129 (2007) 7421-7426.

[18] P.G. Pai, S.S. Chao, Y. Takagi, G. Lucovsky, J. Vac. Sci. Technol. A, 4 (1986) 689-694.

[19] C. Su, D.L. Suarez, Clay. Clay. Miner., 45 (1997) 814-825.

[20] M.T. Hernández, M. González, J. Eur. Ceram. Soc., 22 (2002) 2861-2868.

[21] F. Domine, B. Piriou, J. Non-cryst. Solids., 55 (1983) 125-130.

[22] R.L. Frost, D.L. Wain, W.N. Martens, B.J. Reddy, Spectrochimca Acta A Mol. Biomol. Spectrosc., 66 (2007) 1068-1074.

[23] G. Kwak, J. Hwang, J.-Y. Cheon, M.H. Woo, K.-W. Jun, J. Lee, K.-S. Ha, J. Phys. Chem. C, 117 (2013) 1773-1779.

[24] W. Chen, Z. Fan, X. Pan, X. Bao, J. Am. Chem. Soc., 130 (2008) 9414-9419.

[25] Istadi, N.A.S. Amin, J. Catal. Mol. Catal. A: Chem., 259 (2006) 61-66.

[26] J. Liu, P. Ying, Q. Xin, C. Li, Appl. Spectrosc., 53 (1999) 40-42.

[27] M. Yamamura, H. Okado, K. Chaki, T. Wakatsuki, K. Inaba, S. Suzuki, T. Yoshinari, Catal. Today, 24 (1995) 299-300.

[28] D.M. Stockwell, D. Bianchi, C.O. Bennett, J. Catal., 113 (1988) 13-24.

[29] H. Matsumoto, C.O. Bennett, J. Catal., 53 (1978) 331-344.

[30] V.V. Ordomsky, K. Cheng, M. Virginie, B. Legras, P.A. Chernavskii, V.O. Kazak, C. Cordier, S. Paul, Y. Wang, A.Y. Khodakov, Appl. Catal. A, (2014) 10.1016/j.apcata.2014.1009.1033.

[31] W. Ngantsoue-Hoc, Y. Zhang, R.J. O'Brien, M. Luo, B.H. Davis, Appl. Catal. A, 236 (2002) 77-89.

Chapter 8. General Conclusions and Perspectives

Fischer–Tropsch synthesis is a key reaction in the utilization of non-petroleum carbon resources, such as methane (natural gas, shale gas, and biogas), coal, and biomass, for the sustainable production of clean liquid fuels, lower olefins and other valuable chemicals from synthesis gas. Selectivity control is one of the biggest challenges in FT synthesis. Recently, many efforts have been made to develop novel FT catalysts with high selectivity towards desired products. The understanding of key factors determining the activity and selectivity is crucial for the rational design of efficient catalysts.

This thesis was performed at “Unité de catalyse et de chimie du solide” (UCCS), USTL, France, and the Department of Chemistry, XMU, China in 2011-2014. The thesis has been focused on two topics: (1) design of bifunctional catalysts which integrated CO hydrogenation metals and acidic zeolites, with the target to transform syngas into gasoline fraction with high selectivity; (2) the effects of pore size, support and Na promoter in high temperature FT synthesis over supported iron catalysts.

8.1 General Conclusion

8.1.1 Bifunctional FT catalysts for C_{5-11} isoparaffins

We have demonstrated that bifunctional catalysts capable of catalyzing both CO hydrogenation to heavier hydrocarbons and hydrocracking/isomerization of the heavier hydrocarbons are very promising for the production of middle-distillate liquid fuels (Figure 8-1). The use of an acid zeolite in combination with a conventional FT catalyst or a FT-active metal could catalyze the production of C_{5-11} gasoline-range hydrocarbons with a high C_{iso}/C_n ratio.

A simple way to prepare zeolite-based bifunctional FT catalyst is the direct loading of an active FT metal onto a zeolite. But the active metal particles located on the external surface of zeolites are poorly dispersed and a larger part of the acid sites inside the long microporescannot be used effectively. Besides, diffusion limitation inside the micropores can also cause high selectivities to undesirable CH_4 and C_{2-4} hydrocarbons. The utilization of mesoporous zeolites can overcome the disadvantages of zeolites. The use of a mesoporous zeolite instead of a microporous zeolite significantly increases the selectivity to C_{5-11}

hydrocarbons, and decreases those to CH_4 and C_{2-4}. The C_{5-11} selectivity over the mesoporous zeolite-supported Ru or Co catalyst can be significantly higher than the maximum 45% expected from ASF distribution.

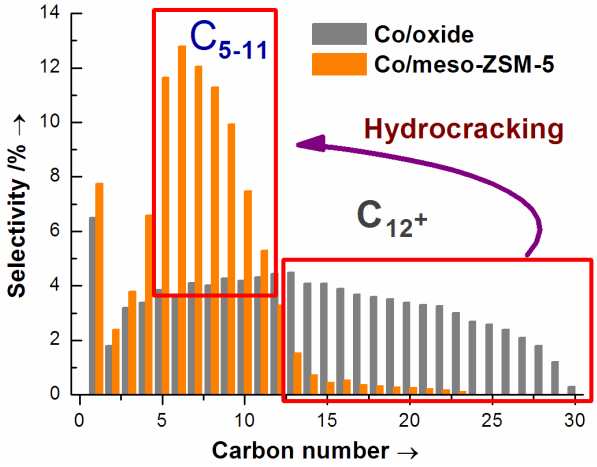

Figure 8-1. Product distributions for conventional Co/oxide catalyst and bifunctional Co/H-meso-ZSM-5 catalyst

Through systematic studies using catalysts with tuned mesoporosity and Brønsted acidity, we clarified that the presence of mesoporosity mainly contributed to suppressing the formation of lighter hydrocarbons, while the Brønsted acidity was required for the hydrocracking of heavier ($C_{\geqslant 12}$) hydrocarbons. A 70% selectivity to C_{5-11} hydrocarbons with a ratio of *iso*-paraffins to *n*-paraffins being 2.3 could be attained from syngas over the Co/H-meso-ZSM-5-0.5M catalyst. Using *n*-hexadecane as a model molecule of heavier hydrocarbons, we confirmed the role of Brønsted acidity in the hydrocracking/isomerization reactions and the role of mesoporosity in determining the product selectivity. The uniform Co nanoparticles with optimized sizes loaded on mesoporous zeolites with strong Brønsted acidity and tuned mesoporosity are promising catalysts for the production of gasoline-range hydrocarbons from syngas.

8.1.2 Pore size effects for supported iron catalysts

A combination of characterization techniques and catalytic tests indicates a strong impact of pore sizes in mesoporous silicas on the structure of supported iron species and their catalytic performance in high temperature FT synthesis. After calcination with flow air, Fe_2O_3 is the dominant phase in the catalysts. Compared with activation with H_2, for iron catalysts CO is kind of preferable activation gas, which could reduce iron oxIde to iron carbide.

Smaller pores in mesoporous silicas lead to higher iron dispersion with low extent of carbidization during catalyst activation. Strong interaction was found between small pore silica and iron species. An increase in pore size results in larger iron particles which exhibit however higher extent of carbidization. The magnetization intensity of activated catalysts is correlated with catalyst pore size. The larger pore catalysts possess higher magnetization intensity. The magnetic characterization shows that the iron carbides are the main magnetic phases after activation. Catalytic performance of iron catalysts supported by mesoporous silicas seems to be attributed to the presence of Hägg iron carbide (χ-Fe_5C_2).

The catalytic performance of iron nanoparticles in the catalysts with different pore size principally correlates with the extent of iron carbidization, while higher dispersion of iron oxide in calcined catalysts supported by smaller pore mesoporous silicas is detrimental for carbon monoxide hydrogenation activity, because of poor iron reducibility and low concentration of iron carbide species these catalysts after activation. The hydrocarnon selelctivity is also affected by the pore size in the silicas supports. Lower CH_4 and higher C_5^+ selectivities were observed on large pore supports. The olefin to paraffin ratio was about 1.2-1.9 in large pore catalysts compared to 0.6-0.7 smaller pore counterparts. In our study, although the C_5^+ selectivity is below 50% and C_2-C_4 lowers olefin selectivity is below 20%, we tend to acquire some fundamental information about pore size effect and activation behavior on pure iron catalyst.

8.1.3 Support Effect on Performace of Iron FT Catalysts

Silica and carbon supported iron catalysts show the presence of different iron species at different catalyst preparation and activation stages. The chemical composition and texture of the support affect iron particle size, iron carbidization, catalyst phase composition and finally catalytic performance in carbon monoxide hydrogenation. After iron nitrate decomposition, α-Fe_2O_3 was a dominant phase in the silica supported catalysts, while the carbon materials contain magnetite/maghemite. Catalyst activation in carbon monoxide results in conversion of iron oxides into mostly χ-Fe_2C_5 carbide. The extent of carbidization seems to be higher in carbon than in silica supported catalysts. Compared with Fe/CMK-3S and Fe/AC catalysts with small iron particles (3.8-6.7 nm), the Fe/CMK-3L and Fe/CNT with large particle sizes (12.3-15.4 nm) possesses higher magnetization intensity. The iron carbides are strongly stabilized by CNT support, which can encapsulate the carbide nanoparticles in depth. It is interesting that the encapsulation is enhanced after catalytic reaction.

The catalytic performance iron species on different supports principally depends on iron phase composition rather than on iron dispersion. For the Fe/CNT and Fe/AC catalysts with high activity, residual Fe_3O_4 was found in these catalysts after reation. However, the catalytic tests conducted with catalysts containing only Fe_3O_4 showed no catalytic activity. So the higher activityover Fe/CNT and Fe/AC could be explained by formation of these carbide-magnetite composites. The higher CO conversion leads to higher CO_2 selectivity but lower CH_4 selectivity. The increased CO_2 selectivity was due to the promoted WGS reaction, while lower CH4 selectivity could be explained by suppression of methanation in the presence of higher water pressures at high CO conversion level. The olefin/paraffin ratio for all studied catalysts is in the range of 0.6-1.4, with slight increase with the increase of CO conversion. In genaral, the preferable supports for iron catalysts are carbon materials, which can facilitate the generation of iron carbides and stabilize the iron carbide nanoparticles during the reaction.

8.1.4 Na Effect on Performace of Iron FT Catalysts

Silica and carbon supported iron catalysts show the presence of different iron species at different catalyst preparation and activation stages. The iron nitrate decomposition behavior of silica and carbon supported catalysts are different. After decomposition, Fe_2O_3 was a dominant phase in the silica supported catalysts, while magnetite was the main phase in carbon materials. Presence of sodium does not lead to significant changes in the sizes of oxide nanoparticles for all the supported catalysts, while the sizes are affected by the types of supports. Catalyst activation in carbon monoxide results in direct conversion of both Fe_2O_3 and Fe_3O_4 into mostly χ-Fe_2C_5 carbide. The extent of carbidization seems to be higher in carbon supported catalysts.

For Fe/Al_2O_3 catalysts promoted with Na, most of the Na interacted with the support. Inactive aluminate was found in these catalysts. The catalytic performance of promoted and unpromoted Fe/Al_2O_3 was similar. In the case of more inert supports like silica and CMK-3 impregnation of sodium results in the strong interaction between Fe and Na with formation of mixed oxides inactive in FT synthesis. The effect of Na might be related mostly due to presence of mixed oxide in the close proximity to carbide particle. In the case of CNT iron carbide is strongly stabilized by CNT with effect of sodium over the surface of carbide particles. It leads to the highest catalytic activity and selectivity to olefins for the whole range of products, CO_2 and the lowest selectivity to methane. The Fe/CNT with Na addition also shows better stability, which could be explained by modification of the carbide properties by

Na, without formation of inactive mixed oxides.

The characterizaitons show that carbon based catalysts possess strong basicity due to the presence of sodium over the catalyst, especially for Fe/CNT catalyst. CO tends to absorp on catalyst with strong basicity. The decoration of Na is significant even at the Na/Fe ratio of 0.1. Excessive presence of sodium would decrease the catalytic activity, which means strong interaction of sodium with carbide. The addition of Na leads to significant suppression of paraffins formation and causes high olefin and C_5^+ selectivity. Due to the fact that the paraffins formation is mainly secondary reaction of olefins hydrogenation, the general effect of Na addition just enhances its suppressing hydrogenation. The CH_4 selectivity can be suppressed to 3.4% in Fe/CNT catalyst with Na addition. The inceased olefin/paraffin ratio often goes with with inceased C_5^+ selelctivity, which restricts the enhancement of C_2-C_4 olefin selelctivity

8.2 Perspectives

8.2.1 Bifunctional FT catalysts

Control of the secondary hydrocracking reactions by using new solid-acid materials with tailored porosity and acidity is a very useful strategy to tune the product selectivity of FT synthesis. By using this strategy, excellent selectivities to $C_{5\text{-}11}$ and $C_{10\text{-}20}$ hydrocarbons have been achieved over mesoporous beta, mesoporous ZSM-5 and acidic CNT supported catalysts. Future studies are needed to further improve the selectivity to liquid fuels under industrially relevant conditions. The catalyst cost should also be considered. In this context, the development of more selective and highly stable Fe- or Co-based or multifunctional catalysts should be future research targets. Furthermore, the design of core–shell-structured bimetallic active phases with highly active and selective metals in the shell and less expensive metals in the core, such as Fe@Co and Fe@Ru, is also a useful strategy. New multifunctional catalytic systems composed of this type of active phase and solid-acid materials will make interesting targets.

Acidic zeolites have a large family with different morphology, pore size and adidity. By coupling different zeolites and hydrogenation metal, the distribution of cracking products could be tuned, and this process have been realized in petroleum cracking industry. Thus, it is reasonable to construct bifuctional FT catalysts with higher selelctivity to diesel-range and even jet-fuel-range hydrocarbons. Nonetheless, zeolites with strong Brønsted acid sites are

easily deactivated by carbon deposition, which may block active sites for secondary reaction. Future studies must overcome this difficulty.

8.2.2 Effect of support and promotion for iron catalysts in FT synthesis

Reaearchers have attempted to develop iron-based catalysts to direct the product selectivity of the FT synthesis toward the high production of lower olefin for several decades. However, this process has not been industrialized yet. One of the obstacles is the lower selectivity to C_{2-4} lower olefins. The active species, catalyst support and promoters have strong impact on catalytic performance of FT synthesis. Alkaline additives are supposed to be electron donor to increase the selectivity of the light olefins, and different supports also have a crucial effect on the selectivity of these catalysts due to the different electronic interactions between them. Unfortunately, the increased olefin/paraffin ratio often goes with the shift of product to heavy hydrocarbons, which restricts the lower olefin selectivity. Therefore, we should continue to study the mechanism of supports and promoters, and increase selectivity to olefin products, not to CH_4, CO_2 or heavy hydrocarbons. The suitable support should facilitate the formation of active phase, probably magnetic iron carbides. Then, the selected promoter should increase the olefin/paraffin ratio. Reaction conditions could be tuned to shift the product distribution to lower hydrocarbons, probably relative high temperature and high gas velocity. Meanwhile, with the development of materials science, more catalytic materials and preparation techniques should be introduced to design FT catalysts with expectation. The long-term tests are also necessary for FTO catalysts.

Author Introduction

Kang Cheng was born in December 1986 in Jiangsu Province, China. After obtaining his BSc degree in light chemical engineering from the University of Sichuan in 2009, he continued his studies in physical chemistry at Xiamen University, under the guidance of Prof. Qinghong Zhang and Prof. Huilin Wan. In 2011, he started the PhD programs in Xiamen University in the group of Prof. Ye Wang. During November 2012 to November 2013, he was sponsored by China Scholarship Council to study at Unité de catalyse et de chimie du solide (UCCS), Université des Sciences et Technologies de Lille, France. His PhD thesis was co-supervised by Dr. Andrei Khodakov, Dr. Mirella Virginie and Prof. Ye Wang. His research, described in this thesis, focuses on the development of novel catalysts for Fischer-Tropsch synthesis.

List of Published Papers

[1] **K**. **Cheng**, J. Kang, S. Huang, Z. You, Q. Zhang, J. Ding, W. Hua, Y. Lou, W. Deng, Y. Wang, Mesoporous beta zeolite-supported ruthenium nanoparticles for selective conversion of synthesis gas to C_5-C_{11} isoparaffins. *ACS Catal.*, **2012**, *2*, 441-449.

[2] **K. Cheng**, M. Virginie, V. V. Ordomsky, C. Cordier, P. A. Chernavsky, M. I. Ivantsov, S. Paul, Y. Wang and A. Y. Khodakov, Pore Size Effects in High Temperature Fischer-Tropsch Synthesis over Supported Iron Catalysts, *J. Catal.*, **2014**, DOI: 10.1016/j.jcat.2014.12.007.

[3] **K. Cheng**, L. Zhang, X. Peng, J. Kang, Q. Zhang, and Y. Wang, Transformation of syngas into gasoline-range hydrocarbons over mesoporous H-ZSM-5 supported cobalt catalyst, *Chem. Eur. J.*, **2014**, DOI: 10.1002/chem.201405277. (inside cover paper)

[4] **K. Cheng**, V.V. Ordomsky, M. Virginie, B. Legras, P.A. Chernavskii, V.O. Kazak, C. Cordier, S. Paul, Ye Wang and A.Y. Khodakov, Support effects in high temperature Fischer-Tropsch synthesis on iron catalysts, *Appl. Catal. A*, **2014**, *488*, 66-77.

[5] Q. Zhang, **K**. **Cheng**, J. Kang, Y. Wang, Fischer–Tropsch Catalysts for the Production of Hydrocarbon Fuels with High Selectivity. *ChemSusChem*, **2014**, *7*, 1251-1264. (Mini Review)

[6] J. Kang, **K**. **Cheng**, L. Zhang, Q. Zhang, J. Ding, W. Hua, Y. Lou, Q. Zhai, Y. Wang, Mesoporous Zeolite-Supported Ruthenium Nanoparticles as Highly Selective Fischer-Tropsch Catalysts for the Production of $C_{(5)}$-$C_{(11)}$ Isoparaffins. *Angew. Chem. Int. Ed.*, **2011**, *50*, 5200-5203.

[7] **K. Cheng,** V. V. Ordomsky, B. Legras, M. Virginie, S. Paul, Y. Wang and A. Y. Khodakov, The effect of Na addition over different supports in high temperature Fischer-Tropsch

synthesis on iron catalysts, **2014**, in preparation.

[8] X. Peng, **K. Cheng**, J. Kang, Q. Zhang, and Y. Wang, Impact of Hydrogenolysis on Product Selectivity in Fischer-Tropsch Synthesis: Mesoporous Zeolite Y-Supported Cobalt Nanoparticles for Selective Production of Diesel Fuel, *Angew. Chem. Int. Ed.*, **2015**, DOI: 10.1002/ange.201411708. (co-first auther, VIP Paper)

[9] V.V. Ordomsky, B. Legras, **K. Cheng**, S. Paul and A.Y. Khodakov, Role of carbon atoms of supported iron carbides in Fischer-Tropsch synthesis, *Catal. Sci. Technol*, 2015, DOI: 10.1039/C4CY01631A

Conference papers

[1] **K. Cheng**, L. Zhang, S. Huang, Q. Zhang, Y. Wang, J. Ding, J. Kang, W. Hua, Y. Lou, Mesoporous ZSM-5-Supported Cobalt Nanoparticles as Efficient Bifunctional Fischer-Tropsch Catalysts for the production of C_5-C_{11} Isoparaffins, *SynFuel 2012 Symposium*, Germany, **2012**, oral presentation.

[2] **K. Cheng**, L. Zhang, Q. Zhang, Y. Wang, Highly Selective Bifunctional Fischer-Tropsch Catalysts Based on Mesoporous Zeolites, *15th International Congress on Catalysis*, Germany, **2012**, poster, 1.11-7035.

[3] **K. Cheng**, X. Peng, L. Zhang, Q. Zhang, W. Deng, Y. Wang, Mesoporous ZSM-5-Supported Co Nanoparticles as Efficient Fischer-Tropsch Catalysts for Selective Production of C_5-C_{11} Isoparaffins, *11th European Congress on Catalysis*, France, **2013**, oral presentation, S9-T4-OR-06.

[4] **K. Cheng**, M. Virginie, A. Y. Khodakov, Q. Zhang, Y. Wang, Fischer-Tropsch synthesis over metal carbide catalysts, *2rd Franco-Chinese Synposium: Catalysis and Sustainable Development*, France, **2013**, oral presentation.

[5] **K. Cheng**, M. Virginie, V. V. Ordomsky, C. Cordier, P. A. Chernavskii, V. I. Kazak, Q. Zhang, Y. Wang and A. Y. Khodakov, Pore Size Effects in High Temperature Fischer-Tropsch Synthesis over Iron Catalysts Supported by Mesoporous Silicas, *The Seventh Tokyo Conference on Advanced Catalytic Science and Technology*, Japan, **2014**, oral presentation, O-A09.

[6] **K. Cheng**, M. Virginie, V. V. Ordomsky, P. A. Chernavskii, M.I. Ivantsov, Q. Zhang, Y. Wang and A. Y. Khodakov, Novel Iron Fischer-Tropsch Catalysts Supported on Ordered Mesoporous Carbons with Low Methane Selectivity, *The Seventh Tokyo Conference on Advanced Catalytic Science and Technology*, Japan, **2014**, poster, GP1033.